University of Bath

PHD

Development of III-N Site-Controlled Quantum Dots
(Alternative Format Thesis)

Armstrong, Robert

Award date:
2022

Awarding institution:
University of Bath

Link to publication

Alternative formats
If you require this document in an alternative format, please contact:
openaccess@bath.ac.uk

Copyright of this thesis rests with the author. Access is subject to the above licence, if given. If no licence is specified above, original content in this thesis is licensed under the terms of the Creative Commons Attribution-NonCommercial 4.0 International (CC BY-NC-ND 4.0) Licence (https://creativecommons.org/licenses/by-nc-nd/4.0/). Any third-party copyright material present remains the property of its respective owner(s) and is licensed under its existing terms.

Take down policy
If you consider content within Bath's Research Portal to be in breach of UK law, please contact: openaccess@bath.ac.uk with the details. Your claim will be investigated and, where appropriate, the item will be removed from public view as soon as possible.

Download date: 24. Jul. 2023

Development of III-N Site-Controlled Quantum Dots

submitted by

Robert Fraser Armstrong

for the degree of Doctor of Philosophy

of the

University of Bath

Department of Electronic and Electrical Engineering

November 2022

COPYRIGHT

Attention is drawn to the fact that copyright of this thesis/portfolio rests with the author and copyright of any previously published materials included may rest with third parties. A copy of this thesis/portfolio has been supplied on condition that anyone who consults it understands that they must not copy it or use material from it except as licenced, permitted by law or with the consent of the author or other copyright owners, as applicable.

This thesis may be made available for consultation within the University Library and may be photocopied or lent to other libraries for the purposes of consultation with effect from 11/2022. Access to this thesis/portfolio in print or electronically is restricted until 11/2022.

Signed on behalf of the Doctoral College..

Abstract

Quantum information science (QIS) has the potential to revolutionise technology and, indeed, modern day life as as we know it. Applications range from vastly improved encryption technology in the form of quantum key distribution to revolutionising computation in the form of quantum computing. Development of the latter could drastically change the ability to model many systems from financial markets to the folding of proteins. There are a number of different technologies being developed to realise quantum information applications ranging from photonics to superconducting architectures. Semiconductor quantum dots are particularly attractive solutions for QIS applications due to the possibility of their integration with existing, mature, semiconductor technology. In particular, site-controlled quantum dots (SCQDs) could revolutionise QIS by wafer scale fabrication and growth of large numbers of quantum devices. This is as SCQD technology has the ease of scalability whereby it can be developed on smaller samples and then extended to be manufactured on the wafer scale.

The III-N's materials group hold a great deal of promise for site-controlled quantum dot applications owing to their large band-gap off-sets and large excitonic binding energies allowing for the creation of quantum devices that could operate at or close to room temperature. The GaN/AlN system is particularly promising for such endeavours, however, due to the difficulty in creating uniform arrays of AlN sites to house GaN quantum dots, this area of the field has been largely unexplored.

In this thesis, regular arrays of spatially predetermined, faceted AlN nanostructures, suitable to house GaN quantum dots are realised. This is achieved by combining top-down dry etching with bottom-up regrowth. The dynamics of the regrowth step are explored and explained. This is followed by the exploration of a combination of dry and wet etching, in order to again realise periodic arrays of AlN nanostructures. The aspect ratios of the dry etched nanostructures after wet etching were investigated and a model of the wet etching dynamics was proposed. Additionally, thermal etching and an investigation of the impact of the annealing conditions and fabrication processing was undertaken. It was found that the cleaning stages of the fabrication had a significant impact on the resulting morphology of the GaN after thermal etching. In all three cases, sites arguably suitable to house site-controlled quantum dots were achieved.

Finally, site-controlled GaN quantum dot growth was attempted on the AlN nanostructures developed. Whilst the growth of site-controlled quantum dots at the specifically

targeted regions of the nanostructures wasn't achieved, it is certainly arguable that there was site-controlled quantum dot growth in other regions of the nanostructures.

III-N SCQDs hold immense promise to further advance QIS technology at temperature achievable by thermoelectric cooling or even room temperature. Further development of the field could lead to the realisation of more practical QIS devices that could become far more ubiquitous in everyday life and technology. Thus, III-N SCQDs present an exciting field of present day and future research.

Dedication

I would like to dedicate this thesis to the memory of Matthew Reeves. Matt was my housemate and friend for 3 years as we both undertook our PhDs. Matt tragically, and unexpectedly, died in July 2021. He was a talented physicist, and we had many interesting and stimulating conversations. Matt, you should have been here submitting your thesis alongside us all from our CDT cohort. I hope this thesis goes some way to do your memory justice.

Your friend, Rob.

Acknowledgements

This work was made possible due to the support of a number of people at the University of Bath in addition to other research groups and the Centre for Doctoral Training in Condensed Matter Physics (CDT-CMP). Financially, this includes the funding received from EPSRC for the CDT-CMP and funding from the "Manufacturing nano-engineered III-nitride semiconductors" EPSRC grants EP/M015181/1 & EP/M022862/1. There are many individuals that deserve explicit thanks, without of which, this work would not have been possible.

Firstly, I want to thank my supervisor Dr Philip Shields. His faith and support of me during the course of this PhD were vital for the guidance and excellent supervision of the research undertaken. Not only did you give me the opportunity to undertake this research project, you taught me how to be a researcher, in a rigorous scientific fashion. I have certainly learnt a great deal from you, your knowledge and experience is remarkable. Without your troubleshooting and skill we would have struggled to keep our MOVPE growth reactor operational for any significant amount of time. Thank you. My transferable skills were also enhanced significantly by your supervision, from helping to teach undergraduate students to presenting at conferences. I would also like to thank my second supervisor Professor Daniel Wolverson for his faith in me and supervision during the optical characterisation stages of my PhD.

I want to give special thanks to Dr Pierre-Marie Coulon, who instructed me in many aspects of of nanofabrication and MOVPE growth. Additionally, your support and discussions helped me grow as a researcher. I, one day, hope to be as effective a researcher as you.

I would also like to thank all the training provided on different nanofabrication tools by both Dr S. Wedge and Dr S. Sivaraya. Your training was excellent. I would also like to further thank Dr S. Sivaraya for the continued help in maintaining the MOVPE growth reactor.

It is also important to mention the vital role our collaborators at the University of Strathclyde played in this work, specifically the cathodoluminscence characterisation. Specifically, I want to thank Professor Robert Martin, Dr Jochen Bruckbauer and Dr Pavlos Bozinakis for all the characterisation they performed on my samples and the discussions that followed.

I was lucky enough to benefit from the expertise of many academics from the CDT-CMP, specifically during my first year of the CDT before applying for my PhD project. This helped me prepare for a research project and I learnt a lot in the process.

Special thanks goes to those who have supported my well being during the course of this PhD, namely Shane Craig and Keely Strange. Additionally, I want to thank Dr David Sands, Dr Ali Adawi, Dr Jean-Sebastian Bouillard and Joules Cornes from the University of Hull where I was an undergraduate. Without your support and encouragement I would not be where I am today. Thank you.

I want to thank my colleagues and friends Dr Pierre Chausse, Dr Kowsar Shabazi and Dr Jayanta Sarma for the pleasant and positive working environment we shared together and the interesting conversations we had.

I also want to thank my family. Your support over the last 4-5 years and indeed my life has been critical for me to undertake such a challenging endeavour as a PhD. I want to especially thank my father Derek and my mother Christine who spent many hours talking with me on the phone and giving me encouragement when I have found things difficult. Thank you so much.

Finally, I want to thank you, the reader. I hope that you enjoy reading this thesis and find the III-N material group and III-N site-controlled quantum dots just as fascinating and enthralling as I do.

Publications and Conferences

Publications

First author:

Chapter 4: Armstrong R, Coulon PM, Bozinakis P, Martin RW, Shields PA. Creation of regular arrays of faceted AlN nanostructures via a combined top-down, bottom-up approach. Journal of Crystal Growth. 2020 Oct 15;548:125824.

Co-author:

Coulon PM, Damilano B, Alloing B, Chausse P, Walde S, Enslin J, Armstrong R, Vézian S, Hagedorn S, Wernicke T, Massies J. Displacement Talbot lithography for nano-engineering of III-nitride materials. Microsystems & Nanoengineering. 2019 Dec 2;5(1):1-2.

Gamża M, Abrami P, Gammond LV, Ayres J, Osmond I, Muramatsu T, Armstrong R, Perryman H, Daisenberger D, Das S, Friedemann S. Pressure-induced reconstructive phase transition in Cd 3 As 2. Physical Review Materials. 2021 Feb 26;5(2):024209.

Conferences

Oral presentations:

In person:

UKNC 2020. Creation of a topographical surface for the site-control of III-N quantum dots

Virtual:

UKNC 2022. Sculpturing of AlN nanostructures to realise sites for quantum dots

Declaration

Declaration of any previous submission of the work

The material presented here for examination for the award of a higher degree by research has not been incorporated into a submission for another degree.

Declaration of authorship

I am the author of this thesis, and the work described therein was carried out by myself personally, with the exception of which is detailed below.

All of the sample fabrication and characterisation in the results chapters was performed by myself unless otherwise specified. However, specific mention of any work not undertaken by myself will now be mentioned.

Figure 4-8 in Chapter 4, diagrammatically explaining the growth dynamics of our nanostructures was produced by Dr Pierre Chausse under my instruction. Additionally, the SEM image presented in Figure 4-7 was taken by Dr Pavlos Bozinakis at the Univeristy of Strathclyde.

In Chapter 6, the samples shown in Figure 6-1 (b) and (c) were fabricated by Dr Pierre-Marie Coulon. The sublimation runs upon the samples and the SEM characterisation was carried out by myself.

Finally, in Chapter 7, all of the presented cathodoluminescence measurements and the corresponding SEM maps were carried out by Dr Jochen Bruckbauer at the University of Strathclyde.

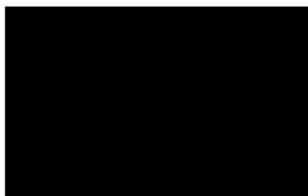

Robert Armstrong

Contents

Abstract **1**

Dedication **3**

Acknowledgements **4**

Publications and Conferences **6**

Declaration **7**

Table of Contents **8**

List of Figures **14**

List of Tables **37**

Abbreviations **39**

1 Introduction and Background - Quantum Dots **43**

1.1 Aims and objectives 43
1.2 Quantum dots - definitions and basic information 44
1.3 Historical quantum dot information 45
1.4 Types of quantum dots and how they are created 46
1.5 Self-assembled quantum dots 50
1.5.1 Droplet epitaxy and modified droplet epitaxy 50
1.5.2 Stranski-Krastanov grown quantum dots 51
1.5.3 Self-assembled, Stranski Krastanov quantum dots, specific to AlN/GaN or AlGaN/GaN 53
1.6 Site-controlled quantum dots 58

1.7 Quantum information processing 59
1.7.1 Quantum information processing - applications for site-controlled quantum dots 59
1.7.2 Fine structure splitting 60
1.7.3 The second order correlation function 61
1.8 Brief overview of the III-N materials group 63
1.9 Wurtzite crystal structure – a closer observation 65
1.10 Disadvantages of the III-N's 66
1.10.1 Quantum Confined Stark Effect 66
1.10.2 Defects and dislocations in the III-N material group 69
1.10.3 Overall assessment of the disadvantages 71
1.11 Advantages of the III-N materials group when creating SCQDs . . 71
1.12 Conclusion 72

2 Experimental Techniques 73
2.1 Growth 73
2.1.1 MOVPE growth of the III-N materials group 74
2.1.2 Considerations for MOVPE AlN growth 77
2.2 Fabrication Techniques 79
2.2.1 Photolithography 79
2.2.1.1 Principle of photolithography 79
2.2.1.2 Displacement Talbot Lithography 80
2.2.2 Mask Deposition techniques 83
2.2.2.1 Electron beam evaporation 83
2.2.2.2 Plasma formation via an RF field for Plasma Enhanced Chemical Vapour Deposition 84
2.2.2.3 Plasma Enhanced Chemical Vapour Deposition 84
2.2.3 Etching and cleaning 85
2.2.3.1 Plasma based dry etching 85
2.2.3.2 Inductively Coupled Plasma etching 88
2.2.3.3 Wet etching 90
2.2.4 Chemical cleaning steps 91
2.2.4.1 Piranha Clean 91
2.2.4.2 Aqua Regia 91
2.2.4.3 Buffered Oxide Etch 91
2.2.5 Processes 92

2.2.5.1 Lift-off Process 92
2.2.5.2 Nanohole Fabrication Process 94
2.3 Characterisation 96
2.3.1 Microscopy 96
2.3.1.1 Electron Microscopy 96
2.3.1.2 Scanning Electron Microscopy 98
2.3.1.3 Atomic Force Microscopy 98
2.3.2 Luminescence spectroscopy 102
2.3.2.1 Photoluminescence 102
2.3.2.2 Considerations for low temperature and high temperature measurements 102
2.3.2.3 Photoluminescence of GaN quantum dots 104
2.3.2.4 Cathodoluminescence 106
2.3.2.5 Cathodoluminescence of quantum dots 108
2.4 Conclusion 113

3 III-N Site-Controlled Quantum Dots 114
3.1 Historical or less scalable methods used to achieve site controlled quantum dots 114
3.1.1 Jet probe tomography 114
3.1.2 Nanoimprint lithography 116
3.1.3 Electron beam lithography 118
3.1.4 Dry etching of Quantum well sandwiches 120
3.1.5 Summary of historical or less scalable techniques and reasons for these methods being undesirable in certain circumstances 123
3.2 Selective area growth 124
3.2.1 Selective area growth - general principle 124
3.2.2 Selective area growth – what has been achieved in the literature – basic pyramids 125
3.2.3 Selective area growth – more exotic results 131
3.2.4 Selective area growth – disadvantages 139
3.3 Other routes for achieving site-controlled III-N quantum dots . . . 140
3.4 Conclusion 140

4 Top-down, bottom-up approach for the creation of uniform arrays of facted AlN nanostructures 141

4.1 Introduction 141
4.2 Statement of Authorship 142
4.3 Background & motivation 142
4.4 Materials & Methods 145
4.5 Growth parameter investigations 147
4.5.1 The effect of growth temperature 148
4.5.2 The effect of V/III ratio 152
4.5.3 The effect of the increase in growth time 155
4.6 Discussion of Growth Mechanisms 157
4.7 Optimisation of AlN nanostructures for applications 160
4.8 Conclusions 163
4.9 Final comments 163

5 Wet etching of AlN to realise sites for quantum dots 164
5.1 Introduction 164
5.2 Introduction to wet etching 164
5.2.1 Introduction to the principle of wet etching of AlN 165
5.2.2 Wet etching of AlN – what has been realised before in the literature 168
5.2.3 Gaps in the current knowledge of AlN wet etching 168
5.3 Wet etching of planar AlN 169
5.4 Wet etching of dry etched AlN structures 172
5.4.1 Wet etching of dry etched nanoholes 172
5.4.2 Study of the effect of wet etching on deliberately tapered dry etched nanoholes 175
5.4.2.1 Tapered dry etching of nanoholes 175
5.4.2.2 Wet etching of the tapered nanoholes 178
5.4.3 Wet etching dynamics of the nanohole structures 183
5.4.4 Wet etching of dry etched shallow nanorod samples 186
5.4.5 Wet etching of dry etched nanorods of different aspect ratios188
5.4.6 Wet etching dynamics of nanorod structures 191
5.5 Conclusions 195

6 Selective area sublimation of GaN as a route towards site-controlled quantum dots 196
6.1 Introduction to selective area thermal etching and its advantages . 196
6.2 Initial reproduction attempts of reproducing sublimation sites . . 202

6.3 Study of the impact of fabrication/processing and reactor cleanliness 207
6.3.1 Temperature study on sample G1 207
6.3.2 Effect of reduction of contamination via cleaning of reactor parts on sample G1 207
6.3.3 Deep etch study (N_2:H_2 carrier gas) 207
6.3.4 Fabrication of a new template 209
6.3.5 Further cleaning with long O_2 descum 209
6.3.6 Further cleaning with a short O_2 descum 210
6.3.7 Effect of reactor pressure 210
6.3.8 Effect of the CHF_3 dry etching 210
6.4 Initial study into the effect of sublimation time on the morphology of the samples 212
6.5 Impact of oxidisation on the sample surface and resulting sublimation 214
6.6 Further optimisation of the sublimation time 217
6.7 Study of the effect of the piranha clean duration 217
6.8 Mechanism of GaN sublimation under N_2 221
6.9 Conclusions of the sublimation investigation and final optimisations 227

7 Attempted site-controlled GaN quantum dot growth 229
7.1 Introduction 229
7.2 GaN growth rate 231
7.3 GaN growth on AlN nanopyramids 234
7.4 Initial Investigation of GaN growth on AlN nanorods 238
7.5 Further investigation of GaN growth on AlN rods – room temperature and low temperature PL 247
7.6 Sample 5420 in more detail 253
7.7 Conclusion 255

8 Summary, Conclusion, Future Exploration and Outlook 257
8.1 Introduction 257
8.2 Summary and conclusions of research completed 258
8.3 Possible future exploration 260
8.4 Outlook and final comments 261

Bibliography 263

Appendix 1 286

Appendix 2 **291**

Appendix 3 **294**

List of Figures

1-1 This figure shows the density of states for 3D (bulk), 2D (quantum well), 1D (quantum wire) and 0D (quantum dot) semiconductor systems. Reprinted/adapted by permission from Copyright Clearance Center: Springer Nature, 'Single-particle states of quantum dots': Quantum Dots by Professor Lucjan Jacak, Dr. Arkadiusz Wöjs, Dr. Paweł Hawrylak Copywrite @ Springer-Verlag Berlin Heidelberg 1998. ([1]). 45

1-2 In (a), a schematic of the cross-section of the quantum well system grown by Reed et al. [2] is shown (Reprinted with permission from [2]. Copyright [1986], American Vacuum Society). The photoluminescence spectra in (b) is that of a quantum well (2 DOF), quantum wire (1 DOF) and quantum dot (0 DOF). The spectra are normalised for comparative observation. All photoluminescence measurements were taken at 4.4 Kelvin. Reprinted with permission from [2]. Copyright [1986], American Vacuum Society. 46

1-3 This figure shows a TEM image of the quantum dots synthesised in [3]. As can be seen there is a small spread in sizes and shape which will render different emission properties. The scale bar represents 50 nm (figure reproduced and unmodifed from [3] supplementary information under Creative Commons Attribution 4.0 International Licence https://creativecommons.org/licenses/by/4.0/). 47

1-4 In (a) is a quantum dot formed by electrodes, with the four inner electrodes squeezing electrons in the quantum-well layer into a quantum dot. The outer electrodes act as contacts for electron tunnelling in an out of the quantum dot (figure reproduced from [4]). In (b) there is a schematic of the device used by Ashoori et al. [5] for capacitance spectroscopy of few particle systems. The quantum dot is represented by the ellipse within the GaAs quantum well. Figure (b) is reprinted (Figure 1b) with permission from [5] R. C. Ashoori, H. L. Stormer, J. S. Weiner, L. N. Pfeiffer, S. J. Pearton, K. W. Baldwin, and K. W. West. Single-electron capacitance spectroscopy of discrete quantum levels. Phys. Rev.Lett., 68:3088–3091, May 1992. Copyright (2006) by the American Physical Society, https://doi.org/10.1103/PhysRevLett.68.3088. 49

1-5 This figure shows the three heteroepitaxial growth modes: (a) the 2D Frank-Van der Merwe growth mode, (b) the Stranski-Krastanov 2D-3D growth mode and (c) the purely 3D Volmer-Weber growth mode. For more information on the process in (b) see Figure 1-6 [6]. 52

1-6 This figure shows the evolution of a surface morphology during Stranski-Krastanov growth. In (a) the sample is shown before the deposition of a wetting layer. In (b) a small thickness, smaller than the lower critical thickness, of lattice mismatched material has been deposited. In (c) the amount of material deposited has exceeded the lower critical thickness leading to the spontaneous 3D island formation to relive the strain in the system [7]. In (d) growth is continued, once the layer thickness has surpassed the upper critical thickness, plastic deformation [7] occurs introducing defects into the system. In all Figures (a) - (d) the blue dashed line represents the lower critical thickness and the yellow the upper critical thickness. 54

1-7 Figure (a) shows a schematic of a single quantum dot based LED structure. Copyright © IOP Publishing (2014). Reproduced with permission from [8]. All rights reserved. In (b) a schematic of the green quantum dot laser mentioned is presented (Reprinted from [9], with permission of AIP Publishing. Copyright © 2011 American Institute of Physics). Figure (c) shows a schematic of a single photon emitting diode (reproduced from [10]. Copyright © 2003 WILEY-VCH Verlag GmbH & Co. KGaA, Weinheim). . . . 55

1-8 Schematic of the single electron transistor device creates by Nakaoka et. al. [11]. Also shown is an SEM image of the quantum dot between the electrodes and an AFM image of the self-assembled quantum dots after growth (Reprinted from [11], with permission of AIP Publishing, Copyright © AIP publishing 2007). 57

1-9 The figure on the left shows the biexciton state (denoted by XX) and the exciton state (denoted by X). In (a) fine structure splitting is present in the system with all four transitions having different energies meaning that entanglement is not possible. In (b) the biexciton (XX) and exciton (X) energies are tuned into resonance meaning the red transitions are equal to each other in energy as are the blue. This should allow entanglement of the emission which would be linearly polarised. In (c) the fine structure splitting in less than the linewidth and so the information encoded in the FSS is erased. This results in entanglement of the emitted photons which will be circularly polarised [12] (figure reproduced and unmodified from [12] under Creative Commons Attribution 2/0 International Licence https://creativecommons.org/licenses/by/2.0). 60

1-10 Figure (a) shows a typical Hanbury-Brown Twiss set-up for determining the second order correlation function for a sample (Reprinted from [13] supplementary material, with permission of AIP Publishing, Copyright © AIP Publishing (2013)). Figure (b) shows some typical second order correlation function data, in this case the value of $g^{(2)}(0)$ is found to be 0.36 (figure reproduced from [14], Copyright © 2008 WILEY-VCH Verlag GmbH & Co. KGaA, Weinheim). 62

1-11 This figure shows the autocorrelated histogram of a site controlled GaN quantum dot at 350 K. There is a suppression of coincidence counts at $\tau = 0$. This is clear evidence of anti-bunched light to great enough extent for the criteria of single photon emission [15]. Reprinted with permission from [15]. Copyright © 2016 American Chemical Society. 63

1-12 This figure shows a plot of the band gaps of AlN, GaN and InN for both wurtzite and zinc-blende crystal polytypes vs lattice constants (Reprinted from [16] Copyright © (2013) with permission from Elsevier). 64

1-13 Figure (a) shows the general wurtzite crystal structure. In (b) the zinc-blende crystal structure is shown. In (c) the rocksalt crystal structure is presented. All figures reprinted with permission from [17] © The Optical Society. 66

1-14 This figure shows the GaN wurtzite crystal structure with the Ga-polar face, on the left and the N-polar face on the right. Reprinted/adapted by permission from Copyright Clearance Center: Springer Nature, Properties and Advantages of Gallium Nitride by Daisuke Ueda, Copyright © 2017, Springer International Publishing Switzerland) figure reproduced from [18]). 67

1-15 Schematic of the band profiles and electron and hole wavefunctions two quantum well systems. On the left there is no internal field and so no changes to the band profile allowing for a good overlap in the electron and hole wavefunctions. On the right is the profile for a polar III-N quantum well. This illustrates how the internal fields separate the electron and hole wavefunctions leading to a reduction in radiative recombination efficiency [16]. Reprinted from [16], Copyright © (2013), with permission from Elsevier. 68

1-16 This Figure shows a schematic of the polar, non-polar and semi-polar crystal planes of wurtzite GaN (figure reproduced from [19] Copyright © 2008 WILEY-VCH Verlag GmbH & Co. KGaA, Weinheim). 68

1-17 Figure (a) shows a schematic of an edge dislocation whilst (b) shows a screw dislocation is shown. Both pertain to that of a cubic crystal. Reproduced from [20] under Creative Commons Licence (http://creativecommons.org/licenses/by/4.0/). Figure (c) again shows an edge dislocation on the left and a screw dislocation on the right from a slightly different perspective for additional clarity. Reprinted from [21], Copyright (1964) ©, with permission from Elsevier. Figure (d) shows the Burgers vector of a dislocation. It is represented by the failure of the closure between A' and E' in the circuit on the right resulting in distance, b. Here b is relative to the circuit on the left which represents a dislocation free crystal. 70

2-1 This figure shows the mechanisms at play during growth within the MOVPE reaction chamber. The reactions occurring during an MOVPE growth process are still not well understood, hence, this figure is a gross oversimplification. 76

2-2 This figure shows a schematic of the MOVPE growth reactor (AIX200RF) chamber. 77

2-3 This figure shows an attempt at selective area regrowth of AlN through a patterned SiN_x mask upon an AlN template. 77

2-4 In (a) a schematic of the DTL process is shown. Here a photoresist covered wafer is moved 1 Talbot length towards the mask during exposure. In (b) a calculated intensity distribution is shown for an illuminated linear grating. Two self-images are highlighted with dashed lines, a sub-image is highlighted with a dotted line. This sub-image has twice the frequency of the original grating. Both (a) and (b) reprinted and adapted with permission from [22] © The Optical Society. In (c), an AlN nanotube is shown made via patterning a ring into resist via utilising a high exposure dose with DTL to generate a secondary interference pattern. This is then transferred into a SiN_x mask which is used to dry etch a tube into an AlN template. 81

2-5 In (a), a basic schematic of a parallel plate RIE system is shown, highlighting the plasma, ion sheath and DC bias. In (b), on the left a high density plasma is shown with low pressure, small ion sheath and large mean free path. This is the sort of plasma generated via ICP. On the right a lower density plasma with higher pressure, larger ion sheath and smaller mean free path is shown. This is more typical of an RIE plasma. In (c), on the left, a high pressure etching schematic, whilst on the right a low pressure etching schematic. All images reprinted/adapted by permission from Copyright Clearance Center: Springer Nature, Dry Etching Technology for Semiconductors by Kazuo Nojiri Copyright © 2015, Springer International Publishing Switzerland ([23]). 86

2-6 This figure shows a basic schematic of the Oxford Instruments Plasma Technology PlasmaPro 100 Cobra ICP system used in this thesis. 89

2-7 Starting with the initial wafer, in 1, BARC (Back anti-reflection coating) and resist are spin coated upon the wafer with appropriate baking steps (a soft bake for the BARC). At 2, Displacement Talbot Lithography is used to expose the resist. In 3, the resist is developed for a long enough time such that an undercut is now present in the BARC layer. Electron-beam evaporation is used in 4 to first deposit a thin layer of Au followed by a thicker layer of Ni to realise a metal dot array. The sample is then put back into developer for the final part of this 'lift-off' procedure where the remaining resist and BARC are removed (or lifted-off) at stage 5. An O_2 based plasma etch can now able applied to remove any remaining unwanted organic material. This dot array in 6, is then used as a mask to etch into the underlying wafer. Finally, in 7, this is followed by an Aqua Regia, Piranha clean and Buffered oxide etch in that order, in order to remove the mental mask and clean the sample. 93

2-8 The process starts with the initial wafer. At stage 1 a SiN_x mask is deposited via PECVD. At stage 2 BARC (back anti-reflection coating) and photoresist are spin coating with appropriate baking steps. At 3, displacement talbot lithography is used to expose the resit. The sample is then developed in MF-CD26 developer at stage 4. The resist is then used as a dry etch mask for CHF_3 etching into the SiN_x mask. The organic layers are then removed and the SiN_x is used as a mask to dry etch into the underlying wafer. Finally, a buffered oxide etch (BOE) is used to remove the remaining SiN_x mask. 95

2-9 Figure (a) shows some of the detectable signals which can be used for imaging in SEM. Republished with permission of Taylor & Francis group ©, from [24]; permission conveyed through Copyright Clearance Center, Inc. Figure (b) shows the interaction volume and regions from which secondary electrons, backscattered electrons and X-rays may be detected. 97

2-10 Figure (a) shows a typical schematic of a SEM. Reprinted/adapted by permission from Copyright Clearance Center: Springer Nature, Transmission Electron Microscopy: Physics of Image Formation and Microanalysis by Ludwig Reimer Copyright © 1997, Springer-Verlag Berlin Heidelberg ([25]). Figure (b) show an SEM image of some nanostructures. 99

2-11 Figure (a) show a schematic of a typical AFM operational set-up. Figure (b) shows a schematic of AFM during contact mode. Figure (c) shows a schematic of AFM during tapping mode. Figure (d) shows an AFM image of some self-assembled (uncapped) GaN quantum dots upon a smooth, terraced AlN surface (Figures (a)-(c) modified and reproduced from [26] Copyright © 2010 Wiley Periodicals, Inc. Figure (d) reprinted from [27], with the permission from AIP Publishing, Copyright © 2006.) 101

2-12 This figure shows diagrammatically the process of photoluminescence. In this figure the colour schemes used are arbitrary. 103

2-13 In (a) a continuous wave (CW) PL spectrum of a sample with 10 planes of GaN/AlN QDs is shown. The QDs here have typical heights of 4.3 nm. In (b), PL spectra recorded at different delays after pulsed laser excitation is shown. Intensity of the spectra have been normalised. The dashed line indicates the CW PL peak from (a). For short delays, spectra are artificially broadened by the presence of long lived PL at 3.2 eV, arising from defects in the GaN buffer layer, whose short-lived PL line appears at 3.48 eV. Here (a) and (b) are reproduced from [28]. Copyright © 2008 Elsevier Masson SAS. All rights reserved. In (c), a plot of the measured radiative lifetimes as a function of PL peak for different quantum dot samples is shown. Solid lines show the calculated value of lifetime as a function of energy of the fundamental transition for an effective electric field of 7, 9 and 11 MV/cm respectively. The calculated QD height corresponding to the transition energies for 9 MV/cm electric field is shown at the top axis. Electron and hole energy levels and wavefunctions are sketched in the regimes dominated by the QCSE (left) and quantum confinement (right). Figure (c) is reprinted (Figure 3) with permission from [29]. Copyright (2006) by the American Physical Society, https://doi.org/10.1103/PhysRevB.73.113304. 105

2-14 Figure (a) shows a tilted SEM image of a III-N nanorod with an AlGaN single quantum well structure. In (a) ((b)) the corresponding intensity map over the single quantum well emission range of 4.9-5.5 eV is shown, measured with the use of Cathodoluminescence hyperspectral imaging (figure reproduced and unmodified from [30] under Creative Commons Attribution 4.0 International license). Figure (b) shows diagrammatically the process of cathodoluminescence. In this figure the colour schemes used are arbitrary. 107

2-15 This figure shows a schematic of the CL system used for the characterisation undertaken in this thesis. All the CL maps presented in this thesis were measured by Dr. Jochen Bruckbauer at the University of Strathclyde. 109

2-16 Here the images are constructed from parameters determined by fitting 3 Gaussian peaks to each of 150x150 spectra obtained during CL hyperspectral imaging. In (a) and (c) the peak intensity and energy respectively of the QW emission from the inclined facets are shown. In (b) the intensity of the apex-related 2.37 eV emission is shown. The line scan in (d), shows the QW peak energy varying across the pyramid. This was extracted via a horizontal line through the apex in (c). Reprinted from [31], with the permission of AIP Publishing, Copyright © (2004). 110

2-17 Monochromatic STEM-CL intensity images are shown recorded at spectral positions of a GaN/AlN quantum well in (a) and GaN/AlN islands (thought to be quantum dots) in (b) - (d). (a) - (e) are reprinted from [32], with the permission of AIP Publishing, Copyright © (2015). In (e) a panchromatic CL intensity map is presented, taken at 15 K. In (f) A TEM cross-sectional image of cubic GaN/AlN quantum dots is shown. The GaN quantum dots (highlighted by the white boxes) grow along the stacking faults. In (g) CL spectra of two single quantum dots are presented. Here (f) and (g) are reprinted from [33], Copyright © (2005), with permission from Elsevier. 112

3-1 This figure shows a schematic of the nano-jet probe device created by Ohkouchi et al. [34] for the creation of site controlled InAS quantum dots upon a GaAs barrier layer (Reprinted from [34]), Copyright © (2004), with permission from Elsevier). 115

3-2 Figure (a) shows an SEM image with an AFM image insert of the surface of the buffer layer prior to epitaxy as fabricated by UV-NIL. Figure (b) shows and AFM image of the site-controlled InAs quantum dots on the UV-NIL patterned GaAs buffer layer. Reprinted from [35], Copyright © 2010 Elsevier B.V. All rights reserved, with permission from Elsevier. 116

3-3 This figure shows a low temperature PL spectra of the reference sample and the nanopatterned sample. The insert shows the power-dependent micro-PL spectra of a single quantum dot on the pattern. Reprinted from [35], Copyright © 2010 Elsevier B.V. All rights reserved, with permission from Elsevier. 117

3-4 This figure shows a schematic of the EBL patterning process (Reprinted/adapted by permission from Spinger Nature : Springer eBook, Fabrication Processes for Sensors for Automotive Applications: A Review, by Aviru Kumar Basu, Shreyansh Tatiya, Geeta Bhatt et al. Copyright © (2019) [36]). 118

3-5 AFM image of the patterned wafer shown the preferential nucleation of the quantum dots within the holes. In insert (A) an AFM image of the hole array after the 10 nm GaAs buffer layer is deposited. In (B) an AFM image of the surface is presented after a thermal desorption of an oxide layer. In (C) there is shown the occupancy of the holes [37] (Reprinted from [37], Copyright © (2006), with permission from Elsevier). 119

3-6 In figure (a), a schematic of the quantum dot etched out of the quantum well structure is shown. The photoluminescence spectra in (b) is that of a quantum well (2 DOF), quantum wire (1 DOF) and quantum dot (0 DOF). The spectra are normalised for comparative observation. All photoluminescence measurements were taken at 4.4 Kelvin. Reprinted with permission from [2]. Copyright © [1986], American Vacuum Society. 121

3-7 Figure (a) shows a schematic of the quantum dot-pillars created in [38]. Figure (b) shows a planar SEM image of the array of quantum dot-pillars. Figure (c) shows an SEM image of a single quantum dot-pillar structure. Reprinted with permission from [38]. Copyright © 2015 American Chemical Society. 122

3-8 This figure shows the total lifetime reduction and integrated intensity enhancement for each individual dot measured, an excitation intensity of 283 W/cm^2 was used. Ag cavity – black circles, Al cavity – red squares and control – blue diamonds. Reprinted with permission from [38]. Copyright © 2015 American Chemical Society.122

3-9 This figure shows a schematic of the device created by Zhang. L et al. Reprinted (Figures 1a and 1b) with permission from [39] Lei Zhang, Chu Hsiang Teng, Pei Cheng Ku, and Hui Deng, Charge-tunable indium gallium nitride quantum dots, Physical Review B, 93(8):1–7, 2016. Copyright (2016) by the American Physical Society, https://doi.org/10.1103/PhysRevB.93.085301. 123

3-10 This figure shows SEM images of the SAG of GaN in [40] at (a) 1010 ^{o}C, (b) 1025°C and (c) 1050 ^{o}C [40]. All figures reproduced from [40], Copyright © (1995), The Physical Society of Japan and The Japan Society of Applied Physics). 126

3-11 Figure (a) shows the time evolution of the PL after the laser excitation pulse on an InGaN QD on GaN nanopyramid sample in [41]. Figure (b) shows the time-integrated PL spectra at 5K of the GaN/InGaN nanopyramids in [41] (both figures reproduced from [41]. Copyright © 2005 WILEY-VCH Verlag GmbH & Co. KGaA, Weinheim). 127

3-12 Figure (a) shows the power dependent PL of the InGaN/GaN nanopyramids. Figure (b) shows the low-temperature time-integrated PL spectra of the InGaN/GaN nanopyramids. Figure (c) shows the CL of the InGaN/GaN nanopyramids at the emission wavelengths stated [42] (Reprinted from [42] with the permission of AIP Publishing. Copyright © (2005) 128

3-13 Figure (a) shows the single photon PL on the structure described in [43], this has a clear broad quantum well signal with the discrete quantum dot signal at 2.61 eV (figure reproduced from [43]. Copyright © 2005 WILEY-VCH Verlag GmbH & Co. KGaA, Weinheim). Figure (b) is the two-photon excitation PL spectra for different excitation powers for the structure described in [43]. This shows a clear suppression of the quantum well signal when compared to (a) [43] (figure reproduced from [43]. Copyright © 2005 WILEY-VCH Verlag GmbH & Co. KGaA, Weinheim). Figure (c) shows micro-PL data for the metal coated InGaN/GaN quantum dots described in [44]. On the left is the spectra from single photon excitation and on the right that of two photon excitation (both carried out at a temperature of 7K). Reprinted (adapted) with permission from [44]. Copyright © 2018 American Chemical Society. 130

3-14 Figure (a) shows the micro-PL spectra of nanopyramids with single quantum dots grown at different temperatures. Figure (b) shows a polar plot for the normalised PL intensity against the recorder polarisation direction. Figure (c) shows the polarisation directions and ratios for the quantum dots shown in Figure (a) [45]. All figures reprinted with permission from [45]. Copyright © 2011 American Chemical Society. 132

3-15 Figure (a) shows the micro-PL spectra of an elongated hexagonal pyramid with quantum dot structure/s on the top ridge. The polariser analyses is set to $\theta_{max}(\theta_{min})$ by which the maximum (minimum) intensity of sharp emission peaks are detected. Figure (b) shows the spatially resolved monochromatic CL spectra of another GaN micropyramid with InGaN quantum dot structure/s on the top ridge (both figures reproduced and reformatted but unaltered from [46] (2014) under Creative Commons Attribution-NonCommercial-No Derivative Works 3.0 Unported License). . . . 133

3-16 This figure shows the PL spectra from a single quantum dot as detailed in [47] at different temperatures (Reprinted from [47], with the permission of AIP Publishing, Copyright © (2013)). 135

3-17 This figure shows an SEM image of the matrix of GaN nanorods with InGaN quantum dots. As can be seen there is a lack of homogeneity between different rods. Reprinted with permission from [48]. Copyright © 2017 American Chemical Society. 137

4-1 SEM images of the four nanostructures created. Shown are the deep etched nanorods (a) and nanoholes (c) ($\sim$ 1 µm deep) and shallow etched nanorods (b) and nanoholes (d) ($\sim$ 100 nm deep). The insets show the plan-view SEM images of the rods and the cross-section SEM images of the holes. 146

4-2 This figure shows what is meant by 'point-to-point' morphology (a) and 'edge-to-edge' morphology (b). 147

4-3 This figure shows some of the crystallographic planes in the wurtzite crystal structure. In (a) the polar c-plane ($\{0001\}$), the non-polar m-plane ($\{10\bar{1}0\}$) and the non-polar a-plane ($\{11\bar{2}0\}$) are shown. In (b) the semi-polar m-plane ($\{10\bar{1}2\}$) is shown. In (c) the semi-polar a-plane is shown a-plane ($\{11\bar{2}2\}$). 148

4-4 SEM images corresponding to the four templates grown at different temperatures. The green hexagons in (g)-(l) represent the original morphology of the dry etched structure superimposed on the regrown holes. The red arrows in (k) indicate some of the macrosteps that are discussed in the text. 150

4-5 SEM images of the four structures grown with different V/III ratios. The green hexagons in (j) - (l) and (n) - (p) represent the original morphology of the dry etched structure superimposed on the regrown holes. 152

4-6 SEM images corresponding to the growth on the four structures for different regrowth times. The green hexagons in (i)-(p) represent the original morphology of the dry etched structure superimposed on the regrown holes. 156

4-7 High resolution tilted SEM image of the sample from growth run 9 (sample in Figure 4-6 (d)). This SEM data was taken by Dr Pavlos Bozinakis, University of Strathclyde 156

4-8 Schematic representation of the convex and concave nature of all four structures. The images on the left are before regrowth and the images on the right after regrowth. The deep rod, shallow rod, deep hole and shallow hole structures are shown in (a), (b), (c) and (d) respectively. Blue arrows indicate convex morphology whereas yellow arrows indicate concave morphology. This figure was made by Dr Pierre Chausse for the publication [49]. 158

4-9 SEM images showing the morphology after different growth durations for the deep nanorod samples at a V/III ratio of $\sim$ 19000. (a) 60 min, (b) 120 min, (c) 180 min, (d) 210 min, (e) 270 min. . 161

4-10 Plot of the size of the top c-plane truncations as a function of rod growth time for the rods grown at V/III $\sim$ 7600 and $\sim$ 19000. The truncation sizes were extracted from SEM images using ImageJ with estimates of the measurement errors. 162

5-1 Figure (a) – (d) shows the etching mechanism for GaN in KOH. Reprinted from [50], with the permission of AIP Publishing, Copyright © 2001. Figure (e) shows an SEM image of a GaN sample where the N-polar regions have etched to form hexagonal nanopyrmaids and the Ga-polar regions have been left intact. Reprinted from [51], with the permission of AIP Publishing, Copyright © 2003. Figure (f) shows N-polar AlN after aqueous KOH etching. Reprinted from [52] Copyright © (2004), with permission from Elsevier. Figure (g) shows an SEM cross-section of hillocks on N-polar AlN after KOH etching. Figure (h) shows an SEM micrograph of N-polar AlN etched in KOH. Figures (g) and (h) reprinted from [53], Copyright © (2013), with permission from Elsevier. Figure (i) shows an NEMS resonator structure, where the freestanding AlN beam was prepared via KOH etching. Reproduced from [54]. Copyright © 2006 WILEY-VCH Verlag GmbH & Co. KGaA, Weinheim. 167

5-2 All figures here are SEM images. Figure (a) shows the planar AlN template with a patterned SiN_x mask upon it before any wet etching. The inset is the corresponding cross-section. Figure (b) shows the planar AlN template after 5 mins KOH etching at 150 ^{o}C. The blue hexagon in (b) shows the wet etched region of the planar AlN template. 170

5-3 Figure (a) shows a cross-section of the shallowest dry etched nanohole sample prior to wet etching. Figure (b) shows a cross-section of a nanohole of a deeper dry etch than in (a) prior to wet etching. Figure (c) shows a cross-section of the deepest dry etched nanohole sample prior to wet etching. In (a) - (c) the inset images are tilt views of the main images. In (d) the sample in (a) is shown after 2 minutes of KOH etching at 150 ^{o}C. In (e) the sample in (b) is shown after 2 minutes of KOH etching at 150 ^{o}C. In (f) the sample in (c) is shown after 2 minutes of KOH etching at 150 ^{o}C. The insets of (d), (e) and (f) shows part of the respective main figures in at a higher magnification 173

5-4 In this figure, a plot of the average length of the inclined planes as a function of initial dry etch depth is shown. The length of these planes were calculated by measuring the horizontal length of the planes and dividing this by the cosine of the average angle of the planes. The error bars in x represent the standard deviation of 10 measured values of the initial dry etch depth. The error bars in y represent the standard deviation of 10 measurements of the horizontal length of the planes. 174

5-5 Figure (a) shows Cl_2 based dry etching of AlN nanoholes at high etch temperature and standard DC bias. In (b) Cl_2 dry etching of AlN nanoholes is shown at low temperature with a high DC bias. The blue material represents the AlN. The green material represents etch by-products that passivate the sidewalls of the holes. The green arrows show if this layer is likely to evaporate. The blue arrows show the direction of the ions incident on the nanoholes. A thicker longer arrow represents a greater concentration of ions. . . 179

5-6 Figures (a) - (d) show SEM cross-sections of samples A, B, C and E respectively. Figures (e) - (h) show a planar SEM images of samples A - E respectively after 2 minutes of wet etching with KOH at 150 ^{o}C unless otherwise specified. The main image of Figure (f) shows a planar SEM image of sample B after a 1 minute KOH wet etch at 150 ^{o}C. Inset (i) shows the sample after 30 seconds wet etch and sample (ii) after 2 minutes wet etch under the same conditions as the main image. In all cases if the SiN_x mask had been present before the wet etch, it would have rapidly etched away, not affecting the morphology of the AlN nanostructures. . . 180

5-7 Figure (a) shows a plot of the c-plane triangle altitudes in as a function of the initial dry etch depths. Figure (b) shows a plot of the diameter of the bottom c-plane as a function of initial dry etch depth. Figure (c) shows a plot of the angle of the inclined planes as a function of the dry etch depth. All three plots show samples A, C and E. In (a)-(c) the dry etch depths and other feature dimensions were measured from cross-sectional SEM images. In (c) the angles of the planes were extracted from AFM maps of the samples (see Appendix 2). 182

5-8 In (a) three dry etch nanohole schematics are shown. Before indicates prior to wet etching, after indicates after wet etching. (i) is shallow such as the sample in Figures 5-3 (a) and (d), (ii) is deep such as the sample in Figures 5-3 (c) and (f), and (iii) is very deep such as sample B (Figures 5-6 (b) and (f)). Figure (b) shows the increase in the semi-polar plane size as dry etch depth increases, from the argument perspective of a triangle. Before indicates, before an increase in the dry etch depth and after refers to after an increase in the dry etch depth. All sides after are longer than before whilst the angle remains roughly the same. 184

5-9 In (a), an SEM image of a dry etched $\sim$ 100 nm tall nanorod after undergoing a 30 second etch with KOH at 120 ^{o}C is presented. The inset in (a) is an SEM image of the rods prior to wet etching. In (b) the same as in (a) is presented but this time the wet etch was for a total of 60 seconds. In (c) the same as (a)/(b) is presented but with a wet etch time of 120 seconds. In (d) an AFM image of the sample presented in (a) is displayed. In (e) an AFM image of the sample presented in (b) is displayed. In (f) an AFM image of the sample presented in (c) is displayed. In (g) the average angle of the nanopyramid semi-polar facets as a function of etch time is presented. In (h) a plot of the average height of the nanopyramids as a function of etch time is presented. In (i) a plot of the average diameter of the nanopyramids as a function of etch time is presented. 187

5-10 In (a) – (c) cross-sectional SEM images of nanorods after dry etching, mask removal and cleaning from nanorod samples fabricated at a 1.5 μm pitch are shown for 70 s, 240 s and 540 s of dry etching duration respectively. The insets are the corresponding planar SEM images of each sample. Figures (d) – (f) show AFM maps of the nanopyramidal structures revealed after KOH based wet etching of the samples shown in (a) – (c) respectively. The insets in (d) - (f) are magnified images of a single nanopyramid from the main figures of each map. In (g) - (i) tilted maps of the AFM maps shown in (d) - (f) respectively are presented. 189

5-11 In (a) a plot of the total height of the 1.5 μm pitch rods wet etched for 30 s as a function of the initial dry etched depth is shown. In (b) a plot of the mean angles of the inclined planes of the 1.5 μm pitch nanopyramids are shown as a function of the dry etch time for all three wet etch durations. 192

5-12 In (a) wet etching of the shallow dry etched nanorod. Top before/at the start of wet etching, bottom after a given amount of wet etching such as 30 s at 120 ^oC. Figure (b) shows the wet etching of a tall nanorod, again into a nanopyramid. Again the top is before/at the start of etching. The bottom is after a short period of wet etching such as 30 s at 120 ^oC. This nanopyramid is taller than in (a), in reality this is only slight but has been exaggerated in this figure for clarity. 193

6-1 In (a) sublimation of GaN under an N_2 atmosphere performed by Coulon et al. [55] is presented (Figure (a) is reproduced and cropped from [55] under Creative Commons Attribution 4.0 International License, http://creativecommons.org/licenses/by/4.0/). In (b) and (c) reproductions of this work from the same original template as that in (a) are presented at sublimation set temperatures of 875 ^oC and 925 ^oC respectively. All other sublimation conditions were the same as in Figure 6-1 (a). 198

6-2 Here a schematic of the fabrication process is presented. The planar GaN template is the starting wafer in 1. In 2, PECVD is used to deposit a $\sim$ 35 nm thick layer of SiN_x. In 3, BARC and photoresist are spin coated upon the template with appropriate baking steps. In 4, DTL is used to expose the resist with a specific periodic pattern. In 5, the resist is developed to reveal a hole array within the resist. In 6, CHF_3 based ICP dry etching is performed to transfer the pattern in the resist into the SiN_x hard mask. In 7, appropriate cleaning steps are taken to remove any remaining BARC, photoresist and oxides. 200

6-3 In (a) a planar SEM image of sample A1 (see Table 6.1) sample after initial cleaning is presented. In (b) and (c) initial sublimation tests are presented, at a set temperature of 900 ^{o}C in the latter. In (d) a planar image of the sample is shown after the second cleaning process (A2 in Table 6.1). In (e) sublimation upon sample A2 is shown. In (f) a planar image of the sample surface after the third cleaning process is shown (A3 in Table 6.1). In (g) a corresponding sublimation upon A3 is presented. Figure (h) shows the results of sublimation on a sample from A3 with the SiN_x mask stripped off via a BOE 5:1 treatment. All samples were sublimed at a set temperature of 875 ^{o}C unless otherwise specified. 203

6-4 This figure shows a summary of the possible hypotheses for the failure of sample A and in particular A2 and A3 to recreate the results presented in Figures 6-1 (a) and (b). 205

6-5 In the main figure of (a) sublimation upon a sample from G1 (shown prior to sublimation in the inset) is presented. In (b) sublimation upon a sample from G1 is shown after a thorough cleaning of the reactor chamber quartz components and replacement of susceptors and covering sapphire wafers. The main image is the centre of the sample whilst the inset is that of the edge of the sample. In (c) planar (main image) and cross-sectional (inset) SEM images are presented after a sublimation of a sample from G1 with a mix of H_2 and N_2 carrier gas (1:1). In the main figure of (d), sublimation of sample G2 is shown. In the inset, sublimation of sample G3 is shown. In the main figure of (e), sublimation of sample B2 is presented. In the inset, sublimation of sample B1 is presented. In (f), sublimation of sample B3 is shown. The main image is taken at the centre of the sample and the inset at the edge. In the main figure of (g), sublimation of sample B4 is presented. In the inset, sublimation of sample B5 is presented. In the main figure of (h), sublimation of sample B6 is presented. In the inset, sublimation of sample B7 is presented. All samples were sublimated at 900 ^{o}C set temperature. 208

6-6 This figure shows the results for the initial sublimation time study. 30 minutes sublimation time is shown for samples B5, B7, B8 in (a), (b) and (c) respectively. 60 minutes sublimation time is shown for samples B5, B7, B8 in (d), (e) and (f) respectively. 120 minutes sublimation time is shown for samples B5, B7, B8 in (g) and (i) respectively. All main figures are images of the centres of the samples and the insets are those of the sample edges. 213

6-7 In this figure, samples have undergone sublimation for 30 minutes at a set temperature of 900 ^{o}C after a BOE 5:1 treatment, unless otherwise specified. In (a), sample A3 is presented. In (b), sample B8 is presented. In (c), sample A3 without a BOE 5:1 treatment and with the HCl:D.I. water treatment is shown. In (d), sample B8 without a BOE 5:1 treatment and with the HCl:D.I. water treatment is shown. In (e), sample A3 is presented but this sample, critically, has not undergone any BOE 5:1 treatment. In (f), sample A3 with a BOE 5:1 treatment and with the HCl:D.I. water treatment is shown. All main images show the centre of the samples, the insets show the edges of the samples. 215

6-8 In (a) sample B8 is shown after sublimation at for 10 minutes. In (b) sample A3 is shown after sublimation at for 10 minutes. In (c) sample B8 is shown after sublimation at for 20 minutes. In (d) sample A3 is shown after sublimation for 20 minutes. In (e) sample B8 is shown after sublimation at for 40 minutes. In (f) sample A3 is shown after sublimation at for 40 minutes. All samples underwent a BOE 5:1 treatment prior to sublimated at 900 ^{o}C set temperature. For images (a), (b) (c), (e), the main image is at the centre of the sample and the inset is at the sample edge. For figures (d) and (f) the main image is the most successful region of the sample. The inset is a less successful edge of the sample. 218

6-9 In (a), sublimation of sample B9 is shown. In (b), sublimation of sample B11 is shown. In (c), sublimation of sample B13 is shown. In (d), sublimation of sample B10 is shown. In (e), sublimation of sample B12 is shown. In (f), sublimation of sample B14 is shown. None of the samples (a) – (f) had a BOE 5:1 treatment, only a BOE 100:1 $\sim 20-30$ second dip. All samples were sublimated for 30 minute at a set temperature of 900 ^{o}C. 219

6-10 Figure 12 shows an AFM scan of part of the G1 sample, prior to sublimation (see Table 6.1). In (a) a 5x5 μm AFM map of the sample is shown. In (b) a 1x1 μm AFM map of the sample is shown. In (c) a zoom of a region of the AFM map shown in the dashed rectangle in (b) is presented. In (i) the planar AFM image is shown and in (ii) a 3D map of the image in (ii) is shown. 222

6-11 In (a) the diagram of Figure 6-4 is shown with the incorrect possible explanations for the poor morphology observed in the A3 sample crossed through. From the experiments preformed the most likely mechanism to explain the morphology of A3 is left without a red cross through. In (b) the mechanism of surface migration of sublimated species is shown, resulting in more material near the edge of the window and a hole at the centre of the window (right) after sublimation. This corresponds to an initially smooth, minimally damaged, GaN surface (left). In (c) the surface of the GaN window is roughened and damaged by over processing (black lines on window of left figure). This then leads to a lumpy, rough morphology after sublimation (right figure). In (b) and (c) both tilted and cross-sectional diagrams are shown. 225

6-12 In (a), sample B13 is shown. In (b), sample B8 is shown. In (c), sample A3, after a BOE 5:1 treatment, is shown. All main figures in (a)-(c) are that of the centre of the sample, the insets are that of the edge. In (d) sample B9 is shown. All images show samples after sublimation with optimised conditions. 228

7-1 This figure shows a diagram of interference effects within a GaN thin film leading to Fabry-Perot fringes, as diagrammatically represented in the box to the bottom left. This figure is diagrammatically only and not to scale. 231

7-2 In this figure, the black line shows a plot of the reflected pyrometry signal from the in-situ growth monitoring system after 3338 seconds recipe run time. In blue the signal is again presented but after 6238 seconds run time. The red line at 500 nm is shown as a reference point from which to see the evolution of the plot in black to the plot in blue. This data was extracted from the 'Laytec Episense' software and plotted using MATLAB. 233

7-3 In (a) a nanopyramid sample is shown after wet etching and prior to any growth/anneal. In (b) shows a nanopyramid sample after a short anneal. In (c) shows a nanopyramid sample after 1 minute of GaN growth without an AlN cap. All the images were amplitude-retrace maps as this aids the viewing of the sharpness of the apices. This data was extracted via the WXsM software [56] 235

7-4 Figure (a) shows an SEM image of sample 5401. In (b) and SEM image of 5402 is presented. Figure (c) shows a panchromatic CL image of the sample presented in (a). In (d) shows a panchromatic CL image of the sample presented in (b). In (e) a mean CL spectrum of the sample, and region, shown in (a) is presented. In (f) a mean CL spectrum of the sample, and region, shown in (b) is shown. This data was taken by Dr Jochen Bruckbauer, University of Strathclyde. These measurements were performed at room temperature and under vacuum. The electron beam acceleration voltage used was 20 kV. 237

7-5 Figure (a) shows an SEM image of sample 5415 and in (c) the corresponding panchromatic CL map of the same area. Figure (b) shows an SEM image of sample 5412 and in (d) a panchromatic CL map of the same area. In (e) and (f) are two example spectra from the centres of two rods from the panchromatic CL images in (c) and (d) respectively. The red circles on (c) and (d) show the approximate area within which the spectra in (e) and (f) were taken. This data was taken by Dr Jochen Bruckbauer, University of Strathclyde. These measurements were performed at room temperature and under vacuum. An acceleration voltage of 5 kV was used. 239

7-6 Figures (a), (c) and (e) show 3 targeted pixels from the panchromatic CL map shown in Figure 7-5 (d). The corresponding CL spectra for these three pixel are presented in Figures (b), (d) and (f) respectively. This data was taken by Dr Jochen Bruckbauer, University of Strathclyde. These measurements were performed at room temperature and under vacuum. An acceleration voltage of 5 kV was used. 241

7-7 Figure (a) shows an SEM image of sample 5412 near the cleaved edge. In (b) a schematic of the growth occurring on 5412 is presented. In (c) a specific pixel of the panchromatic CL image which corresponds to the same location as shown in (a) is presented. The corresponding detected CL spectrum of the pixel highlighted in (c) is shown in (d). In (e) another pixel (different to (c)) in the panchromatic CL image is selected. The corresponding detected CL spectrum for the pixel in (e) is shown in (f). This data was taken by Dr Jochen Bruckbauer, University of Strathclyde. These measurements were performed at room temperature and under vacuum. An acceleration voltage of 5 kV was used. 242

7-8 This figure shows a plot of the room temperature PL measurements for all the samples presented in Table 7.5. 249

7-9 Figure (a) shows a plot of the room temperature PL of samples 5412, 5420 and 5422 whilst house in the cryostat. Figure (b) shows a plot of the PL of 5412, 5420, 5422 whilst housed in the cryostat at a temperature of $\sim$ 77 K. 251

7-10 In (a) a plot of the entire PL spectra for samples 5420 is plotted at both room temperature and 77 K. No log scale has been used on the data, although cosmic ray removal has been performed via a mean function and the data is normalised to 1. In (b) a plot of the evolution of the peak centred at $\sim$ 260 nm as a function of measurement temperature is presented. 254

8-1 Calibration image of the AFM data. The black lines indicate measurement lines from which the difference between the know size of 1 μm and the measure size is obtained. 286

8-2 AFM data of the deep (a - d) and shallow (e - h) holes grown at different V/III ratios. 287

8-3 AFM data of the growth time study of the deep holes at a V/III ratio of $\sim$ 7600. 289
8-4 Plot of the height of the nanohole structures from the initial dry etch depth as a function of growth time for V/III ratios of $\sim$ 74 and $\sim$ 7600. 290
8-5 In (a) a 5x5 um AFM scan of a nanohole array sample with an initial dry etch depth of $\sim$ 100 nm is shown after 2 minutes of KOH wet etching at 150 ^{o}C (same sample as that shown in Figure 5-3 (d)). In (b) a 5x5 um AFM scan of a nanohole array sample with an initial dry etch depth of $\sim$ 150 nm is shown after 2 minutes of KOH wet etching at 150 ^{o}C (same sample as that shown in Figure 5-3 (e)). In (c) a 5x5 um AFM scan of a nanohole array sample with an initial dry etch depth of $\sim$ 1000 nm is shown after 2 minutes of KOH wet etching at 150 ^{o}C (same sample as that shown in Figure 5-3 (f)). 292
8-6 In (a) and AFM map of sample A (Figure 5-6 (a)) after wet etching in KOH at 150 ^{o}C for 120 seconds is presented. In (b) an AFM map of sample B (Figure 5-6 (b)) after wet etching in KOH at 150 ^{o}C for 75 seconds is presented. In (c) and AFM map of sample C (Figure 5-6 (c)) after wet etching in KOH at 150 ^{o}C for 120 seconds is presented. In (d) and AFM map of sample E (Figure 5-6 (d)) after wet etching in KOH at 150 ^{o}C for 120 seconds is presented. In (e) an AFM map of sample B after wet etching in KOH at 150 ^{o}C for 90 seconds is presented. In (f) an AFM map of sample B after wet etching in KOH at 150 ^{o}C for 105 seconds is presented. . 293

List of Tables

1.1 This table presents some of the different properties of AlN, GaN and InN. 65

1.2 This table presents a comparison of the lattice mismatch between different III-N compounds and commonly used foreign substrates for growth. 71

4.1 Details of the growth experiments with the changes highlighted in red. For all growth experiments the TMAl flow was 20 sccm, the pressure was 20 mbar and the carrier gas was H_2. 149

5.1 Etch details of the tapered nanohole samples and the corresponding estimates of the dimensions. All etching was performed with a Cl_2/Ar gas chemistry with flow rates of 50 and 10 sccm respectively. All etching was performed at room temperature (other than the no taper sample which was etched at 150 ^{o}C). All dimension estimates were performed by measuring dimensions of cross-sectional SEM images via ImageJ. 176

5.2 Diameters of the 1.5 μm pitch rods for different dry etch durations. The diameters of the rods were measured at the top of the rods. Measurements were performed upon cross-sectional SEM images . 189

5.3 This table shows the structure height dimensions for the 1.5 μm pitch pyramid samples after wet etching 190

5.4 This table shows the average angles of the inclined planes of the 1.5 μm pitch pyramids extracted from AFM maps. 191

6.1 Fabrication and cleaning details of all samples within this study. Samples taken from the same initial wafer are denoted with the same letter. Those with different numbers have different fabrication/cleaning conditions applied to them. 201

7.1 Initial quantum dot growth conditions identified from the literature. 230
7.2 Summary of conditions of attempted GaN quantum dot growth on AlN nanopyramids. 236
7.3 Summary of conditions of attempted GaN quantum dot growth on AlN nanorods. 240
7.4 Measured linewidths of sharp peaks observed in CL spectra. . . . 244
7.5 Further exploration of GaN quantum dot growth conditions on AlN nanorods. 248

8.1 This table provides the semi-polar facet angles measured for the deep and shallow hole structures grown at different V/III ratios. 288
8.2 This table provides the semi-polar the facet angles measured for the deep hole structures grown at a V/III ratio of $\sim$ 7600 for prolonged growth times. 288
8.3 Measurements of features (mask opening size and etched hexagon size) present in Figures 5-2 (a) and (b). Measurements were performed upon SEM images using the ImageJ software package [57]. 291
8.4 Fabrication details of a number of samples within this study. Samples taken from the same initial wafer are denoted with the same letter. Those with different numbers have different fabrication/processing conditions applied to them. On all samples the first fabrication step was to deposit a $\sim$ 35 nm SiN_x mask layer via PECVD. . . . 295
8.5 Fabrication details of samples not presented in Table 8.4 in this study. Samples taken from the same initial wafer are denoted with the same letter. Those with different numbers have different fabrication/processing conditions applied to them. On all samples the first fabrication step was to deposit a $\sim$ 35 nm SiN_x mask layer via PECVD. 296

Abbreviations

0D	Zero dimensional
1D	One dimensional
2D	Two dimensional
3D	Three dimensional
AFM	Atomic force microscopy
Al_2O_3	Sapphire (aluminium oxide)
AlGaN	Aluminiumgallium nitride
AlN	Aluminium nitride
BARC	Back anti-reflection coating
BOE	Buffered oxide etch
CHF_3	Trifluoromethane
CL	Cathodoluminescence
CVD	Chemical vapour deposition
CW	Continuous wave
DBR	Distributed Bragg reflector
DC	Direct current
DE	Droplet epitaxy
DOF	Degree of freedom
DTL	Displacement talbot lithography
EBL	Electron beam lithography
FSS	Fine structure splitting

FWHM Full width half maximum

Ga_2O_3 Gallium oxide

GaAs Gallium arsenide

GaN Gallium nitride

H_2O Water

H_2O_2 Hydrogen peroxide

H_2SO_4 Sulphuric acid

H_3PO_4 Phosphoric acid

HCl Hydrochloric acid

HF Hydrofluoric acid

HNO_3 Nitric acid

HT-MOCVD High Temperature Metalorganic Chemical Vapour Deposition

HVPE Hydride Vapour Phase Epitaxy

ICP Inductively coupled plasma

III-As Three-arsenide

III-N Three-nitride

III-P Three-phosphide

III-V Five-three

InAs Indium arsenide

InGaN Indiumgallium nitride

InN Indium nitride

IQE Internal quantum efficiency

KOH Potassium hydroxide

LED Light emitting diode

LT-PLD Low temperature pulsed laser deposition

MBE	Molecular beam epitaxy
MDE	Modified droplet epitaxy
MOCVD	Metalorganic Chemical Vapour Deposition
MOVPE	Metalorganic Vapour Phase Epitaxy
NaOH	Sodium hyrdoxide
NEMS	Nano-electromechanical systems
NH_3	Ammonia
NIL	Nanoimprint lithography
NJP	Nano-jet probe
PA-MBE	Plasma-assisted molecular beam epitaxy
PECVD	Plasma enhanced chemical vapour deposition
PL	Photoluminscence
PVD	Physical vapour deposition
PVT	Physical vapour transport
QCSE	Quantum confined stark effect
QD	Quantum dot
QIP	Quantum information processing
QIS	Quantum information science
QKD	Quantum key distribution
QW	Quantum well
RF	Radiofrequency
RIE	Reactive ion etching
SAG	Selective area growth
SCQD	Site-controlled quantum dot
SD	Standard deviation

SEM	Scanning electron microscope
SiC	Silicon carbide
SiH_4	Silane
SiN_x	Silicon nitride
SiO_2	Silicon oxide
SK	Stranski-Krastanov
SPE	Single photon emitter
SPS	Single photon source
STEM	Scanning transmission electron microscope
STM	Scanning tunnelling microscope
TEM	Transmission electron microscope
TM	Transverse magnetic
TMAl	Trimethylaluminium
TMGa	Trimethylgallium
UV-NIL	Ultraviolet nanoimprint lithography
UV	Ultraviolet
UVC	Ultraviolet C (far UV)

Chapter 1

Introduction and Background - Quantum Dots

1.1 Aims and objectives

The aims of this PhD project were to develop and investigate the creation of III-N sites to house III-N site-controlled quantum dots. Additionally, further aims of this project were to grow site-controlled quantum dots upon periodic arrays of the sites created. Specifically, further exploration of the GaN/AlN materials system was targeted. Finally, demonstration of a quantum dot single photo source at as high a temperature as possible was the last aim, and the most ambitious aim, of this project. Thus, this project has involved aspects of nanofabrication, crystallographic growth and characterisation of nanostructures.

As this thesis concerns the development of sites for site-controlled III-N quantum dots and the growth of such quantum dots. Thus, it is appropriate to present some of the background theory of quantum dots and indeed site-controlled quantum dots compared to other types of quantum dots. Additionally, in this chapter, the III-N materials group is presented and the motivation of why the creation of site-controlled quantum dots with this materials group is particularly promising for real world quantum information devices.

1.2 Quantum dots - definitions and basic information

Semiconductor quantum dots (QDs) can be described as very small regions within a semiconductor matrix whereby band offsets lead to 3-dimensional quantum confinement of charge carriers [58] [31]. Hence, due to this spatial 3D quantum confinement quantum dots can be described as 0-dimensional structures [59] [60]. This results in these structures having discrete energy spectra similar to that of atoms [58] [31], thus they have been also described as 'artificial atoms' [61]. To illustrate this further, observe in Figure 1-1 the plot of the density of states for 3D (bulk), 2D (quantum well), 1D (quantum wire/rod) and 0D (quantum dot) structures [60]. As can be seen from Figure 1-1, the density of states of a quantum dot (0D) are discrete, Dirac delta-function like, levels. Thus, carriers can only occupy specific, fully quantised energy levels. In terms of spatial dimensions of quantum dots, one can consider something to be a quantum dot when the nanoparticle radius is smaller than the Bohr radius of the electron, hole (carriers) or exciton of a given material. Thus, this changes from material to material [62]. Specifically, a system can be considered to be in the strong confinement regime when the quantum dot radius is smaller than the Bohr radii of both carriers as well as the exciton. Hybrid confinement regime is when the quantum dot radius is smaller than the Bohr radius of the electron but not that of the hole as the hole has a higher effective mass and so a smaller Bohr radii. This means that the hole is not strongly confined and interacts with the electron via the Coulomb potential. Weak confinement is when the quantum dot radius is larger than both the carriers' Bohr radii but when the exciton is formed, its motion is quantised [63].

There are numerous uses, both current and in development, concerning quantum dots in all their forms. These applications range from improvement in the design of light emitting diodes (LEDs) [64] [65] and laser diodes [9], in addition to applications in quantum information processing (QIP) [66], such as quantum cryptography [67] and quantum optical computing [68]. Further applications include the detection of cancerous cells [69] [70], improvement in the design of solar cells [71], applications in field effect transistors and photo resistors [72] and, even in consumer products in the form of the 'quantum dot' television set [73]. As carriers in a quantum dot are strongly quantized their energy spectrum is very discrete, resulting in emission peaks which are very sharp due to this Delta function-like density of states [1]. As the emission is of specific energies, this can potentially allow for the entanglement of emitted photons, which is useful for QIP [45]. Moreover, these entangled photon pairs have the possibility of being emitted on demand [74]. Quantum dots also allow the study and use of electron-electron interactions [75]. Furthermore, their spatial confinement allows them

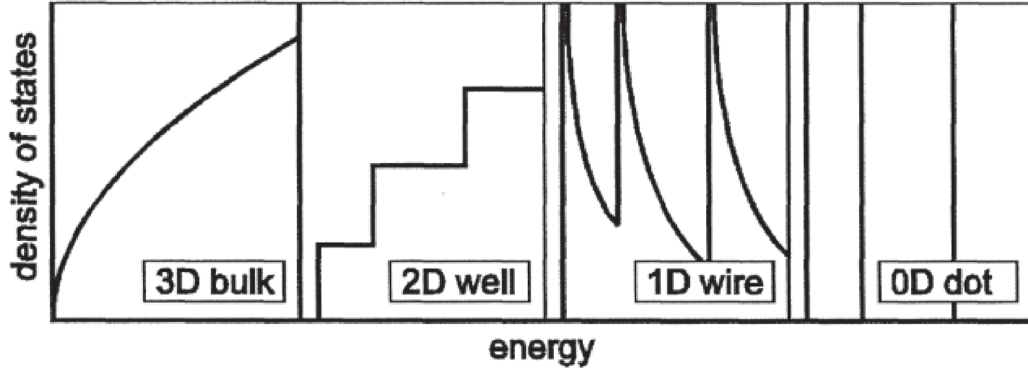

Figure 1-1: This figure shows the density of states for 3D (bulk), 2D (quantum well), 1D (quantum wire) and 0D (quantum dot) semiconductor systems. Reprinted/adapted by permission from Copyright Clearance Center: Springer Nature, 'Single-particle states of quantum dots': Quantum Dots by Professor Lucjan Jacak, Dr. Arkadiusz Wöjs, Dr. Paweł Hawrylak Copywrite @ Springer-Verlag Berlin Heidelberg 1998. ([1]).

to isolate carriers from defects such as dislocations which are sources of nonradiative recombination in optoelectronic applications [9]. Before further information is presented, a very brief historical introduction will be given.

1.3 Historical quantum dot information

Reed et al. [2] [1] were the first to intentionally create semiconductor quantum dots, without the use of a chemical synthesising process. A schematic of the device which they created is shown in Figure 1-2 (a). As can be seen from the photoluminescence spectra of the quantum dot which they fabricated in Figure 1-2 (b), there is a large difference in comparison to the spectra obtained from a quantum wire or well. The peak in the PL spectra in Figure 1-2 (b) with far higher intensity for the 0D structure is evidence of total spatial confinement. This is because, hole states available for occupation are discrete and the inter-branch scattering time from the light hole band to heavy hole band is observed to lead to a bottleneck. This is the first evidence of intentionally created epitaxial quantum dots.

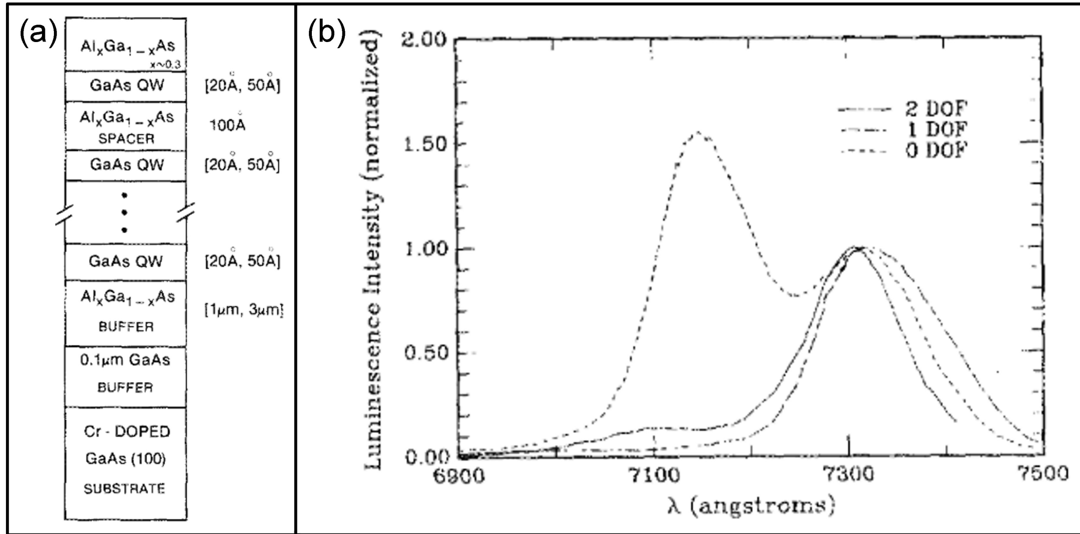

Figure 1-2: In (a), a schematic of the cross-section of the quantum well system grown by Reed et al. [2] is shown (Reprinted with permission from [2]. Copyright [1986], American Vacuum Society). The photoluminescence spectra in (b) is that of a quantum well (2 DOF), quantum wire (1 DOF) and quantum dot (0 DOF). The spectra are normalised for comparative observation. All photoluminescence measurements were taken at 4.4 Kelvin. Reprinted with permission from [2]. Copyright [1986], American Vacuum Society.

1.4 Types of quantum dots and how they are created

There are a number of different routes which can be taken in order to create quantum dots, each of which have their benefits, draw-backs and applications, both potential and in current use. Site-controlled quantum dots are one such form, having pre-determined size and location. Other 'categories' of quantum dots include: colloidal quantum dots [76], self-assembled quantum dots [27], quantum dots formed via the modulation of an electric field across a quantum well [1] and quantum dots created via the dry etching of quantum well sandwiches [77] [2].

Colloidal quantum dots are effectively very small semiconductor nanocrystals [78] capped with surfactant molecules and dispersed in solution [79]. They are typically created via chemical synthesis methods. The first published work on synthesising quantum dots, albeit not purely colloidal, was by Ekimov et al. in 1985 [80], just a few months before the fabrication of quantum dots by Reed et al. [2]. Here, semiconductor microcrystals were formed within a silicate glass matrix, the details of which will not be presented here [80]. Since then, more work has been undertaken using synthetic routes to form nanocrystals within a solvent resulting in quantum dots. In order to convert

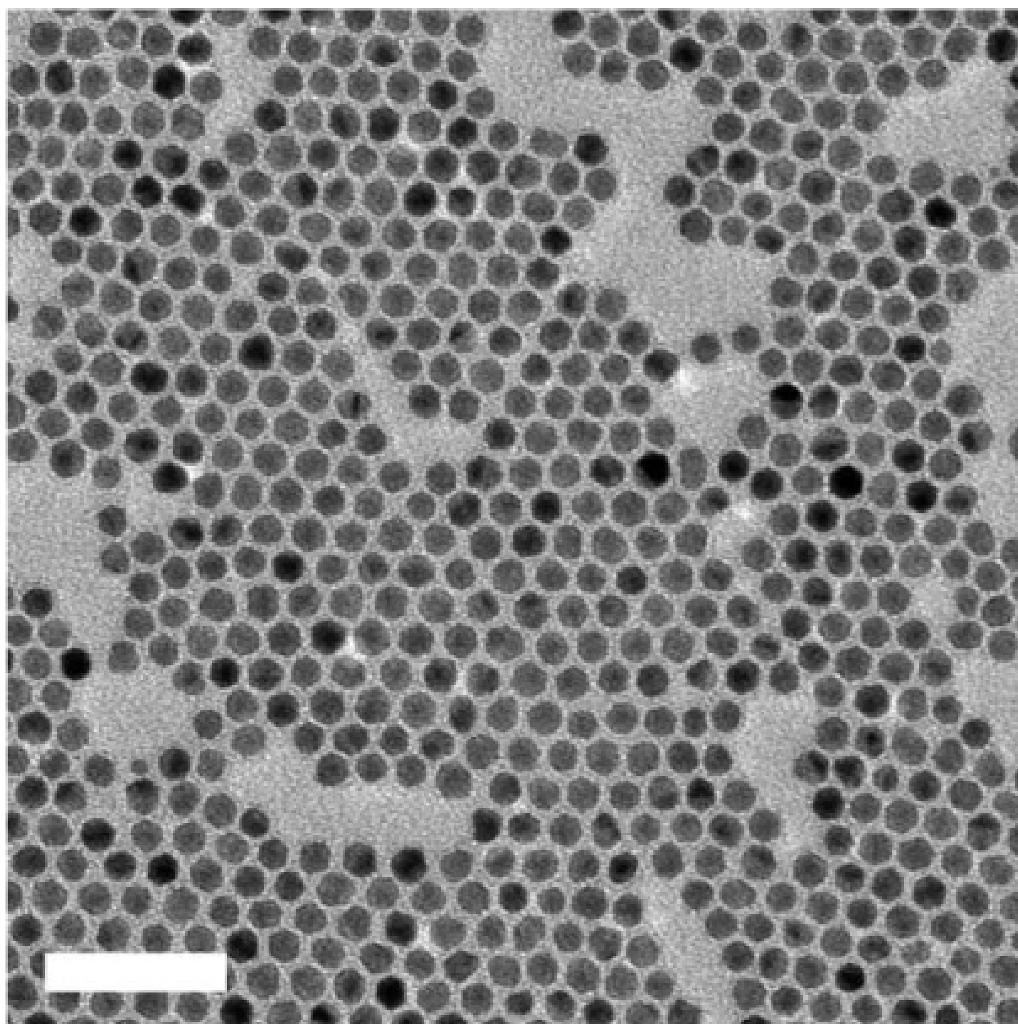

Figure 1-3: This figure shows a TEM image of the quantum dots synthesised in [3]. As can be seen there is a small spread in sizes and shape which will render different emission properties. The scale bar represents 50 nm (figure reproduced and unmodifed from [3] supplementary information under Creative Commons Attribution 4.0 International Licence https://creativecommons.org/licenses/by/4.0/).

a solution of quantum dots into a solid film one must deposit a small volume of the solution onto a substrate and then evaporate the solvent. This will leave behind a film of immobile quantum dots for processing [79]. Research into utilising colloidal quantum dots in devices include integration in solar cells [71], use in LED systems [64], including the now commercially available 'quantum dot TV' sets [73], and even as single photon sources [3]. The major advantage of these types of quantum dots is that they are relatively cheap to synthesise [71]. Their drawback is that as they are deposited onto a substrate as a solution for creation of a quantum dot film [79]; it can be very difficult to individually operate such quantum dots. Moreover, these quantum dots tend to have varying shapes, sizes and locations (see Figure 1-3), thus this renders identical emission characteristics from an array of such quantum dots realistically unattainable [81]. It is important to mention that other synthetic routes such as spontaneous plasma processing via chemical vapour deposition [82] and electrochemical synthesis [83] also exist.

Modulated electric field quantum dots are quantum dots formed by the application of a spatially modulated electric field upon [1] (see Figure 1-4) or within a quantum well [5]. Both techniques result in a spatially localised system of electrons. The subsequent electrical properties of these types of quantum dots can be investigated to experimentally probe the effects of few particle systems [5]. In the paper by Ashoori et al. [5], using a device shown in Figure 1-4 (b), capacitance spectroscopy was carried out using a quantum dot created by modulating an electric field within a quantum well. This allowed for the study of discrete quantum energy levels [5]. Whilst this is a useful method for such studies, it is unlikely quantum dots formed in this way will ever be usable for device applications. This is as making large scale arrays of devices with the same or vary similar proprieties using this method would be particularly challenging. Additionally, integration into other, current technology may also be difficult.

A fabrication based method for creating quantum dots includes the dry etching of quantum wells [77] such as that mentioned earlier in the work by Reed et al. [2]. However, this fabrication technique can lead to large amounts of damage (especially at the side-walls), resulting in severe carrier depletion [77]. Thus, this technique no longer has use for practical device application. Another method, which renders spatially determined quantum dots is via the use of a Nano-Jet Probe [84]. This is essentially an atomic force microscope probe with an aperture in the tip allowing for precise deposition of very small amounts of material [84]. Whilst an intriguing concept, this technique is not useful for wafer scale quantum dot fabrication, as will be discussed in Chapter 3.

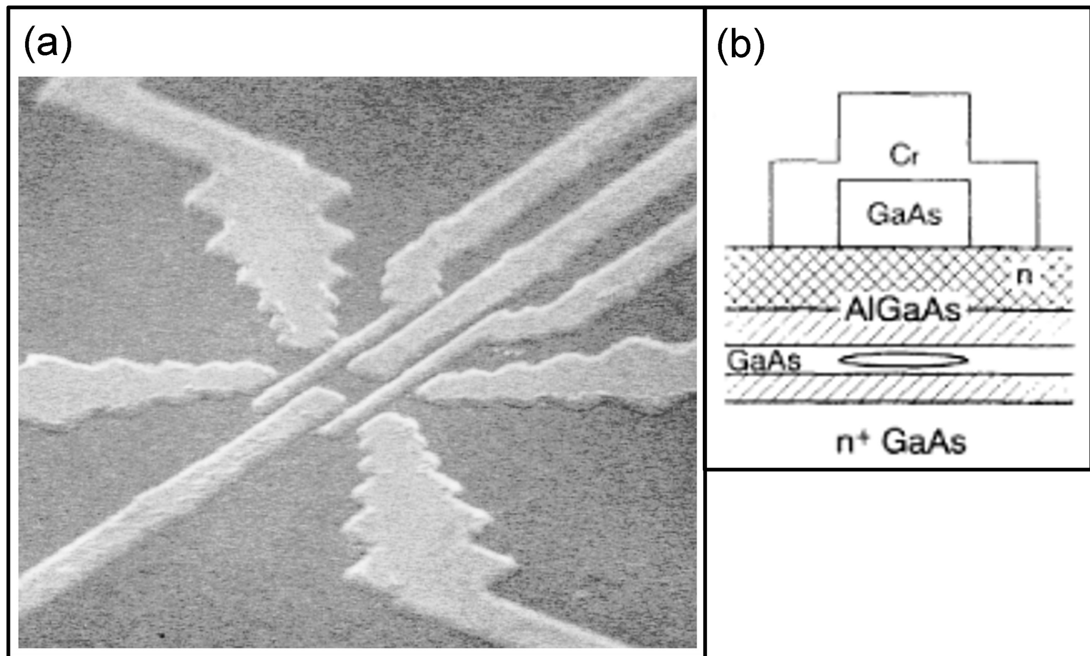

Figure 1-4: In (a) is a quantum dot formed by electrodes, with the four inner electrodes squeezing electrons in the quantum-well layer into a quantum dot. The outer electrodes act as contacts for electron tunnelling in an out of the quantum dot (figure reproduced from [4]). In (b) there is a schematic of the device used by Ashoori et al. [5] for capacitance spectroscopy of few particle systems. The quantum dot is represented by the ellipse within the GaAs quantum well. Figure (b) is reprinted (Figure 1b) with permission from [5] R. C. Ashoori, H. L. Stormer, J. S. Weiner, L. N. Pfeiffer, S. J. Pearton, K. W. Baldwin, and K. W. West. Single-electron capacitance spectroscopy of discrete quantum levels. Phys. Rev.Lett., 68:3088–3091, May 1992. Copyright (2006) by the American Physical Society, https://doi.org/10.1103/PhysRevLett.68.3088.

Applying a thermal annealing stage to InGaN quantum well layers can induce the formation of indium rich clusters within the quantum well and even extend into the barriers [85] [86]. These clusters can act like quantum dots within the quantum well matrix [86]. These dot-in-well structures have also been demonstrated for GaN quantum dots formed at the macrostep edges in GaN/AlGaN quantum wells [87]. These quantum dots tend to be of a high quality in terms of optical characteristics, with low spectral diffusion [87], but suffer from difficulty in controlling the formation sites, as they form due to interface fluctuations.

1.5 Self-assembled quantum dots

Another category of methods to create quantum dots are so-called 'self-assembled' quantum dots. Such methods will be discussed further here.

1.5.1 Droplet epitaxy and modified droplet epitaxy

Two interesting self assembly methods to create quantum dots are via the droplet expitaxy (DE) and modified droplet epitaxy (MDE) techniques. DE involves two separate growth steps. In the first, metal droplets (such as Ga for a group-III metal) are formed. This droplet formation can be controlled by optimising the growth conditions, allowing control of the size and density of the metal droplets [88]. Secondly, the metal droplets are crystallised in a group-V rich environment to form the semiconductor quantum dots [88]. The kinetics of crystallising the metal droplets into quantum dots is strongly dependent on the flow of the group-V material and the crystallisation temperature, allowing for control in the composition and shape of the quantum dots [88]. Atomic exchange between the metal dot and the group-V material starts first at the surface of the dot and then extends deeper into the dot. A high temperature annealing step can then be used to improve the crystalline quality of a, as an example, GaAs quantum dot [89]. The dots can then be capped with a higher bandgap material. Droplet epitaxy can be used to create quantum dots in both lattice-matched and lattice-mismatched material system [90].

In MDE of InGaN, developed by Oliver. R, one grows an InGaN epilayer upon a GaN substrate followed by an anneal in a N_2 atmosphere. This results in the formation of a number of small pits [91]. The pits are created via the decomposition of indium-rich regions in the InGaN film which are formed due to spinodal decomposition [91]. These regions become unstable in the purely N_2 atmosphere, resulting in islands of metallic In and/or Ga on the substrate surface [92]. These islands then react with

reactive nitrogen from NH_3 [91] during the growth step of the GaN capping layer [93]. There is also interdiffusion with the GaN capping layer during this growth step. Both these factors lead to the formation of the InGaN quantum dots [91]. MDE of InGaN quantum dots is typically performed in a MOVPE growth reactor, such as in the work in [92] and [93]. Alternatively, as in the original proposal of DE [94], the DE growth of quantum dots is typically grown in a MBE growth reactor. Another, very popular method, to achieve high quality quantum dots is via the Stranski-Krastanov growth mode to reveal self-assembled quantum dots [95]. Quantum dot growth via this mode will now be briefly discussed.

1.5.2 Stranski-Krastanov grown quantum dots

Another form of self-assembled quantum dots rely on the Stranski-Krastanov epitaxial growth mode [96]. Here, a wetting layer of one semiconductor material is deposited onto a buffer layer of another semiconductor material. The solid adsorbate essentially acts like a liquid drop on the surface of a solid [60]. Hence during thin layer deposition, a material may 'wet' another material [97]. This is defined by the relation [97]:

$$\sigma_s > \sigma_f + \sigma_i \quad [97] \tag{1.1}$$

where σ_s is the surface free energy of the substrate, σ_f is the surface free energy of the heteroepitaxial layer and σ_i the interface free energy (neglecting the strain energy of the film) [97]. As this is heteroepitaxial growth there will be a lattice mismatch between the two materials, which will lead to strain in the system. There will be, as expressed above, an inherent surface free energy across the material [6]. Concerning Stranski-Krastanov growth, the strain favours 3D growth, whereas the surface free energy is minimised via minimising the surface area, thus favouring 2D growth [6]. From this it is clear that there is a competition between the strain of the system and the surface free energy, with each favouring different growth modes [60]. If the lattice mismatch is large enough [98] then the strain, after enough deposition (above the lower critical heteroepitaxial thickness) [7], will induce a transformation from 2D to 3D growth. The lower critical thickness is the thickness at which the growth will transform from 2D to 3D as a relief mechanism of the strain in the system. This thickness arises due to an increase in total strain in the system as more material is deposited [99]. This growth mode, which includes 2D growth followed by a transition to 3D growth, is Stranski-Krastanov (SK) growth [60]. It is interesting to note that this island formation does

not completely release all the strain energy of the system [6]. The two other growth modes which may take place are firstly Frank-Van-der Merwe growth, which is purely 2-dimensional. In this case the expression above (Equation 1.1) is fulfilled. Secondly we have Volmer-Weber growth, which is purely 3-dimensional [60]. Here, mathematically the expression is opposite in sign to that above (Equation 1.1) [97]. All three growth modes are shown in Figure 1-5.

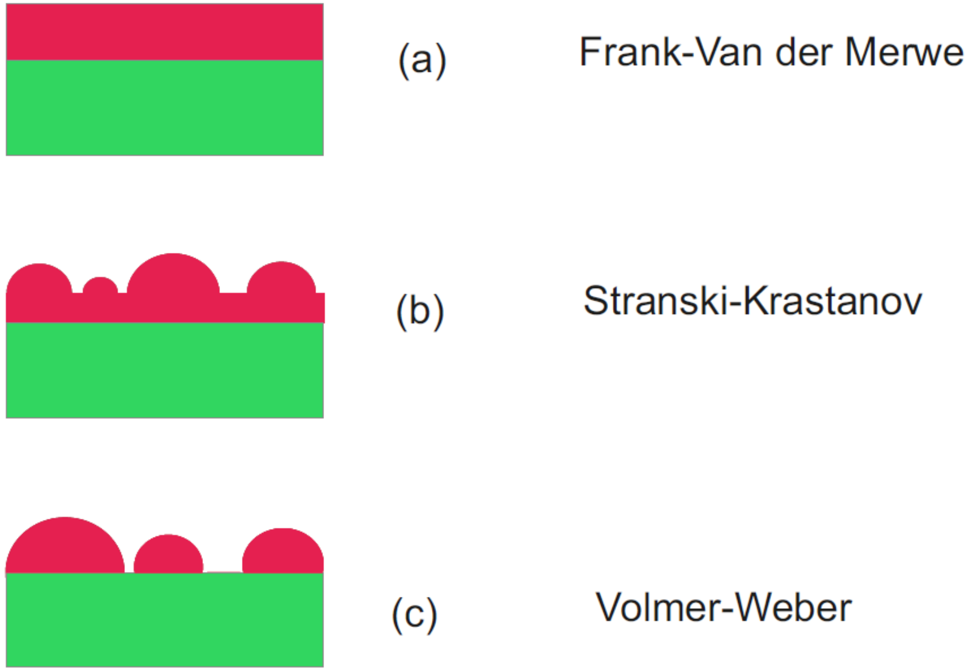

Figure 1-5: This figure shows the three heteroepitaxial growth modes: (a) the 2D Frank-Van der Merwe growth mode, (b) the Stranski-Krastanov 2D-3D growth mode and (c) the purely 3D Volmer-Weber growth mode. For more information on the process in (b) see Figure 1-6 [6].

As can be seen in 1-6 (b), with SK growth of a layer thickness below the lower critical thickness, this renders simple 2D growth at this stage [7]. After deposition of a thickness above the lower critical thickness [7], 3D islands spontaneously form (see Figure 1-6 (c)). This occurs as an elastic relaxation mechanism to relieve strain in the system [7]. These islands, if small enough, will act as quantum dots, once capped with a higher bandgap material [100]. These are called self-assembled, Stranski-Krastanov, quantum dots. In the case that further material is grown on top of the self-assembled quantum dots, another critical thickness is present, the upper critical thickness. Above this

thickness plastic deformation occurs [7] (Figure 1-6 (d)). This significantly impacts the quality of the layer introducing many defects into the system [7].

The critical lattice mismatch required for SK growth is 2.5% for a large range of material systems. In the case of GaN and AlN the mismatch is 2.4% [98]. Thus, SK growth would not typically occur. However, it has been shown that it is in fact possible to achieve self-assembled quantum dots with these two materials via lowering the surface free energy of the system [98]. Thus, this will lower the amount of strain required for the 3D growth transition.

1.5.3 Self-assembled, Stranski Krastanov quantum dots, specific to AlN/GaN or AlGaN/GaN

The next body of discussion will be concerning GaN quantum dots grown upon AlN or AlGaN and utilising MOVPE. There are a few methods used to do this as reported in the literature. The first is a desorption step [101] (or very similarly a growth interruption step), the second is by the use of very low V/III ratios during growth and finally the third, via the use of an anti-surfactant [102]. All of these techniques involve the reduction of the surface free energy in order to induce the transition from 2D growth to 3D, island growth.

1. (a) In a desorption step, as the name suggests, material is desorbed allowing for 3D surface reconstruction. The mechanism is likely due to interactions with the surface due to the removal of Ga and corresponding changes in chemical potential [98].

   (b) In a growth interruption step, a similar process occurs, but this is usually performed under NH_3 flow. As with desorption, growth interruption likely changes the surface free energy of the sample via a change in chemical potential [98]. This leads to strain dominating over surface free energy thus leading to 3D surface reorganisation as a relief mechanism [98].

2. For the use of very low V/III ratios, migration and evaporation of Gallium atoms plays a key role, and this will affect the surface free energy of the sample [103], allowing for the growth of quantum dots.

3. For the same desired effect an anti-surfactant can be used in order to modify the surface free energy to induce 3D island formation [102].

The self-assembled quantum dots discussed above have a number of uses such as pos-

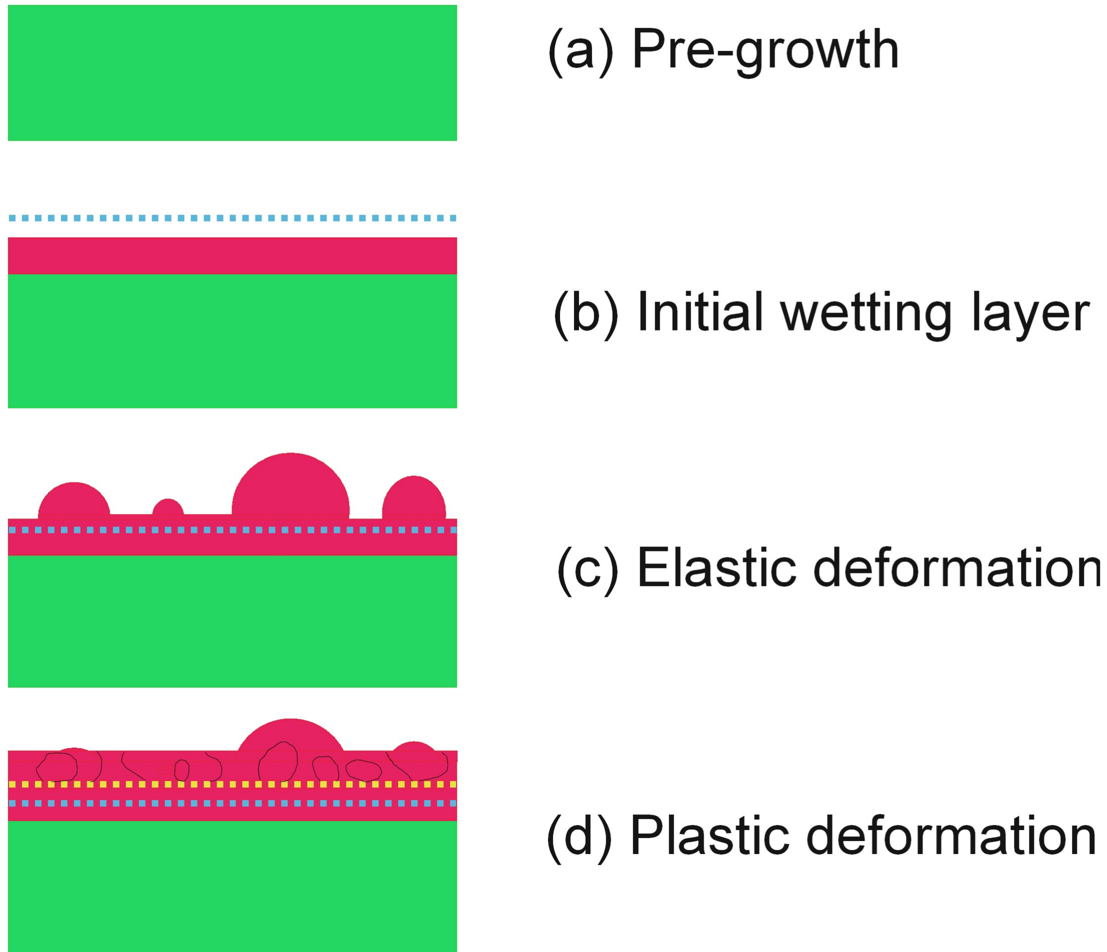

Figure 1-6: This figure shows the evolution of a surface morphology during Stranski-Krastanov growth. In (a) the sample is shown before the deposition of a wetting layer. In (b) a small thickness, smaller than the lower critical thickness, of lattice mismatched material has been deposited. In (c) the amount of material deposited has exceeded the lower critical thickness leading to the spontaneous 3D island formation to relive the strain in the system [7]. In (d) growth is continued, once the layer thickness has surpassed the upper critical thickness, plastic deformation [7] occurs introducing defects into the system. In all Figures (a) - (d) the blue dashed line represents the lower critical thickness and the yellow the upper critical thickness.

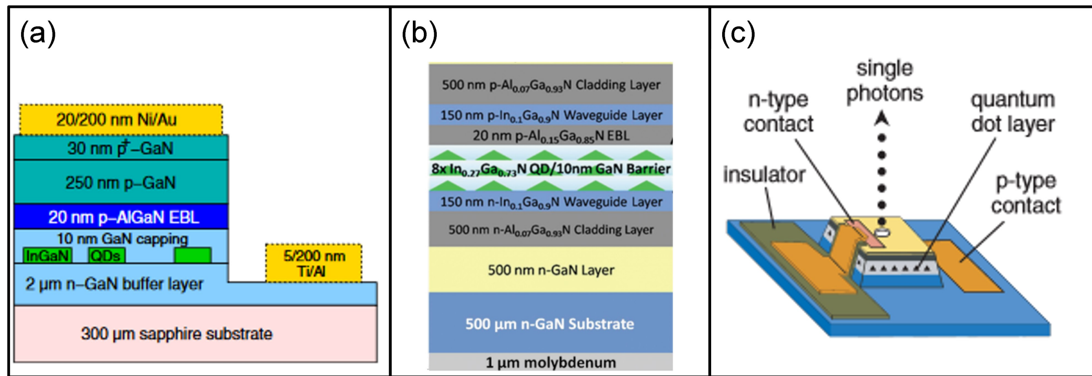

Figure 1-7: Figure (a) shows a schematic of a single quantum dot based LED structure. Copyright © IOP Publishing (2014). Reproduced with permission from [8]. All rights reserved. In (b) a schematic of the green quantum dot laser mentioned is presented (Reprinted from [9], with permission of AIP Publishing. Copyright © 2011 American Institute of Physics). Figure (c) shows a schematic of a single photon emitting diode (reproduced from [10]. Copyright © 2003 WILEY-VCH Verlag GmbH & Co. KGaA, Weinheim).

sibly improving LED efficiency and lowering semiconductor lasing thresholds. The argued LED efficiency improvements arise from the use of quantum dots in the active regions [65], since the 3D quantum confinement isolates carriers from defects such as threading dislocations. Threading dislocations can act as sources of nonradiative recombination, lowering the efficiency of a device [104] [105]. Moreover, the reduced, Delta function-like, density of states lead to high material and differential gain, and good temperature stability [106]. Such a self-assembled quantum dot based LED device can be seen in Figure 1-7. It is worth mentioning that the proposed improvements of LEDs via use of QDs is not a consensus within the scientific community.

Laser diodes can also benefit from the use of self-assembled quantum dots. With regards to devices emitting in the green region of the visible spectrum, InGaN/GaN multi-quantum well systems have typically been used in the past. However, due to a reduced electron-hole overlap resulting from the Quantum Confined Stark Effect (which will be addressed later), these lasers have, typically, high threshold current densities [9]. Not only that, poor indium incorporation during growth of quantum wells will further reduce the effectiveness of the lasers. The Quantum Confined Stark Effect is significantly lower in self-assembled quantum dots compared to that of quantum wells. Also, similarly with LED's, quantum dots may isolate carriers from sites of nonradiative recombinations, such as dislocations [9]. This will lead to a more effective lasing device, lowering the required threshold current. The benefits of isolating carriers

from defects via the use of quantum dots is not limited to the case of green emitting, InGaN/GaN based devices. This can be applied to other material systems too, such as other members of the nitrides and the III-As group [107].

There has been some progress in using self-assembled quantum dots for single photon emitters such as the results shown by Shields et al. [10] (see Figure 1-7 (c)). In fact, the first quantum dot single photon emitter was created by Michler et al. [108], who used self-assembled InAs quantum dots. However, due to the nature of the self-assembly process with these quantum dots, although a very high quality of quantum dot is achievable [109], both the location and size (within a range) are random [110]. Whilst some of the research presented above shows that the creation of single photon emitters is possible [111], the nature of the random position, shape and size render these unrealistic for practical quantum information processing devices. Additionally, the single photon emission yield tends to be low [112].

The difficulty in realising quantum information processing devices arises from the arduous post-growth selection of the quantum dots with desired size and shape that is required for device integration [46]. Regarding individual SK quantum dots their positions are undetermined before the SK growth. Hence, for applications, it is effectively impossible to have electrical contacts in place prior to growth connected to each individual quantum dot for individual on demand operation. One could add the contacts in after growth [113] but again this adds a large complication as the location of the quantum dots from sample to sample will be different and would require very time consuming and particularly taxing fabrication steps for successful implementation (see Figure 1-7). The other option would be to put contacts down in spatially random locations across one's QD sample, hoping that, by chance, one would have a suitable single quantum dot between the contacts. This can be illustrated in the work by Nakaoka et al. [11], whereby a single electron transistor is fabricated using a self-assembled quantum dot. A total of 144 nanojunctions were fabricated, with 10 containing a single quantum dot between the junctions. This indicates that Naksaoka et al. were relying on luck for a single GaN quantum dot to be within the nanojunctions, as many were fabricated without any quantum dots between them (Figure 1-8). This is both not particularly scalable and certainly not reproducible, in terms of yield, from sample to sample. If one wanted to specifically select appropriate quantum dots, a suitable quantum dot would first have to be identified, followed by the very precise patterning and contact deposition for the electrical experiments. This would be by no means trivial and not realistically scalable to full chip implementation.

Moreover, as mentioned, self-assembled quantum dots have, within a range, a random

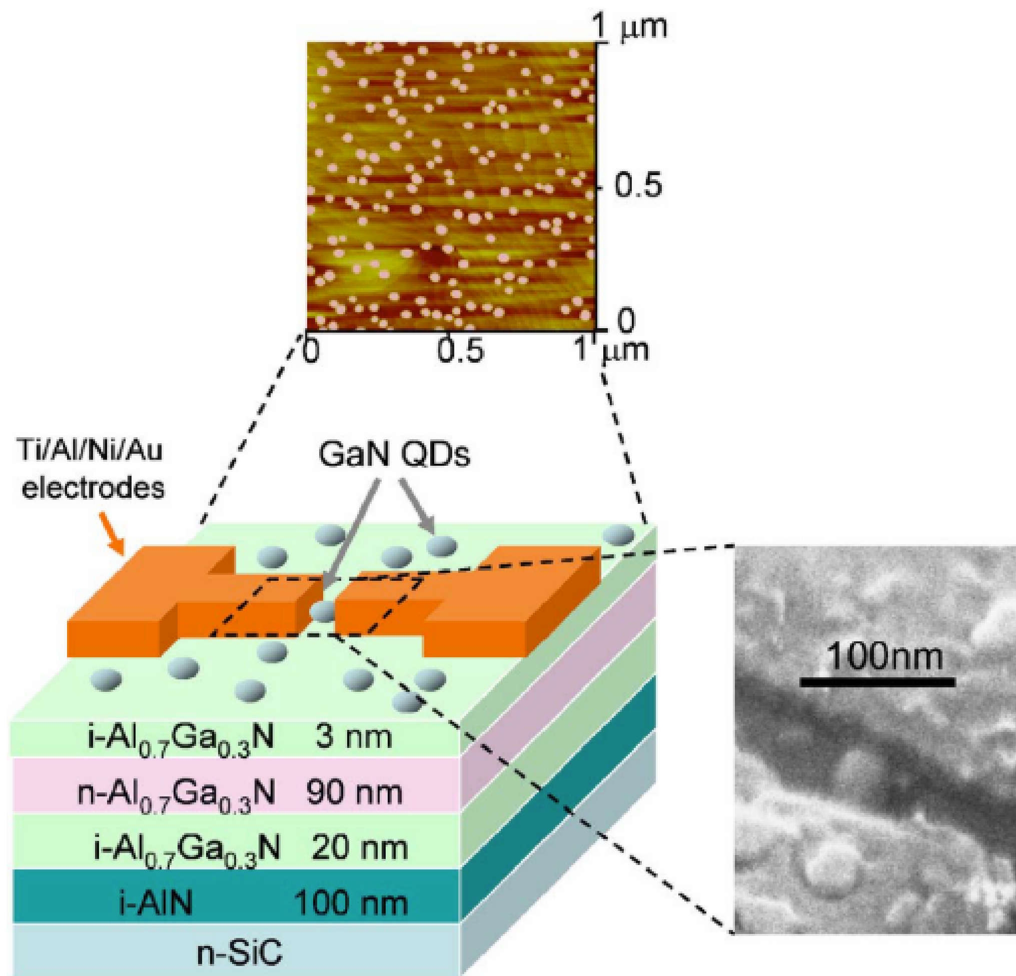

Figure 1-8: Schematic of the single electron transistor device creates by Nakaoka et. al. [11]. Also shown is an SEM image of the quantum dot between the electrodes and an AFM image of the self-assembled quantum dots after growth (Reprinted from [11], with permission of AIP Publishing, Copyright © AIP publishing 2007).

distribution in sizes [110]. This distribution in sizes is important as the dimensions of the quantum dot helps to determine the confinement properties, specifically the shape and size has a bearing on the exciton ground state energy of the quantum dot system [114] [115]. Thus, the optical properties of these quantum dots will likewise be inhomogeneously distributed over a range [99]. This is not practicable for SPE (single photon emission) devices, because for successful optical transistor devices, as an example, one desires a quantum dot array with specific and uniform emission characteristics across an entire chip [116]. This means the requirement is that not only are all quantum dots emitting photons of the same wavelength but also photons need to indistinguishable, both from every other dot in the sample but also from the same dot. Investigating a sample with self-assembled quantum dots in order to identify suitable dots is clearly not effective for mass production purposes [117].

From the above discussion, one is aware that whilst self-assembled quantum dots have some areas of use for which they are successful, quantum information processing and single photon emission devices are not a practical application for the wafer scale [117]. We will now return our attention to site-controlled quantum dots, which have the potential for quantum information processing, as will now be discussed.

1.6 Site-controlled quantum dots

Site-controlled quantum dots have predetermined sites. Not only that, as the site of the quantum dot is effectively fixed and controlled one can achieve the growth of quantum dots with similar, if not identical (in theory), sizes and shapes across an entire sample/wafer. This has numerous advantages. The lack of location determinability (as an example), when creating contacts for individual electrical injection of the quantum dot, such as the single electron transistor created in [11], use in photonic crystals [118], or for the use in a some form of cavity [119]) for device fabrication, is mentioned as a major drawback in the previous section concerning self-assembled quantum dots [120] [121]. This can be effectively solved here as the locations of the quantum dots are deterministic [122] [123]. This is especially promising in deterministic qubit generator positioning [124].

1.7 Quantum information processing

Quantum information science is the exploitation of fundamental quantum phenomena for information and communication applications [125]. Quantum information processing (QIP) encompasses quantum cryptography (such as quantum key distribution) [126], quantum teleportation, quantum metrology and quantum computing [127].

1.7.1 Quantum information processing - applications for site-controlled quantum dots

The main requirements of quantum dots for utilisation in photonic QIP applications are as follows. First, the quantum dot will need to act as a single photon source. This means that the quantum dot will act as a non-classical light source [128] whereby it will not obey Poissonian statistics [108]. Ideally, this means it will produce exactly one photon, preferably on demand, and at any one time [129]. This is called photon-antibunching, whereby there is a very low probability of detecting a second photon from the source immediately after the detection of the first photon [130], or indeed at the same time. Another requirement for, in particular, optical quantum computing is that the produced photons are indistinguishable [131] [132]. In terms of experiment, if two indistinguishable photons are sent through separate arms of a beam splitter, this results in full interference [129] (Hong-Ou-Mandel quantum interference effect [130]), as they are effectively identical. It is also highly desirable for single photon emitters to be operated via the use of electrical injection, for practical devices [113].

As alluded to above, different areas of QIP have different requirements regarding the nature of the single photon emitter. For instance, for optical quantum computing, indistinguishability between the emitted photons from the source is a mandatory requirement [130]. Concerning the successful operation of a quantum computer, a two-state quantum system which is well isolated from the environment but which can also be controllably interacted and measured is necessary for quantum logic gates [133]. Using a single photons to achieve this is highly desirable as they are largely free of noise. For universal quantum computing, a requirement is the entangling of logic gates. To facilitate this, an optical quantum computer requires entangled photon pairs, to implement the required quantum logic gates [134]. These photons need to be indistinguishable for successful operation. Perfect indistinguishability of the emitted photons is required for the successful operation of a quantum relay, which is a necessary component for quantum computing [135]. This is as, perfect energy matching by all photons, emitted from all different sources, is needed. If this requirement is met, it will result in the

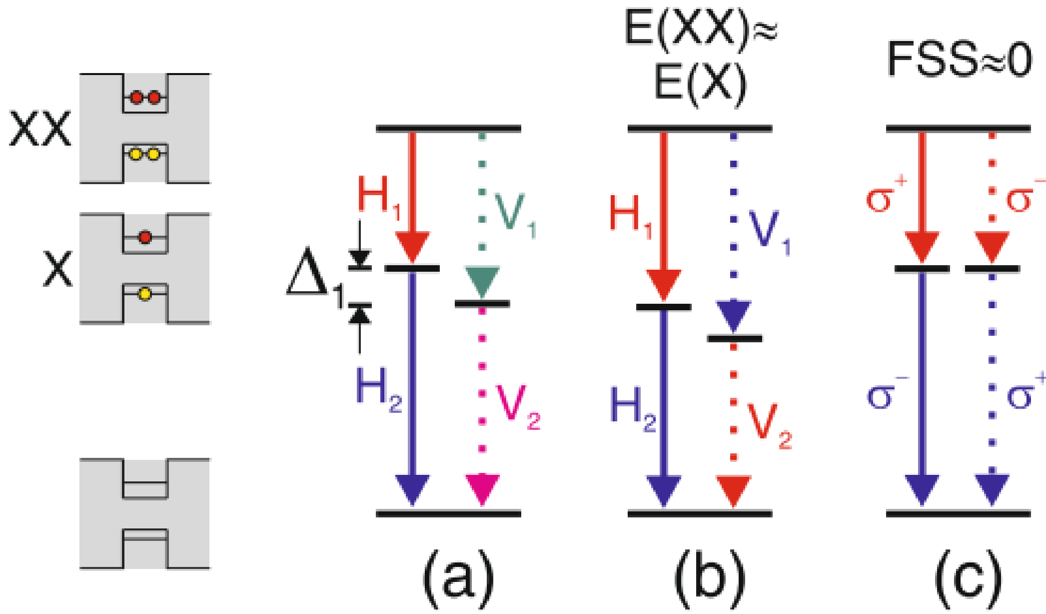

Figure 1-9: The figure on the left shows the biexciton state (denoted by XX) and the exciton state (denoted by X). In (a) fine structure splitting is present in the system with all four transitions having different energies meaning that entanglement is not possible. In (b) the biexciton (XX) and exciton (X) energies are tuned into resonance meaning the red transitions are equal to each other in energy as are the blue. This should allow entanglement of the emission which would be linearly polarised. In (c) the fine structure splitting in less than the linewidth and so the information encoded in the FSS is erased. This results in entanglement of the emitted photons which will be circularly polarised [12] (figure reproduced and unmodified from [12] under Creative Commons Attribution 2/0 International Licence https://creativecommons.org/licenses/by/2.0).

emission of fully identical entangled photons from each quantum dot [135]. The indistinguishability of emitted photons can be tested via a Hong-Ou-Mandel two-photon interference experiment [131], as mentioned above. With regards to quantum key distribution (QKD), this indistinguishability is not necessary [130]. This is as QKD is able to use protocols, such as BB84, whereby photon polarisation states are used and entanglement is not a fundamental requirement for operation [136].

1.7.2 Fine structure splitting

Fine structure splitting (FSS) is an important phenomenon when creating devices for QIP. During a biexciton-exciton cascade, the emission from two excitons can result in polarisation entangled photon pairs [12]. This entanglement requires the photons to

be indistinguishable in energy [137]. FSS in quantum dots is related to the spatial symmetry of the quantum dot [12], specifically the symmetry breaking of the excitonic wavefunction [137]. This can originate from the shape of the quantum dot, symmetry of the underlying crystal, anisotropy in the quantum dot strain field and alloy fluctuations. This leads to different energies of the excitons, and thus the resulting photons, due to having a different exchange interaction. The exchange interaction consists of short and long range interactions between the electron and hole, both of which contribute to the FSS [12]. The short range interaction depends on the crystal symmetry whereas the long range interaction depends on the macroscopic symmetry of the quantum dots. There can also be a contribution to the FSS via valence band mixing [138]. Thus, the FSS in quantum dots is manifested in an energy splitting of the excitonic states. The FSS can lead to a difference in energy of the photons originating from the biexciton-exciton decay. Thus, this leads to the existence of two decay paths which are distinguishable from one another. This has the effect that it prevents the entanglement of the photon pair produced in the biexciton-exciton cascade [12] (see Figure 1-9). As can be seen in Figure 1-9 the transitions in (a) and (b) are linearly polarised. The photons emitted in the different channels usually have orthogonal polarisation. In (a) polarisation entanglement is prevented due to the FSS being large, making the paths distinguishable. In (b) the FSS is still as in (a) but the average emission energies of the biexciton transition is equal to that of the exciton transition in the other cascade path. This should allow linear (horizontally and vertically) polarisation entanglement. However, the mechanism in (c) is the most desirable. Here the FSS is smaller than the linewidth of the emission and this leads to degeneracy in the two cascade paths. Thus, the FSS can be assumed in this case to be zero resulting in the emission of polarisation entangled photon pairs which are circularly polarised [12].

1.7.3 The second order correlation function

The measurement of the second order correlation function, $g^{(2)}(0)$, is a common method for the determination of whether an emitter is a single photon source [13]. The second order correlation function is defined as [139]:

$$g^{(2)}(\tau) = \frac{< I(t)I(t+\tau) >}{< I(t) >^2} \quad [139] \qquad (1.2)$$

where I(t) and I(t + τ) are the intensities of the emitted light at time t and after a time delay τ, respectively [139]. At zero delay time the second order correlation function

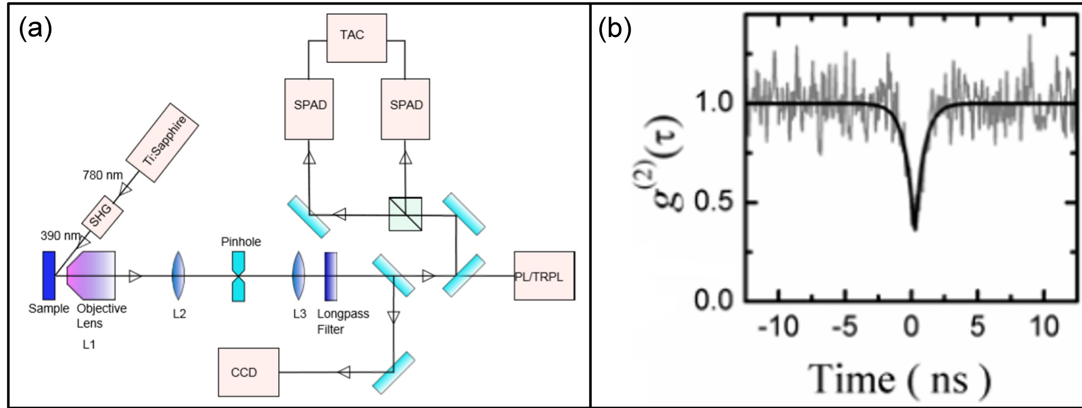

Figure 1-10: Figure (a) shows a typical Hanbury-Brown Twiss set-up for determining the second order correlation function for a sample (Reprinted from [13] supplementary material, with permission of AIP Publishing, Copyright © AIP Publishing (2013)). Figure (b) shows some typical second order correlation function data, in this case the value of $g^{(2)}(0)$ is found to be 0.36 (figure reproduced from [14], Copyright © 2008 WILEY-VCH Verlag GmbH & Co. KGaA, Weinheim).

can be expressed as [139]:

$$g^{(2)}(0) = 1 - \frac{1}{N} \quad [139] \tag{1.3}$$

where N is the number of photons of the electromagnetic field. The second order correlation function, acts as a measure of the anti-bunching of light, whereby photons travel separately from each other [140]. As the name single photon emitter suggests, the delivery of individual quanta of light is a core requirement for this type of device. When $g^{(2)}(0) = 0$ this indicates a pure single photon source, however, in practice, a single photon source is defined as when $g^{(2)}(0) < 0.5$ [139]. A classical light source can be defined as when $g^{(2)}(0) \geq 1$ [141]. It is worth mentioning, for application purposes, one desires $g^{(2)}(0)$ to be as small as possible. Indeed, it has been reported that practically, one requires the $\mathrm{g}^{(2)}(0)$ value to be < 0.1 for QKD applications but would require the $\mathrm{g}^{(2)}(0)$ value to be < 0.001 for the realisation of linear optical quantum computing applications [142].

The standard measurement for the second-order correlation function is with the use of a Hanbury-Brown Twiss set up [143]. A typical set up is shown in Figure 1-10. Whilst the Hanbury-Brown Twiss set up was originally used to measure the apparent angular diameter of bright stars [144], it is widely used across quantum dot literature to determine if a single photon source is present.

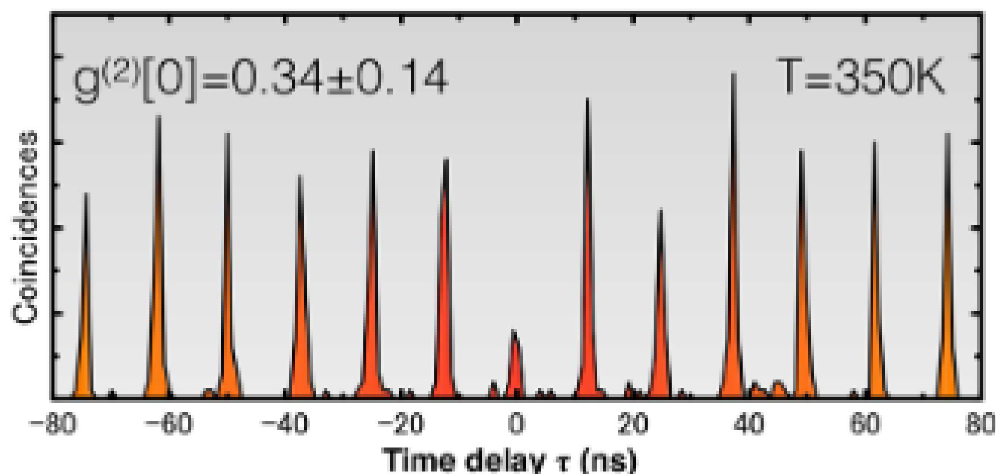

Figure 1-11: This figure shows the autocorrelated histogram of a site controlled GaN quantum dot at 350 K. There is a suppression of coincidence counts at $\tau = 0$. This is clear evidence of anti-bunched light to great enough extent for the criteria of single photon emission [15]. Reprinted with permission from [15]. Copyright © 2016 American Chemical Society.

Although it is true that many site-controlled quantum dot material systems have displayed single photon emission [143] [145] [146], most require operation at cryogenic temperatures, typically at $\sim$ 5 K [146]. This limits their practical use for quantum information processing. However, room temperature [68], and even up to 350 K [15], single photon emission has been achieved by utilising the III-N material system (see Figure 1-11). The properties of the III-nitrides make them a very promising avenue for achieving quantum information processing devices operating at room temperature, or above. Some of the intriguing properties of this material system will now be discussed.

1.8 Brief overview of the III-N materials group

The III-Nitrides are made up of the group-III elements of the periodic table and nitrogen. The most notable of these materials are AlN, GaN, and InN [147]. These materials typically crystallise into the wurtzite structure, as this is the only thermodynamically stable polytype at ambient conditions [148]. They can form other crystallographic structures, either the zinc blende structure, which is metastable [149], or the rock-salt structure, under high pressures [150], see Figure 1-13. AlN, GaN and InN and their alloys are wide [151], direct bandgap semiconductors in their most common, wurtzite,

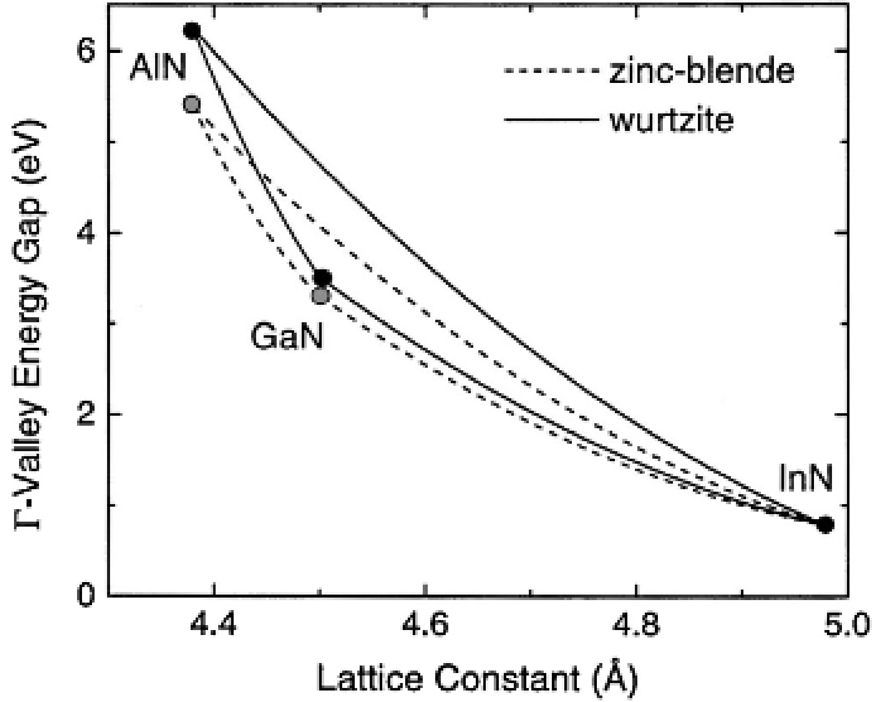

Figure 1-12: This figure shows a plot of the band gaps of AlN, GaN and InN for both wurtzite and zinc-blende crystal polytypes vs lattice constants (Reprinted from [16] Copyright © (2013) with permission from Elsevier).

polytype [152]. The band gaps are, 6.2 eV, 3.4 eV and ∼ 0.7 eV, for AlN, GaN [153] and InN, respectively [154]. Thus, the tuneable band gap range spans from the infra-red deep into the UV, which is very attractive for optoelectronic applications [155]. For the zinc blende structures, only AlN has an indirect band gap. GaN and InN still have direct bandgaps with this crystal structure [147]. The band gaps for this crystal structure are ∼ 5.3 eV [156], 3.2 eV [157] and 0.7 eV[158] for AlN, GaN and InN, respectively. See Figure 1-12 for a plot of the band gaps of all three materials with regards to lattice constants. The wide band gaps of the III-N, along with their transport properties, lead to possible uses in high temperature or high power electronics [159]. Table 1.1 shows some more properties of the III-N demonstrating their interesting thermal and electronic properties. It is, however, worth commenting that there is some conflicting data available concerning the properties of the III-N's in the literature. For the rest of this discussion only the wurtzite polytype of these materials will be considered.

Table 1.1: This table presents some of the different properties of AlN, GaN and InN.

Table of properties of AlN, GaN and InN			
Property	AlN (wurtzite)	GaN (wurtzite)	InN (wurtzite)
Molar Mass	20.495 $gmol^{-1}$ [160]	83.728 $gmol^{-1}$ [161]	128.827 $gmol^{-1}$ [162]
Young's Modulus	308 GPa [160]	150 GPa [161]	184 Gpa [163]
Thermal Conductivity	$\sim$ 285 $Wm^{-1}K^{-1}$ [160]	130 $Wm^{-1}K^{-1}$ [161]	$\sim$ 120 $-$ 150 $Wm^{-1}K^{-1}$ [164]
Specific Heat Capacity	0.6 $Jg^{-1}K^{-1}$ [160]	0.49 $Jg^{-1}K^{-1}$ [157]	0.32 $Jg^{-1}K^{-1}$ [157]
Refractive Index	$\sim$ 2.2 [160]	$\sim$ 2.3 [157]	$\sim$ 2.9 [157]
Melting Point	3273 K [165] [160]	2773 K [157]	1373 K [165]
Mobility: electrons (e), holes (h)	683 $cm^2V^{-1}s^{-1}$ (e) [165]; 14 $cm^2V^{-1}s^{-1}$ (h) [157]	1400 $cm^2V^{-1}s^{-1}$ (e); [165] 170 $cm^2V^{-1}s^{-1}$ (h) [165]	100 $cm^2V^{-1}s^{-1}$ (e) [165];
Lattice Constants (a and c)	a = 3.112 Å; c = 4.982 Å[166]	a = 3.189 Å; c = 5.185 Å[166]	a = 3.533 Å; c = 5.693 Å[165]

*All parameters presented specific to a temperature of 300 K.

1.9 Wurtzite crystal structure – a closer observation

Wurtzite materials have a hexagonal crystal structure [18] consisting of two interpenetrating close-packed hexagonal lattices [167], where the axial direction of the hexagonal column is called the c-axis [18]. Looking at the wurtzite crystal structure, one can see from Figure 1-13 that there is stacking of alternating layers of III-N pairs [168]. This is shown in more detail in Figure 1-14. Although Figure 1-14 shows this specific to GaN, this is also the case with AlN and InN. This results in the material being either group-III polar or N-polar [168]. The crystal can have different faces perpendicular to the c-axis [18]. This plane, the c-plane, is also known as the polar plane. Group-III polar material has the crystal structure configured such that the group-III atoms are at the top layer of the unit cell. Conversely, in N-polar material the structure is configured so that the nitrogen atoms are at the top of the unit cell. In itself, this affects the surface chemistry of the material [169], in addition to the possession of different electrical characteristics [18]. In particular, when considering KOH wet etching of AlN, GaN and InN, the group-III polar faces are much more chemically stable than that of N-polar faces [169] [170]. This results in much faster etching of N-polar material compared to group-III polar material [53]. Defects also cause a greater rate of wet etching [169]. The high degree of selectivity of wet etching is due to the different bonding

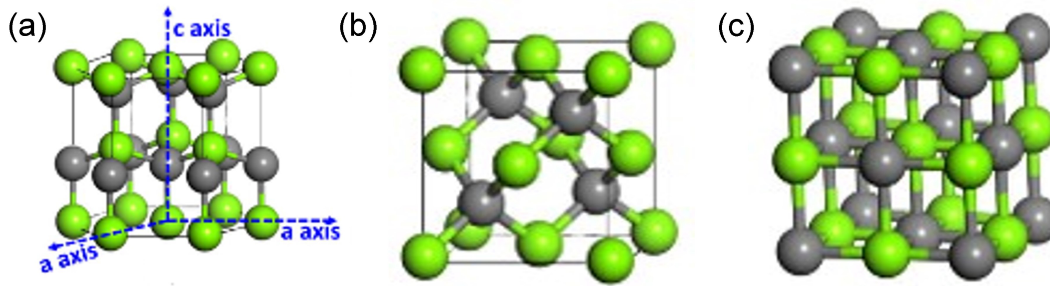

Figure 1-13: Figure (a) shows the general wurtzite crystal structure. In (b) the zinc-blende crystal structure is shown. In (c) the rocksalt crystal structure is presented. All figures reprinted with permission from [17] © The Optical Society.

conditions of both the faces, with the N-polar faces being more vulnerable to chemical reactions with the OH^- molecule [53]. Concerning the group-III polar material, once the group-III top layer is removed, an N-terminated surface with three occupied dangling bonds of nitrogen remains. These dangling bonds heavily repel the OH^- ion significantly reducing the etch rate/success. In comparison, the N-polar material only has one nitrogen dangling bond allowing the OH^- ions to attack the back bond of the group-III element. Thus, this etching is far easier and consequently occurs quicker in comparison to III-polar etching [50].

1.10 Disadvantages of the III-N's

1.10.1 Quantum Confined Stark Effect

A material with a polar wurtzite crystal configuration exhibits noncentrosymmetricity [100]. This results in a strong, intrinsic polarisation field [171] along with a large piezoelectric field for systems or structures with strain, such as systems with lattice mismatch [16]. This has the effect of bending the bands of the system leading to a spatial separation of the electron and hole wavefunctions [172] (see Figure 1-15). This is the Quantum Confined Stark effect (QCSE) [173]. In optoelectronic devices it leads to a reduction in the radiative recombination rate [172] and a redshift in the emissions [173]. This is an issue for optoelectronic application with the III-nitrides.

Tactics utilised in order to mitigate the QCSE in the III-N's

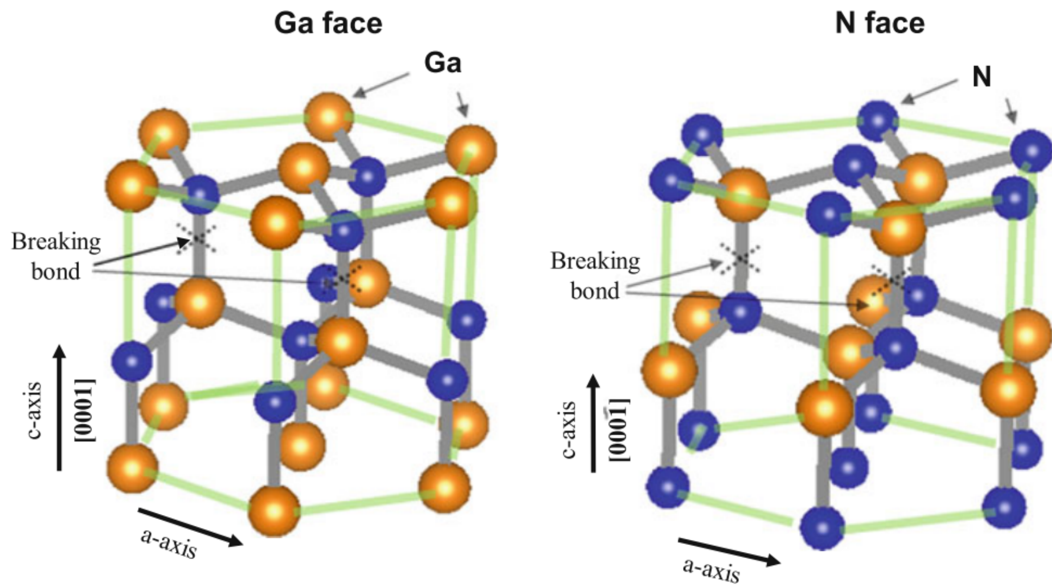

Figure 1-14: This figure shows the GaN wurtzite crystal structure with the Ga-polar face, on the left and the N-polar face on the right. Reprinted/adapted by permission from Copyright Clearance Center: Springer Nature, Properties and Advantages of Gallium Nitride by Daisuke Ueda, Copyright © 2017, Springer International Publishing Switzerland) figure reproduced from [18]).

The Quantum Confined Stark Effect (QCSE) is predominantly a limitation to polar III-N optoelectronic structures such as quantum wells. In the case of nonpolar quantum wells the polarisation fields are perpendicular to the growth axis. Thus, there is the presence of no internal, in-plane electric field from the spontaneous polarisation present in the wurtzite structure. Thus, this contributes towards solving the problem of the QCSE [174]. There may however, still be the presence of some piezoelectric field due to strain in the system. In terms of quantum dots, the internal electric field can be significantly reduced via growth of the QD structures on nonpolar or semi-polar planes [48]. However, it is worth mentioning that the growth of nonpolar and semi-polar material is rather challenging [175] [176]. This is because growth on nonpolar or semi-polar non-native substrates results in high dislocation densities and stacking faults. There is also difficulty in achieving smooth film morphology [175] [176]. It has been reported that semi-polar growth is easier than purely nonpolar growth [16]. Figure 1-16 shows semi-polar and nonpolar surfaces for a wurtzite crystal structure.

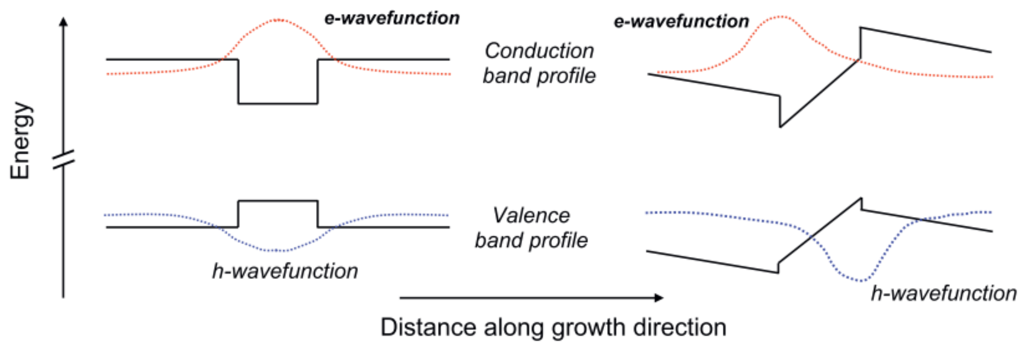

Figure 1-15: Schematic of the band profiles and electron and hole wavefunctions two quantum well systems. On the left there is no internal field and so no changes to the band profile allowing for a good overlap in the electron and hole wavefunctions. On the right is the profile for a polar III-N quantum well. This illustrates how the internal fields separate the electron and hole wavefunctions leading to a reduction in radiative recombination efficiency [16]. Reprinted from [16], Copyright © (2013), with permission from Elsevier.

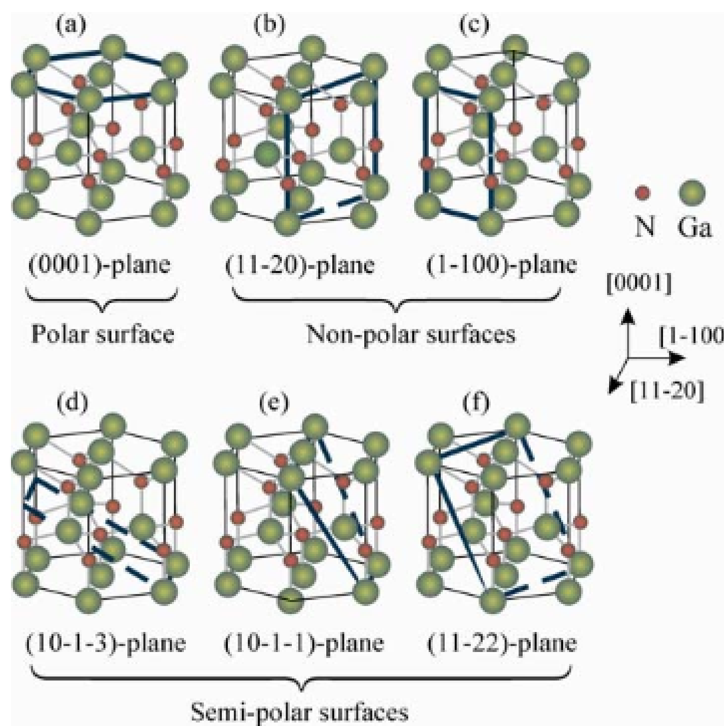

Figure 1-16: This Figure shows a schematic of the polar, non-polar and semi-polar crystal planes of wurtzite GaN (figure reproduced from [19] Copyright © 2008 WILEY-VCH Verlag GmbH & Co. KGaA, Weinheim).

1.10.2 Defects and dislocations in the III-N material group

Heteroepitaxial growth of III-nitrides is performed on non-native substrates (sapphire, silicon, silicon carbide). This introduces a large amount of defects due to the strain in the system from the lattice mismatch and the differences in thermal expansion coefficients [177] [178]. A large difference in the thermal expansion coefficients of the substrates and the III-N material, in addition to the large lattice mismatch can lead to epilayer cracking above a certain growth thickness [179]. However, even with large defect densities, III-nitride devices typically still perform efficiently [177]. Different types of defects present in crystallographic structures include interfaces, dislocations, stacking faults [180], vacancies, interstitials, impurities [181] and grain boundaries [182].

Vacancies, as the name suggests, are regions of the lattice where atoms are missing. Interstitials are where atoms are located within the lattice, additionally, whereby they should not be. Thus, this results in an atom residing in between atoms of respectable lattice positions. These point defects fall into three categories, the first where there is just a vacancy is a Schottky defect. The second, where there is a vacancy and interstitial pair, is a Frenkel defect and the third, with just an interstitial, is an anti-Schottky defect [181]. Another type of defect, impurities, are the occurrence of a foreign atom replacing that of the native material within the lattice [181].

Dislocations are a form of defect existing along the line of a solid [181] or extended structural discontinuity within a material [180] and can also be described as linear defects [183]. In real crystals, slip occurs where a part of the crystal slides across a neighbouring part. The surface of a planar or almost planar slip surface is called the slip plane. Not all the atoms on the slip plane slip simultaneously, therefore the slip effectively has a start and an end point. The boundary line between a slipped and unslipped area is the dislocation line, with the dislocation being the atomic configuration at this boundary [184]. The Burgers vector defines the magnitude of the slip process [182]. A Burgers circuit showing a Burgers vector can be seen in Figure 1-17 (d). There are two types of dislocation of major interest to epitaxially grown III-N materials, the edge and screw dislocation. An edge dislocation can be defined as having a Burgers vector perpendicular to the dislocation line. Conversely, the screw dislocation has a Burgers vector parallel to the dislocation line [21]. Dislocations are detrimental to the electronic properties of almost any semiconductor material [180].

Stacking faults arise from a fault in the stacking sequence of the planes of the lattice's layers of atoms. When a dislocation disassociates into two partial dislocations, a planar fault results between them as they move apart. This movement apart, eventually stops

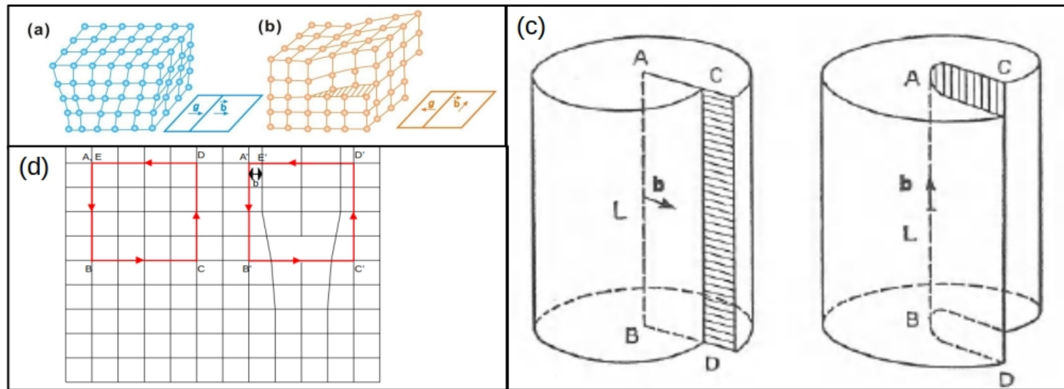

Figure 1-17: Figure (a) shows a schematic of an edge dislocation whilst (b) shows a screw dislocation is shown. Both pertain to that of a cubic crystal. Reproduced from [20] under Creative Commons Licence (http://creativecommons.org/licenses/by/4.0/). Figure (c) again shows an edge dislocation on the left and a screw dislocation on the right from a slightly different perspective for additional clarity. Reprinted from [21], Copyright (1964) ©, with permission from Elsevier. Figure (d) shows the Burgers vector of a dislocation. It is represented by the failure of the closure between A' and E' in the circuit on the right resulting in distance, b. Here b is relative to the circuit on the left which represents a dislocation free crystal.

due to a balance between the stress field pushing the partial dislocations apart and the attractive force due to the surface tension of the fault. This leaves a stacking fault remaining in the crystal [185]. A grain boundary is the boundary between aggregates of randomly oriented single crystal grains of which the bulk crystal is composed. These typically form during the growth process [185].

III-N semiconductors are regularly grown upon foreign substrates (such as SiC, sapphire) due to a lack of bulk III-N single crystal [168]. The large lattice mismatch between the epilayer and substrate results in very large dislocation densities [168] (see Table 1.2). These dislocations are formed in order to relieve strain in the system induced by the mismatch [148]. Even though III-N materials can be used as part of functioning devices with relatively high defect densities, this still has an impact on device performance if the densities are too great.

Table 1.2: This table presents a comparison of the lattice mismatch between different III-N compounds and commonly used foreign substrates for growth.

Table of lattice mismatch between substrates and III-N materials		
Material	Sapphire Lattice Mismatch	6H-SiC Mismatch
AlN	13.3% [186]	0.9% (at 1100 ^oC) [187]
GaN	13.84% [188]	3.41% [188]
InN	29% [189]	62% [190]

*All parameters presented specific to a temperature of 300 K unless otherwise specified.

1.10.3 Overall assessment of the disadvantages

The QCSE is a large problem in polar III-N materials when considering their use for optoelectronic applications. This can result in a lower efficiency of carrier radiative recombination in optoelectronic devices and thus lower efficiency for the device as a whole [16]. As mentioned, these materials also have very large dislocation densities when grown on foreign substrate [191]. Whilst they perform well with high dislocation densities compared to that of other material systems (such as III-As [192]), this is still a problem for the creation of high efficiency active regions [193]. Additionally, although this will not be discussed in detail, the growth of high quality InN and high Indium content III-N alloys also remains difficult [194] [195].

1.11 Advantages of the III-N materials group when creating SCQDs

As mentioned earlier, site-controlled quantum dots have potential applications in quantum information processing (QIP), leading to a possible realisation of quantum optical computing via the production of qubits [124]. III-N based quantum dots have the advantage over other systems of being capable of being operated at higher temperatures for single photon emission [47]. Conversely, the III-As and III-P material systems requires cryogenic operating temperatures for single photon emission. This is due to the small exciton binding energies and small barrier band offsets within the system [13]. As the III-N's have large barrier band offsets and large exciton binding energies, this makes them capable of single photon emission at relatively high temperatures [13].

1.12 Conclusion

Single photon emission has been demonstrated up to a temperature of 350 K with III-N quantum dots [15]. However, further progress is required before successful, electrically injected, arrays of room temperature single photon emitters suitable for QIP are realised. Additionally, large arrays of wafer scale SCQDs were not created in the work in [15]. Thus, greater exploration into the creation of periodic arrays of SCQD sites with the III-N's is necessary for scalable, high temperature, quantum device creation. The work in this thesis presents new avenues for sites for such quantum dots. Whilst it is appropriate to discuss III-N site-controlled quantum dots further, an overview of some of the techniques used to grow, fabricate and characterise these devices will first be presented in the next chapter.

Chapter 2

Experimental Techniques

This chapter details the various experimental techniques used through this thesis. Specifically, experimental techniques concerning the semiconductor growth, nanofabrication processes and characterisation have been presented and discussed. This chapter only concerns techniques explicitly used in this thesis.

2.1 Growth

Generally, semiconductor single crystals can be grown via a number of methods. These include growth from the melt, from solution and from the vapour phase [196]. Epitaxy can be defined as an ordered growth of one crystal upon another resulting in a well defined orientation relationship between the two crystals. Growth of one crystal upon a substrate of a different substance is called heteroepitaxy, whilst growth of a material upon a substrate of the same material is homoepitaxy [197]. With the III-N's however, growth of sufficiently large (2-inch or more) single crystals for epitaxial substrates, at low cost, has been found to be challenging. Standard growth from the melt, as is performed for silicon, of AlN is difficult to achieve due to the material's very high melting temperature of 3200 ^{o}C. Additionally, solution growth techniques with AlN are also challenging due to the very low solubility of nitrogen in liquid aluminium [198]. When one considers GaN, standard growth from the melt is also not possible due to high covalency and very high decomposition pressure at the melting point [199]. Whilst there have been some more exotic routes to create relatively large III-N single crystals, these technologies have not yet reached maturity and cost effectiveness when one compares to current silicon wafer manufacture.

Some examples of how bulk AlN templates can be grown will now briefly mentioned. Whilst strictly heteroepitaxial growth, thick AlN templates (up to 1 mm) can be grown via growth of AlN upon foreign substrates utilising HVPE (Hydride Vapour Phase Epitaxy). The foreign substrate can then be removed, leaving a thick, purely AlN template [200]. Another route for the creation of single crystal AlN bulk templates is solution based growth from the liquid phase upon a foreign substrate, followed by the removal of the substrate from the bulk AlN crystal. One-inch diameter and 200 μm thick AlN single crystals have been grown in this way [201]. Additionally, sublimation-re-condensation and physical vapour transport (PVT) can be used to grow AlN boules with diameters of 10-50 mm. Sublimation-re-condensation allows for the production of 2-inch bulk AlN wafers at temperatures of 1850-2250 ^oC, at atmospheric pressure with an 85% usable area [202]. PVT grown bulk AlN boules have been grown with dimensions of 25 mm in diameter and 15 mm in length, utilising AlN powder and N_2 gas precursors at temperatures of 2100-2300 ^oC [202].

Due to the relative ease of growth and cost effectiveness, foreign substrates are usually combined with the employment of heteroepitaxial growth [152], instead of using native substrates. The use of foreign substrates does have the disadvantages of lattice mismatch, thermal expansion coefficient mismatch and, in some cases, chemical incompatibility. This leads to highly stressed epilayers with high dislocation densities [199]. The epitaxial growth technique used for the work in this thesis was Metal Organic Vapour Phase Epitaxy (MOVPE) and so this technique will now be discussed further.

2.1.1 MOVPE growth of the III-N materials group

MOVPE is a method for depositing condensed phase material from a vapour phase. This is facilitated by chemical reactions from metal-organic precursors [203]. A carrier gas is use to supply the precursor materials to the reaction chamber for pyrolysis, chemical reaction and subsequently material growth upon the substrate [203]. The metal precursors for III-N growth are typically group-III metal alkys (such as trimethly gallium/aluminium/indium). These are typically in the liquid phase and stored in 'bubblers'. The nitrogen precursor source is usually ammonia (NH_3) [203]. The chemical reactions involve gas-phase reactions which are homogeneous and surface reactions which are heterogeneous. Homogeneous reactions are those where only one phase of matter is involved [204] (hence for MOVPE this is why the purely gas-phase reactions are homogeneous). Heterogeneous reactions are those that involve a number of phases [204]. In terms of MOVPE, this refers to reactions between the gas and solid

phases near and upon the surface of the substrate. When the gas-phase reactions limit the efficiency of the growth or lead to the formation of unwanted by-products, these are termed parasitic reactions [203]. Such reactions are undesirable and can lead to the growth of morphologically poor and crystallographically defective material in addition to a reduction in the growth efficiency. Typical carrier gases are highly pure H_2 or N_2, or a mixture of the two [203].

Thermodynamically, MOVPE is a non-equilibrium process. This means it has a negative difference in Gibbs free energy. The non-equilibrium state is deliberately targeted. This is achieved via the supply of reactants in the vapour phase in order to create super-saturation. In chemistry, a saturated solution is one where the concentration of the solute will not increase further. Supersaturation is where there is more dissolved solute than for a saturated solution. This can be achieved by dissolving solute in a solution at higher temperature (in the case of dissolving ionic salts ion water), where the saturation point is higher, followed by lowering the temperature. In such a solution, all the solute remains dissolved but interestingly when the solution is disturbed, such as insertion of a seed crystal (of the same material as the solute) the supersaturated solution comes to equilibrium via precipitating solute [205]. In a CVD (Chemical Vapour Deposition) process, such as MOVPE, the vapour phase is supersaturated. The system will to try and restore, or 'drive towards', equilibrium, via the deposition of a solid film of material from the vapour phase. This is as, at off-equilibrium, it is more favourable for gas phase precursor molecules to crystallise on the substrate surface as opposed to remaining in the gas phase. One can also define the supersaturation as the ratio of impinging flow to re-evaporated flow. Thus, in equilibrium conditions, this supersaturation has a value of is 1, and hence there is no crystal growth as all impinging adatoms re-evaporate [206]. In order for growth to occur, an energy barrier, the activation free energy, of the overall reaction must be overcome [203]. Heating the substrate to a suitable temperature can be undertaken to achieve this.

The general operation of a MOVPE system will now be briefly discussed. The carrier gas is 'bubbled' through the metal-organic liquid precursor bubbler/s. This allows the carrier gas to adsorb precursor material from the liquid bubbler, into the carrier gas, in order to transport the material into the reactor chamber. The hydride source is also transported to the reaction chamber via the carrier gas. Under the right conditions in the chamber (temperature, pressure and ratio of precursors) reactions occur, resulting in the deposition of an epitaxial layer upon a substrate [207]. More detail with regards to growth upon the substrate is provided in Figure 2-1 and will now be discussed.

A number of processes occur during epitaxial growth. Homogeneous gas phase reac-

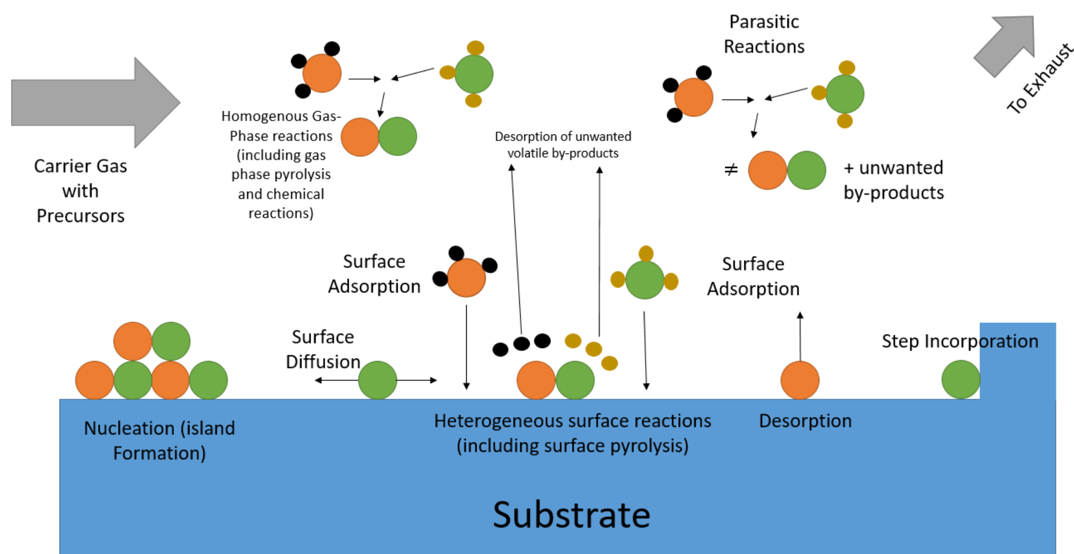

Figure 2-1: This figure shows the mechanisms at play during growth within the MOVPE reaction chamber. The reactions occurring during an MOVPE growth process are still not well understood, hence, this figure is a gross oversimplification.

tions can occur before deposition onto the substrate surface. These can be gas phase pyrolysis and chemical reactions in addition to undesirable parasitic reactions. The latter results in the generation of unwanted species. Adsorption of precursor species can also occur onto the heated substrate. Surface pyrolysis of the precursor species can occur on the heated substrate. The group-III precursors used in the work in this thesis were trimethygallium/aluminium/indium. Typically, pyrolysis would lead to dimethlygallium/aluminium/indium and then monomethlygallium/aluminium/indium which would then undergo further pyrolysis and then chemical reaction with N to form GaN/AlN/InN and their alloys. Adatoms upon the surface can then diffuse across the surface itself, nucleate new growth islands, or join pre-existing nucleated islands, incorporate onto step edges or desorb from the surface. However, the exact reactions which occur during MOVPE growth are still not fully understood and so this description is an oversimplification.

Waste by-products are then removed from the reaction chamber via the exhaust. The waste is transported to a chemical 'scrubber' whereby it is partially cleaned before removal from the system entirely [203]. A schematic of the specific MOVPE system used in this thesis is shown in Figure 2-2. The MOVPE growth reactor was an AIX 200/4HT RF-S, AIXTRON system. It was a 1 x 2" horizontal chamber, where the

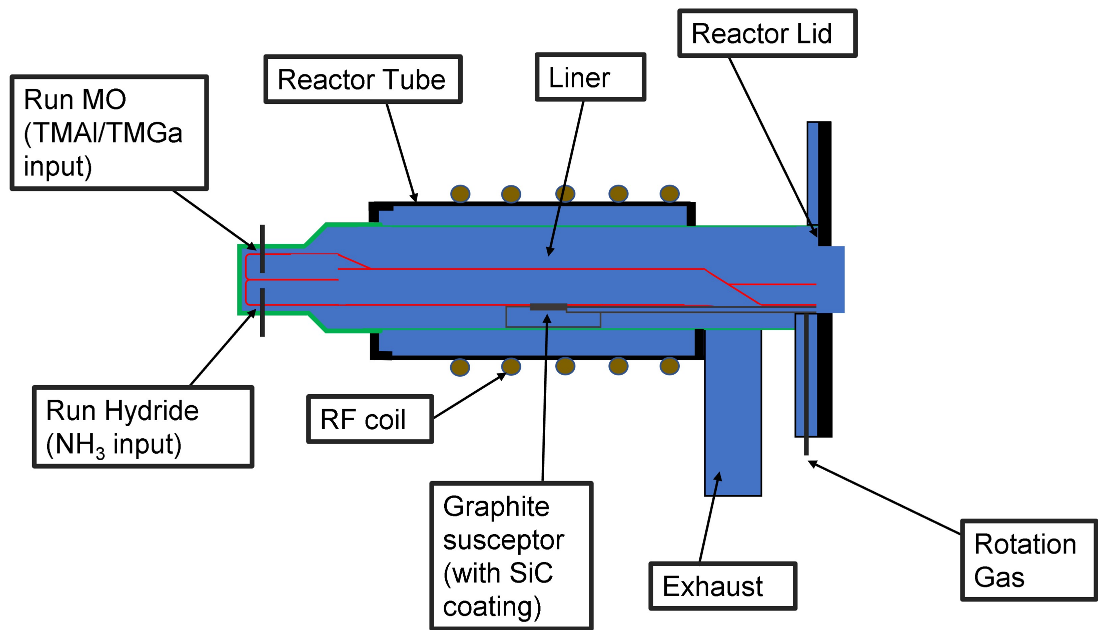

Figure 2-2: This figure shows a schematic of the MOVPE growth reactor (AIX200RF) chamber.

gaseous precursors enter from one end and exit through an exhaust at the opposite end, as opposed to a shower head delivery system.

2.1.2 Considerations for MOVPE AlN growth

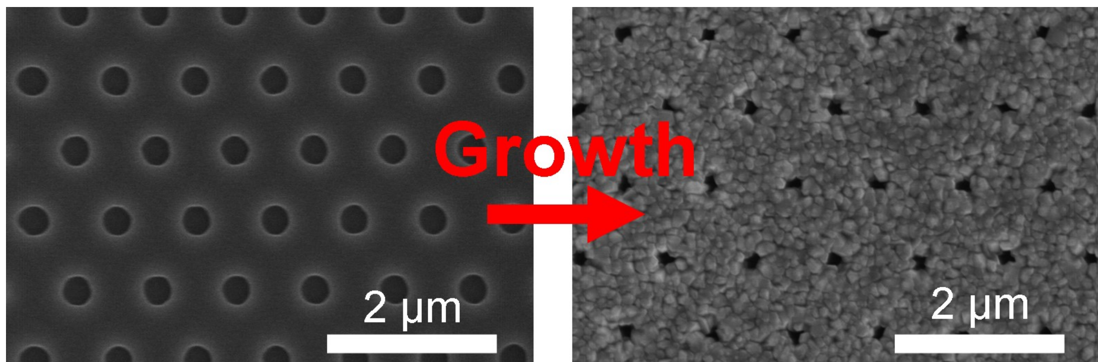

Figure 2-3: This figure shows an attempt at selective area regrowth of AlN through a patterned SiN_x mask upon an AlN template.

Aluminium adatoms have a high sticking coefficient [208] and low diffusion length [209]. This makes techniques such as selective area growth (SAG), utilising growth through a mask, impossible via MOVPE. SAG is essentially the site determined growth of a

material upon exposed seed windows. These windows are usually created via openings in a patterned dielectric mask [210]. This can be shown in Figure 2-3, where an attempt at selective area growth of AlN through a SiN_x mask is shown. As one can see, there is mostly deposition on the mask itself and not the growth of nanopyramids within the mask openings as has been reported previously with GaN [211].

2.2 Fabrication Techniques

2.2.1 Photolithography

Lithography is the technique of transferring copies of a master pattern onto the surface of another material. The word 'Lithography' is derived from Greek, and means writing on stone [212]. Photolithography, is a sub-group of the lithography family, and means the writing of a pattern using light. 'The advances in photolithography' have been a critical part in the rapid development of the semiconductor industry [213].

2.2.1.1 Principle of photolithography

A light sensitive liquid, the photoresist, is spin coated upon a wafer/sample to be patterned [213]. This layer, is key for the creation of the desired micro/nanostructure patterns. A photoresist is typically composed of a polymer, a sensitiser and a casting solvent [214]. The wafer is then baked, evaporating most of the solvent, and turning the wafer into a photographic plate suitable for the illumination process. This coated wafer is then exposed to UV (Ultraviolet) light through a mask with a specific pattern. This mask then alters the light distribution and thus, the illuminating shape transferred from the mask to the photoresist. Regions of exposed resist are either softened, in the case of positive resit, or hardened in the case of a negative resist [213]. For a positive resist, polymer chain scissions occur within regions exposed to UV light, making these regions more soluble within a specific solvent (developer), as there are fewer polymer bonds in these regions. For negative resists, cross-linking of polymer chains occurs when exposed to the UV radiation, making the exposed regions less soluble within a developer [214], as there are more polymer bonds in these regions (the wafer/sample can be either dipped or sprayed in a suitable photoresist developer after UV exposure and the choice of developer is dependent on the photoresist itself).

The wafer can then be etched using the photoresist as a mask. This can either be used to directly transfer the pattern into the wafer underneath or to transfer it into a more robust mask deposited before the lithography process. The patterned mask can then be used as a dry etch mask to pattern the wafer/layer below. Alternatively, the patterned resist, providing that an undercut has been formed, can be used to reverse the pattern by the deposition of a metallic mask. The remaining photoresist, including the metal layer deposited upon this resist, then can be removed in developer. This is the so-called 'lift-off' process [214]. This metal dot array can then be used as an etch mask for the wafer, allowing one to create structures such as uniform, spatially

predetermined nanorods [215] or metamaterial structures [216]. The wafer can then be cleaned for the removal of any residual organic material, contamination and removal of the remaining mask. Examples of the creation of nanorod structures via the 'lift-off' process can be seen in Chapters 4 and 5.

There are three more traditional forms of photolithography. These are contact printing, proximity printing and projection printing. Contact printing places the mask in contact with the the photoresist and proximity printing places the mask in a close proximity to the photo-resist [217]. The gap present in proximity printing removes the possibility of any potential damage created by mask contact with the sample as is the case in contact printing. This also increases the lifetime of the mask but does result in a loss in resolution because of defocusing due to diffraction [218]. Typically, these two techniques can achieve features of a few microns. Alternatively, projection printing utilises optics to project a pattern from a mask allowing for the creation of patterns of a few 10's of nanometers [217]. However, projection lithography suffers from both depth of focus limitations and high cost [22]. The need to control the light diffraction before and after the mask is the source of the high cost as expensive optics are required [219]. An alternative photolithography technique that has high resolution, low cost, high throughput and can produce periodic pattern across large areas is Displacement Talbot Lithography (DTL) [22]. As this is the lithographic technique used in the work in this thesis, further information on DTL will be given here.

2.2.1.2 Displacement Talbot Lithography

The Talbot effect is the manifestation of a series of self-images in planes beyond a grating when illuminated by coherent light [220]. This results in a periodic interference pattern that appears beyond the grating/mask. The periodicity of this pattern is dependent on the periodicity of the grating/mask used. There is also the formation of Talbot sub-images at distances equivalent to integer fractions of the Talbot period. They have frequencies which are multiples of that of the grating frequency. The Talbot effect alone can be used to pattern a wafer with photoresist. However, the depth of field of Talbot images scales with the square of the grating period and so is often small [22]. This renders execution of photolithography with purely the Talbot effect alone, very difficult practically. Additionally, it rules out being able to use this technique on rough surfaces or on wafers where there is significant wafer bow.

The depth of field problem arising in Talbot lithography can be overcome however, by changing the distance between the mask and substrate by at least 1 Talbot period

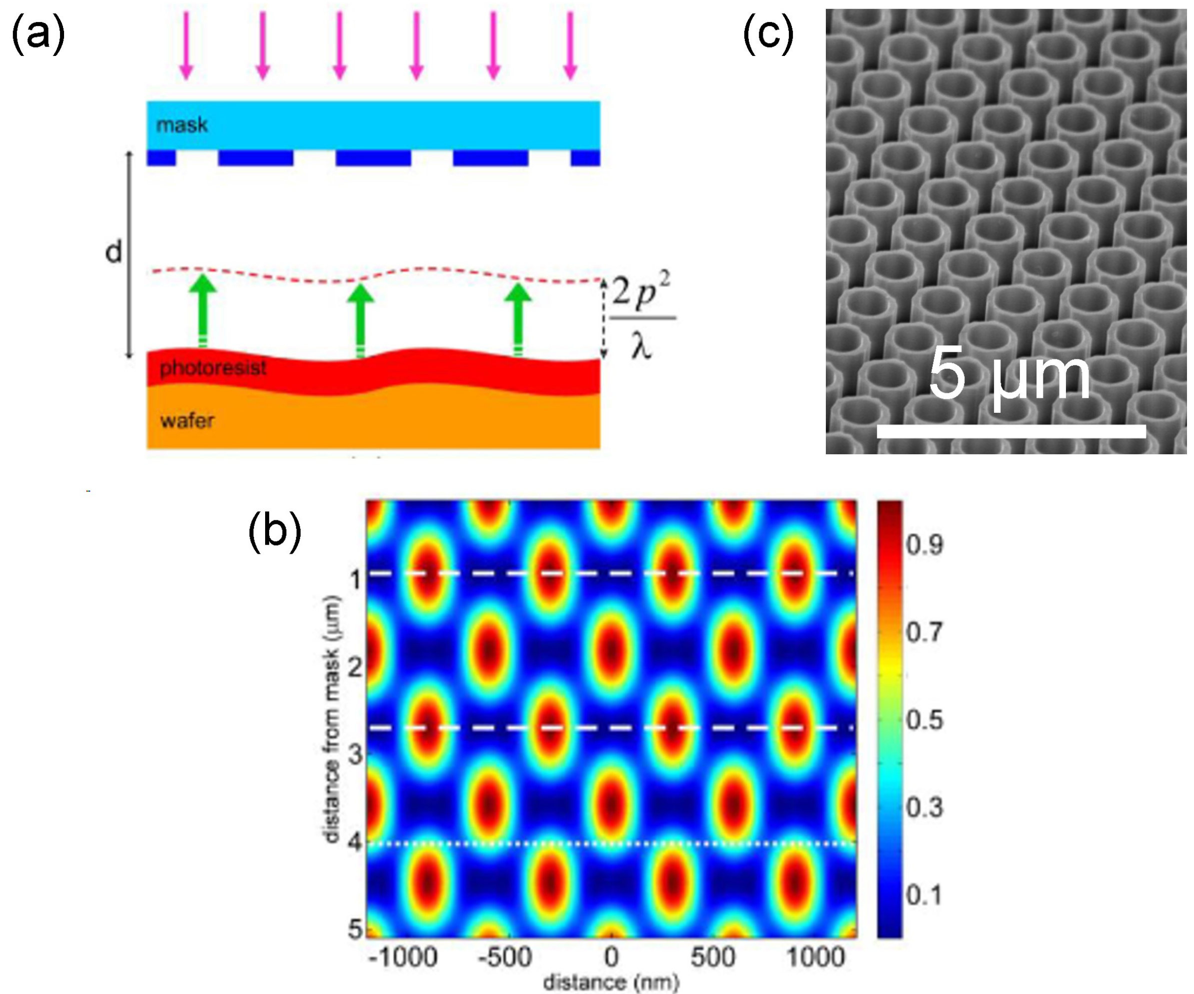

Figure 2-4: In (a) a schematic of the DTL process is shown. Here a photoresist covered wafer is moved 1 Talbot length towards the mask during exposure. In (b) a calculated intensity distribution is shown for an illuminated linear grating. Two self-images are highlighted with dashed lines, a sub-image is highlighted with a dotted line. This sub-image has twice the frequency of the original grating. Both (a) and (b) reprinted and adapted with permission from [22] © The Optical Society. In (c), an AlN nanotube is shown made via patterning a ring into resist via utilising a high exposure dose with DTL to generate a secondary interference pattern. This is then transferred into a SiN_x mask which is used to dry etch a tube into an AlN template.

during the exposure process. This is called 'Displacement Talbot Lithography', or DTL. This displacement causes the recording of an effective image. This effective image is independent of the absolute gap value [22]. Thus, rough/non-planar samples can be patterned in this way, without the depth of field limitation, as this technique has effectively unlimited depth of focus [221].

A number of different masks can be used in DTL. An example of one type of mask is a grating, where the mask is made up of a periodic array of lines. Another example is a periodic hole array, either in a hexagonal or square pattern. Performing DTL upon a grating mask can result in a periodic pattern upon the wafer half the pitch of that of the mask. However, this is not also the case for a hexagonal hole array. In this latter case, a one-to-one copy (in terms of pitch) of the hexagonal pattern from the mask to the wafer is transferred [221]. The calculated Talbot length (L_T) for a hexagonal mask is [222]:

$$L_T = \frac{\lambda}{1 - \sqrt{1 - \frac{4\lambda^2}{3p^2}}} \quad [222] \tag{2.1}$$

Here, p is the pitch of the mask and λ is the wavelength of illuminating light [222]. By varying the exposure dose, a large range of feature diameters can be achieved. Even the realisation of ring structures, when the exposure dose is high enough, is possible via harnessing the effects of the secondary interference pattern. See Figure 2-4 (c) for a dry etched tube structure made by patterning a ring into photoresist using the secondary interference pattern.

DTL does have disadvantages, however. These include low contrast between exposed and unexposed regions of the sample and the restriction to simple periodic features. The former is a result of the mixing of the self-images and secondary constructive interference features [222]. The latter disadvantage can be remedied by the use of 'Double-displacement Talbot Lithography' to create more complex periodic structures [223].

The DTL system used in the work in this thesis is a Phable 100 EULITHA system. It has a 375 nm UV laser as the illumination source with optics that generate a plane wave to illuminate a conventional lithography mask at normal incidence. The masks used were hexagonal amplitude masks with either a 1.5 μm pitch and 800 nm openings or a 1 μm pitch with 550 nm openings.

2.2.2 Mask Deposition techniques

Vapour phase deposition includes both chemical vapour deposition (CVD) and physical vapour deposition (PVD). Examples of PVD include thermal evaporation, sputtering, cathodic arc deposition, ion plating [224] and electron beam evaporation [224]. This latter method is the only form of PVD used in the work in this thesis and so will be discussed further here.

2.2.2.1 Electron beam evaporation

In electron beam evaporation, a high-intensity electron beam gun is focused onto a target. The electron beam is magnetically directed onto the evaporant target (such as some solid gold or nickel), this locally melts and evaporates the target [214]. Both the target, the electron beam, and the evaporant are all housed within an evacuated chamber. This is necessary as under vacuum the electrons have a longer mean free path compared to atmospheric pressure and so there is a reduction in unwanted collisions. This high intensity beam then impinges upon the target deposition source, evaporating some of this material [225]. The evaporating material then condenses onto the surface of the target substrate resulting in the deposition of a thin layer. Rotation of the substrate in the vapour cloud is desirable for uniform coating as this technique is a 'line-of-sight' process [224].

The electron beam locally heats the metal source, as opposed to directly heating the entire chamber, including the sample. This allows for evaporation and subsequent deposition of the metal without the degradation of the photoresist. Another advantage of e-beam evaporation is that it offers a deposition technique with fewer source-contamination problems than resistive heating [214]. Electron beam evaporation can have disadvantages. One such disadvantage is that the process may induce x-ray damage. This is as the electron beam is driven to a high voltage, highly accelerating electrons, which can cause x-ray emission [214].

The lift-off process can be used to apply a metal mask/metal layer to a sample in specific location. Electron beam evaporation is a tool that can be used for relevant metal deposition. Typically, with lift-off, metal deposition is limited to temperatures below 200-300 ^oC as above these temperatures photoresists often start to degrade [214]. For this reason electron beam evaporation is a particularly attractive method for metal mask deposition as part of a lift-off process. The electron beam evaporator used for metal layer deposition in this thesis was an Edwards FL-400. A rotating sample mount was used to ensure uniform deposition.

2.2.2.2 Plasma formation via an RF field for Plasma Enhanced Chemical Vapour Deposition

Before further discussion of Plasma Enhanced Chemical Vapour Deposition (PECVD), Reactive Ion Etching (RIE) and Inductively Coupled Plasma (ICP), the formation of a plasma via application of a radiofrequency (RF) field will be discussed.

A plasma is a macroscopically, electrically neutral, ionised gas. Plasmas are conductive as electrons can move freely within it. One can generate a plasma via the application of RF power to a pair of electrodes within an etch chamber. The applied RF power generates an oscillating electric field which, in turn, accelerates electrons back and fourth within the chamber [23] [226]. Comparatively, any ions present move very little as they are much more massive [226]. The accelerated electrons collide with atoms and molecules. If the kinetic energy of the accelerated electrons is greater than the ionisation energy of the atoms/molecules, ejection of an outermost shell electron results. Thus, an additional electron and an ion are now present in the gas. This ejected electron can then be accelerated by the electric field itself causing further electron ejection and ionisation of atoms and molecules. The number of electrons and ions continues to increase until, over a certain threshold, a discharge begins, creating a plasma [23].

A glow discharge plasma is the type of plasma used for both PECVD and dry etching processes. This type of plasma is weakly ionised. Due to their low mass, the electrons in the plasma can move much more and much quicker than the ions in the plasma (hence, the temperature of the electrons is effectively much larger than the rest of the gas, the latter being at or close to room temperature). The fact that the electrons are highly energetic allows them to cause excitation, ionisation, and disassociation of the atoms and molecules in the gas (whilst the gas can remain at ~ 300 K if that is what one desires). Excitation, ionisation and dissociation come about due to inelastic collisions with the highly accelerated electrons and the atoms or molecules. The excitation process results in the emission of a photon. In ionisation, a neutral atom is ionised into a positive ion and a free electron. Dissociation occurs when the accelerated electron splits a molecule into its constituent parts. These resulting parts of the molecule are often highly reactive and in the form of excited radicals [23].

2.2.2.3 Plasma Enhanced Chemical Vapour Deposition

Chemical vapour deposition (CVD) can be described as the formation of a thin solid film on a substrate material via the chemical reaction of vapour-phase precursors. These chemical reactions can be promoted or initiated by heat, high frequency (UV) radiation or via a plasma. The advantage of using a plasma is that deposition can occur at relatively low temperatures allowing for the use of temperature sensitive substrates [227].

The PECVD system specific to the work in this thesis is a Plasma-therm 790. In order to generate the plasma, a RF voltage (13.56 MHz) is applied between two parallel plates. Typically, an upper electrode is connected to ground, and the lower electrode, which also supports the wafer for deposition, is connected to a RF power supply. The lower electrode is also connected to a heating assembly to heat this up to an appropriate temperature, such as 300 ^oC (the temperature used in this thesis). A shower head is attached to the upper part of the chamber to supply the appropriate precursor gases and a vacuum pump is used to ensure a suitable vacuum for plasma generation [228]. Typically, NH_3 is used as the reaction gas for the nitrogen source and SiH_4 is used as the reaction gas for the silicon source. These two precursors arrive at the sample and allow for the growth of a SiN_x film [229]. SiN_x was the material used as a dielectric mask for the work involved in this thesis.

2.2.3 Etching and cleaning

2.2.3.1 Plasma based dry etching

In reactive ion etching, an etch chamber pumped down to high vacuum is used. Specific etch gases are then introduced into the chamber. There are two electrodes which face each other in the chamber and a 13.56 MHz radiofrequency (RF) power is applied to them, see Figure 2-5 (a). This results in the formation of a plasma as described in Section 2.2.2.2. The reactive species transport to the wafer surface and react with the target material [23].

Concerning the two electrodes, the upper electrode in the system is connected to ground, whilst the lower electrode is connected to the RF power supply via a blocking capacitor. The 13.56 MHz RF frequency used allows for rapid oscillation of the direction of the electric field between the electrodes. Only electrons can follow the oscillating field due to their small mass, moving between the electrodes. As a result of the bottom electrode being connected to a blocking capacitor, this electrode gradually biases negatively. This direct current bias (DC bias) that is generated is the self-bias

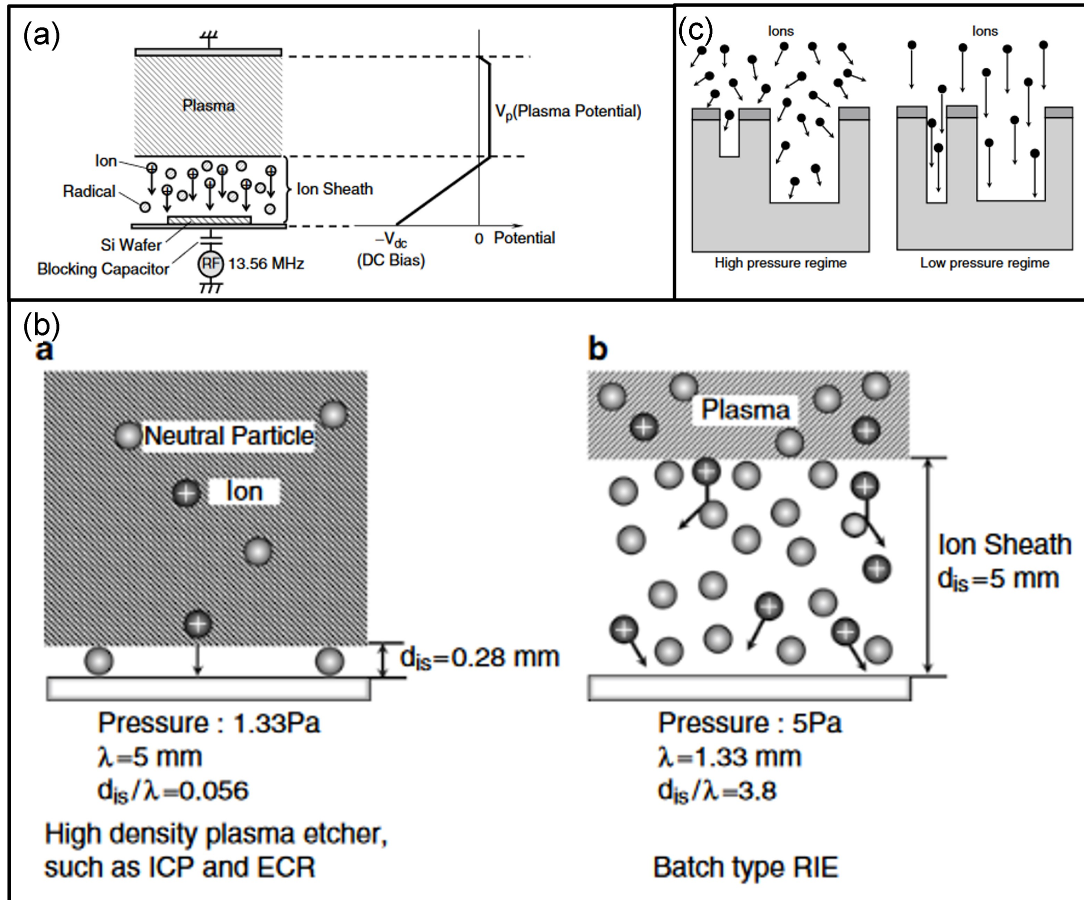

Figure 2-5: In (a), a basic schematic of a parallel plate RIE system is shown, highlighting the plasma, ion sheath and DC bias. In (b), on the left a high density plasma is shown with low pressure, small ion sheath and large mean free path. This is the sort of plasma generated via ICP. On the right a lower density plasma with higher pressure, larger ion sheath and smaller mean free path is shown. This is more typical of an RIE plasma. In (c), on the left, a high pressure etching schematic, whilst on the right a low pressure etching schematic. All images reprinted/adapted by permission from Copyright Clearance Center: Springer Nature, Dry Etching Technology for Semiconductors by Kazuo Nojiri Copyright © 2015, Springer International Publishing Switzerland ([23]).

of the system and depends on the RF power. As the negatively biased electrode repels electrons this leads to a region near the bottom electrode of no electrons and only ions, and is called the ion sheath, see Figures 2-5 (a), (b) [23]. Whilst this negative bias repels the electrons, it accelerates the ions to an energy given by the potential difference. Thus, the larger the negative bias, the more energetic the ions [230]. This, in turn, leads to greater etch rate for a given material since the etch rate of physical etching is dependent on ion energy and surface binding energy of the etch target. Physical etching can be termed sputtering [230].

As has been mentioned in Section 2.2.2.2, highly reactive disassociated radicals are also formed within the plasma. Such radicals will react with the sample surface chemically. When etching with purely these radicals, the target is typically etched isotropically, it can however be highly selective [230] [23]. In ion-assisted reactions, incoming ions enhance surface chemical reactions via simultaneous action of the reactive species and ions upon the target surface [23] [230]. In such a reaction, the etch rate is much larger than the etch rate by simply neutral radicals. Additionally, this promotes anisotropic etching as the ions strike the target surface at normal incidence [23]. The most widely believed model for ion assisted etching, according to Nojiri [23], is the hot spot model. Here, the local temperature of regions under ion irradiation are much higher, resulting in much faster radical reactions in these regions. Thus, due to the much faster etching in regions of ion irradiation, anisotropic etching profiles can be obtained [23]. It is worth mentioning that often the etch profiles achieved via ion-assisted etching alone are not always perfectly isotropic and can be tapered to some extent. With the additional component of ion-enhanced inhibitor etching more anisotropic etch profiles can be realised. Here, the reactive species and ions combine with inhibitor precursor molecules. These complexes can then deposit on the sidewalls of the etched structure, passivating it. This inhibits further lateral etching of the sidewalls whilst allowing a continued etch of the trench at the bottom of the structure (for the case of nanohole etching).

The dry etching process proceeds in what can be separated into four steps:

1. Reactive species (atoms, radicals, molecules and ions) are generated in the plasma
2. Species transported and the adsorbed onto the target (physisorption or chemisorption depending on if the species are ions or reactive molecules)
3. Reactions take place on the target surface
4. Etch byproducts desorb from the surface of target and transport away from the surface back to the plasma

5. Possible redeposition of etching byproducts [23] [230]

The gas pressure is an important parameter. This is as the scattering of ions in the sheath has an important impact on the etch behaviour. The mean free path (average distance over which a particle travels from one collision to the next), is inversely proportional to the pressure. When the mean free path is sufficiently larger than the ion sheath thickness, the ions undergo almost no scattering before arrival to the wafer, see Figure 2-5 (c). The selectivity of the mask is the ratio of the rate of etching between the target layer and the mask.

2.2.3.2 Inductively Coupled Plasma etching

In inductively coupled plasma etching (ICP), an additional induction coil with a 13.56 MHz RF power supply (ICP power) is used to generate the plasma. A magnetic field is generated when the high frequency current flows through the induction coil. This, in turn, creates an electric field in the chamber [23]. The electric field causes a helical motion to the electrons and forms the plasma in the chamber. Plasmas produced via ICP are high density plasmas compared with those usually generated by simply RIE. This is as the ICP power from the induction coil can be controlled separately to the RIE forward power. High density plasmas such as an ICP plasma have small sheath thicknesses such that there is minimal ion scattering compared to batch type RIE, see Figure 2-5 (b). This allows for better fine etching as fewer ions are impinging on the patterned wafer at off-normal angles [23], see Figure 2-5 (c). This allows for very anisotropic etching, Figures 2-5 (b) - (c). The 13.56 MHz RF RIE power supply is connected to the wafer stage (RF power) and is used for controlling the ion energy, independently of the plasma discharge [23]. The control and flexibility offered by ICP compared to that of RIE allows for well controlled etch profiles and higher selectivity. The ICP used for the work in this thesis, was an Oxford Instruments Plasma Technology PlasmaPro 100 Cobra. A basic schematic of this ICP can be seen in Figure 2-6.

In the work by Coulon et al. [231], an investigation of the dry etch conditions on AlN nanorods was undertaken. It was found that by increasing the pressure for the ICP dry etch, etch rate decreased. This was as a result of the reduction in the mean free path of ions at higher pressure leading to more ion collisions and hence lower ion energy. As the etching of the AlN was assisted by the ion bombardment this led to the observed reduced etch rate. An increase in pressure, did however increase the selectivity of the etch, leading to less tapered nanorods. This was partially down to the reduced ion energy, which led to reduced physical sputtering. Additionally, the greater range of

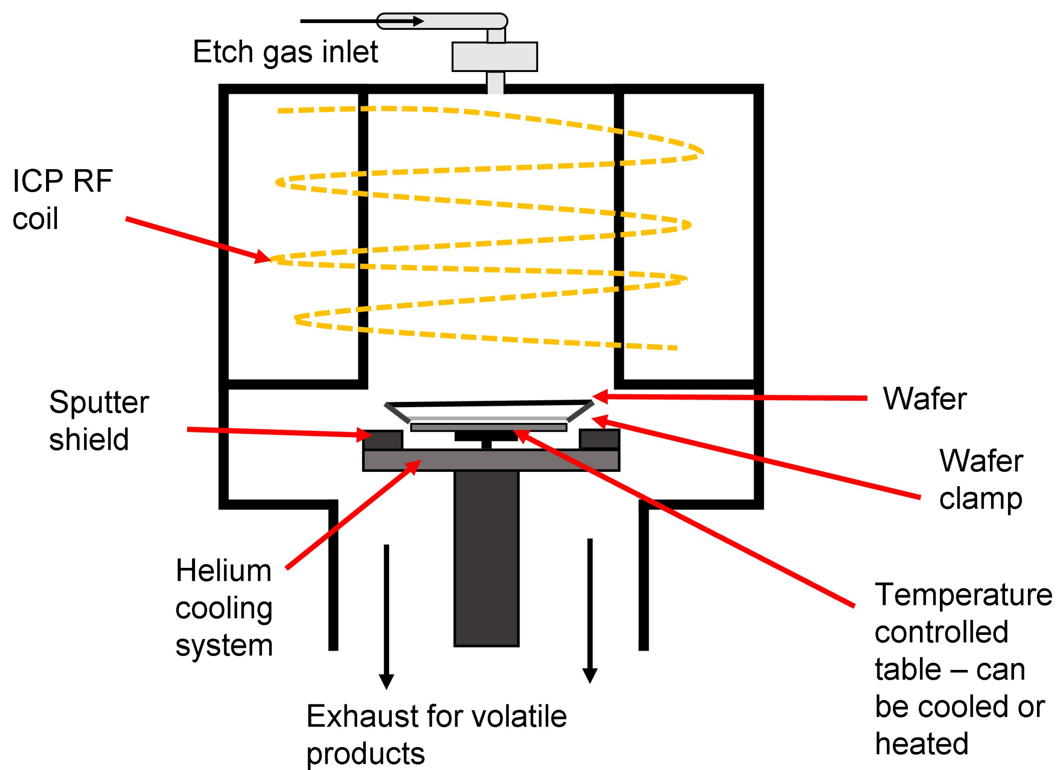

Figure 2-6: This figure shows a basic schematic of the Oxford Instruments Plasma Technology PlasmaPro 100 Cobra ICP system used in this thesis.

incident ion angles due to the higher pressure aided the sputtering of etch by-products on the nanorod sidewalls which would normally act to passivate the sidewall surface, restricting the lateral etch rate [231].

Also investigated was the impact of the RF power. As the RF power increases, whilst there is no change in the tapering profile of the rods, the etch rate increases and the selectivity decreases. The increased RF power leads to a much higher DC bias which therefore leads to a higher ion energy. This both increases the physical sputtering component and also assisting bond breaking and enhances surface chemical reactions, increasing the chemical component of etching [231]. What is clear from the work by Coulon [231], is that the profiles and etch rates of AlN nanostructures can be controlled via the tuning of different dry etch parameters. This can be important in the fabrication process of nanorod and nanohole arrays.

In this thesis, a number of different dry etch gas chemistries were used. For dry etching into BARC and subsequently a SiN_x mask, CHF_3 gas was used. The reason for this is that whilst CHF_3 readily etches BARC and SiN_x it is relatively inert to the III-N's. For dry etching of AlN itself a Cl_2/Ar gas chemistry was used. This is as the Cl_2 component of the gas is highly reactive with III-N materials, whilst the Ar component supplies ions in order to enhance the chemical dry etch process, as discussed above.

2.2.3.3 Wet etching

Wet etching is the etching of a material in baths of wet chemicals [213]. This provides a higher degree of selectivity in comparison with dry etching. The process of wet etching involves:

1. Reactant transport to the surface of the target material via diffusion
2. Surface reactions
3. Reactant transport away from the surface via diffusion [214]

If steps 1 or 3 are rate determining, the etching is diffusion limited. This means that the etch rate can be increased by stirring the etchant solution. If step 2 is the rate-determining step, the etch is reaction-rate limited. This means the etch rate strongly depends on etch temperature, etching material and solution composition [214]. Isotropic etchants etch in all crystallographic directions at the same rate and are typically diffusion limited. Anisotropic etchants etch away different crystal planes at different rates are are typically reaction rate limited. These latter etchants can result in geometrical

shapes bounded by perfectly defined crystallographic planes [214].

2.2.4 Chemical cleaning steps

2.2.4.1 Piranha Clean

A Piranha solution is a mixture of concentrated sulphuric acid (H_2SO_4, 95% concentration) and hydrogen peroxide (H_2O_2, 30% concentration). A ratio of 3 parts H_2SO_4 to 1 part H_2O_2 is used to clean organic material from samples (3:1 ratio). For the cleaning of lithography masks, especially in the case of DTL masks, a ratio of 2:1 is used. Piranha solution is successful at removing organic material from a sample or mask as it is a strong oxidant [232]. It oxidises the surface of the sample, targeting and removing organic material.

2.2.4.2 Aqua Regia

This is a chemical mixture of a ratio of 3:1 of concentrated hydrochloric acid (HCl, 37% concentration) and nitric acid (HNO_3, 69% concentration) respectively. This acts as a powerful oxidising agent which will dissolve metals [233]. This chemical mixture was used to remove remaining metal dot masks during the process for nanorod creation.

2.2.4.3 Buffered Oxide Etch

Buffered oxide etch (BOE) is a diluted form of hydrofluoric acid (HF). It usually contains buffering agents such as ammonium fluoride. These buffering agents are used to help prevent fluoride ion depletion. This acts to maintain a more stable etch characteristic of the solution. This is desirable as it allows more control over the wet etch as a whole [234]. HF based solutions are typically used for the etching of silicates [235] and silicon nitride [236]. Some of the masks used in this thesis are SiN_x and therefore BOE was used to remove these masks as part of the process. Additionally, as BOE is an oxide etch, treatment with BOE is a very effective way of removing oxides from a sample. This is an important step if preceded by steps such as Piranha or Aqua Regia cleaning which oxidises the sample surface. The dilution level used was either a 5:1 or 100:1 ratio of the buffering agent to hydroflouric acid in water. Specifically, the buffering agent was 5 or 100 parts 40% ammonium fluoride to 1 part 49% HF.

2.2.5 Processes

2.2.5.1 Lift-off Process

In this process, BARC (Back Anti-Reflection Coating) and photoresist are spin coated onto an initially planar wafer. A soft bake is then performed. This BARC is required to be an appropriated thickness, such that one can despoit a tall enough metal dot to be used for a dry etch mask. Additionally, the BARC needs to be able to be developable, in order to allow both lateral and vertical removal of the BARC layer. After photolithographic exposure (via DTL), the sample is then over developed. This has the effect of removing the BARC within the developed photoresist down to the template layer in addition to the removal of BARC on the sidewalls to create an undercut, see 3 of Figure 2-7. Electron beam evaporation is used for the deposition of a metal dot array upon the undercut wafer. The sample is then reintroduced into developer to complete the 'lift-off' process, removing the majority of the remaining BARC and resist. These metal dots can then be used as a hard mask for dry etching nanorod structures into a material such as AlN [49]. Finally, the remaining mask can be removed followed by appropriate cleaning ready for growth experiments. A schematic of the entire lift-off process for such an application is shown in Figure 2-7.

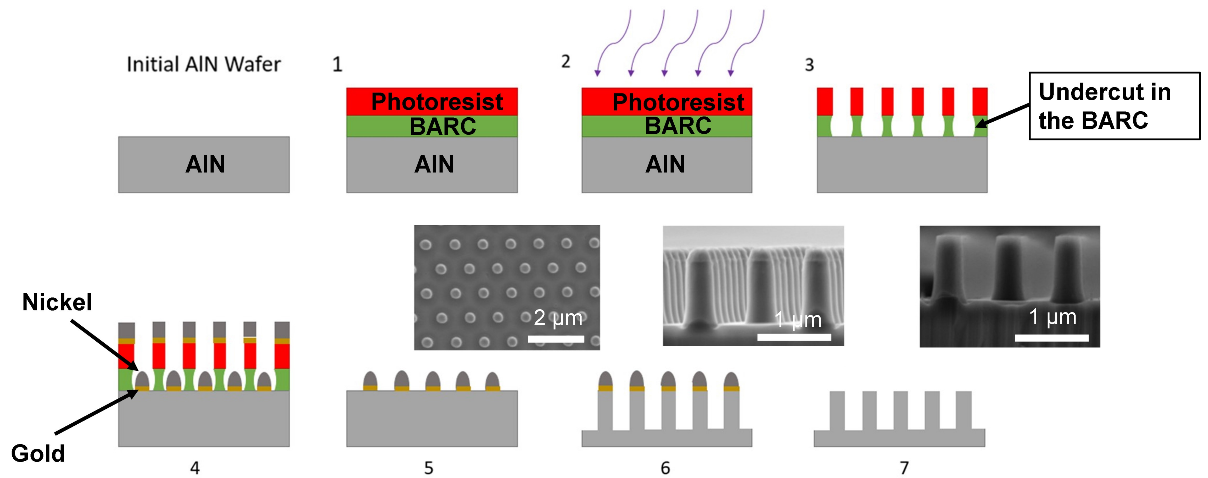

Figure 2-7: Starting with the initial wafer, in 1, BARC (Back anti-reflection coating) and resist are spin coated upon the wafer with appropriate baking steps (a soft bake for the BARC). At 2, Displacement Talbot Lithography is used to expose the resist. In 3, the resist is developed for a long enough time such that an undercut is now present in the BARC layer. Electron-beam evaporation is used in 4 to first deposit a thin layer of Au followed by a thicker layer of Ni to realise a metal dot array. The sample is then put back into developer for the final part of this 'lift-off' procedure where the remaining resist and BARC are removed (or lifted-off) at stage 5. An O_2 based plasma etch can now able applied to remove any remaining unwanted organic material. This dot array in 6, is then used as a mask to etch into the underlying wafer. Finally, in 7, this is followed by an Aqua Regia, Piranha clean and Buffered oxide etch in that order, in order to remove the mental mask and clean the sample.

2.2.5.2 Nanohole Fabrication Process

In this fabrication processes, PECVD is first used for the deposition of an initial dielectric hard mask to be used for etching. A BARC and photoresist can then be spin coated upon it with appropriate baking steps. The photoresist is then patterned via DTL followed by development. This patterned resist can then be used as a mask for dry etching in order to transfer the pattern into the dielectric hard mask. After removal of the remaining BARC and resist, this patterned hard mask can be used to etch into the sample below. The advantage of this is that at this stage the dry etching can be performed at a relatively high temperature, such as 150 ^{o}C [49], and the mask itself is fairly robust. This fabrication process can be seen in Figure 2-8. Additionally, if one did not want to etch into the underlying wafer/sample, one could stop the process at step 5 in Figure 2-8. One could now proceed straight to cleaning stages for the removal of organics and oxides, leaving a patterned dielectric mask, with periodic openings, upon a planar wafer.

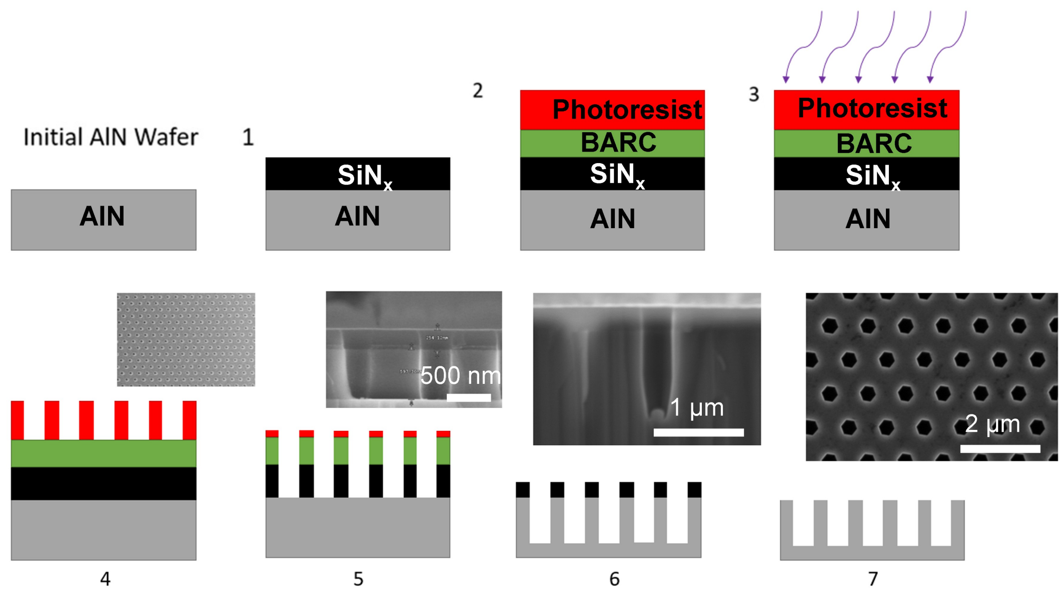

Figure 2-8: The process starts with the initial wafer. At stage 1 a SiN_x mask is deposited via PECVD. At stage 2 BARC (back anti-reflection coating) and photoresist are spin coating with appropriate baking steps. At 3, displacement talbot lithography is used to expose the resit. The sample is then developed in MF-CD26 developer at stage 4. The resist is then used as a dry etch mask for CHF_3 etching into the SiN_x mask. The organic layers are then removed and the SiN_x is used as a mask to dry etch into the underlying wafer. Finally, a buffered oxide etch (BOE) is used to remove the remaining SiN_x mask.

2.3 Characterisation

Characterisation is the determination of the properties or behaviours of a material. In terms of semiconductor materials this can be achieved by a large number of different methods which will give different information about the properties of the material being investigated. Such information which is characterisable and relevant to this discussion are properties concerning the structure, shape, size, morphology and optoelectronic properties of nanostructures. With regards to quantum dots, these properties are of particular importance, as has been alluded to in the first chapter of this thesis. Before looking at some characterisation techniques in greater detail an overview of some of the available and suitable techniques will be briefly discussed.

2.3.1 Microscopy

Standard microscopy uses visible photons in an optical set up to create a magnified image of the object being studied [24].

2.3.1.1 Electron Microscopy

In order to increase the possible resolution, instead of photons, electrons can be used in microscopy as they have a much smaller de Broglie wavelength than the wavelength of optical photons. This means far greater resolutions can be achieved [237]. Electron microscopy must however, be performed under vacuum as electrons are scattered much more strongly by gas than light [24].

A variety of signals can be detected in electron microscopy. These can scatter elastically or inelastically [238]. With elastic scattering there is often large deflection angles involved. If the sample is thin enough then some of the beam can be transmitted through the sample. This will incur Bragg scattering of the beam rendering a diffraction pattern as a result of the structural nature of the material being probed. This is the basic principle of TEM [24]. Backscattered electrons are primary electrons which have undergone a number of elastic scattering collisions before exiting the sample [239]. These electrons penetrate relatively deep into the sample and typically have relatively high energies [24]. Secondary electrons are typically low energy electrons generated by energy transfer between the primary beam and surface, or close to surface, electrons, ejecting them from the sample [238]. Subsequently, an image of the sample surface can be formed using the signal detected from these electrons [25]. As has been alluded

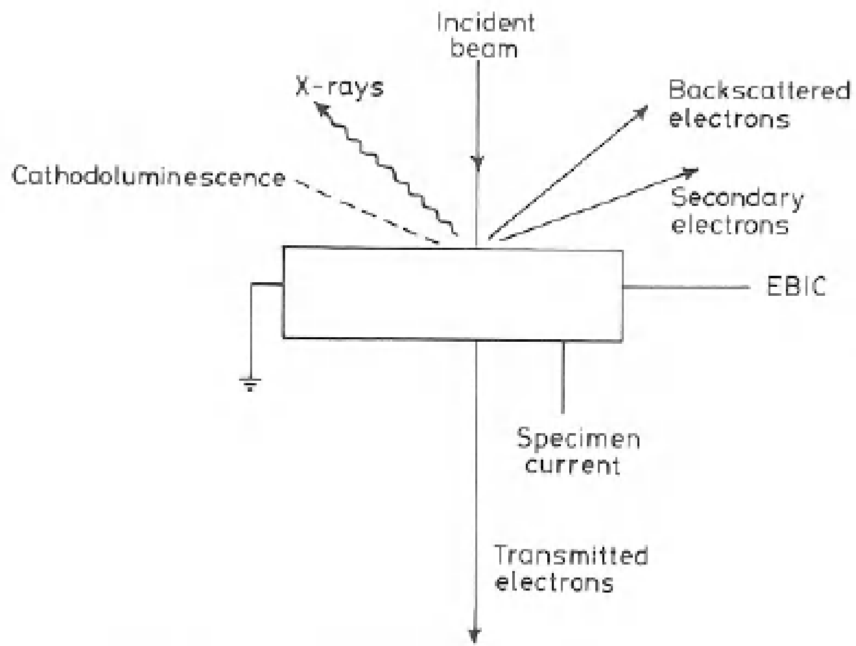

(a)

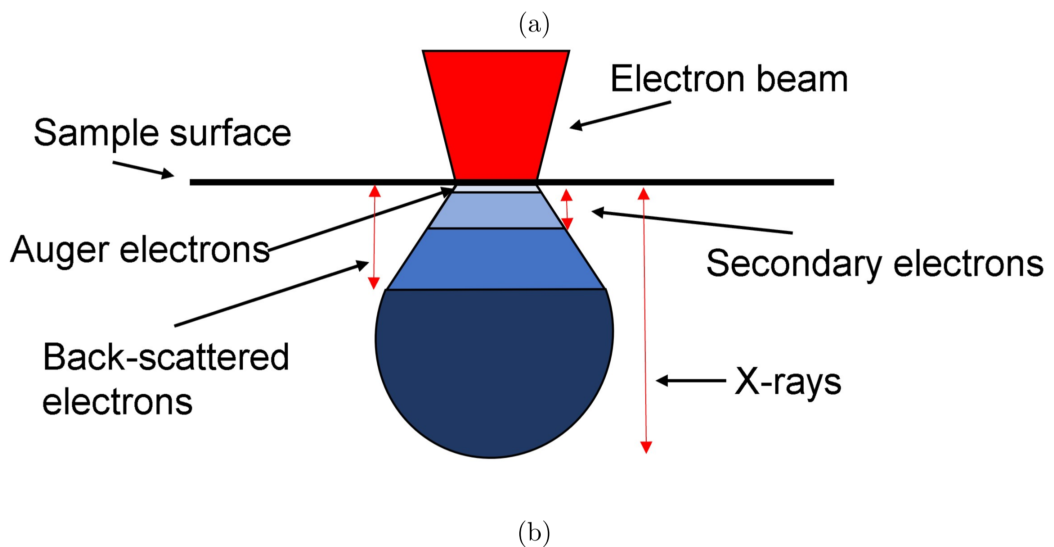

(b)

Figure 2-9: Figure (a) shows some of the detectable signals which can be used for imaging in SEM. Republished with permission of Taylor & Francis group ©, from [24]; permission conveyed through Copyright Clearance Center, Inc. Figure (b) shows the interaction volume and regions from which secondary electrons, backscattered electrons and X-rays may be detected.

to, they originate from regions of very low penetration depth [24]. These electrons are typically weakly bound, conduction band electrons and can even be produced by backscattered electrons themselves [239]. Other detectable signals include cathodoluminescence (the emission of light on electron bombardment), characteristic x-ray emission and Auger electron emission [238], see Figure 2-9. Electrons also carry charge which is an important attribute when considering the scanning electron microscope (SEM) [24], which will now be discussed in more detail.

2.3.1.2 Scanning Electron Microscopy

An SEM (Scanning electron microscope) gives information on the surface structure of a sample. It allows direct observation of the external form of micro/nanostructures [238]. An SEM system uses electromagnetic lenses in a similar configuration to an optical microscope. Two orthogonal scan coils are placed between the final condenser lens and the objective lens. These are used to enable the electron beam to be rastered across the sample, with the beam manipulated via use of the electron charge [24]. Detectors for secondary electrons and backscattered electrons from the sample surface (although they do originate from within the sample to some extent) are used to produce an image of the samples surface structure [24]. The usual mode of operation is the detection of secondary electrons which are knocked out of the surface atoms in order to form an image [238] and these provide the most important detection signal [25]. Secondary electrons provide the best resolution due to their very small exit depth [25]. In some systems x-ray detection is also possible giving some compositional information close to the surface of the sample [24]. SEM systems can be used for bulk specimens as thickness and roughness of the surface of the sample is not an imaging limitation [25]. Figure 2-10 (a) shows a typical schematic of an SEM system and some SEM images of nanostructures. SEM can give important information of the structure and morphological quality of sites created to house quantum dots. Moreover, it is also capable of providing some characterisation of uncapped self-assembled quantum dots. The SEM used to characterise samples in this thesis was a Hitachi Field-Emission S-4300 SE system using a 5 kV electron beam voltage and using secondary electron signal detection unless otherwise specified.

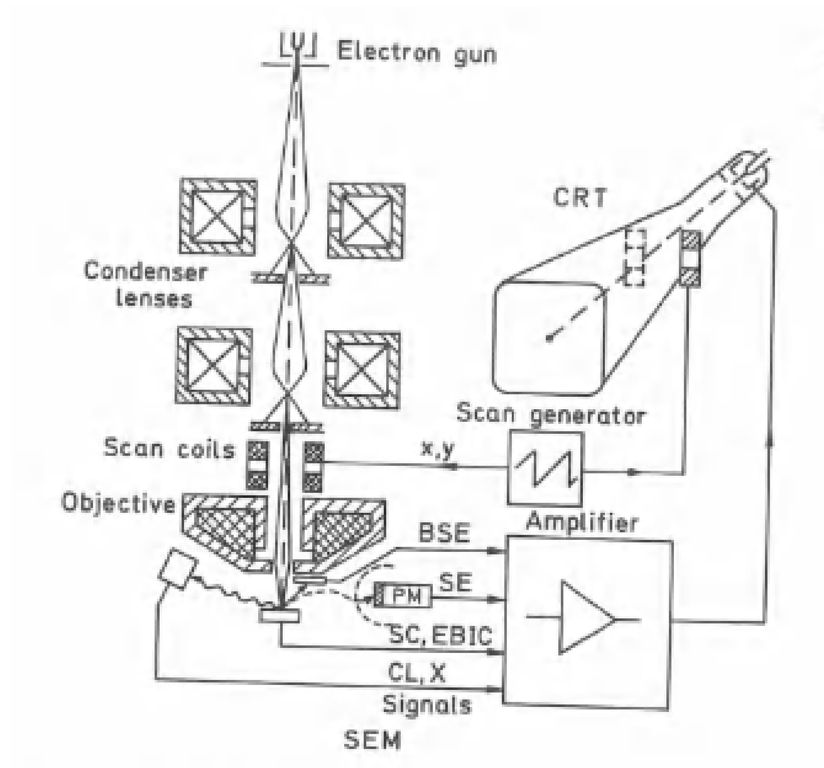

(a)

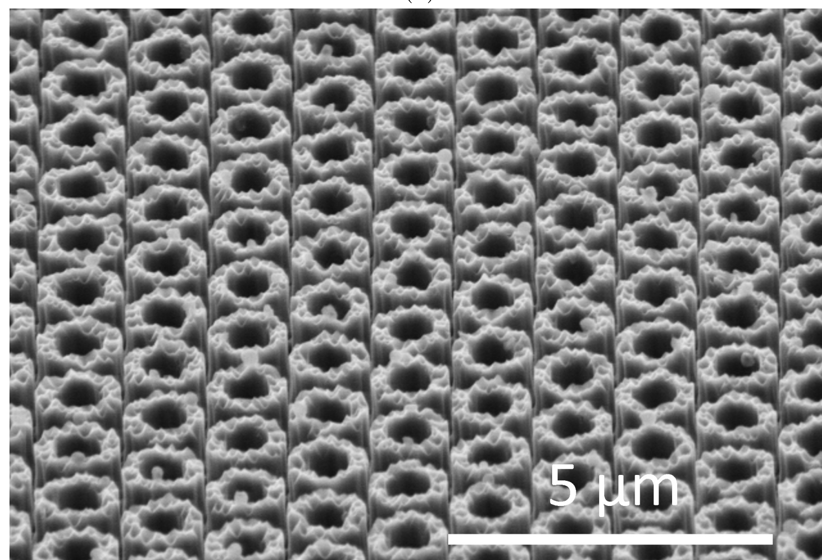

(b)

Figure 2-10: Figure (a) shows a typical schematic of a SEM. Reprinted/adapted by permission from Copyright Clearance Center: Springer Nature, Transmission Electron Microscopy: Physics of Image Formation and Microanalysis by Ludwig Reimer Copyright © 1997, Springer-Verlag Berlin Heidelberg ([25]). Figure (b) show an SEM image of some nanostructures.

2.3.1.3 Atomic Force Microscopy

Atomic force microscopy (AFM) can provide high-resolution topological information on a sample. In AFM, a sharp tip is scanned over the surface of a sample. The tip is connected to a cantilever and the sample mounted on a piezoelectric stage which can be used for precise sample movement [26]. The repulsive force between the tip and the sample is measured via measurement of the cantilever deflection. From the change in force across the sample or the changes in the tip height and the corresponding cantilever deflection, an image of the sample's surface can be produced [240]. The cantilever deflection is usually measured via the change in angular deflection of a laser beam reflecting off the cantilever itself and detected by a position sensitive photodiode [26]. As this is a force based microscopy a wide range of different materials with different properties can be imaged. For instance, whereas STM (scanning tunnelling microscopy) requires semiconducting or conducting samples for successful imaging, AFM (atomic force microscopy) has the ability to also investigate insulating materials [240] and even biological samples such as microbes [26]. Surface morphology, nanoscale structures and atomic scale lattices can all be imaged via AFM [240].

AFM can operate in different modes, two of which are contact mode and tapping mode. In contact mode, as mentioned above, the force on the tip is measured via the cantilever deflection. From this, a surface image of the sample can be produced. There is the disadvantage that for soft samples such as organic material, the constant force of the AFM tip acting on the sample can cause surface modification and damage [240]. This also needs to be considered with fragile, non-organic samples. However, there is another option with the use of a partially non-contact method for measuring samples [240]. This is tapping mode.

In tapping mode, the cantilever vibrates such that the AFM tip makes contact with the sample intermittently. This acts to lessen the surface modification resultant from keeping the tip in contact with the sample. The cantilever is set to vibrate at, or near its resonant frequency [240]. When there is a hill in the surface morphology the vibrating frequency of the cantilever will increase, when there is a valley/crater the frequency will decrease. In order to rectify this the Z scanner of the cantilever will displace the distance between the tip and the sample, in order to keep the tip amplitude constant. Thus, from measurement of the Z displacements taking place, a topological image of the sample surface can be formed [241]. By only making intermittent contact with the sample this reduces surface changes and damage to soft samples, such as biological matter [240]. Tapping mode also has the advantage that it helps prevent AFM tips from being trapped by a capillary force which is usually present on all samples due to a

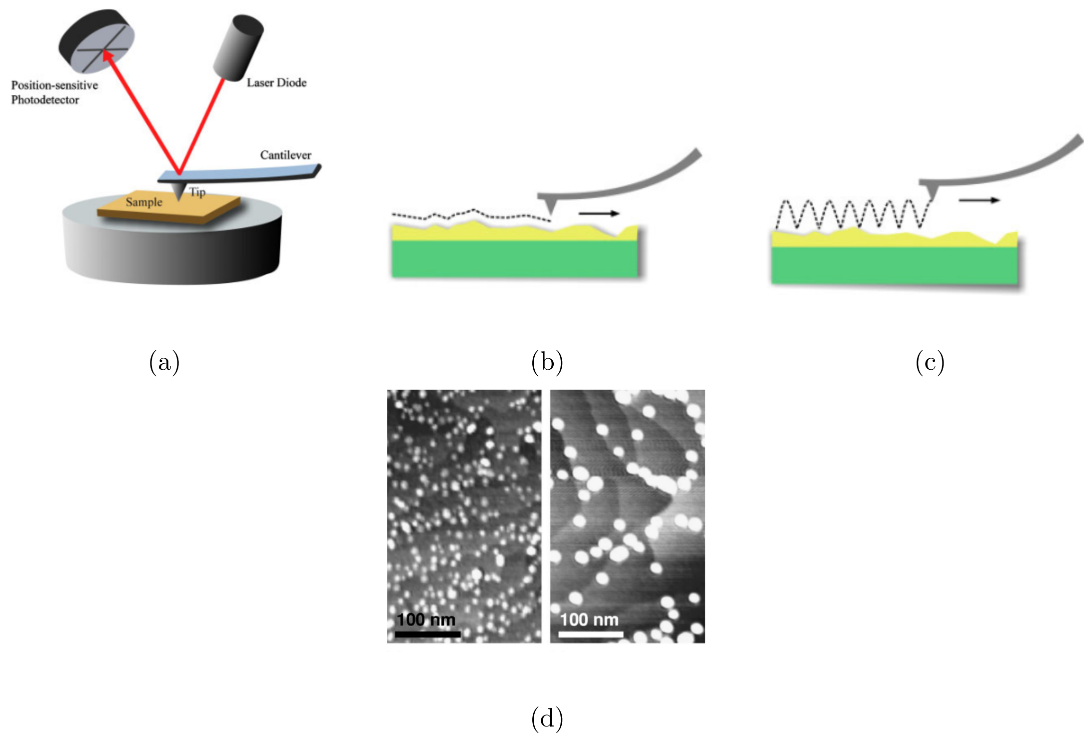

Figure 2-11: Figure (a) show a schematic of a typical AFM operational set-up. Figure (b) shows a schematic of AFM during contact mode. Figure (c) shows a schematic of AFM during tapping mode. Figure (d) shows an AFM image of some self-assembled (uncapped) GaN quantum dots upon a smooth, terraced AlN surface (Figures (a)-(c) modified and reproduced from [26] Copyright © 2010 Wiley Periodicals, Inc. Figure (d) reprinted from [27], with the permission from AIP Publishing, Copyright © 2006.)

very thin layer of water residing on the surface when the sample is in air [242]. Figure 2-11 shows a schematic of a typical AFM and a diagrammatic representation of contact and tapping modes. Concerning quantum dots in particular AFM is widely used across the literature to characterise the shapes, sizes, densities and distributions of uncapped self-assembled quantum dots (Figure 2-11 (d)) [243]. The AFM systems used in this thesis were the Bruker Multimode IIIA and the Oxford Instruments Jupiter XR. It will be explicitly specified as part of the figure caption which of the data has been taken by each microscope when the data is presented.

2.3.2 Luminescence spectroscopy

Luminescence can reveal information about the chemical composition of a material. When light is used to induce luminescence this is called photoluminescence [244]. This is the starting point of the brief luminescence discussion which follows and how it can be used as a characterisation tool.

2.3.2.1 Photoluminescence

The emission of a photon can occur when an excited electron makes a transition into a lower energy state (the electron radiatively recombines with a hole) with the energy difference of the transition equating the energy of the photon. In photoluminescence (PL), the electron in the excited state is promoted to this state via optical absorption from a light source incident on the sample. When considering a semiconductor material this corresponds to an excitation of an electron from the valance band to the conduction band. The impinging light source will typically have a higher energy than the band-gap of the material one wants to excite. Basic PL can be used to determine the optical emission efficiencies, alloy composition of a material and the level of impurities. The characteristic energy range of PL is related to the bandgap [245]. This results in emission of light with the energy equating to the bandgap of a material when there is a transition between the bottom of the conduction band and the top of the valence band, see Figure 2-12. However, there are other possible transition paths which may be taken such as intra-band gap transitions which involve energy level within the band gap. These arise from surface or near-surface states or due to the presence of deep traps, present due to crystallographic defects or impurities [246]. The quantum efficiency of photoluminescence can be defined as the quantity of light emitted per that of the light adsorbed by the sample [244]. Whilst PL is a useful characterisation tool for materials it by no means gives a complete view of the properties of a material or even just the optical properties of a material. Having said that it can be very useful when studying the properties of materials, complementary to other techniques [245]. Considerable work has been done to improve the versatility of PL from its most basic form to some of the more specific, niche, expansions of the technique [245]. The impact of temperature on PL measurements will now be discussed.

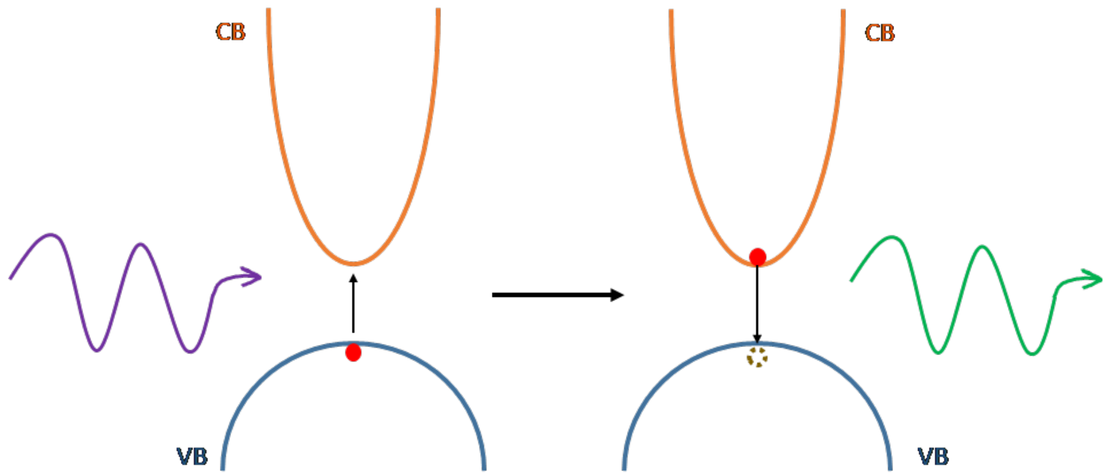

Figure 2-12: This figure shows diagrammatically the process of photoluminescence. In this figure the colour schemes used are arbitrary.

2.3.2.2 Considerations for low temperature and high temperature measurements

Semiconductor bandgaps are temperature dependent and so PL measurements at different temperatures will naturally give slightly different spectral results [245]. This is not the only consideration concerning the influence of temperature on PL though. The intensity of a PL spectra decreases with increasing temperature due to thermal quenching. This is due to the redistribution of carriers into different energy levels following carrier excitation [247]. Subsequently, high quality room temperature PL measurements can be challenging in some circumstances. PL at higher temperatures also leads to spectral linewidth broadening. This is due to thermal population of higher energy levels and phonon effects. This is important as the linewidth of a PL peak can be used as a measure of the quality of a semiconductor active region and thus high temperature measurements may not represent a true indication of the material quality [248].

Optical transition linewidths can be used as measures of coherence of the excitons and are indicative of the environmental interactions. These environmental interactions will cause broadening of the linewidths. These interactions can be with acoustic phonons and electronic fluctuations. The term spectral diffusion is attributed to the linewidth broadening associated with Coulombic interactions with the fluctuating electronic environment [249]. In terms of quantum dots, this can result from traps in the vicinity of dots and defects acting as sources of confined charge in the environment [250].

Individual quantum dots will typically have narrow, discrete, sharp peaks [251]. The

emission linewidth of a quantum dot is important as it can give an indirect measure of the dephasing time (which is related to the coherence), which is important in QIP applications [252]. Spectral diffusion can occur in quantum dot emissions and this will impact the successful production of indistinguishable photons [249]. Quantum dot spectra also (typically) exhibit rapid PL quenching at higher temperatures [253]. As the temperature of measurement is increased the quantum dot peak becomes broadened and also lessens in height with respect to the background due to increasing acoustic photon coupling [44]. This makes low temperature studies of quantum dots more preferable in order to obtain cleaner and clearer PL spectra.

However, with III-N quantum dots even with low temperature measurements there can still be significant linewidth broadening. This is due to the large interaction strengths of the quantum dot and the rest of the system and high density of defects in III-N materials. The high interaction strengths are due to the presence of the internal fields which leads to large permanent dipole moments for the excitons [249]. This leads to large linewidths being detected relative to that of other material systems even at cryogenic temperatures. The inhomogeneous broadening of the emission linewidths of quantum dots can deteriorate the purity of single photon generation. Suppression of spectral diffusion is also preferable for high quality single photon emission [87]. To quantify this, one would expect linewidths of ~ 1 μeV for temporal processes occurring on ~ 1 ns timescales in the absence of spectral diffusion [250]. Most studies on III-N quantum dots however, find values far higher than this. Other useful photoluminescence techniques include photoluminescecne excitation spectroscopy, polarisation dependent photoluminescence, two-photon excitation, and time resolved photoluminescene. As these techniques were not used for the work in this thesis they will be discussed no further here.

2.3.2.3 Photoluminescence of GaN quantum dots

Here GaN/AlN quantum dots will, in particular, be briefly discussed. In Figure 2-13 one can see in (a) the CW PL spectra of 10 planes of GaN/AlN quantum dots and in (b) the PL spectra as recorded under different time delays for pulse laser excitation.

As a result of the strong internal polarisation fields in GaN/AlN polar quantum dots, height variations of one atomic monolayer yield energy variations over several hundred eV. These variations are as a result of on-axis confinement combined with the QCSE [28]. Thus, as QCSE dominates over confinement for quantum dot sizes more that ~ 2 nm, there is a significant impact of the emission wavelengths when comparing

quantum dots with smaller and larger height, see Figure 2-13 (c). In addition, this also results in much longer radiative lifetimes when the quantum dot is larger in height. Again, this is as a result of a greater impact of the internal field which will inevitably separate the electron and hole wavefunctions more in taller dots [29]. The internal fields can be screened to some extent when there is an accumulation of large densities of electron-hole pairs in the dots [28].

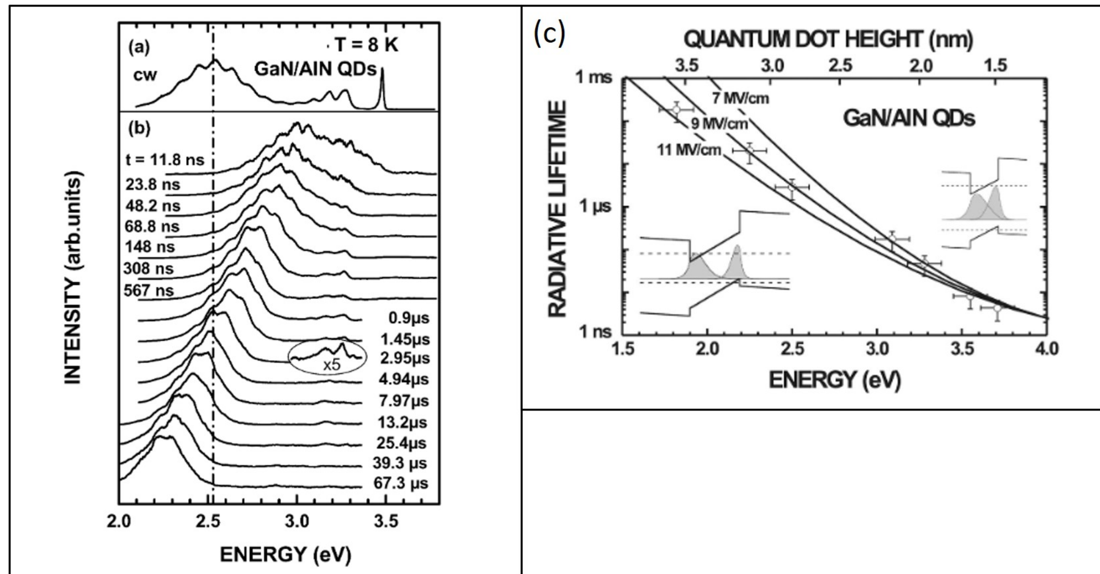

Figure 2-13: In (a) a continuous wave (CW) PL spectrum of a sample with 10 planes of GaN/AlN QDs is shown. The QDs here have typical heights of 4.3 nm. In (b), PL spectra recorded at different delays after pulsed laser excitation is shown. Intensity of the spectra have been normalised. The dashed line indicates the CW PL peak from (a). For short delays, spectra are artificially broadened by the presence of long lived PL at 3.2 eV, arising from defects in the GaN buffer layer, whose short-lived PL line appears at 3.48 eV. Here (a) and (b) are reproduced from [28]. Copyright © 2008 Elsevier Masson SAS. All rights reserved. In (c), a plot of the measured radiative lifetimes as a function of PL peak for different quantum dot samples is shown. Solid lines show the calculated value of lifetime as a function of energy of the fundamental transition for an effective electric field of 7, 9 and 11 MV/cm respectively. The calculated QD height corresponding to the transition energies for 9 MV/cm electric field is shown at the top axis. Electron and hole energy levels and wavefunctions are sketched in the regimes dominated by the QCSE (left) and quantum confinement (right). Figure (c) is reprinted (Figure 3) with permission from [29]. Copyright (2006) by the American Physical Society, https://doi.org/10.1103/PhysRevB.73.113304.

In Figure 2-13 (a) one can see a huge red-shift in emission of the quantum dot ensemble compared to bulk GaN. The internal electric field lead to very large radiative lifetimes for such quantum dots, this means that by using only moderate optical excitation one

can generate a large number of electron-hole pairs within the dot at any one time. This is demonstrated in Figure 2-13 (b), where screening is observed when the time delay is reduced during pulse laser excitation. This leads to a relative blue shifting of the emission at short time delay [28]. Clearly with GaN quantum dots there are many considerations when performing photoluminescence based characterisation upon them.

2.3.2.4 Cathodoluminescence

Cathodoluminscence (CL) is effectively the emission of light of a material upon electron bombardment [24], see Figure 2-14 (b). The CL signal detected will vary with the composition of the material, allowing one to discern between the different materials in heterostructure devices [24]. Defects within optoelectronic materials and their effects on a devices performance can also be analysed with CL [24]. The sample itself, after being bombarded with electrons relaxes back to its equilibrium condition. In order to release the energy obtained via the primary electron bombardment, light is emitted [238]. In closer detail, the bombardment of electrons causes some of the materials valence band electrons to excite to the conduction band, leaving a hole behind in the valence band. This resultant electron-hole pair can then radiatively recombine, leading to the emission of a photon with the wavelength equating to an energy close to the energy gap between the conduction and valence band. There is also electron and hole cooling via phonon emission however. Thus, the photons are characteristic of the material of which is being investigated (as the band gap is characteristic of a given material) [239]. Materials which display CL typically will reveal a spectrum which is highly dependent on the levels of impurities present and the species of impurity. This will reflect in the CL spectra obtained in regards to both wavelengths detected and the overall brightness measured [238]. In addition, crystallographic defects will also have an impact on the detected CL spectra [239]. For instance, it is well known that dislocations act as non-radiative recombination centres [193]. Cathodoluminescence can be performed via an adapted SEM (providing it has the ability to accelerate electrons to high enough energies) [254]. Some cathodoluminescence measurements performed on III-N nanostructures are shown in Figure 2-14 (a). In this figure, an intensity map of a particular emission band on a nanorod structure is shown. This allows for the spatial resolution of luminescent features within a small wavelength range. Thus, one is able to spatially resolve the source of, and intensity of, an emission band across the geometry of the rod structure.

CL is a non-destructive characterisation method that can be used for determining the

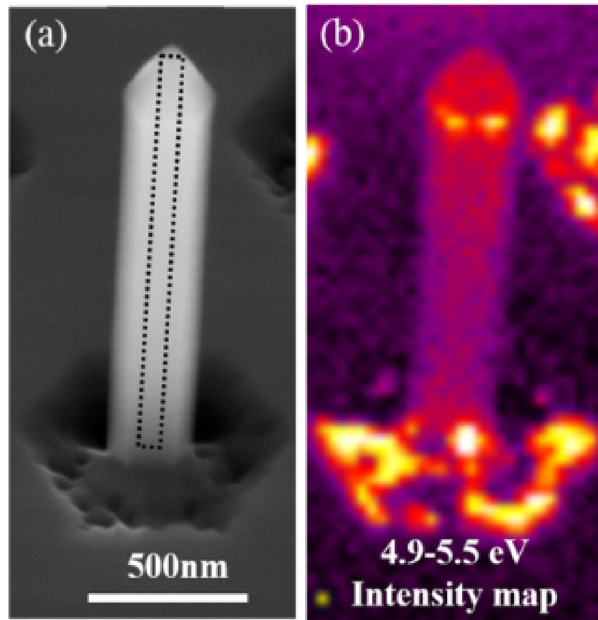

(a)

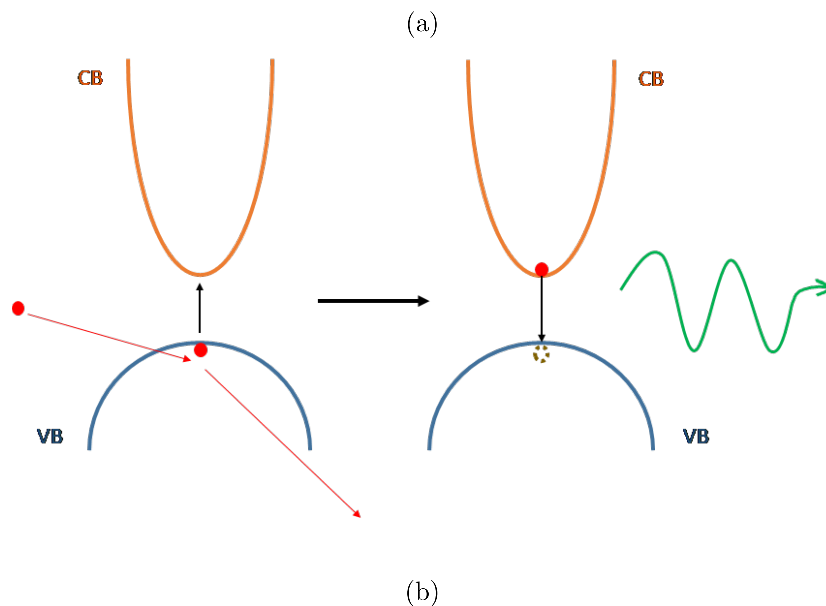

(b)

Figure 2-14: Figure (a) shows a tilted SEM image of a III-N nanorod with an AlGaN single quantum well structure. In (a) ((b)) the corresponding intensity map over the single quantum well emission range of 4.9-5.5 eV is shown, measured with the use of Cathodoluminescence hyperspectral imaging (figure reproduced and unmodified from [30] under Creative Commons Attribution 4.0 International license). Figure (b) shows diagrammatically the process of cathodoluminescence. In this figure the colour schemes used are arbitrary.

distribution of dislocations at the surface of a material. This has an advantage over TEM, as destructive sample preparation is not required, which is the case for TEM samples as they are required to be very thin [255]. Furthermore, CL can be used to measure luminescence of different facets of individual nanostructures or multifaceted thin films [256]. As an example in the work by Kusch et al. [257], nanorods with quantum wells on the pyramid side facets and the c-plane apex of the rod were first detected from the sample and then measured with the use of CL hyperspectral imaging. The emission properties of the quantum well structures on the semipolar and polar planes were investigated. Different emission ranges were detected from the quantum wells on the semipolar and polar planes. Thus, using CL, properties of different faceted regions of nanostructures could be probed [257]. CL hyperspectral imaging is a CL system which can record a full luminescence spectrum at each point on a sample. Analysis on the multidimensional datasets can be completed providing a wealth of information about the region of the sample probed [258].

In CL, the spatial resolution of the technique is determined by the distribution of excess carriers in the sample and this allows the possibility of nanometre-scale semiconductor characterisation [258]. However, in order to achieve the highest resolution, measurement depth within a sample must be sacrificed. This is often the case when performing CL upon quantum well or quantum dot structures [258]. Whilst CL typically has excellent spatially resolved luminescence, it does usually have inferior spectral resolution and control over excitation densities compared to PL.

The CL performed upon samples presented in the results chapters of this thesis was conducted using a custom built hyperspectral CL acquisition system on a FEI Quantum 250 field-emission-gun SEM at the University of Strathclyde by Dr. Pavlos Bozinakis and Dr. Jochen Bruckbauer. Spectra interpretation and analysis was performed using Dr. Paul Edwards 'Chimp' software. A schematic of the CL system and set-up can be seen in Figure 2-15. As can be seen in this figure the filed emission gun SEM impinges a very small (minimum spot diameter $\sim$ 1 nm), high brightness electron beam spot upon a sample. The beam acceleration voltage applied was either 20 kV or 5 kV as specified in the respective figure captions. The sample is mounted on a stub titled at 45°. The emitted light is collected and collimated by the reflecting objective through a silica window. This emitted light is then focused by a parabolic mirror into a slit opening of a spectrograph and (50 μm opening) with exchangeable diffraction gratings. A 600 lines/mm diffraction grating (blazed at 400 nm) was used for the CL data collected in he results chapter of this thesis.

As mentioned, the spatial resolution of CL in terms of nanostructure luminescence is

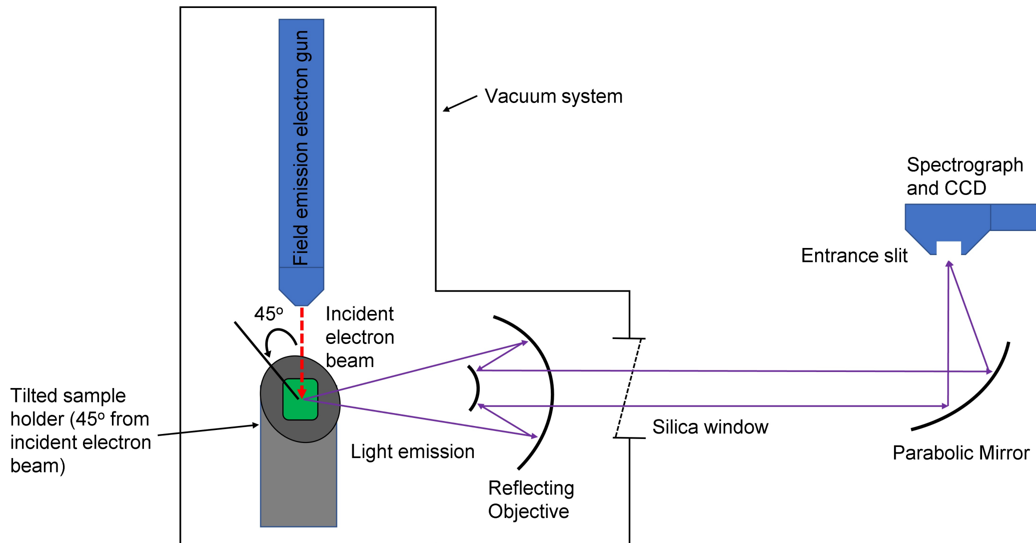

Figure 2-15: This figure shows a schematic of the CL system used for the characterisation undertaken in this thesis. All the CL maps presented in this thesis were measured by Dr. Jochen Bruckbauer at the University of Strathclyde.

a particularly attractive feature. This is demonstrated in the work by Edwards et al. [31], see Figure 2-16, where regions of different luminescence can be observed on the semi-polar facets and apex of a GaN nanopyramid with InGaN active regions grown upon it. Specifically, a 5-period InGaN quantum well structure was deposited upon selectively area growth GaN nanopyramids in order to form QDs at the sharp apices. The apex quantum dots in this work were confirmed via PL rather than CL and the apex emission shown in Figure 2-16 (b) was put down to defect luminescence rather than a quantum dot signature [31]. Even under this consideration this work does highlight the usefulness in CL for spatially resolving active regions on nanostructures with different luminescence properties.

There are a number of examples of the characterisation of GaN/AlN quantum dots systems via CL in the literature. A brief review of some of the literature will now be presented to demonstrate the versatility of the characterisation tool for the identification of GaN/AlN quantum dots and their spatially location.

In the work by Schmidt et al. [32], a GaN layer was grown upon a planar AlN template with a 30 second growth interruption step followed by an AlN cap [32]. Figure 2-17 (e) shows strong CL luminescence originating from regions near to where there are high densities of threading dislocations (dark lines in STEM image). Additionally, monochromatic CL intensity maps are recorded at different emission wavelengths. In

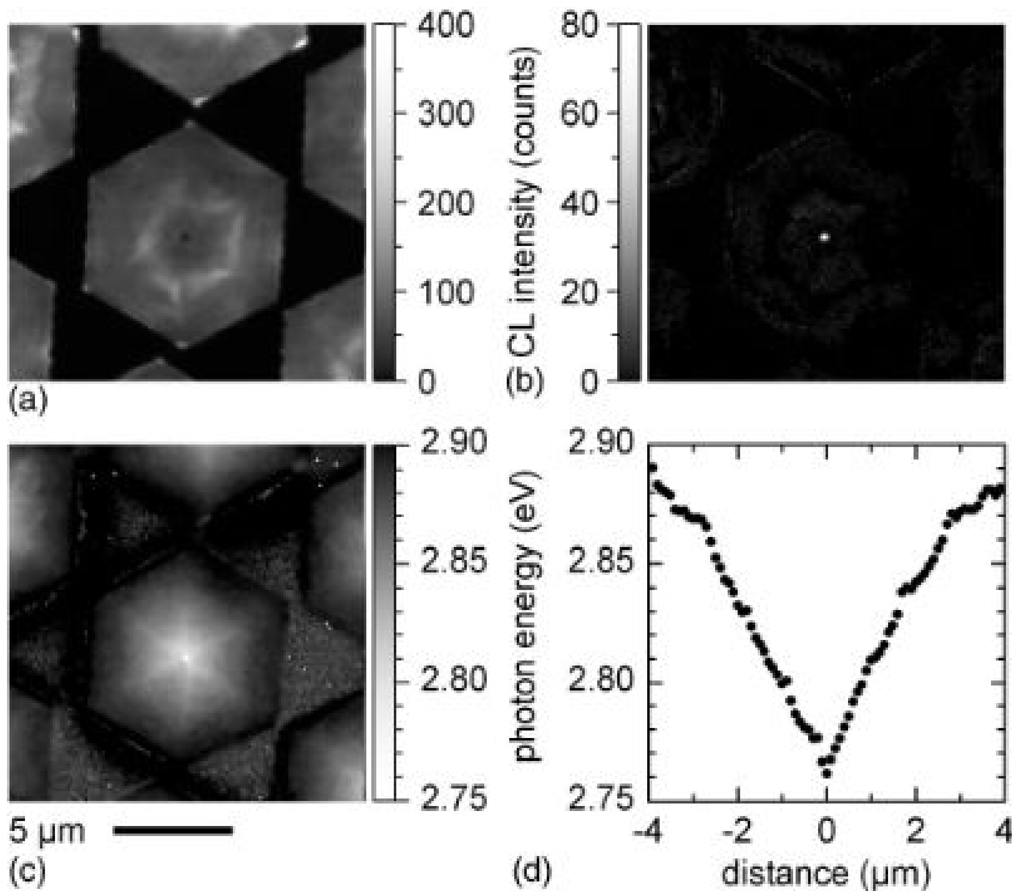

Figure 2-16: Here the images are constructed from parameters determined by fitting 3 Gaussian peaks to each of 150x150 spectra obtained during CL hyperspectral imaging. In (a) and (c) the peak intensity and energy respectively of the QW emission from the inclined facets are shown. In (b) the intensity of the apex-related 2.37 eV emission is shown. The line scan in (d), shows the QW peak energy varying across the pyramid. This was extracted via a horizontal line through the apex in (c). Reprinted from [31], with the permission of AIP Publishing, Copyright © (2004).

Figure 2-17 (a), what appears to be a quantum well signature can be seen. In contrast, at slightly longer wavelengths, emission predominantly comes from GaN islands ((b) - (d)) where are further confirmed to likely be quantum dots via their sharp PL signature and SPE characteristics [32]. The quantum dots are preferentially formed upon regions of high dislocation density. It is thought that this is due to threading dislocations providing regions of tensile strain and therefore reduce the lattice mismatch in a localised region leading to these areas being preferential for GaN quantum dot nucleation [32]. This work demonstrates the ability of CL to spatially resolve the sources of luminescence. This would not be possible to such an extent with a tool such at PL.

Whilst the CL characterisation of GaN quantum dots discussed above have been in the wurtzite crystal phase, Garayt et al. [33] has studied cubic phase GaN quantum dots via CL. Here a smooth cubic AlN buffer layer was first grown followed by growth of stacks of GaN dots and an AlN capping layer. As can be seen the TEM image in Figure 2-17 (f), the QD's preferentially grow along the stacking faults as these fronts are areas of local strain relaxation. Mesas were patterned upon the sample to isolate single quantum dots for characterisation [33]. As can be seen from the spectra shown in Figure 2-17 (g) relatively narrow linewidths are present for individual quantum dot spectra. These spectra have linewidths narrower than that of wurtzite GaN quantum dots at 80 K (not shown) [33]. What is particularly important here is that entire spectra can be extracted on a pixel-by-pixel basis, allowing for a spatially 'finecombed' investigation of localised luminescence features. This is particularly attractive for QD characterisation as it allows one to isolate the spectra originating from a quantum dot from the background emission of other features or the bulk material. Indeed, it allows one to collected data without being overwhelmed by bulk emission spectral features such as a large defect band in the underlying template. This capability is not possible with simply a PL measurement.

What can be discerned from the results presented in [31], [32] and [33] is that in additional to being able to resolve luminescence spatially with CL, spectra at each of the pixels can be recorded. As this is used in tandem with electron microscopy, one can build up a microscopy image with a corresponding spatial map of luminescence. This can be used to find areas of specific luminescence such as those shown in Figures 2-16 (b) and 2-17 (a) - (e). This can be very useful in identifying active regions and thus could be used to identify the location of quantum dots within/upon a nanostructure. Additionally, one can see the individual luminescence pixel by pixel allowing one to extract spectra from areas one believes to be active regions (such as in Figure 2-17 (g)).

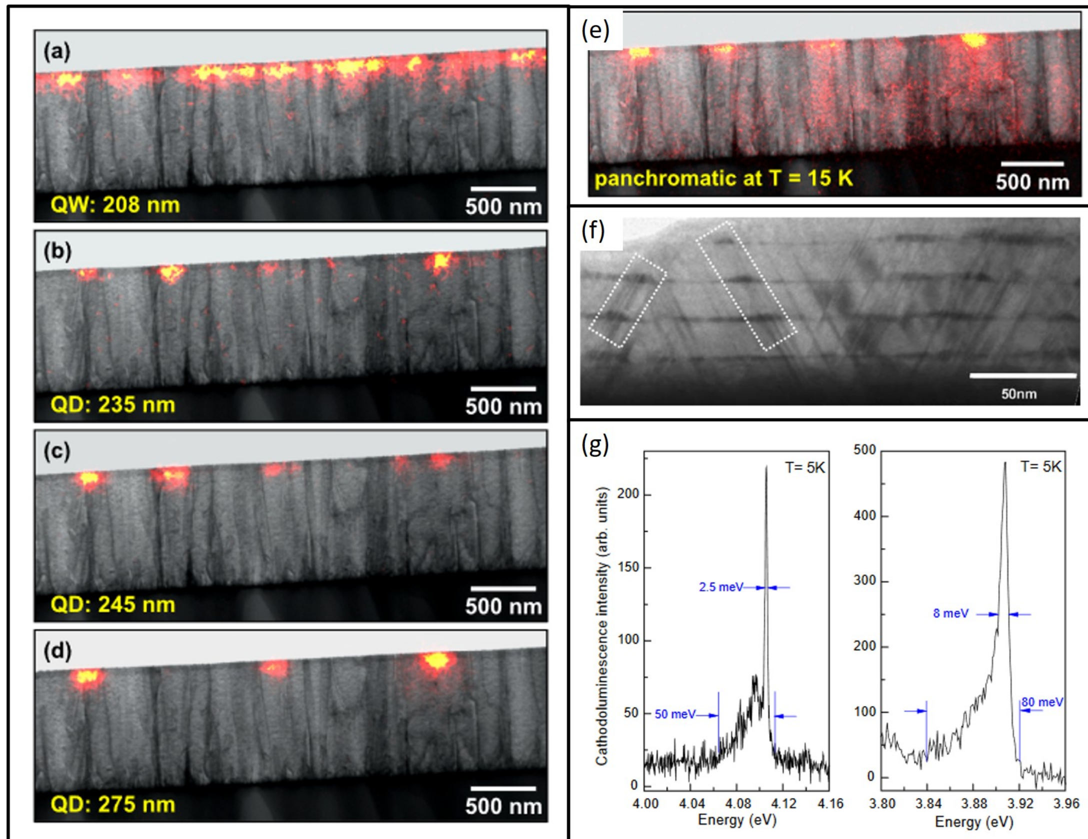

Figure 2-17: Monochromatic STEM-CL intensity images are shown recorded at spectral positions of a GaN/AlN quantum well in (a) and GaN/AlN islands (thought to be quantum dots) in (b) - (d). (a) - (e) are reprinted from [32], with the permission of AIP Publishing, Copyright © (2015). In (e) a panchromatic CL intensity map is presented, taken at 15 K. In (f) A TEM cross-sectional image of cubic GaN/AlN quantum dots is shown. The GaN quantum dots (highlighted by the white boxes) grow along the stacking faults. In (g) CL spectra of two single quantum dots are presented. Here (f) and (g) are reprinted from [33], Copyright © (2005), with permission from Elsevier.

2.4 Conclusion

This chapter has given a detailed overview of the experimental, nanofabrication, growth and characterisation techniques that have been used in the work in this thesis. The diversity in techniques and tools required to both create and identify site-controlled quantum dots helps to demonstrate the complex nature in both successfully forming them and determining their presence. Following this chapter, a more detailed survey of the III-N site controlled quantum dot literature, both recent and more historical, will now be presented.

Chapter 3

III-N Site-Controlled Quantum Dots

3.1 Historical or less scalable methods used to achieve site controlled quantum dots

Many procedures have been used historically to achieve site controlled quantum dots. Each of them have their own advantages and disadvantages. Most of the techniques highlighted in this brief section are of historical interest only as their use has become discontinued for various reasons. It is still important to have an awareness of the previous procedures used in order to evaluate the progress which has been made by the field. Moreover, the procedures themselves are interesting especially in the case of the nano-jet probe. It is this method which will be discussed first.

3.1.1 Jet probe tomography

In the Nano-Jet Probe (NJP) method, first demonstrated by Ohkouchi et al. [34], a specially designed AFM which is hollow and has an aperture on its apex is used on a cantilever. Here a material reservoir (usually of the desired metal) is housed within the stylus. On the applications of a voltage pulse between the substrate and the tip, metal deposition occurs via clusters of the material in the reservoir being extracted through the tip aperture. Thus, utilising an AFM set up, the resulting nanodots of metal can be positioned down to nanometre scale precision [34]. A schematic of the device described is shown in Figure 3-1. In the paper by Ohkouchi et al. [34], indium nanodots

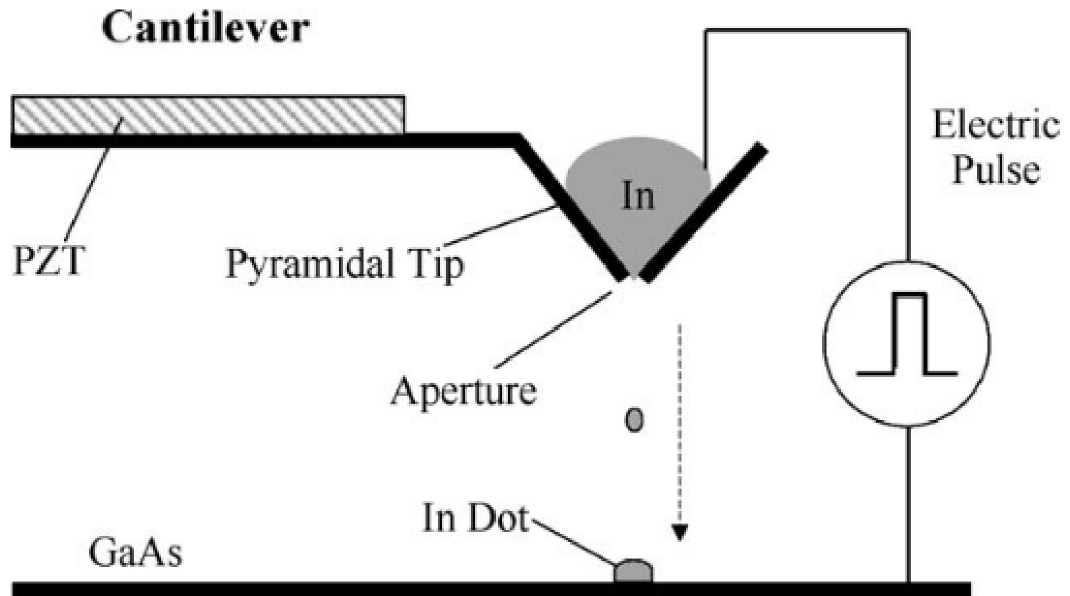

Figure 3-1: This figure shows a schematic of the nano-jet probe device created by Ohkouchi et al. [34] for the creation of site controlled InAS quantum dots upon a GaAs barrier layer (Reprinted from [34]), Copyright © (2004), with permission from Elsevier).

were deposited. This can be followed by a subsequent irradiation of arsenic flux in an MBE chamber. This uses the droplet epitaxy technique in order to crystallise Indium nanodots into InAs quantum dots [34]. The droplet epitaxy method is essentially the incorporation of group-V elements into group-III metal droplets which have been deposited on a passivated buffer layer. Here, group-III metal droplets are deposited followed by flux of a group-V material leading to the creation of III-V microcrystals which are essentially quantum dots [259].

This method is successful in creating spatially specified quantum dots giving full control over the location of quantum dot sites, as desired. However, although the uniformity is generally good, achieving perfectly uniform arrays of metal nanodots can be challenging [34]. Moreover, this is a time consuming method if one requires a large periodic array of quantum dots and as such, is not really practically suitable for this endeavour. Nanoimprint lithography can be used to create large periodic arrangements of quantum dots however; this technique will now be considered.

3.1.2 Nanoimprint lithography

In nanoimprint lithography (NIL), an imprint resist is first coated on a substrate. Then a stamp with the desired pattern is mechanically pressed into the resist. This resist is cured with pressure along with thermal or ultraviolet exposure, followed by the removal of the stamp. Dry etching can then be used to transfer the pattern generated by the imprint into the substrate below. It is a high throughput, high resolution method (sub ~ 5 nm), which is relatively cheap and simple to operate [260].

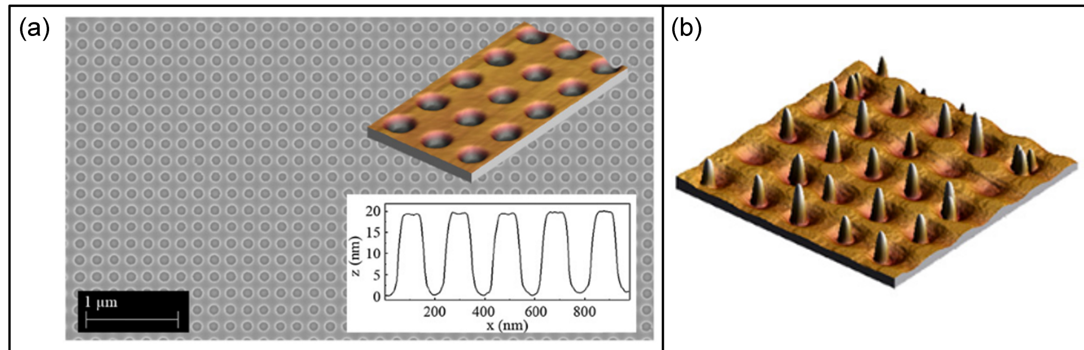

Figure 3-2: Figure (a) shows an SEM image with an AFM image insert of the surface of the buffer layer prior to epitaxy as fabricated by UV-NIL. Figure (b) shows and AFM image of the site-controlled InAs quantum dots on the UV-NIL patterned GaAs buffer layer. Reprinted from [35], Copyright © 2010 Elsevier B.V. All rights reserved, with permission from Elsevier.

In the work by Tommila. J et al. [35], soft UV-NIL was used to pattern an AlGaAs on GaAs buffer layer. The soft UV-NIL was performed as of UV NIL mentioned above, then an oxygen plasma and reactive ion etching was used to expose the GaAs surface from the holes imprinted into the resist (see Figure 3-2). The buffer layer was then etched using the resist as a mask before resist removal. This patterned layer was then grown upon via MBE. First a 30 nm GaAs buffer layer was grown followed by a thin InAs layer and then a GaAs capping layer which led to quantum dots located within the patterned holes [35] (see Figure 3-2). The quantum dots were grown by the Stranski-Krastanov growth mode, but were effectively seeded to specific sites via the UV-NIL patterned buffer layer. However, several holes were occupied by more than one quantum dot, sometimes up to three. PL was performed on the seeded quantum dots as well as a layer of standard self-assembled quantum dots for comparison. This can be seen in Figure 3-3. There is evidence of ground state and first excited state recombination in both quantum dots on the nanopatterned surface and flat surface. The ground state room temperature linewidths for the quantum dot ground states are 52.5 nm and 54 nm for the patterned and unpatterned quantum dot

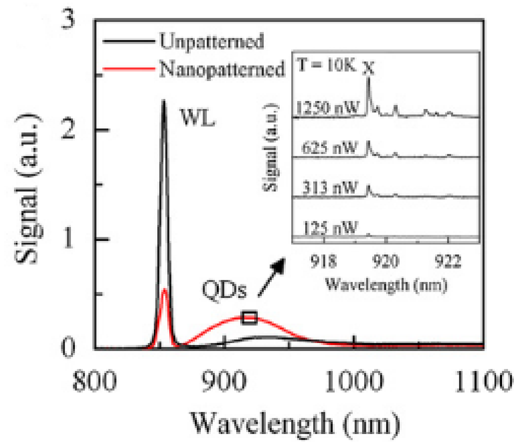

Figure 3-3: This figure shows a low temperature PL spectra of the reference sample and the nanopatterned sample. The insert shows the power-dependent micro-PL spectra of a single quantum dot on the pattern. Reprinted from [35], Copyright © 2010 Elsevier B.V. All rights reserved, with permission from Elsevier.

templates respectively [35]. These values, albeit at room temperature, are still quite large when considering the narrow linewidths required for indistinguishable photon emission for quantum computing applications [250]. However, at low temperature (10 K) the average micro-PL of a single quantum dot revealed a linewidth of $\sim 100\ \mu eV$, which is a relatively small value compared to other literature.

There is a disadvantage of NIL, in that it can suffer from a variety of defects impacting the homogeneity of large area pattern transfer. This is mainly due to defects upon the stamp itself which will be transferred into the resist and subsequently the substrate below upon processing. The stamp will wear over time, adjusting the pattern due to increased defects. Subsequently this will require frequent inspections of the stamp and eventual replacement [260]. Due to the inherent defects which will be inevitable on a stamp which has never even been used, the use of this method toward the creation of sites for quantum dots has been relatively unutilised in comparison to other techniques. Perhaps in the future if higher quality stamps can be produced almost free of defects, then this technique may become a key method toward the creation of site-controlled quantum dots. One method which has been widely utilised in the literature is the use of electron beam lithography to pattern resist and then transfer this into a hard mask below. Due to its importance in the literature, this method will now be discussed.

3.1.3 Electron beam lithography

Electron-beam lithography (EBL) is a popular method for patterning resists to be used as, or pattern, masks as part of a nanofabrication process. A brief overview of the operating principle of electron-beam lithography will now be presented. In EBL, first an electron sensitive resist, is spin coated upon the sample. A focused electron beam is exposed to the sample and writes a pattern in the resist. The exposed regions of resist will have a change in its chemical properties. The resist is then developed in a developer. This, in the case of positive resist, will lead to the removal of the exposed areas. In the case of negative resist, the unexposed areas will be removed (see Figure 3-4). EBL is capable of achieving nanometer resolution [36].

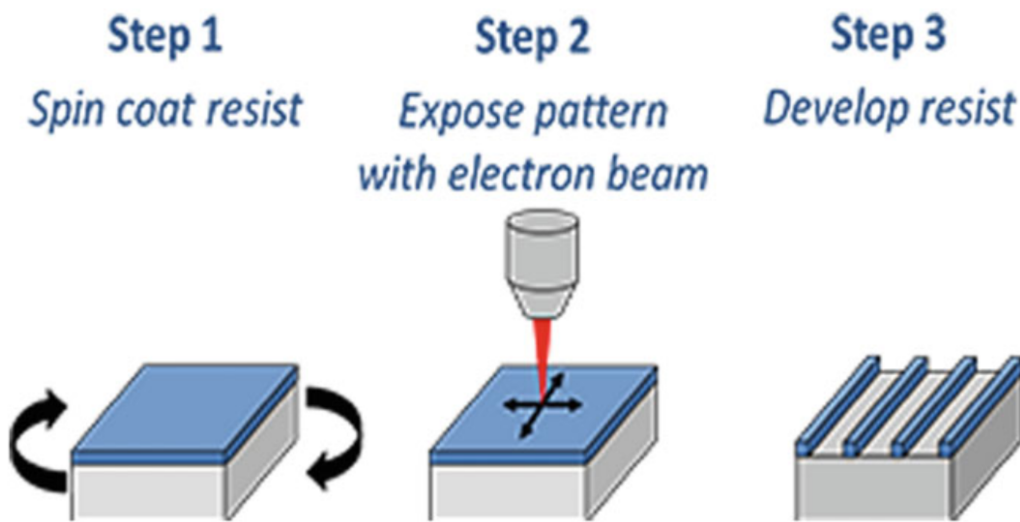

Figure 3-4: This figure shows a schematic of the EBL patterning process (Reprinted/adapted by permission from Spinger Nature : Springer eBook, Fabrication Processes for Sensors for Automotive Applications: A Review, by Aviru Kumar Basu, Shreyansh Tatiya, Geeta Bhatt et al. Copyright © (2019) [36]).

As an example of its utilisation in the creation of sites for spatially deterministic quantum dot growth, the work of Atkinson et al. [37] is worthy of note. Here, EBL followed by reactive ion etching was used to pattern a GaAs substrate with an array of holes of diameters of 60-100 nm and depths of $\sim$ 35 nm. A GaAs buffer layer ($\sim$ 10 nm) was then overgrown on the sample. This was followed by deposition of 2 monolayers of InAs for the quantum dot growth followed by a $\sim$ 70 nm GaAs capping layer [37]. An AFM image of the patterned layer at various stages of the process is shown in Figure 3-5. Whilst this method does largely control the spatial locations of the holes and therefore the dots, albeit with some being nucleated at pits between the holes in the array, it does

still lead to a small distribution in the sizes of the dots themselves. Moreover, more than one dot can nucleate in each hole, as was seen in the work presented utilising NIL. It was found that larger holes tended to lead to more cases of multiple dot occupancy [37]. It is evident that with this method as with that of NIL discussed above, where in both cases there are situations of multiple dot occupancy per hole (site), methods such as these are not suitable for quantum dot production for QIP applications. For such applications, one would desire a single dot occupancy per site and arrays of dots with ideally identical dimensions.

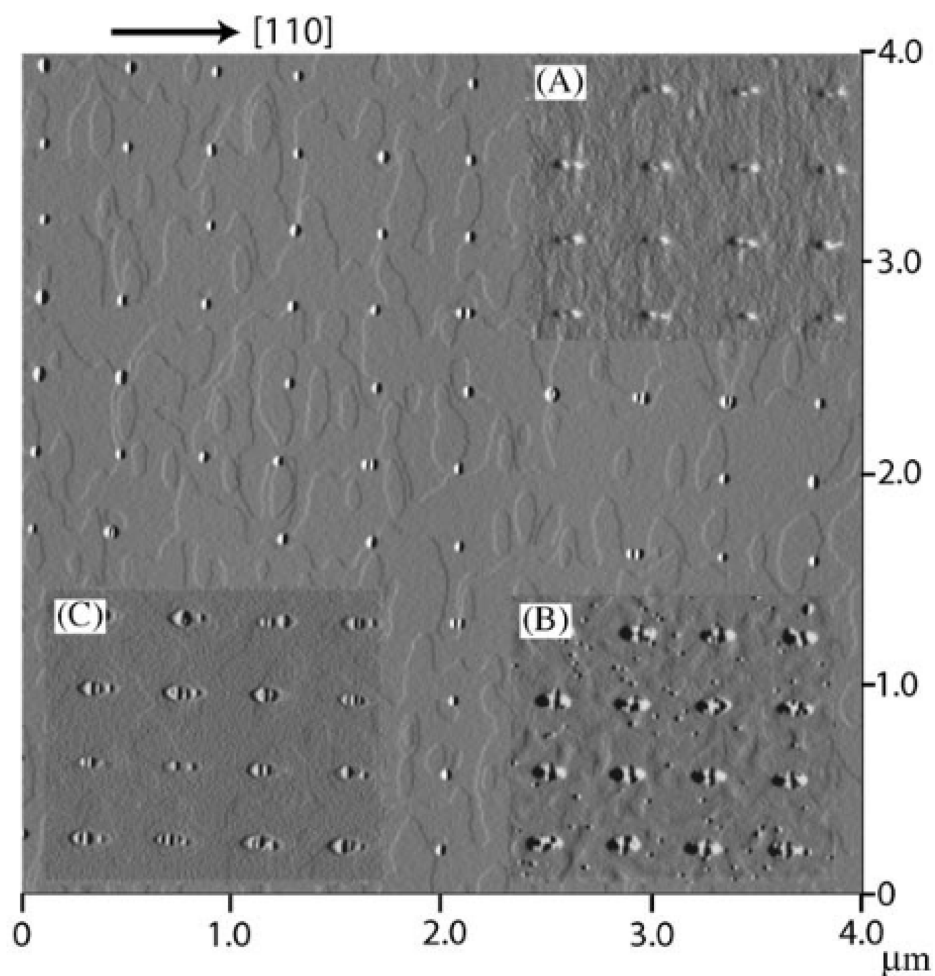

Figure 3-5: AFM image of the patterned wafer shown the preferential nucleation of the quantum dots within the holes. In insert (A) an AFM image of the hole array after the 10 nm GaAs buffer layer is deposited. In (B) an AFM image of the surface is presented after a thermal desorption of an oxide layer. In (C) there is shown the occupancy of the holes [37] (Reprinted from [37], Copyright © (2006), with permission from Elsevier).

EBL is not limited to mostly obsolete applications. For instance, in the work by Holmes et al. [68], the lithography technique was used with reactive ion etching in order to pattern a SiO_2 mask. The mask lay upon a thin AlN layer upon which GaN nanorods were subsequently grown via selective area growth (which will be discussed in more detail in a latter section). A layer of AlGaN was grown upon the rod followed by a GaN quantum dot and an AlGaN capping layer [68]. This demonstrates that EBL certainly still has its uses, especially when desiring patterning to high spatial precision. Patterning via EBL and subsequent dry etching have also been used upon n-GaN-InGaN quantum well-p-GaN structures as a way of creating spatially determined quantum dots [261]. This method involves the top-down dry etching of a planar LED structure in order to create a site controlled quantum dot. Similar procedures to this one, with the use of the top-down approach, will now be discussed.

3.1.4 Dry etching of Quantum well sandwiches

As mentioned in the first chapter, Reed et al. [2] created the first intentional semiconductor quantum dots. The group first grew a GaAs quantum well structure and then after patterning with electron beam lithography, a subsequent metal deposition and lift-off technique was used to create a metal mask upon the structure. This was then dry etched to reveal a system with total spatial confinement (0 degree of freedom device) [2] (see Figure 3-6). As can be seen from the photoluminescence spectra of the quantum dot which they fabricated (see Figure 3-6), there is a large distinguishability in comparison to the spectra obtained from with a quantum wire or well. This shows a peak which has a far higher relative intensity for the quantum dot in comparison to the quantum well and is not present at all for the quantum wire. It is thought that this is due to electron recombination with holes from the light hole band [2]. This is evidence of total spatial confinement as the hole states available for occupation are discrete and the inter-branch scattering time (if large enough) from the light hole band to heavy hole band will cause a bottleneck. This will in turn lead to a much higher relative population of light holes. The result of this larger population of light holes are far more electron-light hole recombinations. Therefore, the system will be forced to have carrier recombination from the light hole band as a long scattering time will render the heavy hole band unpopulated for periods of a given time [2]. This results in the prominent peak observed in the left of the photoluminescence spectra for the quantum dot in Figure 3-6.

This was also, in-fact, the first site-controlled quantum dot created, as via the dry

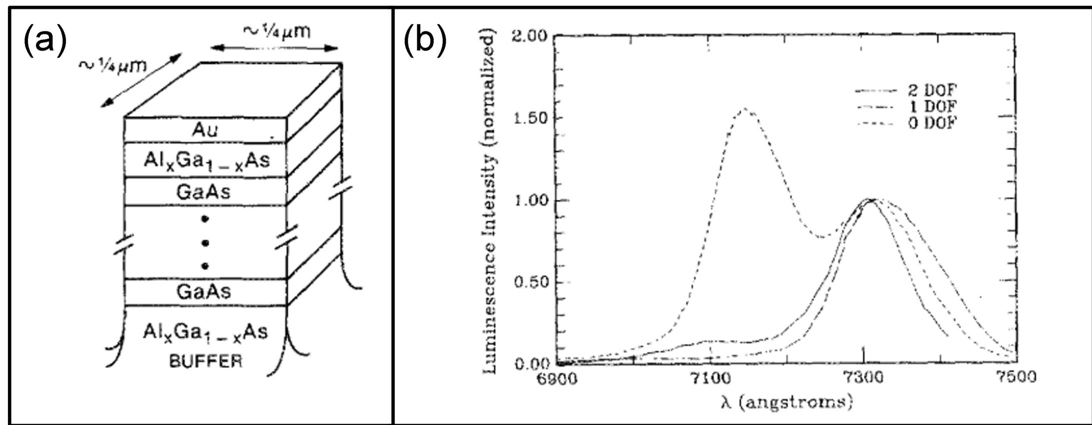

Figure 3-6: In figure (a), a schematic of the quantum dot etched out of the quantum well structure is shown. The photoluminescence spectra in (b) is that of a quantum well (2 DOF), quantum wire (1 DOF) and quantum dot (0 DOF). The spectra are normalised for comparative observation. All photoluminescence measurements were taken at 4.4 Kelvin. Reprinted with permission from [2]. Copyright © [1986], American Vacuum Society.

etching method, the quantum dot's location was spatially predetermined. There have been more recent demonstrations of the creation of site-controlled quantum dots via top down etching of quantum well sandwich structures. In the work by Demory et al. [38], InGaN/GaN quantum wells were first grown between a GaN buffer and capping layer, followed by electron-beam lithography and dry (inductively coupled plasma) etching. This revealed pillars with a small InGaN quantum well sandwich which acts as a quantum dot due to the vertical confinement between the GaN buffer and capping layers. The horizontal confinement is generated by the dot-air barrier where there is band-bending due to surface depletion [38]. Figure 3-7 shows the SEM images of the array of quantum dot structures created. The pillars were then coated in a thin layer of Al_2O_3 followed by a thin layer of Ag. This was done to create a localised surface plasmon resonance cavity surrounding the quantum dot with the aim of utilising the Purcell effect to reduce the radiative lifetimes of the structure. Instead of Ag, Al was also deposited on some of the structures and some just had the Al_2O_3 layer. These were used as controls in order to determine the effect of the plasmonic phenomenon on the quantum dot-pillars and not merely an effect due to a standard metal coating. It was found that the use of the Ag coating on the quantum dot-pillar structures enhanced the intensity on average by ~ 11 times and the radiative lifetimes reduced by ~ 15 times. In contrast the Al coated pillars intensities were reduced by ~ 0.23 times and lifetimes reduced by ~ 3.13 times on average (see Figure 3-8). Thus, the plasmonic effects have a very beneficial effect on the emission rate of the quantum dot-pillar structures [38].

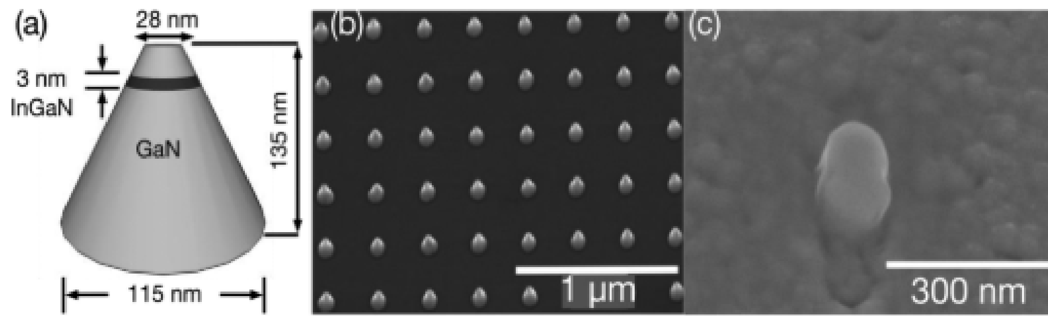

Figure 3-7: Figure (a) shows a schematic of the quantum dot-pillars created in [38]. Figure (b) shows a planar SEM image of the array of quantum dot-pillars. Figure (c) shows an SEM image of a single quantum dot-pillar structure. Reprinted with permission from [38]. Copyright © 2015 American Chemical Society.

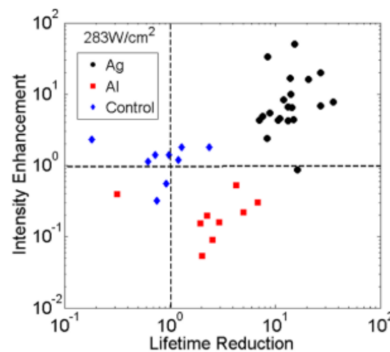

Figure 3-8: This figure shows the total lifetime reduction and integrated intensity enhancement for each individual dot measured, an excitation intensity of 283 W/cm^2 was used. Ag cavity – black circles, Al cavity – red squares and control – blue diamonds. Reprinted with permission from [38]. Copyright © 2015 American Chemical Society.

This shows a relatively successful use of the top down etching of quantum wells on the formation of site controlled quantum dots. However, it is worth noting that this study was not aiming to demonstrate the suitability of the top down approach on the creation of quantum dots, but the plasmonic enhancements which could be achieved by using an Ag cavity.

In the work by Zhang. L et al. (2016) [39], single InGaN/GaN quantum wells were patterned via electron-beam lithography, followed by reactive ion etching. Selective wet etching was then used. The device is as shown in Figure 3-9. Spin-on-glass was deposited on top of the rods, it was etched back to reveal some of the p-GaN material. Upon this, indium-tin-oxide p-contact was deposited before metal contacting of both

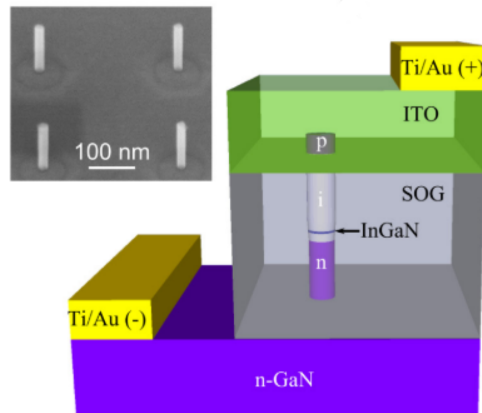

Figure 3-9: This figure shows a schematic of the device created by Zhang. L et al. Reprinted (Figures 1a and 1b) with permission from [39] Lei Zhang, Chu Hsiang Teng, Pei Cheng Ku, and Hui Deng, Charge-tunable indium gallium nitride quantum dots, Physical Review B, 93(8):1–7, 2016. Copyright (2016) by the American Physical Society, https://doi.org/10.1103/PhysRevB.93.085301.

the p- and n-regions. The purpose of their device was to study the effect of applied voltage bias on the tunnelling of electrons into an empty quantum dot. This was successful, and a good demonstration of how a top down approach can be used to make a complex device [39]. However, whilst they performed a wet etch (KOH based) after the dry etching step, the top down approach will inevitable suffer from irreparable sidewall damage which may impact device performance. This is especially compounded in the applications for QIP where it is desirable for all quantum dots to be the same and of a high quality as there may be different degrees of damage to different dot-pillars. This would inevitably result in the properties of the quantum dots to deviate from one another to some extent.

3.1.5 Summary of historical or less scalable techniques and reasons for these methods being undesirable in certain circumstances

The Nano-Jet probe method, whilst extremely creative, does not always produce totally homogeneous results and there may be a limit of the dot size which can be achieved. Nano-imprint lithography, whilst being a relatively cheap and fast process suffers from too many inhomogeneities in the transferred pattern originating from defects in the stamp and its wear over time. Whilst high resolution can be achieved, in cases for QIP

this method is largely unsuitable because of the replication of defective patterns from the stamp.

Although EBL is very effective at producing precise, high resolution patterns, it is typically a very slow process leading to low overall throughput [262]. Subsequently, whilst it still has its uses, such as creating individual patterns or small arrays of periodic patterns, it is not really suitable for wafer scale patterning.

The top down approach, using dry etching of quantum well sandwiched structures is attractive for patterning wafer scale quantum dot arrays. This can be undertaken relatively quickly especially if a patterned etch mask is created via the use of a photo-based lithography technique. However, the damage incurred to the side-walls of the etched structures can be detrimental to device performance. Whilst the group mentioned above, Zhang. L et al. [39], have used wet etching after the initial dry etch to help remove the damage incurred from dry etching, this may not be sufficient to avoid all negative impact to device performance if the damage caused by dry etching has been substantial. Moreover, the lateral confinement of these structures is defined by the band bending at the active region-air interface. It is more desirable to have barriers of semiconducting material; this is likely to give better and more and precise confinement.

3.2 Selective area growth

3.2.1 Selective area growth - general principle

The general principle behind selective area growth (SAG) involves first the deposition of a thin dielectric mask on a semiconductor material. This mask will be subsequently patterned with an array of apertures, revealing the material underneath. Upon regrowth, material will be preferentially grown in the exposed regions of the mask [263]. The growth mechanism itself is thought to be as follows. First, there is preferential growth around the edges of the mask windows, followed by island formation around the centre of the mask apertures [264]. The lateral dimensions of the mask openings are set to be less than the surface diffusion length of the incident atoms, such as gallium, which is also dependent on the growth conditions. This leads to the preferential growth in the mask openings as atoms will choose to migrate here due to the availability of more favourable bonding sites [265]. In this way, there is growth upon the patterned, exposed regions of the mask and not on the mask itself. The seed growth within the mask openings will then coalesce across the whole opening area and after that vertical growth will occur. This will end up being faceted, with perhaps some competition

between faceting before the formation fully hexagonal structure in some form for III-N materials (i.e. such as a hexagonal nanopyramid). This eventuality is reached due to it being the most thermodynamically stable shape, with the lowest surface free energy [266]. The selective area growth structures may be in the form of nanopyramids or nanorods, the former of which will now be discussed and its role for the site control of quantum dots.

3.2.2 Selective area growth – what has been achieved in the literature – basic pyramids

Concerning the III-N's the majority of selective area growth reported has involved GaN. This is as with MOVPE growth of AlN, the Al adatoms have a very high sticking coefficient and low diffusion length [267]. This renders AlN unsuitable for selective area growth with MOVPE, which requires diffusion across a mask to the substrate (usually native) material exposed in the mask openings. In terms of InN, whilst good quality material is difficult to grow due to its low thermal decomposition temperature and large lattice mismatch with most typical substrates, there have been some reports of successful selective area growth [268]. These results are very much in a paucity comparative to the published work on GaN, however both nanopyramid and nanorod structures have been achieved for InN [268] [269]. Being a material of low bandgap, it cannot be used as a barrier layer for a quantum confined system of III-N materials. Subsequently, selective area growth of InN suitable for the creation of sites for quantum dots will not be discussed further. The rest of the discussion will be focusing on SAG of GaN to achieve sites for quantum dots.

The first demonstration of selective area growth, using GaN, on a hole patterned mask was by Kitamura et al. [40]. This group achieved the growth of GaN micropyramid arrays with no visible deposition on the mask. They found that as they increased the growth temperature, a small region of c-plane truncation appeared on the top of the pyramid and, on further increase in temperature, grew in size [40] (see Figure 3-10). This holds significance as the top, truncated c-plane can be used as a quantum dot site. This is possible providing the truncated apex is small enough. The growth of a capping layer after that of the quantum dot would also be necessary. Obviously, the material required for the quantum dot must be of a smaller band gap than GaN in order to have quantum confinement. Hence, InN and InGaN alloys are suitable for quantum dots grown on GaN sites.

There are numerous examples of the creation of site-controlled quantum dots via this

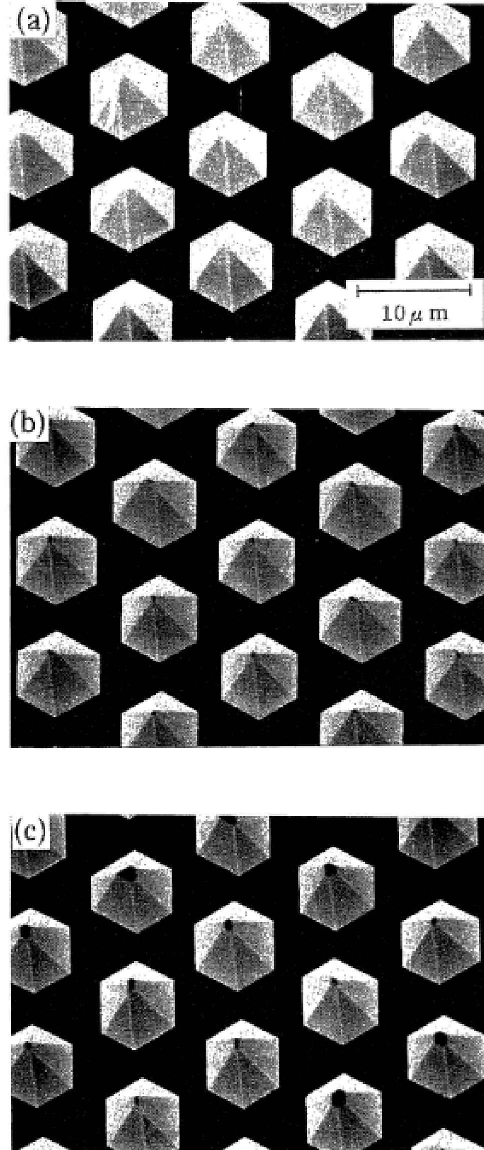

Figure 3-10: This figure shows SEM images of the SAG of GaN in [40] at (a) 1010 ^{o}C, (b) 1025°C and (c) 1050 ^{o}C [40]. All figures reproduced from [40], Copyright © (1995), The Physical Society of Japan and The Japan Society of Applied Physics).

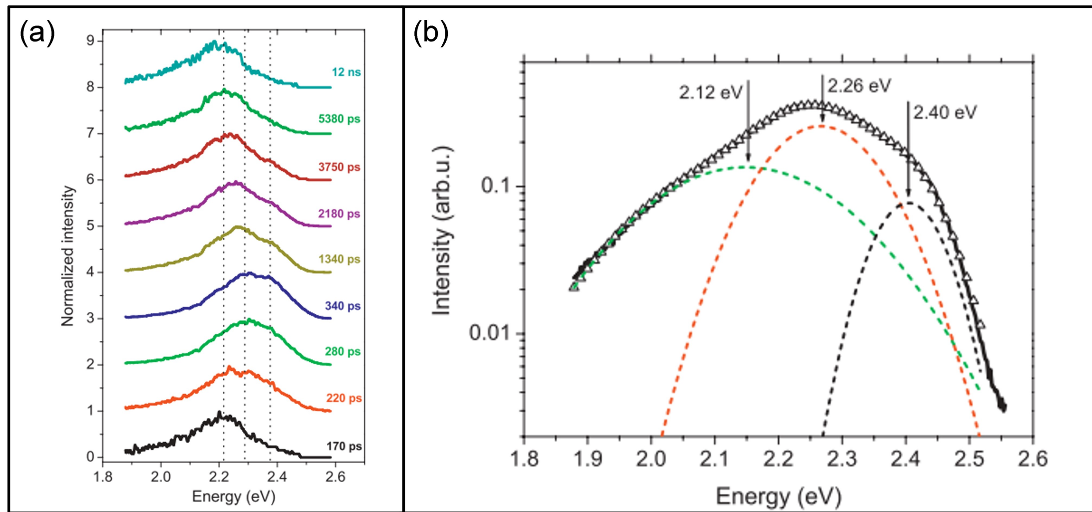

Figure 3-11: Figure (a) shows the time evolution of the PL after the laser excitation pulse on an InGaN QD on GaN nanopyramid sample in [41]. Figure (b) shows the time-integrated PL spectra at 5K of the GaN/InGaN nanopyramids in [41] (both figures reproduced from [41]. Copyright © 2005 WILEY-VCH Verlag GmbH & Co. KGaA, Weinheim).

process. Perez-Solorzano et al. [41] demonstrated this process successfully, creating capped InGaN quantum dots upon GaN micropyramids. Photoluminescence measurements were preformed on their samples. In particular, the time evolution of the PL after an excitation pulse of a laser was recorded. This data is shown in Figure 3-11. The measurements were performed at 5 K, within the 280-340 ps range additional peaks appear. There can be filling of excited states within the low-dimensional structures, due to the ground state being fully occupied. This observed state filling phenomenon is typical for quantum dot structures [41]. Low-temperature time-integrated PL was also performed on the sample revealing a broad peak. It is believed that this peak is made up of three different emission peaks, possibly due to three different confinement dimensions of the semiconductor material (Figure 3-11) [41].

In another study by Perez-Solorzano et al. [42], cathodoluminescence was also performed on the quantum dot on micropyramid structures. It is worth mentioning that power-dependent PL and low-temperature time-integrated PL were also performed on their samples. State filling effects are again observed, this time in the power dependent PL. There is evidence of an excited state filling when the ground state is fully occupied, giving robust evidence for the presence of quantum dots. In the low-temperature, time-integrated PL spectra, three peaks are distinguishable within the broad spectrum, resultant from 0D, 1D and 2D structures. Thus, quantum wires form on the side ridges

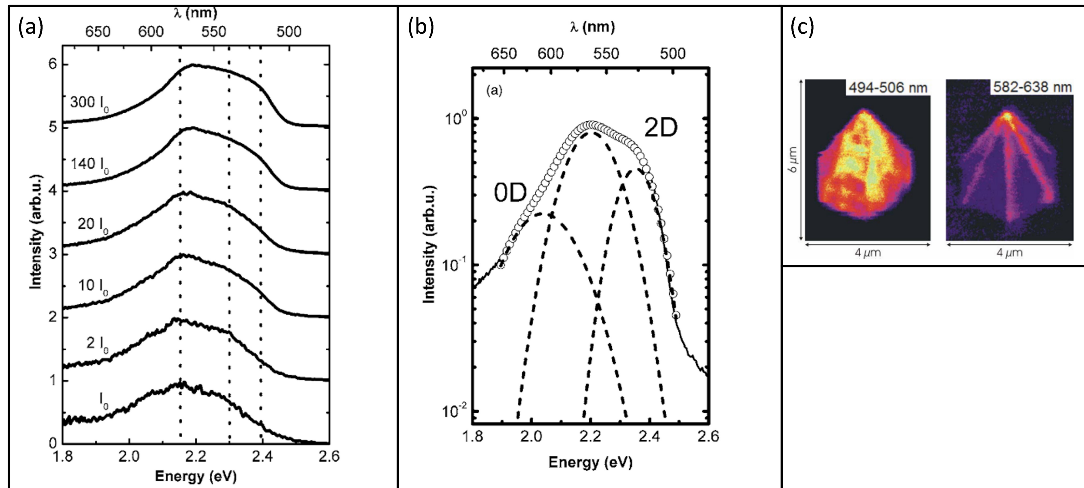

Figure 3-12: Figure (a) shows the power dependent PL of the InGaN/GaN nanopyramids. Figure (b) shows the low-temperature time-integrated PL spectra of the InGaN/GaN nanopyramids. Figure (c) shows the CL of the InGaN/GaN nanopyramids at the emission wavelengths stated [42] (Reprinted from [42] with the permission of AIP Publishing. Copyright © (2005)

and wells on the sidewalls. The radiative decay time of the 0D peak is found to remain more or less constant as temperature increases, which is the indication of excitons in a 0D system. Spatially resolved CL reveal emission from the side walls occurring at a different wavelength to that of the apex, further confirming the presence of quantum dots here [42]. As can be seen from both works presented above, a variety of characterisation techniques can be used to confirm the presence of quantum dots. CL has also been demonstrated to be a good compliment to the state filling effects observed in the PL data, in confirming the presence of the quantum dots. The power-dependent PL, low temperature-time integrated PL and CL results are shown in Figure 3-12.

Jarjour et al. [43], used two-photon excitation photoluminescence spectroscopy to identify the presence of InGaN/GaN quantum dot micropyramid structures. The structure grown was a 5-period InGaN quantum well and GaN barrier layer system upon a micropyramid, such that full spatial quantisation is resultant at the pyramid apex. The motivation for using two-photon excitation is that the underlying quantum well leads to a significant background signal in a one-photon excitation spectrographic measurement of this system. The use of two-photon excitation spectroscopy suppresses the emission from these quantum wells leading to a far more distinguishable quantum dot spectra [43] (see Figure 3-13). As reported by Kim et al. [270], the emission direction of nanopyramids quantum dots can be controlled. The architecture used consisted of a GaN nanopyramid, with a quantum dot at the apex and all coated in silver. This

architecture produces in a 3D plasmonic cavity which results in a Purcell enhancement. This allows efficient light coupling toward the bottom of the pyramid whilst preventing light escape from the top or sidewalls. The decay time of quantum dots in such a system also reduces. Modelling suggested that 91% of extracted light from the quantum dot could be directed to the bottom hemisphere of the nanopyramid. In order to measure from the bottom of the pyramids, the silver coated quantum dot nanopyramids were removed from the substrate. The experimental information found from the now inverted nanopyramids show that the emission is mainly toward the normal direction out of the original base of the pyramid. In contrast, the as grown nanopyramids have directional emission typically in two lobes. The inverted quantum dots were also confirmed to be single-photon emitters via the use of a Hanbury-Brown Twiss experiment. The $g^{(2)}(0)$ value was found to be 0.39 which is less than the 0.5 threshold, below which an emitter is described as a single photon source [270]. This however, is far from a remarkable value for the second order correlation function when one compares its value to others in the literature.

In another study by Gong et al. [44], plasmonic effects were also taken advantage of. Two-photon photoluminescence, which is desirable when one wants to avoid having a large background signal, was strongly enhanced. Here a metal-pyramid hybrid structure was used to take advantage of plasmonic nanofocusing, allowing for spatially selective individual quantum dot excitation. The quantum dots themselves were InGaN dots upon apices of selective area grown GaN nanopyramids [44]. As can be seen in Figure 3-13, in the single photon excitation PL of the metal coated InGaN/GaN quantum dots has a far greater signal contribution from the background compared to that of the two-photon excitation PL. Thus, the quantum dot signal can be much more clearly distinguished in the two-photon excitation PL spectra. When comparing the two-photon excitation of an as-grown InGaN/GaN quantum dot (no metal coating) and one with the metal coating it was found that the two-photon excitation intensities were enhanced by ~ 5000 times [44]. Both this and the previous study mentioned highlight that optical characterisation of individual site-controlled quantum dots within an array can be extremely challenging indeed and in some cases require rather innovative techniques in order to achieve this.

Cho et al. [271] utilised Fourier-transform spectroscopy to estimate the linewidth of their quantum dots beyond the spectral limit. They found a homogenous linewidth of 64 ± 8 μeV. This a very good result for III-Nitride quantum dots indeed. To achieve this they used the SAG of nanopyramids of GaN, as with the more recent work discussed above, as opposed to micropyramids, with the apices as the sites for quantum

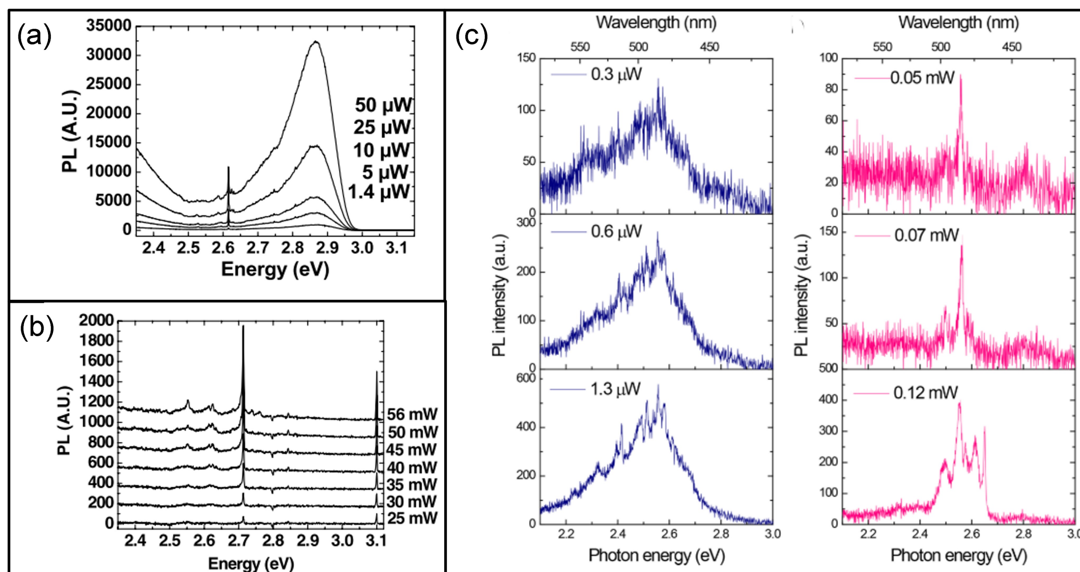

Figure 3-13: Figure (a) shows the single photon PL on the structure described in [43], this has a clear broad quantum well signal with the discrete quantum dot signal at 2.61 eV (figure reproduced from [43]. Copyright © 2005 WILEY-VCH Verlag GmbH & Co. KGaA, Weinheim). Figure (b) is the two-photon excitation PL spectra for different excitation powers for the structure described in [43]. This shows a clear suppression of the quantum well signal when compared to (a) [43] (figure reproduced from [43]. Copyright © 2005 WILEY-VCH Verlag GmbH & Co. KGaA, Weinheim). Figure (c) shows micro-PL data for the metal coated InGaN/GaN quantum dots described in [44]. On the left is the spectra from single photon excitation and on the right that of two photon excitation (both carried out at a temperature of 7K). Reprinted (adapted) with permission from [44]. Copyright © 2018 American Chemical Society.

dot locations. Then a 2 nm layer of InGaN was deposited leading to quantum dot height sizes equal to or less than this. Furthermore, there was no indium accumulation observed within the quantum dots. All this led to quantum dots of a high quality allowing for the measurement of such narrow homogenous linewidths [271]. They also observed a $\sim 99\%$ inherent polarised emission towards one of the crystal axes. At 10 K they measured $g^{(2)}(0) = 0.11$ which is a reasonable, yet not remarkable, value. However, as the temperature rose to 80 K, $g^{(2)}(0)$ became 0.68 which is not a single photon source by definition [271]. Whilst some promising and in places, impressive results, this final second order correlation function measurement shows that this is unsuitable for room temperature operation. This is likely due to the bandgap difference between the GaN nanopyramids and the quantum dots being too small for strong enough confinement at higher temperatures.

Finally, in the work by Hsu et al. [45], InGaN quantum dots were grown on the apices of nanopyramids. It was found that on decreasing the growth temperature of the active layer, the PL spectra red shifted. This was put down to enhanced indium incorporation at lower temperatures. The spectra exhibit FWHM values of 350-1200 μeV, which at the time of the work (2011), was arguably a thin linewidth. It is also worth noting that the minimum detectable value for the FWHM may be limited by the resolution of the system. The quantum dots exhibit a polarisation ratio above 0.9 and are linearly polarised (see Figure 3-14). This was suspected to be due to in-plane anisotropy of the quantum dot potential [45]. The nitrides have a small split-off energy which results in a high degree of linear polarisation for even weakly asymmetric quantum dots [272]. This phenomenon was in fact deliberately studied by Lundskog et al. [46] in a later study. This work, and other more exotic forms of the creation of site-controlled III-N quantum dots via selective area growth will now be discussed.

3.2.3 Selective area growth – more exotic results

Lundskog et al. [46] controlled the emission polarisation of quantum dots via elongating the GaN micropyramids upon which the dots were grown. This was achieved by the creation of oval openings in the selective growth mask upon which SAG of micropyramids could take place. The anisotropy in the strain field of each individual quantum dot determines the polarisation of the emission of the 0D structure [46]. If quantum dots have the same emission polarisation direction this suggest that they possess the same unidirectional in-plane anisotropy. The orientations of the elongated micropyramids and the subsequently formed top ridges of the structures are found to have a high

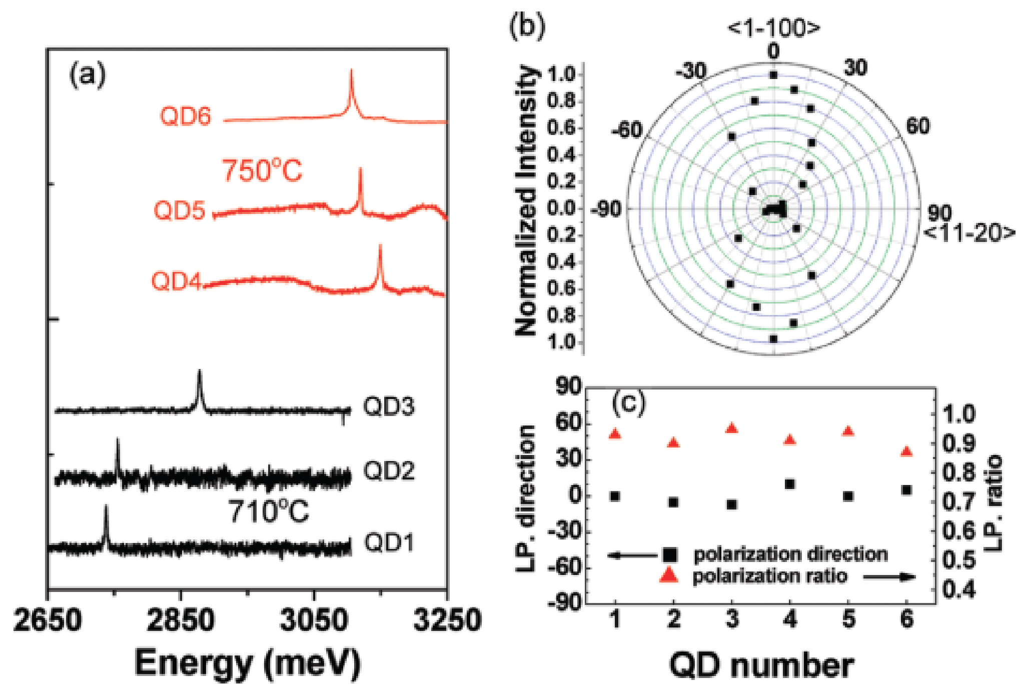

Figure 3-14: Figure (a) shows the micro-PL spectra of nanopyramids with single quantum dots grown at different temperatures. Figure (b) shows a polar plot for the normalised PL intensity against the recorder polarisation direction. Figure (c) shows the polarisation directions and ratios for the quantum dots shown in Figure (a) [45]. All figures reprinted with permission from [45]. Copyright © 2011 American Chemical Society.

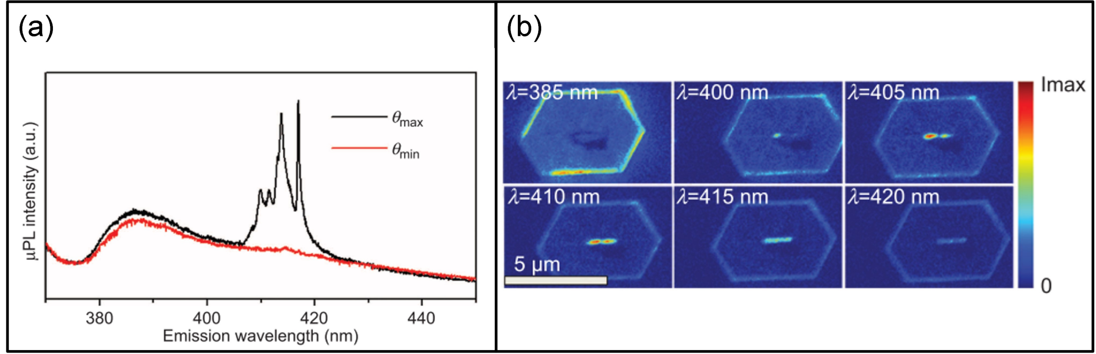

Figure 3-15: Figure (a) shows the micro-PL spectra of an elongated hexagonal pyramid with quantum dot structure/s on the top ridge. The polariser analyses is set to $\theta_{max}(\theta_{min})$ by which the maximum (minimum) intensity of sharp emission peaks are detected. Figure (b) shows the spatially resolved monochromatic CL spectra of another GaN micropyramid with InGaN quantum dot structure/s on the top ridge (both figures reproduced and reformatted but unaltered from [46] (2014) under Creative Commons Attribution-NonCommercial-No Derivative Works 3.0 Unported License).

correlation with the quantum dot emission polarisation direction. Micro-PL and CL confirmed the presence of quantum dots at the top ridges (Figure 3-15). The linewidth was found to be larger than 4 meV. This broad linewidth may be due to the presence of multiple quantum dots on the top ridges of the structures [46]. As observed in Figure 3-15 all of the dot emissions are polarised in the same direction supporting the hypothesis that linear polarisation is due to the in-plane anisotropy of the confinement potential. It was also found that at certain elongation angles polarisation guiding in different directions is controllable. In InGaN quantum dots there is a large sensitivity to the dot asymmetry, and this is put down to a large amount of band mixing due to the small split-off energy [46].

Some advantages of quantum dots grown upon the apices of nanopyramids are as follows. They typically have better light extraction than quantum dots embedded within a planar structure. In addition, via elongation, the orientation of linear polarisation can be controlled, threading dislocations also tend to bend towards the semi-polar planes leading to relatively good material quality at the apex. Furthermore, the piezoelectric field should decrease because of the nanoscale pyramid geometry [271]. The emission polarisation of these quantum dots can be controlled, as mentioned above, via quantum dot elongation. However, this has the disadvantage of resulting in fine structure splitting in the emission [250]. Some other disadvantages of these quantum dots are the poor light extraction when one does not use some of the more complex architectures involving utilising plasmonic effects or pyramidal removal and inversion as discussed

above. Consequently, this makes using these architectures to realise QIP applications relatively improbable. This is particularly true for quantum optical computing and quantum relay devices.

Another attractive route for site-controlled quantum dots via the use of selective area growth is the creation of dots embedded in the apices of nanowires. In such quantum dots, the polarisation direction is parallel to the long axis of the nanowire, thus resulting in having an intrinsic emission polarisation. This is clearly desirable for QIP devices. The reasoning behind this intrinsic emission polarisation is due to the large dielectric contrast between the nanowire and that of the surrounding air. This acts to attenuate the electric field along the long axis of the nanowire, resulting in polarised light emission [46]. Also, the high geometric aspect ratio of the nanowires allows for good light extraction efficiency [47].

Choi et al. [273] found when performing SAG of a GaN nanorod upon a thin, defect heavy AlN layer there was minimal negative impact compared to that of using a thick GaN underlying layer. A shell structure followed by a GaN quantum dot and a capping layer was grown. It was found that MOVPE growth of an AlN shell upon the GaN nanowire resulted in a poor, rough surface due to a short diffusion length and tensile deformation of the AlN. However, an AlGaN shell layer resulted in a much better surface quality in comparison. Moreover, the PL spectra of the AlN-shell-GaN-Quantum-dot structure presented multiple peaks in the region of suspected quantum dot emission. This was put down to localisation centres of GaN at the rough, depressed areas of the AlN shell. The same is not observed for the AlGaN shell. The AlGaN shell nanorod grown upon the underlying AlN template layer showed a strong peak in the PL spectra, indicative of a quantum dot. The spectra also has a high signal to noise ratio as there is minimal contribution to the background from the AlN underlying template due to it being only 25 nm thick. The group found that the PL linewidths of the quantum dot were 2.7 meV, which at the time of publication was competitive compared to other, similar, publications [273]. This approach is a promising one and the use of an AlGaN shell layer dominates literature on SAG GaN nanowire/shell/GaN-quantum-dot structures. However, it is worth mentioning the majority of the literature concerning the MOVPE SAG of nanowire quantum dots concerning the III-N is mainly from the same group.

In further work by Choi et al. in 2013 [47], site-controlled quantum dots of the structure mentioned above were investigated in more detail with regards to their optical properties. It was found that there was still a PL signal even up to 300 K (see Figure 3-16). This is attributed to the presence of strong carrier confinement in the dot. The

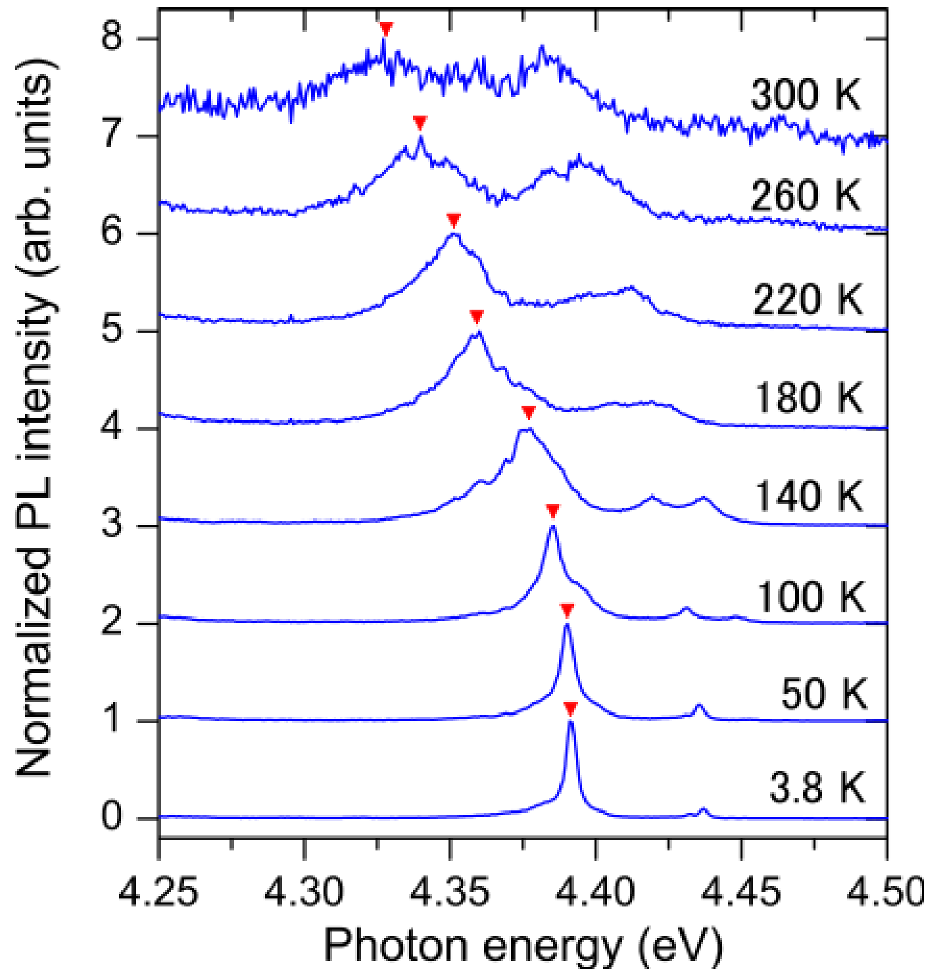

Figure 3-16: This figure shows the PL spectra from a single quantum dot as detailed in [47] at different temperatures (Reprinted from [47], with the permission of AIP Publishing, Copyright © (2013)).

linewidths however, increased from 4 meV at 4 K up to 45 meV at 300 K, the latter is quite a large value. They also observed both exciton and biexciton transitions within their quantum dots. The significance of the last point is important in terms of the biexciton binding energy [47]. The biexciton binding is the energy separation between the exciton and biexciton peaks in the PL [47]. It is resultant from the difference in energy of a bound biexciton and that of two non-interacting excitons [250]. In this work, a value of 52 meV was observed. At the time, this was the largest value for a III-V semiconductor quantum dot. This was thought to be due to the increased confinement present in quantum dots with small heights, as in this structure, and therefore a smaller spatial separation of the electron and hole wavefunctions. It is thought that the reduced piezoelectric polarisation in the nanowire quantum dot could also contribute to the large biexciton binding energy observed [47]. From this they drew the conclusion that as the biexciton binding energy is so large, with even the large linewidth measured at 300 K it still may be possible to avoid significant spectral overlap between the exicton and biexciton emissions. This therefore, allows for the potential for room temperature single photon emission [47].

Room temperature SPE was achieved by the same group mentioned above (Holmes et al. [68]) in 2014. They measured a $g^{(2)}(0)$ value of 0.13 at 300 K, once corrected for background and detector dark counts [68]. This was further improved upon in 2016 when Holmes et al. [15] measured a $g^{(2)}(0)$ value of 0.34 at a temperature of 350 K. This demonstrates the potential suitability for single photon emitters of this nature being integrated to on-chip devices as they can operate at temperatures above that of standard room temperature. This is important as there will be inevitable component heating in integrated on-chip devices. The micro-PL emission of the quantum dots in this study did have a relatively large linewidth (33 meV), however, considering these studies are at 350 K which will lead to a sizable amount of acoustic phonon interactions, this is still a rather remarkable achievement [15].

The same group above also analysed the emission linewidths of their nanorod quantum dots via the use of Fourier transform spectroscopy. It is thought that spectral diffusion should not be as great in nanorod quantum dots due to the higher quality material produced by SAG, the smaller size of quantum dots in these systems (as they are not strain-limited), and as the environment volume is reduced because only the nanorods alone are grown [249]. The homogenous linewidth measured by Fourier transform spectroscopy was found to be 135 $\pm$ 30 μeV, which is a very good value for site-controlled III-N quantum dots and comparable with self-assembled GaN/AlN QDs. This is however, broader than the radiative decay limit and so some other decoherence

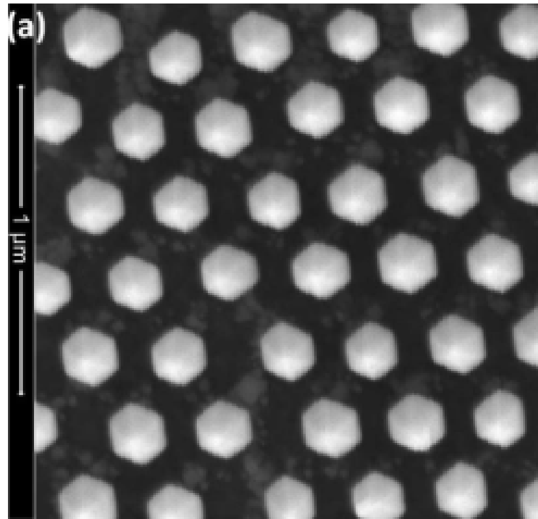

Figure 3-17: This figure shows an SEM image of the matrix of GaN nanorods with InGaN quantum dots. As can be seen there is a lack of homogeneity between different rods. Reprinted with permission from [48]. Copyright © 2017 American Chemical Society.

processes must be taking place [249].

In the work by Gacevic. Z et al. [48] in 2017, SAG GaN nanorods were also used with quantum dots formed within an InGaN nanoshell. This led to quantum dots grown on three different regions of the rod each with different polarities (nonpolar, semi-polar and polar). All three of these quantum dots were demonstrated to be single photon sources. In order to grow the nanorods, colloidal lithography was used to pattern a mask with an array of holes before using SAG of the GaN nanorods. This produces rods with a lack of uniformity to some extent and a diameter variance of 6%. There was also the presence of the occasional nanorod with much larger diameters across the sample [48]. This highlights the limitations of this type of lithography for the production of uniform arrays of nanorods for quantum dot sites. Although this is a promising route for achieving single photon emitting quantum dots, the inhomogeneity between separate nanorods is not desirable for chip-scale QIP applications (see Figure 3-17).

Although the work by Deng et al. [274], concerned MBE (Molecular Beam Epitaxy) grown structures rather than MOVPE, their research is interesting nonetheless. In this work, GaN nanorods were SAG via PA-MBE (Plasma-Assisted Molecular Beam Epitaxy). A purely AlN shell layer was then grown on the GaN rod core, followed by a GaN nanodisk quantum dot and an AlN cap. Upon measuring the second order

correlation function of a single QD-in-rod structure, after correction a $g^{(2)}(0)$ value of 0.19 at 300 K is found. This is similar to the work of Holmes et al. [68] that found a $g^{(2)}(0)$ value of 0.13 at 300 K. This demonstrates that the less mature GaN core AlN/GaN quantum dot-in-rod structures can achieve similar results compared to the more studied GaN core AlGaN/GaN quantum dot-in-rod structures. Further study of AlN/GaN rod structures may therefore lead to an improvement upon the results found by Holmes et al. in [15]. The work of Deng et al. [274] and Holmes et al. [68], [15] also demonstrates that nanorod structures are particularly desirable to house quantum dots; the reasons for which are now briefly discussed.

Some advantages of nanorod structures with quantum dots on their apices are as follows. They typically exhibit large biexciton binding energy, coherently controllable excited states, and have been shown to exhibit single photon emission up to 350 K [249] [15]. They also exhibit intrinsic emission polarisations which is highly desirable for QIP applications [46]. However, most studies on these quantum dots have involved the patterning of a mask via EBL followed by SAG of a GaN nanorod core via either MOVPE [249] or MBE [274]. From there a MOVPE grown AlGaN confining shell (typically with 0.8 Al content) is deposited on the rod [249], or MBE growth of an AlN shell [274], before GaN quantum dot growth and a capping layer. Whilst using SAG can result in high crystal quality of the grown nanowire [249], this technique also has a number of disadvantages. First of all, as AlN cannot be practically selectively area grown in a typical MOVPE reactor, GaN has to be used as the nanorod core. It would be more preferable to have a purely AlN core followed by a GaN quantum dot and an AlN capping layer. This would provide more confinement with the possibility for even higher temperature single photon emission. Whilst an AlN shell has been demonstrated in [274], this was grown via MBE rather than MOVPE. MOVPE grown AlN shells on GaN cores are found to be poor morphology [273]. Furthermore, when growing a shell on a GaN core, the confining shell layer may bring forward more problems in the current nanorod-quantum dot architecture. There will be inherent strain between the high Al content AlGaN layer or AlN and that of the GaN core. This could introduce crystallographic defects into the system. The generation of defects will depend on the thickness of the AlGaN or AlN deposited of course (plastic relaxation), but this still may be a problem even with rather thin layers of AlGaN or AlN. Finally, the use of EBL to define the SAG apertures within the mask is good for studying optical properties of individual quantum dot architectures. Conversely, when desiring large area arrays of nanorod quantum dots for QIP device applications, this is not a suitable patterning technique. Clearly, some of the work presented above is promising and, especially in the case of 350 K single photon emission, is remarkable.

3.2.4 Selective area growth – disadvantages

A lot of literature has been presented concerning selective area growth and how it can be used to successfully create site-controlled quantum dots. However, there are some disadvantages of this technique. These will now be mentioned.

Firstly, selective area grown arrays of quantum dots typically suffer from the growth enhancement effect. This effect results in an inhomogeneous difference in thickness of the quantum dots grown across the width of the dielectric patterned mask growth template [275]. This will then lead to quantum dots with slightly different properties. Additionally, SAG structures can suffer from compositional variations [276]. Dry etching damage upon the surface of the window openings can also be caused due to bombardment from the dry etch plasma during the patterning process in forming the open windows in the dielectric mask [277]. Furthermore, Si-based (such as SiN_x or SiO_x) masks typically utilised for SAG of GaN can decompose at the high growth temperatures required for the MOVPE growth of GaN. This can then lead to unwanted contamination from the mask to the selectively area grown structure itself [278].

When considering the creation of SCQDs via the growth upon SAG nanostructures, such structures can be hard to integrate into devices. For instance if one wanted to sandwich an array of QDs grown upon SAG nanostructures between two DBR's (distributed Bragg reflectors) such that the QD layer is effectively housed between two mirrors, this may be challenging. Furthermore, if one wanted to align single SAG based SCQDs for further fabrication (such as trying to pattern a mesa to isolate a single quantum dots) this could be very challenging considering the likely sub-micron alignment accuracy one would need. Finally, if one wanted to remove the dielectric mask after growth of SAG and SCQD structures and then planarise the sample, one would need to remove the sample from the growth reactor, strip the mask off the sample and place the sample back into the growth reactor for further growth. This could lead to contamination of the surface of the SAG sample, in close proximity to the initially grown QD active region.

3.3 Other routes for achieving site-controlled III-N quantum dots

Other routes toward achieving site controlled quantum dots with different material systems include, buried stressor growth [279], growth into pyramidal recesses [280] and in-situ laser nano-patterning during growth [281]. With regards to III-N quantum dots it is worth mentioning the work by Arita et al. [87] in 2017. In this work, quantum dots were formed via interface fluctuations in thin quantum wells. As they do not rely on the Stranski-Krastanov growth mode, they do not require the lower growth temperatures applied in this growth mode. The linewidth of a single quantum dot in this architecture was measured to be $87 \pm 4\ \mu eV$, which is very impressive indeed. A second order correlation value of $g^{(2)}(0) = 0.085$ (with no correction applied) was found, this is again a very good value for a III-N quantum dot. This was limited by the detector response function and so utilising fitting to negate this limit (without any correction for background emission) a value of $g^{(2)}(0) = 0.02$ was found. They did however, detect a large value of fine structure splitting in both the exciton and biexciton transitions which would hinder the emission of polarisation entangled photon-pairs, a requirement for optical quantum computing [87]. Also, this route for quantum dot production is not strictly site-controlled, losing the advantages of deterministic size and positioning.

3.4 Conclusion

Whilst there appears to be a wealth of research in the creation of GaN nanostructures, mainly due to the ability to perform SAG via MOVPE growth, there has been far less exploration of AlN nanostructures. From the discussion above, it seems evident that an AlN/GaN/AlN nanorod architecture would be a desirable. A top-down bottom-up approach is a hybrid approach to achieving such structures by employing both top-down dry etching and bottom-up regrowth. The work in this thesis involved the investigation of this technique applied to AlN. This exploration is presented in the next chapter, Chapter 4.

Chapter 4

Top-down, bottom-up approach for the creation of uniform arrays of facted AlN nanostructures

4.1 Introduction

The top-down bottom-up approach is a hybrid method for achieving faceted nanostructures which combines some of the advantages of the purely top-down and bottom-up techniques. The top-down bottom-up approach involves the periodic deposition/patterning of a hard mask upon an initial template (in this case AlN). This is followed by top-down dry, plasma based etching (in the case of AlN, using Cl based gas). Bottom-up MOVPE regrowth is then performed in order to enhance the resolution achieved from the lithographic and dry etching steps. This then allows for faceted growth whereby one can achieve a highly uniform array of nanostructures with sharp features.

This technique avoids the AlN-shell-on-GaN-core method investigated with MOVPE in [273] and employed with MBE in [274]. Thus, one can avoid a highly strained shell as results from heteroepitaxy. This may allow for better facet formation and higher quality crystalline material, allowing for higher quality, purely AlN sites to house GaN quantum dots. In addition it avoids absorption from the GaN core.

4.2 Statement of Authorship

The work presented in this chapter, and the corresponding appendix, is taken from a paper written by the author of this thesis, namely the work published in [49]. There is also some slight addition and modification of the content. Some of the material in Section 4.2 repeats content in Chapters 1 and 3 but is included for completeness.

This declaration concerns the article entitled:									
Creation of regular arrays of faceted AlN nanostructures via a combined top-down, bottom-up approach									
Publication status (tick one)									
Draft manuscript		**Submitted**		**In review**		**Accepted**		**Published**	X
Publication details (reference)	Armstrong, R., Coulon, P.M., Bozinakis, P., Martin, R.W. and Shields, P.A., 2020. Creation of regular arrays of faceted AlN nanostructures via a combined top-down, bottom-up approach. *Journal of Crystal Growth*, 548, p.125824.								
Copyright status (tick the appropriate statement)									
The material has been published with a CC-BY license				The publisher has granted permission to replicate the material included here	X				
Candidate's contribution to the paper (provide details, and also indicate as a percentage)	The candidate contributed to / considerably contributed to / predominantly executed the... Formulation of ideas: Considerably contributed to (70%) Design of methodology: Considerably contributed to (50%) Experimental work: Predominantly executed (100%) Presentation of data in journal format: Predominantly executed (100%)								
Statement from Candidate	This paper reports on original research I conducted during the period of my Higher Degree by Research candidature.								
Signed (typed signature)	Robert Armstrong			**Date**	07/11/2022				

4.3 Background & motivation

Aluminium Nitride (AlN), Gallium Nitride (GaN) and their alloys are wide- [151] and direct-band-gap semiconductors when in the stable, wurtzite, crystal polytype [152]. The band gaps for AlN and GaN are ~6.2 eV and ~3.4 eV respectively [153]. The large

band-gap range of AlN and GaN means that alloys of these two materials, with high Al content, are suitable for UVC devices across the range of 200-280 nm. However, planar AlN-based UVC devices suffer from low quantum efficiency and output power [282]. This is partially due to large amounts of non-radiative recombination in these devices. The main cause for non-radiative recombination in AlN and AlGaN based UV LEDs are the high levels of threading dislocation densities and point defects. This leads to an inevitable reduction in the internal and external quantum efficiencies [283]. High device operation voltages are also necessary [284] and the polarisation coefficient of emission also acts as a bottleneck for high-performance UVC applications [285]. The polarisation coefficient is important as TM polarised light is predominantly emitted from high-Al-content-AlGaN- and AlN-based planar LEDs. Light of this polarisation is very difficult to extract from c-plane AlN or high-Al-content-AlGaN material [286] [287]. This, therefore, leads to heavily-reduced light extraction efficiencies [282].

3D structures can, however, be used to overcome these limitations to some extent. Nanopatterning of sapphire/AlN templates has been shown to be effective at lowering threading dislocation densities [267] [288] [289]. 3D nanostructures also allow for stress relaxation, increased active volume [290] and higher extraction efficiencies [291]. In the case of higher extraction efficiencies, utilising nanostructures has been found the be very effective in allowing the escape of TM polarised photons [292] due to the presence of non- and semi-polar planes from which TM polarised light can escape with greater ease.

AlN nanostructures can be used to house more exotic light emitters such as quantum dots. For this, ideally the nanostructures would comprise highly uniform and ideally spatially-predetermined arrays, to aid electrical injection. Single photon emission (SPE) from III-N site-controlled quantum dots has been demonstrated to operate above room temperature [15]. Arrays of quantum dots which offer spatial, shape and size determination leading to identical properties are particularly suitable for quantum information processing (QIP) applications [124, 123, 15]. Previously, SPE from GaN quantum dots at [68] and above room temperature [15] was achieved using GaN nanorods created via selective area growth (SAG). This was followed by growth of an $Al_xGa_{1-x}N$ shell ($x = 0.8$), GaN quantum dot growth and finally a capping layer [273]. Ideally, one would desire a pure AlN barrier layer to increase the band offsets, resulting in better confinement, in order to realise even higher temperature SPE. Additionally, the use of a purely AlN core would avoid photon re-absorption problems associated with a GaN core. However, current methods to achieve AlN nanostructures are not well-developed and, using pure AlN as a shell layer on SAG GaN nanostructures with-

out considering the nanostructure core, is insufficient [273]. Therefore, another route for the creation of uniform, well-faceted, high-quality arrays of AlN nanostructures for both optoelectronic UVC applications and as sites for quantum dots is necessary.

AlN nanostructures have been fabricated via a number of different routes; AlN nanowires [293], via arc discharge [294], vapour-liquid-solid [295] and vapour-solid [296] techniques, in addition to MOVPE growth utilising catalyst droplets [297]. However, achieving dimensionally-uniform structures is very challenging [293] and no spatially-predetermined arrays have been realised. One of the most widely-employed methods is the growth of self-organised AlN nanorods via radio-frequency plasma-assisted molecular beam epitaxy [284]. Whilst these rods are somewhat uniform and vertically aligned [284] they are not homogeneous in their shape and they nucleate randomly. As has been discovered with GaN self-assembled nanorods, these structures will exhibit non-uniform properties and may hinder device processing [298]. Specifically, the non-uniform dimensions of the rods will lead, upon growth of active regions, to inhomogeneous optoelectronic properties of the rod arrays. Circumventing these problems would obviously be desirable in device applications.

Recently, a catalyst- and lithography-free method for the fabrication of AlN nanorods by polarity selective epitaxy and etching has also been demonstrated [291]. Here, an AlN layer of mixed polarity is grown and wet etching is used to selectively etch away N-polar regions of material [284]. Multiple quantum wells were then grown on the resultant nanorods in a core-shell architecture. However, the rods had random spatial locations that led to non-uniform regrowth of the active regions.

Selective area growth (SAG) is an effective method for the creation of faceted, highly-uniform, spatially-predetermined arrays of nanostructures. This has been widely utilised for the growth of GaN nanostructures such as nanopyramids [40] and nanorods [299]. It has also been demonstrated with InN; again the growth of nanopyramids [269] and nanorods [268] have been achieved. However, with AlN, no demonstration of SAG, via MOVPE, has been demonstrated thus far. This is because aluminium (Al) adatoms have a very short diffusion length and a large sticking coefficient [300]. This means that they cannot diffuse effectively across a dielectric mask to any more favourable, native, bonding sites. This results in parasitic growth upon the mask itself instead of the formation of AlN nanostructures within the mask apertures.

The combined top-down, bottom-up approach is a promising approach to achieve complex nanostructures [267] [288] [301] [302]. This process involves the nanopatterning and top-down etching of a material (such as an initial planar AlN template) to create

nanostructures. This is followed by bottom-up regrowth leading to well-faceted nanostructures. Any surface damage introduced from dry etching is buried during regrowth or removed by wet etching to limit its impact on device performance. This technique has been used to create arrays of GaN/InGaN/GaN core-shell structures [303] [301] and AlN/AlGaN/AlN structures [209] [302]. However, this technique is predominantly used for regrowth onto nanorods, with other structures largely unexplored.

The nature of the faceting that occurs during regrowth on structured substrates (as shown later in this paper) allows for an enhancement of the resolution of conventional lithographic processes in order to create small nucleation regions for the growth of quantum dots. Such regions are typically much smaller than the resolution of large-area lithography techniques that are widely available to researchers. Moreover, access to well-organised semi- and non-polar facets opens up avenues to reduce the impact of the quantum-confined Stark effect (QCSE) present in active regions suitable for UVC emission applications in planar devices [209].

In this work, we present the fabrication of AlN nanorod and nanohole structures, followed by a study and analysis of the effect of different MOVPE regrowth conditions. The growth dynamics of planes of different orientations is presented and discussed for both nanorods and nanoholes. We also discuss the results with regards to suitability for the applications mentioned.

4.4 Materials & Methods

Commercially-sourced, planar, ~ 4.5 µm thick, AlN templates (Suzhou Nanowin Science and Technology Co. LTD, Suzhou, China) were used to fabricate nanorod and hole structures at two different etch depths. The fabrication process involved the use of Displacement Talbot Lithography [304] [22] in order to pattern photoresist for either the deposition or patterning of a hard etch mask onto the AlN templates. This hard mask was then used during a ICP (inductively coupled plasma) dry etch to create hole and rod structures with depths of 1 µm and ~ 100 nm. The two different etch depths were chosen to study the impact of the aspect ratio of the structures on the regrowth dynamics taking place.

Figure 4-1 shows the nanostructured templates after the dry etching and removal of the hard mask. This figure presents a number of interesting observations. As one can see in (a) and (b) the rod samples are relatively circular with slight hexagonal faceting exhibiting 'edge-to-edge' morphology (see Figure 4-2) observed in the deep

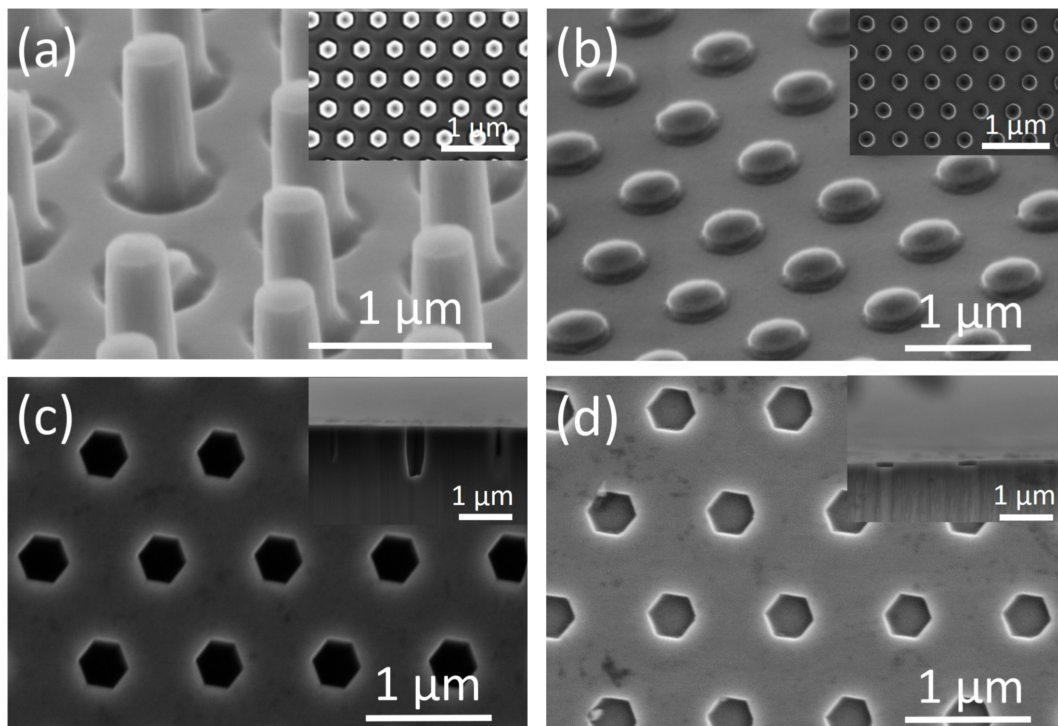

Figure 4-1: SEM images of the four nanostructures created. Shown are the deep etched nanorods (a) and nanoholes (c) ($\sim$ 1 µm deep) and shallow etched nanorods (b) and nanoholes (d) ($\sim$ 100 nm deep). The insets show the plan-view SEM images of the rods and the cross-section SEM images of the holes.

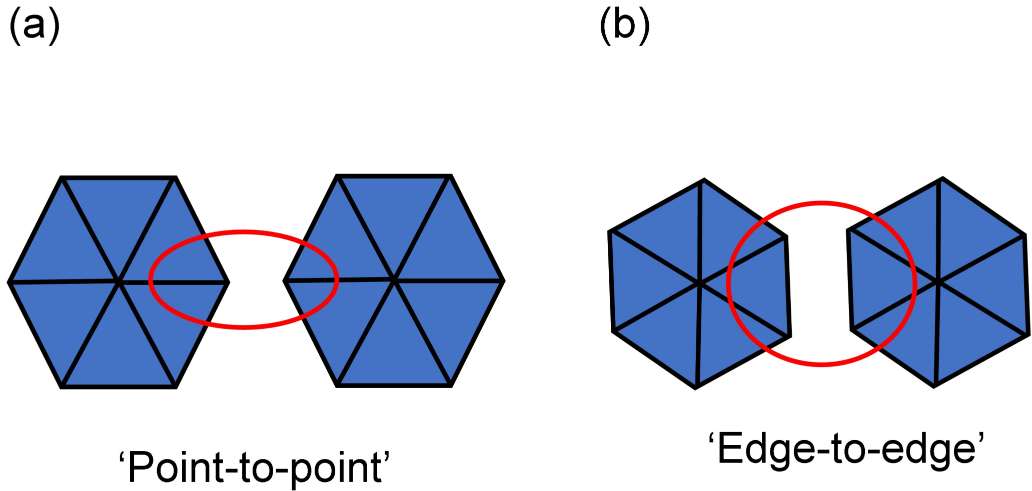

Figure 4-2: This figure shows what is meant by 'point-to-point' morphology (a) and 'edge-to-edge' morphology (b).

rod sample (as can be seen from the inset in (a)). The hole samples ((c), (d)) by contrast, exhibit very clear and distinctive hexagonal faceting with 'point-to-point' morphology (see Figure 4-2). By comparing the geometry with the flat of the sapphire wafer, the sidewall facets can be determined to be m-planes ($\{10\bar{1}0\}$). Also of note, is the clear difference in etch depth as shown by the insets of (c) and (d).

A series of regrowth experiments were performed (see Table 4.1). The effect of the growth temperature (runs 1-3), the V/III ratio (runs 4, 2, 5, 6) and a growth time study (runs 5, 7, 8, 9) was performed. The growth set temperature was the temperature set via the growth reactor and this was measured to have an offset of up to ~ 100 °C less than that of the true temperature measured via an emissivity-corrected pyrometer. The regrown AlN nanostructures were then characterised via SEM and AFM.

4.5 Growth parameter investigations

The wurtzite crystal structure, being the most thermodynamically favourable crystal polytype for AlN, leads to the possible presence of a number of planes which can be categorised as polar (normal to the plane parallel to the c-axis), non-polar (normal perpendicular to the c-axis) and semi-polar upon regrowth of nanostructures. See Figure 4-3 for the relevant planes in this chapter. The resulting shape of the structures depends on the speed of the different planes and the topography of the template.

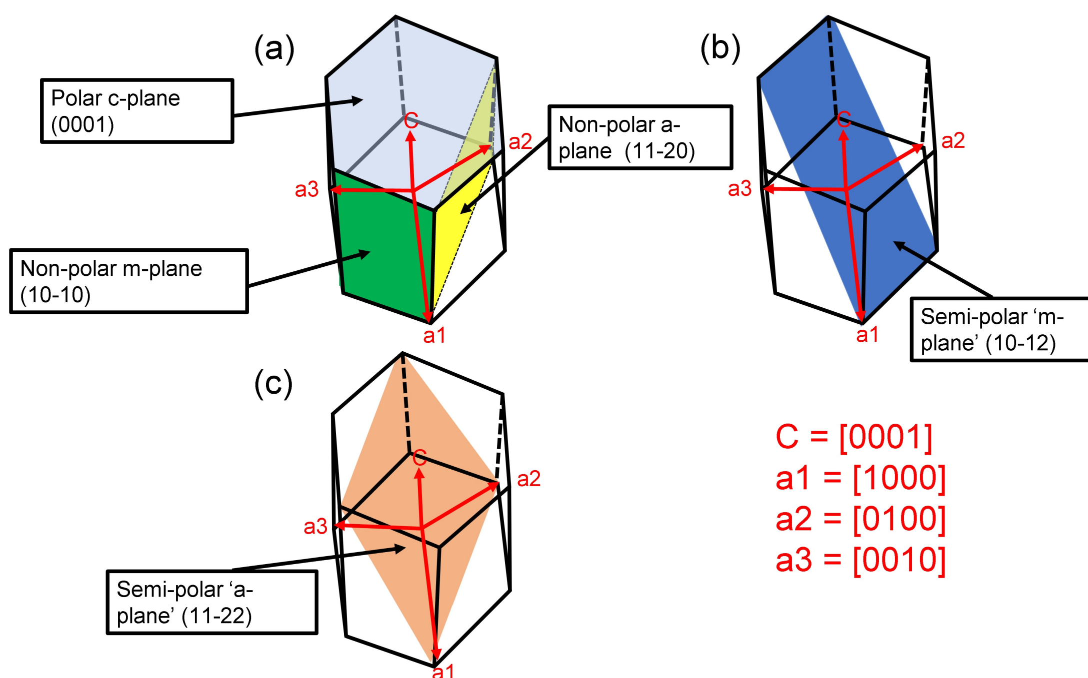

Figure 4-3: This figure shows some of the crystallographic planes in the wurtzite crystal structure. In (a) the polar c-plane ($\{0001\}$), the non-polar m-plane ($\{10\bar{1}0\}$) and the non-polar a-plane ($\{11\bar{2}0\}$) are shown. In (b) the semi-polar m-plane ($\{10\bar{1}2\}$) is shown. In (c) the semi-polar a-plane is shown a-plane ($\{11\bar{2}2\}$).

For convex structures, such as the nanorods, the slowest growing facets determine the resulting geometry of the structure, whereas for concave structures, such as a shrinking void, the fastest growing planes determine the final shape [305]. This means that for convex structures, slow growing facets expand at the expense of faster growing facets, leading to these slow growing facets dominating the morphology of the structures after prolonged growth. Conversely, for concave structures, the fastest growing facets expand at the expense of the slowest growing facets leading to these fast growing facets dominating the morphology of the structures after prolonged growth.

Given that the growth speeds of the different planes will alter depending on the growth conditions, we now present the results of varying the growth temperature, V/III ratio and growth time.

4.5.1 The effect of growth temperature

Figure 4-4 presents SEM images of the growth on the four different templates as a function of the growth temperature whilst keeping all other growth conditions the same. The growth conditions are shown in runs 1-3 of Table 4.1.

Table 4.1: Details of the growth experiments with the changes highlighted in red. For all growth experiments the TMAl flow was 20 sccm, the pressure was 20 mbar and the carrier gas was H_2.

Growth run	Set temperature °C	NH_3 Flow (sccm)	V/III ratio	Growth time (min)	Corresponding figures
1	900	1000	$\sim$ 3800	60	4-4 (a), (d), (g), (j)
2	950	1000	$\sim$ 3800	60	4-4 (b), (e), (h), (k)
3	980/1005[1]	1000	$\sim$ 3800	60	4-4 (c), (f), (i), (l)
4	950	20	$\sim$ 74	60	4-5 (a), (e), (i), (m)
2	950	1000	$\sim$ 3800	60	4-5 (b), (f), (j), (n)
5	950	2000	$\sim$ 7600	60	4-5 (c), (g), (k), (o)
6	950	5000	$\sim$ 19000	60	4-5 (d), (h), (l), (p)
5	950	2000	$\sim$ 7600	60	4-6 (a), (e), (i), (m)
7	950	2000	$\sim$ 7600	120	4-6 (b), (f), (j), (n)
8	950	2000	$\sim$ 7600	150	4-6 (c), (g), (k), (o)
9	950	2000	$\sim$ 7600	180	4-6 (d), (h), (l), (p)

[1] In run 3 the two set temperatures correspond to that of two different growth runs for the deep and shallow structures. These temperatures were measured to be the same true temperature measured via emissivity-corrected pyrometry.

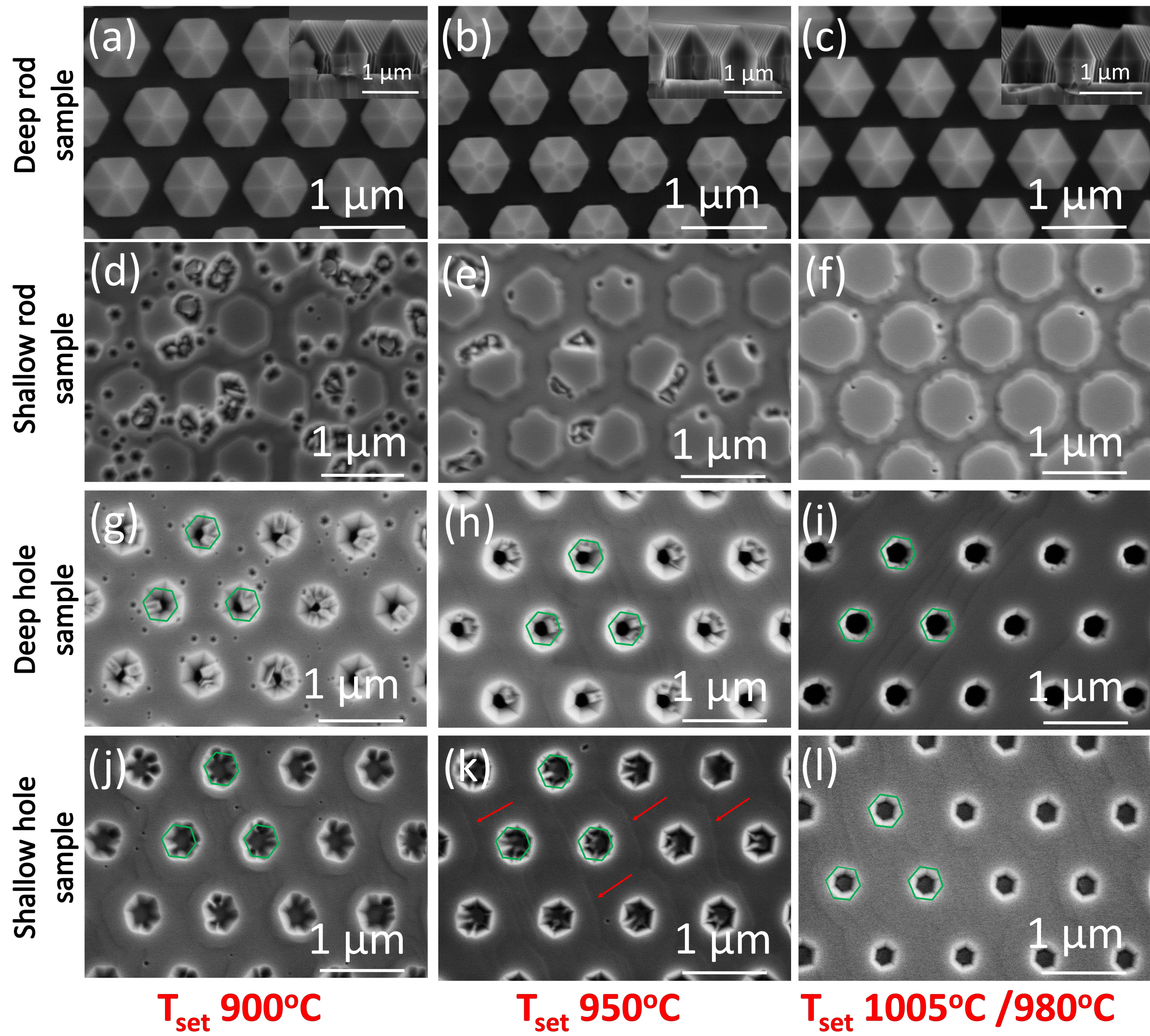

Figure 4-4: SEM images corresponding to the four templates grown at different temperatures. The green hexagons in (g)-(l) represent the original morphology of the dry etched structure superimposed on the regrown holes. The red arrows in (k) indicate some of the macrosteps that are discussed in the text.

The deep rod samples in Figure 4-4 (a) - (c) have a 'pyramid-on-rod' structure with neighbouring structures being 'point-to-point'. The side facets are m-plane as a result of this being the slowest-growing non-polar plane, and therefore expanding at the expense of the faster growing non-polar a-plane plane. However, the sidewall facets are limited and the corners between them are not fully formed. With increasing growth temperature, the hexagonal shape of the rods is more well defined with sharper corners.

This is likely due to the increased adatom diffusion at higher temperatures. The top c-plane truncation is small at all growth temperatures due to the c-plane being fast growing in all cases compared to that of the semi-polar planes, leading to extinguishment of the c-plane and expansion of the semi-polar planes. Finally, the sidewall facets are almost vertical at the base of the rod, with no presence of semi-polar facets, and tapers slightly outwards as they meet the base of the pyramid.

All the shallow rod samples (Figures 4-4 (d) - (f)) have large top c-planes surrounded by semi-polar planes resulting in an 'edge-to-edge' morphology. Non-polar planes are not present due to the small aspect ratio resulting in either a rapid extinction or no initial formation of the non-polar planes. As the growth temperature increases the features appear less hexagonal, indicative of greater competition between different semi-polar facets. In addition, the semi-polar plane relative to the c-plane growth rate increases resulting in rods with an expanded c-plane and therefore large diameters. Therefore, no nanopyramids are formed. Many defects are observed that reduce in number as the growth temperature increases due to the increased adatom diffusion at higher temperatures that allows the defects to be planarised. These defects might have been initiated by the dry-etching step or from pre-existing dislocation pits.

Figure 4-4 shows the effect of temperature on the deep (g) - (i) and the shallow (j) - (l) hole samples. Both sets show improving regularity of the features with increasing temperature. At the lower temperatures, for the deep hole templates in Figure 4-4 (g)-(h), irregular facets are formed on the semi-polar planes, whereas for the shallow hole templates, an unusual morphology is observed for the lowest temperature in Figure 4-4 (j) due to semi-polar facet competition, and a 'star like' growth for a mid-range temperature in Figure 4-4 (k) as a result of growth upon the central c-plane of the hole.

If one looks at the outer contrast of each hole, showing the intersections between the semi-polar sidewalls and the top-c-plane, it can be seen that all of the deep hole samples and all of the shallow hole samples, except for the one at the lowest temperature, exhibit edge-to-edge morphology. This indicates the presence of semi-polar a-planes ($\{11\bar{2}i\}$), in stark contrast to the m-plane faceted holes after etching. Indeed, the

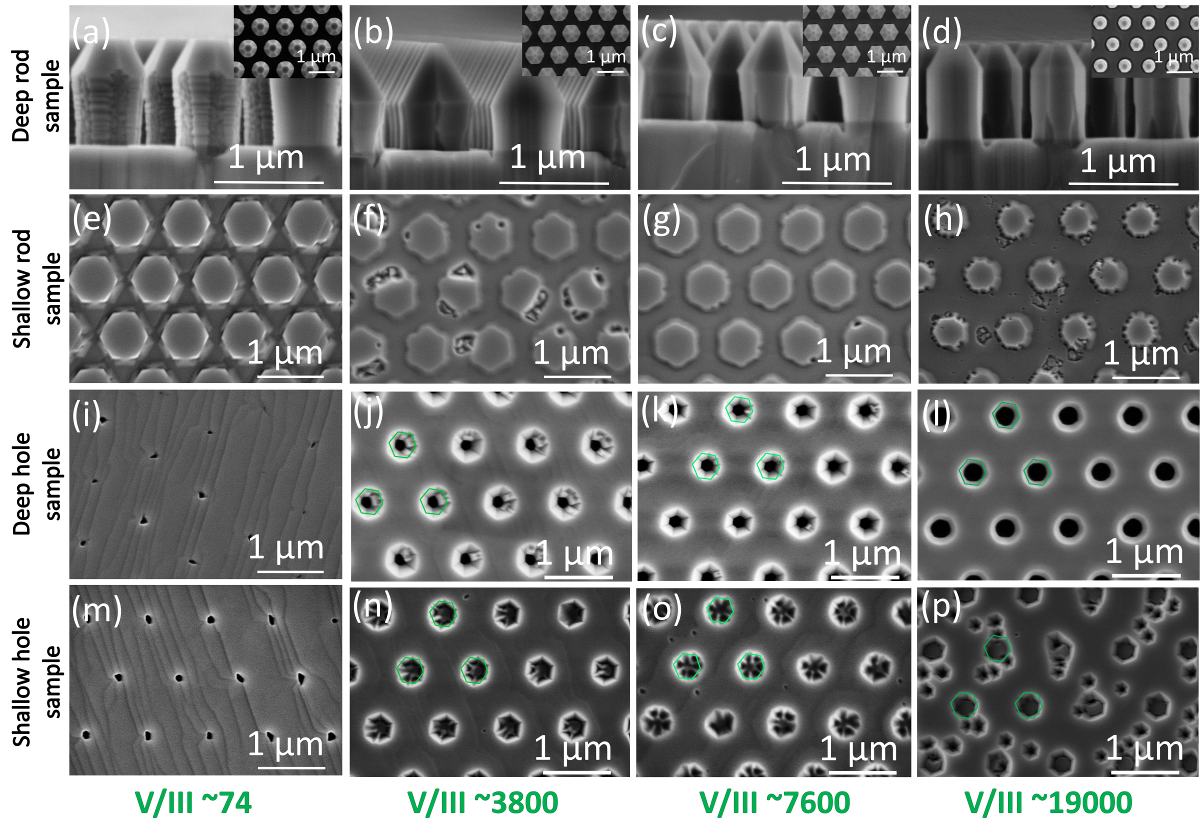

Figure 4-5: SEM images of the four structures grown with different V/III ratios. The green hexagons in (j) - (l) and (n) - (p) represent the original morphology of the dry etched structure superimposed on the regrown holes.

unusual morphologies at low temperature might result from the transition between the m-plane facets ($\{10\bar{1}0\}$) of the dry etch templates to the semi-polar a-planes after regrowth. In contrast, if one looks at the inner contrast of each deep hole sample, the central voids are larger at a higher growth temperature and less hexagonal, indicating less growth and a less dominant non-polar plane.

Macrostep features are visible on the c-plane which appear to bend around both hole samples and appear to bend less at higher growth temperatures.

4.5.2 The effect of V/III ratio

Figure 4-5 depicts the impact of the V/III ratio on the regrowth of AlN for all four types of templates. Four different V/III ratios were chosen ranging from a very low value of ~ 74 to a very high value of ~ 19000 (see Table 4.1, growth runs 4, 2, 5, 6).

Figure 4-5 (a) shows that at very low V/III ratio no smooth non-polar planes are formed on the deep rods. It is likely that rapid extinction, and no real expansion of the non-polar planes gives rise to this very undulating, rough sidewall rather than a smooth non-polar facet. The presence of a large top c-plane is due to the growth of the c-plane being considerably slower than the semi-polar planes with these conditions therefore leading to the expansion of the top c-plane.

As the V/III ratio increases, the non-polar planes form and intersect each other more closely, with the height of the non-polar planes increasing, Figures 4-5 (b) - (d). The tendency for higher non-polar sidewalls and sharper intersections suggests that the relative speed of the m-plane growth decreases as the V/III ratio increases; thus extinguishing any residual a-planes via expansion of the m-plane. The diameter of the top c-plane also increases from Figures 4-5 (b) - (d) indicating that the relative speed of the semi-polar planes increases. This then leads to the semi-polar planes expanding at the expense of the top c-plane less. For the highest V/III ratio, the inset in Figure 4-5 (d) shows a much smaller increase in rod diameter due to a significantly reduced non-polar growth rate.

By examining the height of the nanorods after growth, it can be seen that the nanorods reduce in height with increasing V/III ratio. As the nanorod height is found to be equal or lower than the initial 1 µm tall dry etched nanorod, the c-plane growth rate at the bottom c-plane, in between the rods, is equal or higher than the one on the top nanorod c-plane (see Appendix 1 for more details regarding estimates of the c-plane growth rates at two different V/III ratios). The reason for this is unclear, but the effect of the slower top-nanorod c-plane growth rate is to limit the reduction in lateral size of the c-plane facet on top of the nanorod for the high V/III ratios. This effectively means that the semi-polar planes therefore expand less to the expense of this top c-plane for the higher V/III ratios.

Growth with a very low V/III ratio on shallow rods (Figure 4-5 (e)) gives rise to well-defined 'point-to-point' structures in contrast to all other samples ((f) - (h)). No inclined semi-polar planes are observed, with the structure being defined by slow-growing m-planes; slower than the non-polar a-plane or other semi-polar planes. The lack of semi-polar planes at V/III $\sim$ 74 is also observed in the nanohole samples.

As the V/III ratio increases (Figure 4-5 (f)-(g)), the shallow rods change from being 'point-to-point' to 'edge-to-edge' with the sidewalls switching from non-polar m-planes to semi-polar a-planes. At very high V/III ratio ($\sim$ 19000) (Figure 4-5 (h)) the rods appear multifaceted with a mixture of 'point-to-point' and 'edge-to-edge' morphology.

Given that, like for the deep rods, they also exhibit a smaller diameter, it is likely that the lack of growth has prevented the structure finding more of an equilibrium and uniform shape.

Turning to the hole samples, no semi-polar planes are formed for either shallow or deep holes at the lowest V/III ratio (Figure 4-5 (i) and (m)), leading to rapid planarisation of the hole array and the likely generation of subsurface voids. For higher V/III ratios, the semi-polar *a*-planes appear along with either other irregular facets in the deep hole samples that reduce when the V/III ratio increases from $\sim$ 3800 to $\sim$ 7600, or star-like features in the shallow hole samples originating from the competition with the central *c*-plane of the hole.

At a very high V/III ratio of $\sim$ 19000 the deep holes (Figure 4-5 (l)) are very circular due to facet competition and an overall lack of growth; also observed in the shallow hole sample (Figure 4-5 (p)).

Macrosteps dominate the images of the hole samples at a very low V/III ratio with the height of the steps decreasing with increasing V/III ratio with none being visible in Figure 4-5 (l) and (p). This is due to the increase in nitrogen atoms on the surface reducing Al-adatom diffusion resulting in shallower steps [306]. Furthermore, in both Figures 4-5 (i) and (m) the remaining holes appear to act as sinks for macrosteps, whereby they bend towards and terminate at these nanoholes. This differs from all other growth conditions, both in Figure 4-4 and 4-5 where the macrosteps bend around the holes, likely due to the semi-polar planes that are also present. This 'sink like' behaviour in (i) and (m) is a result of macrostep pinning caused by the presence of the remaining holes within what is predominately a 2D *c*-plane growth regime, under these conditions.

In an attempt to identify the specific semi-polar planes in the hole samples, their angles were extracted from the AFM scans as shown and detailed in Appendix 1. It was found that, for the deep hole samples, at V/III ratios of $\sim$ 3800 and $\sim$ 7600 and the shallow holes at V/III ratios of $\sim$ 3800 and $\sim$ 19000, the planes were oriented around 58-62° to the horizontal. Combining this with the knowledge of the orientation of the sample and the 'edge-to-edge' morphology leads to the likelihood of these being $\{11\bar{2}2\}$ facets. At a V/III ratio of $\sim$ 19000 for the deep holes and $\sim$ 7600 for the shallow holes the facets are not well defined.

To summarise the results from these growth studies with respect to the original aim of creating suitable sites for quantum dots, it was found that the deep nanorod sample with a V/III ratio of $\sim$ 7600 provided a well-faceted structure along with a small

c-plane truncation. Moreover, the deep hole sample under the same growth conditions was also the most promising, with minimal undesirable faceting on the semi-polar planes. Therefore, these conditions were chosen as a starting point for studies of the growth time.

4.5.3 The effect of the increase in growth time

Figure 4-6 displays the effect of increasing the growth time for the four types of templates (see Table 4.1 runs 5, 7 ,8 ,9). For the deep rod samples in Figures 4-6 (a) - (d)), increasingly sharp apices at the peaks of the pyramidal regions are formed with increasing growth time. The tilted SEM image in Figure 4-7 from a system capable of higher resolution shows the sharpness more strikingly along with the considerable lateral expansion of the deep rod sample under prolonged growth time that results in rod coalescence.

An overhang is observed at the base of the nanopyramid that is much more pronounced in Figures 4-6 (c) and (d), after the apex is fully formed. The overhang arises due to preferential incorporation of material around this convex region of the rod (see Section 4.6). More material arrives at the pyramidal section compared to the sidewalls of the rod, but the slow growth rate of the semi-polar planes leads to adatom diffusion to neighbouring planes. Once the c-plane is extinguished, the overhang region is the only sink region for these adatoms; hence the rapid increase in its size. This effect is compounded by restricted gas diffusion to the base of the rod caused by the presence of the large semi-polar planes.

The shallow rods show increasing planarisation and one would expect that further prolonged growth would lead to coalescence. The rods exhibit an 'edge-to-edge' morphology with increased growth time, indicative of much faster semi-polar plane growth compared to that of c-plane [288]. This then leads to the expansion of the top c-plane facet. The fast growing semi-polar a-plane contrasts with the very slow growing semi-polar m-planes forming the nanopyramids for the deep rod structures, and is due to them having a *concave* rather than a *convex* growth nature. This results in the fastest growing planes dominating the rod sidewall morphology, leading to a lateral expansion of the rods.

For the deep hole samples, the semi-polar facets increase in size as the growth time is increased (see Figures 4-6 (i) - (l)) due to its slow growth rate (and therefore expansion) compared with that of the c-plane. The nanopyramidal pits in Figure 4-6 (j) are close

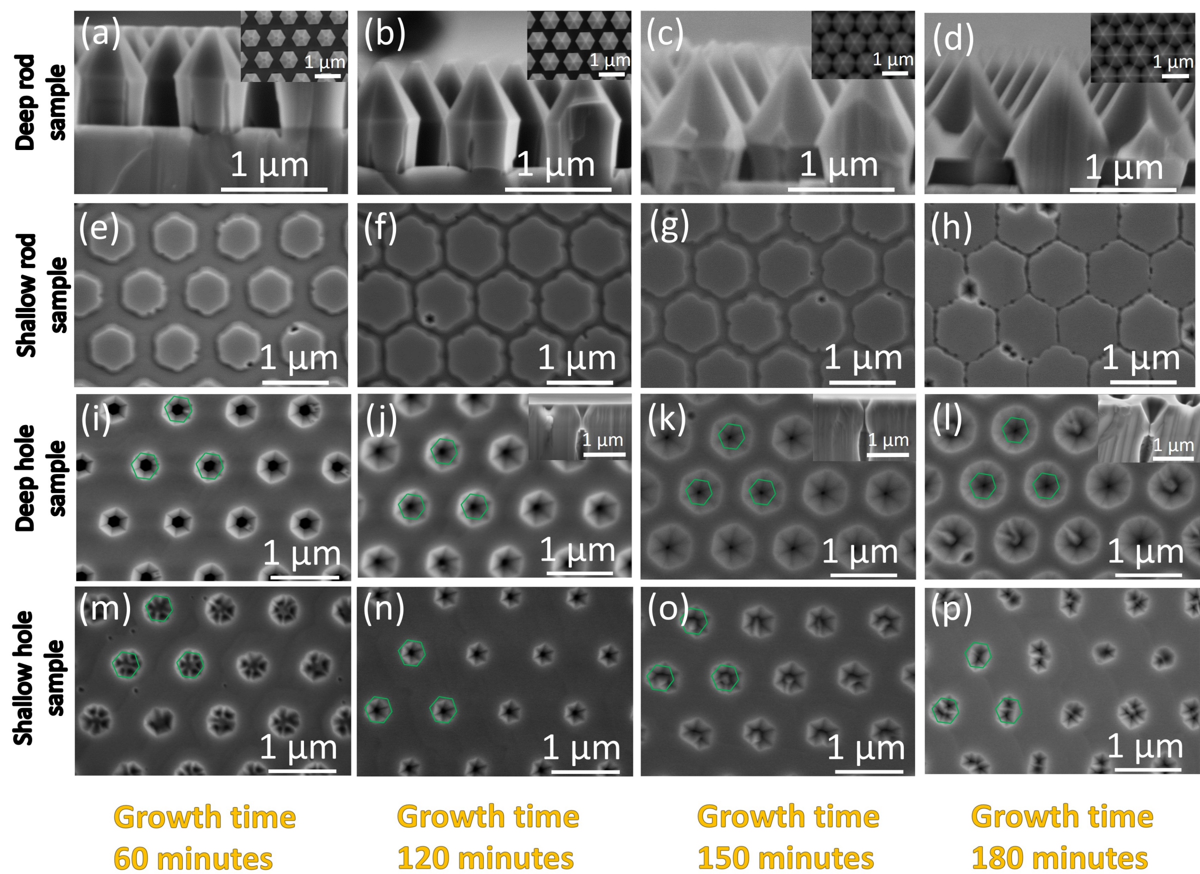

Figure 4-6: SEM images corresponding to the growth on the four structures for different regrowth times. The green hexagons in (i)-(p) represent the original morphology of the dry etched structure superimposed on the regrown holes.

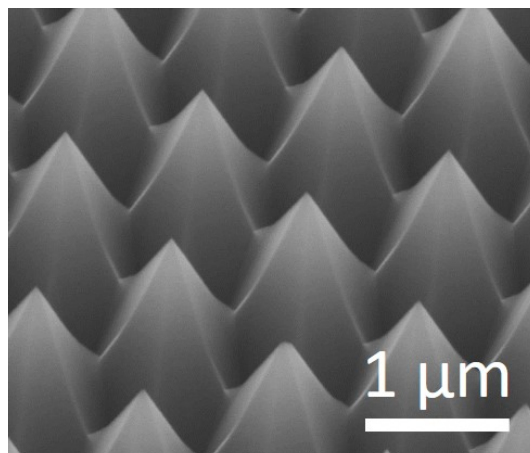

Figure 4-7: High resolution tilted SEM image of the sample from growth run 9 (sample in Figure 4-6 (d)). This SEM data was taken by Dr Pavlos Bozinakis, University of Strathclyde

to coalescing with only one family of 6 facets present. With further growth, the holes are found to never fully coalesce (see insets of Figure 4-6 (j) - (l)) and a second family of facets are visible that compete with each other once this local equilibrium shape has been reached (Figure 4-6 (l)). Irregular facets also appear for the highest growth times (Figure 4-6 (l)).

Figure 4-6 (m) - (p) shows the effect of prolonged growth on the shallow holes. After 120 and 150 min the structures themselves appear to shrink in size. At 120 min growth they have well-defined 'edge-to-edge' facets with minimal competition. However, after a growth time of 150 - 180 min, ridges (or joins) appear to form within the holes leading to an irregular morphology without a well defined hexagonal shape and sometimes elongated in seemingly arbitrary directions. The latter is due to anisotropic planarisation of the hole, on the way to full coalescence and planarisation.

4.6 Discussion of Growth Mechanisms

This section describes the mechanism for how the morphology of each template influences the form of the final structure independently of the growth parameters. Whilst this morphology is the major determining factor, the growth parameters primarily influence the final structure through modifications of the relative growth rates of different planes.

Figure 4-8 shows schematics of the different samples highlighting various critical points and whether they have a convex or concave shape. An important note is that this shape determines whether the equilibrium morphology is determined by the slowest- or fastest-growing crystal facets. However, points on the surface can be characterised by their shape in two dimensions, leading to situations where it is convex along one line (blue arrow in Figure 4-8), and concave along its perpendicular (yellow arrow in Figure 4-8), corresponding to a saddle point. This is in addition to the cases where it is convex or concave in both directions, referred to as double-convex or double-concave in the following descriptions, or indeed where it is flat in one or two dimensions. This convex-concave or double convex (concave) morphological nature then determines the shape of towards which the structure grows, as presented in the model described in [263]. Although in [263] this is considered for GaN SAG structures this can also be applied to our AlN top-down bottom-up nanostructures.

In the deep rod sample (Figure 4-8a) a double-convex base of a semi-polar pyramid forms in the upper region of the rod. Due to the reduced number of bonding sites being

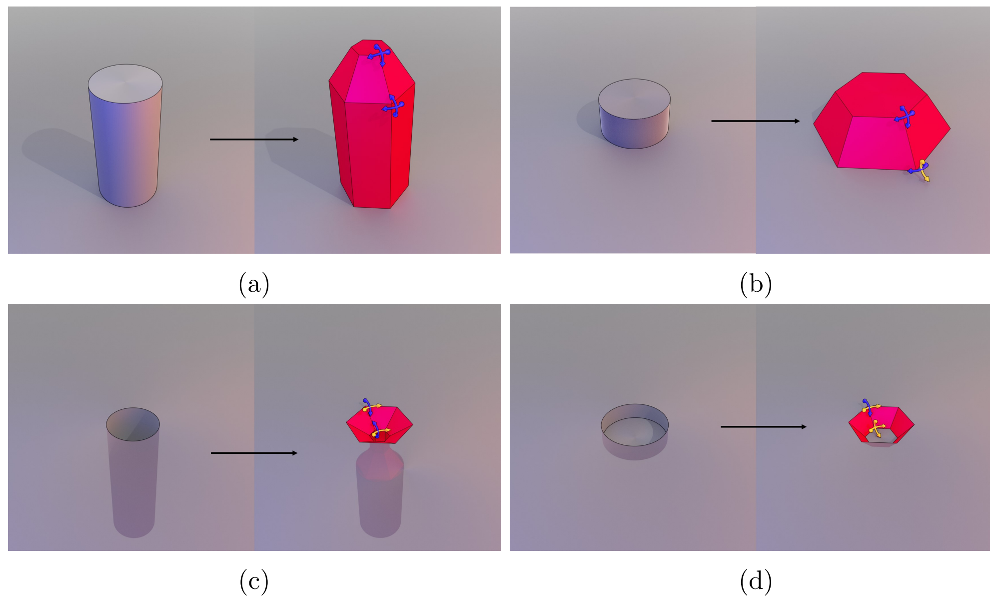

Figure 4-8: Schematic representation of the convex and concave nature of all four structures. The images on the left are before regrowth and the images on the right after regrowth. The deep rod, shallow rod, deep hole and shallow hole structures are shown in (a), (b), (c) and (d) respectively. Blue arrows indicate convex morphology whereas yellow arrows indicate concave morphology. This figure was made by Dr Pierre Chausse for the publication [49].

available at this corner it is more costly for adatoms to bind here. Thus this region is slower growing than other regions and leads to the slow-growing semi-polar planes expanding and dominating the rod structure after prolonged growth times. This manifests itself with a visible overhang and an increase of the size of the semi-polar planes relative to other plane geometries, also leading to the top c-plane being extinguished.

In the shallow rod sample (Figure 4-8b), the base of the rods has a concave morphology in one direction so that there are more bonding sites available than in other regions. This results in a more rapid growth of the semi-polar planes leading to no formation of any non-polar planes and the fast-growing semi-polar planes dictating the final morphology of the structure. In the absence of the non-polar planes, prolonged growth results in lateral expansion of the rods. This also results in an expansion of the top c-plane as it is slower growing relative to the semi-polar planes resulting in an almost coalesced layer after the longest growth time, despite the top of the rods having double convex morphology.

Also of note is that these structures have 'wavy' edges. This is likely due to the impact of the irregular dry etch trench on this critical convex-concave region which is driving the speed of the semi-polar growth.

In the deep hole samples (Figure 4-8c) the intersections of the planes are mostly convex in nature, with concave regions between families of semi-polar planes and between families of non-polar planes. The concave nature leads to the formation of the faster-growing semi-polar and non-polar a-plane facets. However, the growth rate of these semi-polar planes is still slow enough for the semi-polar planes to continue to expand, at the expense of the faster growing c-plane between the holes.

The shallow hole structures (Figure 4-8d) have an additional c-plane within the hole upon which growth can occur. The gives a double-concave morphology at the base of the holes causing rapid growth on the semi-polar planes as with the shallow rods. In this case, the top c-plane surrounding the hole structures is slower growing than these semi-polar planes, causing the c-plane to expand laterally as growth time increases, reducing the size of the hole structures.

It has been found that the aspect ratio of the holes or rods has a key role in determining whether convex or concave growth occurs and this has a profound impact on the morphology of the structures. This is especially visible after prolonged growth. It also has a knock on effect on whether the top c-planes between (holes) or upon (rods) the structures expand or contract.

4.7 Optimisation of AlN nanostructures for applications

The introduction described two possible applications for the use of regular arrays of faceted AlN nanostructures: as sites for the creation of quantum dots, and for core-shell UVC emitters. For quantum dots, one requires features on the order of nanometres, commensurate with the excitonic Bohr radius of these materials of $\sim$ 1.5 nm [307]. The sharp, high-quality, uniform rod apices of the deep rod samples are ideal as sites to house such structures. For core-shell UVC architectures, large, high-quality non- and semi-polar facets for active region growth is desirable to harness the reduced intrinsic QCSE of such devices [209]. Thus a desirable structure would have access to these facets for active region growth and an example of this is a well faceted non-polar rod sidewall.

The small sharp apices of the deep rod samples in Figures 4-6 (c) and (d) are promising as sites for GaN or AlGaN quantum dot growth (see Figure 4-10). However, the rods are coalesced which is undesirable as there may be preferential incorporation of material at these coalesced regions. The coalescence also prevents non-polar sidewalls being available for the growth of non-polar quantum well structures for DUV devices. One solution would be to fabricate rods at a larger pitch to avoid coalescence. Another would be to utilise a higher V/III ratio during prolonged growth, and such an experiment is shown in Figure 4-9.

After prolonged growth (Figure 4-9 (c) - (e)) the sidewall facets fully meet each other all the way down the rod, since the non-polar m-plane growth is considerably slower than that of the a-plane. In addition, as the growth time increases (see Figure 4-9 (e)) the size of the apices becomes very small, beyond the resolution limit of our SEM (see Figure 4-10). Crucially, even after 270 minutes growth, coalescence between rods has not occurred due to the very slow growing m-planes.

In contrast, the deep hole samples are unsuitable for creating sites for quantum dots, for example within the apex of an inverted pyramid, without further optimisation and fine-tuning, as coalescence is never observed. It appears that the persistent, remaining channel at the centre of the holes is evidence of the self-limited growth nature of these deep etched structures. Furthermore, the shallow hole samples are also not promising due to the irregular bridging and joining within the holes after a prolonged growth time (Figure 4-6). However, after optimisation of the dry etch depth of these nanohole structures it may be feasible to achieve fully-formed, well-faceted, inverse pyramid structures. Nevertheless, there is potential for the deep hole and deep rod samples to be utilised for the growth of quantum well structures on the non-polar or semi-polar

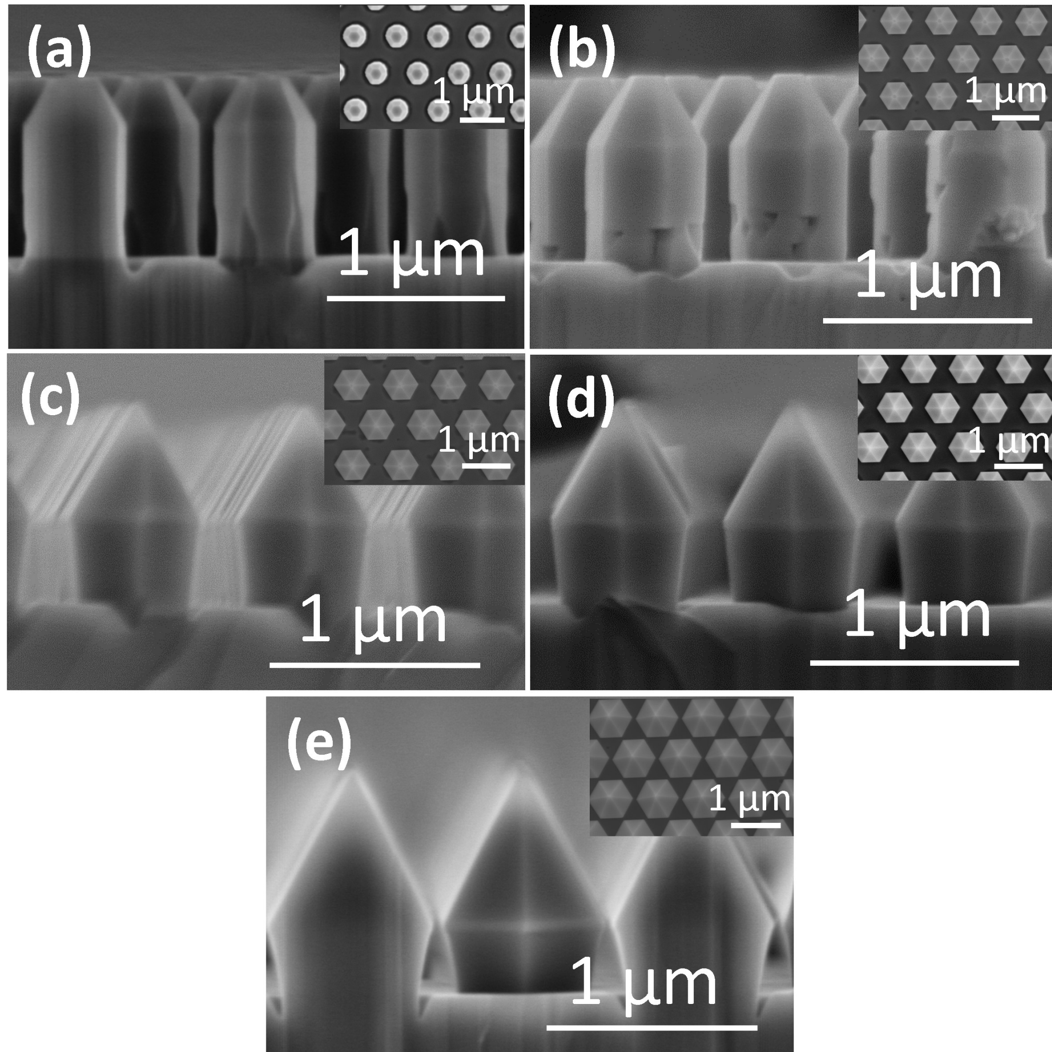

Figure 4-9: SEM images showing the morphology after different growth durations for the deep nanorod samples at a V/III ratio of $\sim$ 19000. (a) 60 min, (b) 120 min, (c) 180 min, (d) 210 min, (e) 270 min.

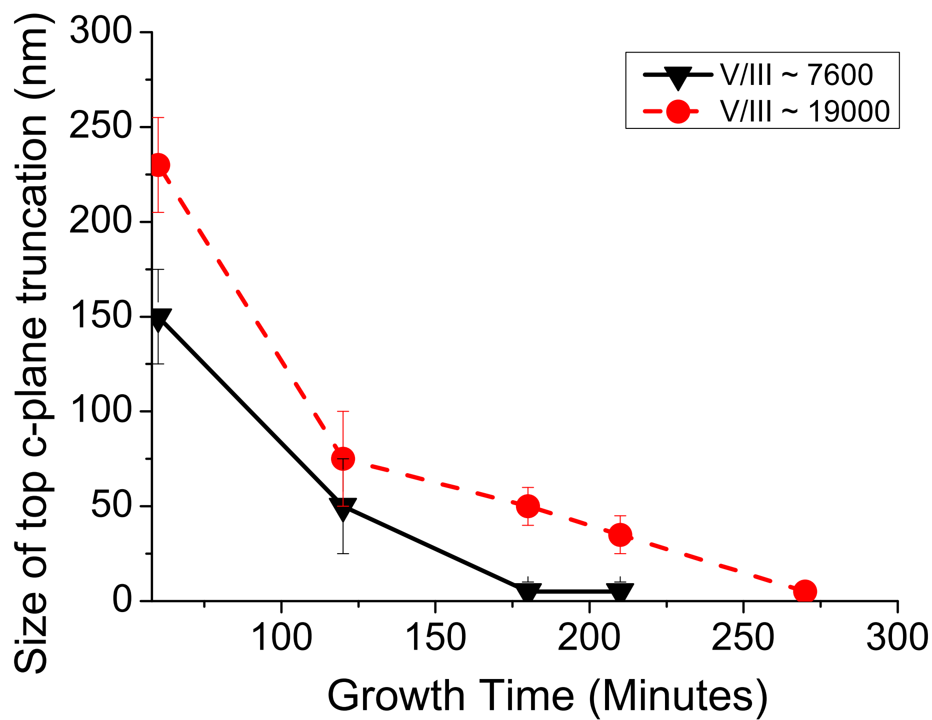

Figure 4-10: Plot of the size of the top c-plane truncations as a function of rod growth time for the rods grown at V/III $\sim$ 7600 and $\sim$ 19000. The truncation sizes were extracted from SEM images using ImageJ with estimates of the measurement errors.

planes for optoelectronic applications in order to take advantage of a reduced quantum confined Stark effect.

4.8 Conclusions

In conclusion, a detailed study of the growth conditions upon the regrowth of AlN nanostructures has been undertaken. The V/III ratio has been found to be more influential than growth temperature on the morphological regrowth of all of the nanostructures investigated. The prolonged growth at a V/III ratio of ~ 19000 realised sharp apices at the tips of the nanorods, suitable for the site-control of quantum dots, with the absence of rod coalescence. In addition, well-formed side-walls in the same samples show promise for their potential use in quantum well core-shell structures.

The deep hole samples appear to be self-limited with a hole always remaining at the centre of the structure. Both deep and shallow hole samples start to exhibit misoriented, competitive growth from the centre of the structures, demonstrating that it is difficult to form nanopyramidal pit structures without facet competition for a wide range of growth conditions.

Overall, we have shown that the hybrid top-down, bottom-up approach has been successful for the realisation of uniform, well faceted AlN nanostructures. This approach shows promise for obtaining previously unattainable devices to be realised with this material.

4.9 Final comments

The results in this chapter present purely AlN nanostructures suitable to house GaN quantum dots, at the sharp apices have been realised. Attempted growth of GaN quantum dots upon such nanostructures is presented in Chapter 7. The next chapter, Chapter 5, presents another route for the creation of AlN nanostructures via a purely subtractive, wet etched based, process to create AlN nanostructures, avoiding the AlN regrowth step. This represents an alternative route for the creation of purely AlN sites to house GaN quantum dots.

Chapter 5

Wet etching of AlN to realise sites for quantum dots

5.1 Introduction

It is important to develop a number of different methods to create purely AlN sites to house GaN quantum dots. The advantages of purely AlN nanostructures to house GaN quantum dots were presented in previous chapters. Whilst the top-down bottom-up process certainly shows promise for the creation of periodic arrays of AlN nanostructures suitable for housing quantum dots, there are still some issues with this approach. For example, regrowth step upon a dry etched nanorod can lead to the incorporation of a large number of defects in the regrown material. Thus, this may then hinder the detection of any optical signature of a quantum dot. Wet etching of nanostructures could be an alternative route for the creation of nanostructures with sharp features to house quantum dots without introducing additional defects. This chapter investigates the attempted creation of periodic arrays of AlN nanostructures via wet etching, with the aim of creating features suitable to house quantum dots.

5.2 Introduction to wet etching

Etching can be defined as the removal of unwanted material. One form it can take is dry etching, which usually employs plasma based processes to generate reactive species that allows for anisotropic material removal via the use of patterned a hard mask, as has been describe in Chapter 2 . Alternatively, wet etching is a process where chemicals

are used (usually acids or bases), in order to remove material via chemical reactions [308]. Etching can occur selectively. This is where unwanted material is removed at a different, preferably higher, rate to that of the desired material. This is possible due to different chemical reactivity of the unwanted and desired material. An example of selectively is the preferential etching of certain crystal planes. Liquid etchants will etch crystalline materials at different rates depending on which crystal face is exposed to the etchant [308].

Comparing wet etching to dry etching, the former has the advantages of a high etch selectivity, lack of damage incurred by the etch and high throughput. However, dry etching has the advantages that it, typically, can be much more anisotropic than wet etching, although wet etching of crystalline structures can also display anisotropy. Dry etching also typically allows for much better fine-pattern definition and better process control [308]. However, the surface and near-surface damage caused by utilising dry etching can cause significant impairment to a potential device [309] and indeed the electrical and optical properties of a material [310]. In addition, whilst local defects of the hard mask will be transferred in dry etching this is not the case in wet etching, if an etch mask is not being used.

The processes of wet etching typically involves the transportation of reactive ions to the etching target from the bulk etchant solution via diffusion. These ions then chemically react with the target material. The reaction products then dissolve and diffuse from the etched material into the bulk solution [308]. In most cases, the critical parameters to control in order to manipulate the etching process, are etchant concentration, etch time, etch temperature, and the agitation method employed [308]. Wet etching specific to the III-N's will now be discussed in more detail.

5.2.1 Introduction to the principle of wet etching of AlN

The III-N's have excellent chemical stability leading to them being robust and resistant to most forms of wet etching. However, these materials can be wet etched by potassium hydroxide (KOH) based aqueous solutions, molten KOH, hot phosphoric acid (H_3PO_4) and a potassium hydroxide/sodium hydroxide (KOH/NaOH) eutectic alloy [168].

Technically, the etching mechanism of III-N's typically involves oxidation of the semiconductor surface followed by subsequent dissolution of the oxides [168]. The polarity of the III-N material (either N-polar or group III-polar) has a huge bearing on the reactivity of these semiconductors to etching. N-polar surfaces have been reported to

have 900 and 20 times higher etch rates compared to group III-polar surfaces for AlN and GaN, respectively [53]. A model for this polarity dependent KOH based etching of GaN is presented in [50] (see Figure 5-1 (a) - (d)). Here, Li et al, propose that in Ga-polar GaN, once the Ga layer is removed, N-termination of the surface results. The hydroxide ions cannot attack this N-terminated surface easily as there are three occupied nitrogen dangling bonds that strongly repel the hydroxide ions. It is likely that this is why the +c polar surface (Ga-polar) is resistant to KOH etching, comparatively, the -c (N-polar) surface etches readily [53]. This is likely due to the fact that there is only a single dangling nitrogen bond in the upward direction, leading to much less repulsion of the hydroxide ions (see Figure 5-1 (a)). The hydroxide ions can then attack the back bonds of the Ga atoms (Figure 5-1 (b)). The hydroxide ions react with the GaN forming gallium oxide and ammonia [53].

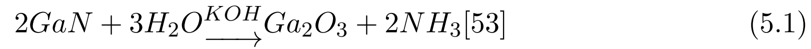

$$2GaN + 3H_2O \xrightarrow{KOH} Ga_2O_3 + 2NH_3[53] \tag{5.1}$$

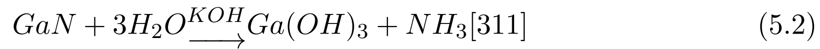

$$GaN + 3H_2O \xrightarrow{KOH} Ga(OH)_3 + NH_3[311] \tag{5.2}$$

The KOH acts like a catalyst. Once the gallium oxide is formed, it dissolves into the KOH solution. The first layers of the Ga atoms would be removed as shown in Figures 5-1 (a) - (c) and then as shown in (d) the resulting surface structure is again the same as that shown in (a) [53]. For a Ga-terminated surface this process would start at Figure 5-1 (c) [53]. The effect of polarity on etching readiness can be seen in Figure 5-1 (e) where N-polar GaN strips are heavily etched by KOH and the adjacent Ga-polar stripes are left visibly unaffected.

This model for GaN can also be similarly applied to AlN. AlN is also thought to be oxidised via being catalysed with KOH. The resultant oxide is then dissolved by the KOH solution.

$$2AlN + 3H_2O \xrightarrow{KOH} Al_2O_3 + 2NH_3[311] \tag{5.3}$$

$$AlN + 3H_2O \xrightarrow{KOH} Al(OH)_3 + NH_3[311] \tag{5.4}$$

Wet etching can also be used as a tool for defect density determination. This is as defective sites, such as threading dislocations, can be more easily attacked by KOH

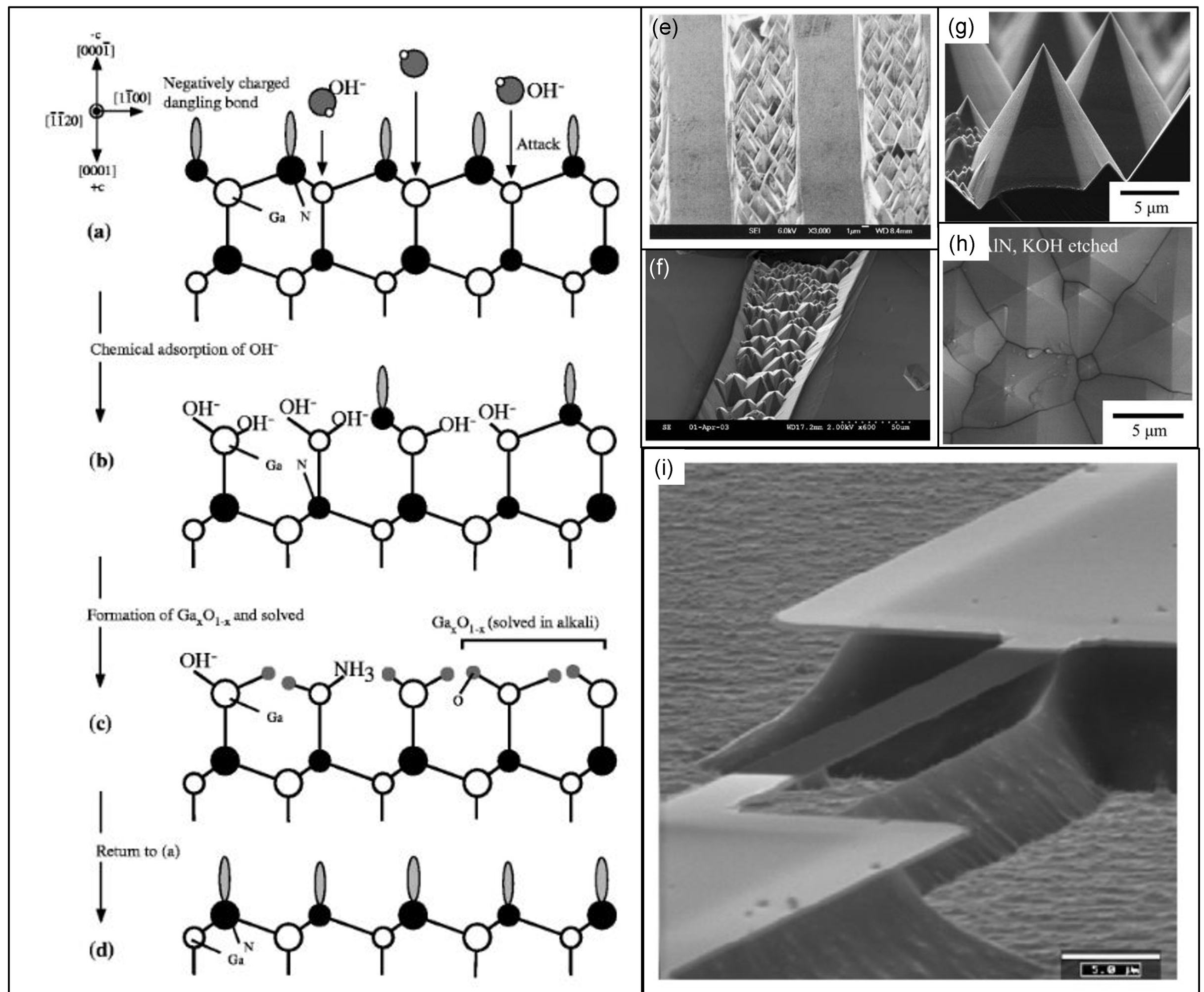

Figure 5-1: Figure (a) – (d) shows the etching mechanism for GaN in KOH. Reprinted from [50], with the permission of AIP Publishing, Copyright © 2001. Figure (e) shows an SEM image of a GaN sample where the N-polar regions have etched to form hexagonal nanopyrmaids and the Ga-polar regions have been left intact. Reprinted from [51], with the permission of AIP Publishing, Copyright © 2003. Figure (f) shows N-polar AlN after aqueous KOH etching. Reprinted from [52] Copyright © (2004), with permission from Elsevier. Figure (g) shows an SEM cross-section of hillocks on N-polar AlN after KOH etching. Figure (h) shows an SEM micrograph of N-polar AlN etched in KOH. Figures (g) and (h) reprinted from [53], Copyright © (2013), with permission from Elsevier. Figure (i) shows an NEMS resonator structure, where the freestanding AlN beam was prepared via KOH etching. Reproduced from [54]. Copyright © 2006 WILEY-VCH Verlag GmbH & Co. KGaA, Weinheim.

compared to non-defective sites. Specifically, wet etching of III-polar GaN or AlN surfaces can be used to preferentially etch hexagonal pits into the sample surface. These pits are spatially located at defect sites, such as threading dislocations [168].

Additionally, as weakened or defective bonds are more susceptible to etchant attack, material quality has a significant impact on the etch rate of the material [312]. For instance, Vartuli et al. [313], found that the etch rate of sputtered AlN in KOH decreased with increasing annealing temperature. This is a consequence of improvement in material quality. Similarly, Cimalla et al. [54] found that etch rate was a function of crystal quality, with sputtered AlN etching much more quickly than MBE or MOVPE grown AlN. Cimalla et al. also reported that etch rate of AlN is also strongly dependent on etch temperature, with a higher etch rate at higher etch temperature [54].

5.2.2 Wet etching of AlN – what has been realised before in the literature

Shown in Figures 5-1 (f) - (i), are some previous results in the literature concerning the wet etching of AlN. As can be seen in (f) - (h), sharp hexagonal nanopyramidal features can be realised when etching N-polar AlN in KOH. The disadvantage of the results here is that these pyramids are not uniform in height or total structure diameter and occur without any spatial determinability.

Wet etching has also been demonstrated to be able to realise complex structures that can be used for device applications. In Figure 5-1 (i), a NEMS resonator with a free-standing AlN beam was realised via wet etching. Additionally, wet etching can be combined with an initial dry etching step such as the work in [314]. Here an initial dry etch is used to create a fin, which is at an angle of 70°, which is then subsequently wet etched to obtain a vertical sidewall [314]. The wet etch would also likely remove surface damage which could impair device performance. This demonstrates how dry and wet etching can be combined to realised micro/nano features which may be difficult to realise by utilising only one of the etching techniques.

5.2.3 Gaps in the current knowledge of AlN wet etching

Wet etching of AlN could be used to create complex arrays of AlN nanostructures. Etching of large arrays of spatially predetermined AlN nanostructures has been largely unexplored. Such structures, with geometries previously not investigated, could house

active regions. Due to the possibly novel geometries revealed by wet etching this could lead to the growth of active regions with different properties to those currently in the literature. An interesting area of exploration would be to spatially selectively etch AlN via wet etching through patterned a mask. Additionally, combining dry and wet etching to create complex AlN nanostructures would also be an interesting area of investigation. This may allow one to access more exotic geometries than those available from simply wet etching planar AlN. Moreover, it may be possible to create sharp features, small enough to house site-controlled quantum dots. There have been no reports yet of utilising wet etching based techniques to create uniform arrays of AlN sites to house quantum dots.

5.3 Wet etching of planar AlN

All the AFM performed in this chapter and the corresponding appendix (Appendix 2), was performed with a Oxford Instruments Asylum Jupiter XR. All x-y dimensions were checked for distortions along either axis, as was performed in Appendix 1. No correction of the x and y dimensions were necessary with the scans used from this AFM. High resolution silicon AFM tips (supplied from Nunano) with a tip radius of curvature of < 10 nm were used in this thesis. Other specifications of the tips include a spring constant of 42 N/m, resonant frequency of 350 kHz, cantilever dimensions of 125 µm, 30 µm and 4.5 µm for the length, width and thickness of the cantilever, respectively. The tips had a high aspect ratio with a cone angle $< 15°$ over the last 1 µm. All AFM maps were extracted and analysed via the Gwyddion software unless otherwise specified. Any SEM images that were analysed for dimensional properties were done so with the ImageJ software [57].

In Chapter 4, the creation of inverse pyramidal pits, to house quantum dots at the inverse apices, via the top-down, bottom-up approach was found to be challenging. Using selective wet etching of planar AlN through a patterned dielectric mask holds promise to realise this geometry by purely wet etching alone.

In order to attempt to create periodic AlN arrays of hexagonal pyramidal pits to house quantum dots, wet etching of planar AlN covered in a patterned SiN_x mask (~ 300 nm thick, deposited via PECVD) was performed. The mask was patterned with a hexagonal array of circular openings (1 μm pitch). Samples from the same template were etched with a KOH based solution at high temperature for different etch durations. The KOH solution was made by dissolving 30 g of solid KOH flakes into a mixture of

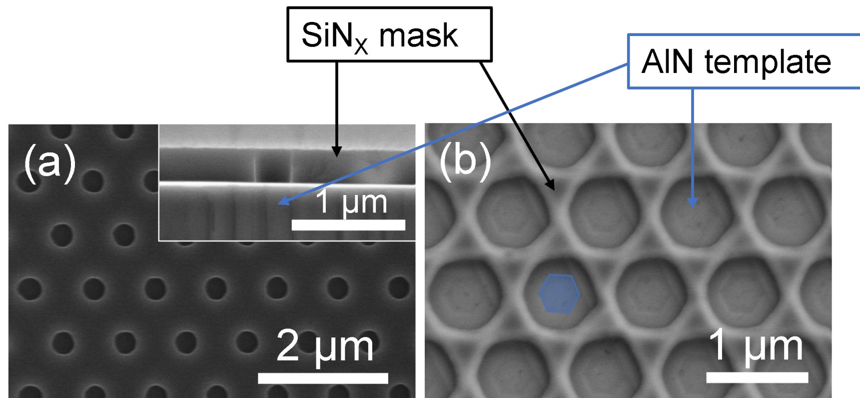

Figure 5-2: All figures here are SEM images. Figure (a) shows the planar AlN template with a patterned SiN_x mask upon it before any wet etching. The inset is the corresponding cross-section. Figure (b) shows the planar AlN template after 5 mins KOH etching at 150 ^{o}C. The blue hexagon in (b) shows the wet etched region of the planar AlN template.

30 ml of ethylene glycol and 5-10 ml of D.I. water. An ethylene based solvent was used since it has a higher evaporation temperature than water and thus would allow for higher temperature etching. The 5-10 ml of D.I water was added to aid dissolution of the KOH flakes into the ethylene glycol. A Teflon thermocouple attached to a hot plate was used, within the etchant solution, to ensure heating of the etchant accurately to the targeted temperature.

The results of etching planar AlN using a periodic SiN_x mask with circular openings is shown in Figure 5-2. In Figure 5-2 (a), the sample (with the patterned SiN_x hexagonal array mask upon it) prior to wet etching is shown. As can be seen by the cross-sectional inset, there is negligible tapering from the top of the mask to the bottom. In (b) the same sample as in (a), etched in KOH at 150 ^{o}C for 5 minutes, is presented. The aim was to use the mask to selectively etch a nanopyramidal pit into the exposed planar AlN. As can be seen from (b) only minimal etching has taken place. There is the presence of a hexagon within the opening in the mask (highlighted with a blue hexagon overlayed across one of the etched hexagons in Figure 5-2 (b)). This hexagon has a diameter roughly equivalent to the size of the diameter of the original SiN_x mask opening (see Table 8.3 in Appendix 2). This hexagon represents the total, mask selective AlN etching that has occurred. The observed lack of etching suggests that the AlN target is indeed Al-polar. Also of note is significant lateral etching of the SiN_x mask. Thus, after only a short etching time the mask would be fully removed with only minimal etching to the planar AlN. Clearly, for successful selective etching of a planar AlN layer a mask more resistant to etching is required.

After 60 minutes of etch time (data not shown), the entire AlN layer has been removed suggesting that planar AlN will etch readily under these conditions provided the etch time is long enough. It is likely once the mask etched away, defects were preferentially etched leading to pits within the AlN surface. These pits will likely have more rapidly etched laterally than the c-plane material, eventually leading to the removal of the entire AlN epilayer.

From the results shown in Figure 5-2, it appears that attempting to wet etch a planar AlN has been largely unsuccessful, especially considering the readiness of the SiN_x mask to etch away as etch time progresses. In the next section, applying wet etching to previously dry etched nanostructures is explored.

5.4 Wet etching of dry etched AlN structures

5.4.1 Wet etching of dry etched nanoholes

Another possible route to create AlN nanostructures is to perform a wet etch upon dry etched nanostructures. The motivation of this avenue of exploration is that dry etching could reveal less stable planes to wet etching, potentially impacting the morphology of the structures after wet etching. This may allow for the creation of complex nanostructures with sharp features to house quantum dots. Additionally, it could avoid one relying on the robustness of the dielectric mask which has been found to be not particularly resistant to KOH at high temperature. Two nanostructure that can be fabricated using the same patterning and dry etching processes presented in the previous chapter are nanohole and nanorod arrays. These are the specific dry etched nanostructures explored here.

KOH wet etching was performed on three nanohole structures of similar starting diameter but with significantly different vertical etch depths. This was undertaken to investigate how hole aspect ratios affected the resulting structural morphology after wet etching. The wet etching was performed at 150 ^{o}C. The results of wet etching for 2 minutes upon these three dry-etched structures is shown in Figure 5-3.

A dry etched nanohole of depth $\sim$ 100 nm is presented in Figure 5-3 (a). In (d) the same sample is shown as that in (a) but after 2 minutes of KOH at 150 ^{o}C. A clear hexagonal structure can be seen with the formation of inclined planes and a relatively large spacing of c-plane material between the hexagonal structures.

In (b) a dry etched nanohole of $\sim$ 150 nm depth is presented with the mask remaining. In (e) the same sample is shown after 2 minutes of wet etching with KOH at 150 ^{o}C. Contrasting (e) with that of (d), what is immediately clear is that the total diameters of the structures realised after wet etching is larger. Specifically, the lengths of the inclined planes in (d) are smaller than those in (e) (Figure 5-4). Additionally, the structures extend across more of the c-plane material in-between the inclined planes. Whilst in (d) there is surrounding c-plane material around each structure, in (e) the corners of the inclined planes between each structure meet. This leaves an almost isolated top c-plane triangle in-between the structures, separated by inclined planes. This then suggests that this triangle could potentially be controlled in size depending on the dimensions of the starting dry etched structure.

The dry etch depth in (c) is dramatically deeper than that in (a) or (b) whilst the diameter is similar. The impact this has on the sample after wet etching, shown in (f),

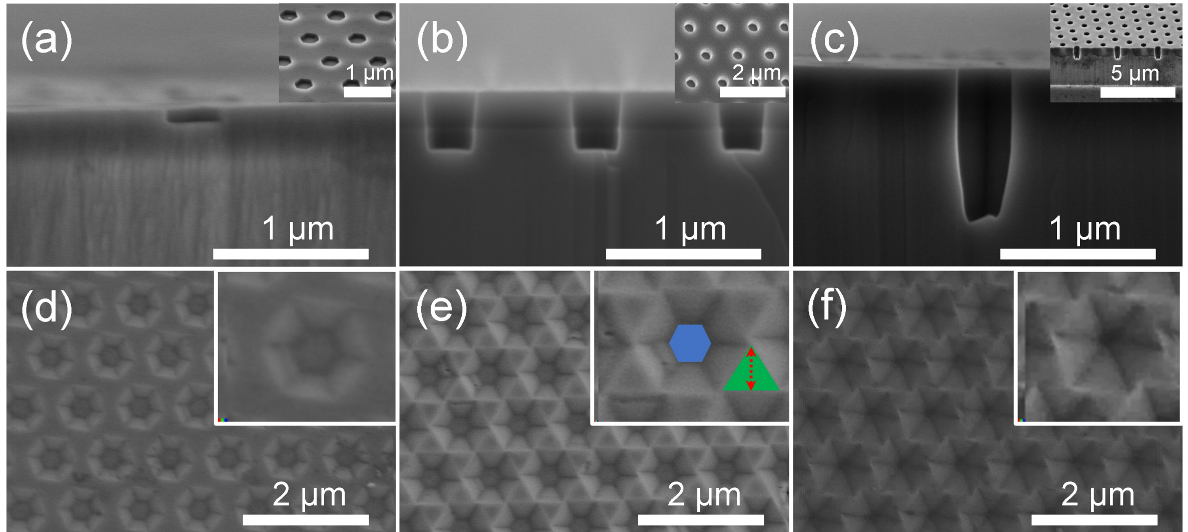

Figure 5-3: Figure (a) shows a cross-section of the shallowest dry etched nanohole sample prior to wet etching. Figure (b) shows a cross-section of a nanohole of a deeper dry etch than in (a) prior to wet etching. Figure (c) shows a cross-section of the deepest dry etched nanohole sample prior to wet etching. In (a) - (c) the inset images are tilt views of the main images. In (d) the sample in (a) is shown after 2 minutes of KOH etching at 150 ^{o}C. In (e) the sample in (b) is shown after 2 minutes of KOH etching at 150 ^{o}C. In (f) the sample in (c) is shown after 2 minutes of KOH etching at 150 ^{o}C. The insets of (d), (e) and (f) shows part of the respective main figures in at a higher magnification

*Some samples were wet etched with the SiN_x mask still in place and others with it removed. It is worth mentioning that starting with or without the SiN_x mask only makes a small impact on the etch rate of the samples. It also does not effect the morphology of the wet etched structures realised. Thus, this can be ignored.

** Figure (e) inset - The blue hexagon indicates what is referred to, in the text, as 'the bottom c-plane'. The green triangle represents what is referred to, in the text, as the 'top c-plane triangles in-between the structures'. The red arrow represents the ' altitude of the c-plane triangles'.

is rather intriguing. Firstly, the size of the bottom c-plane (see inset of Figure 5-3 (e)) is dramatically reduced compared to the samples shown in (d) or (e). This suggests that the diameter of the bottom c-plane obtained after wet etching, is largely dependent on initial vertical dry etch depth. Additionally, the triangles in-between the structures are also smaller (see inset of Figure 5-3 (e)). Thus, there is also a correlation between the initial dry etch depth and size of the c-plane material between the structures after wet etching. This is possible as corners of the structures no longer align and this leads to a reduction in the size of this c-plane triangle. The consequence of this is that this c-plane between structures may be able to be controlled and potentially reduced down to dimensions suitable to house quantum dots.

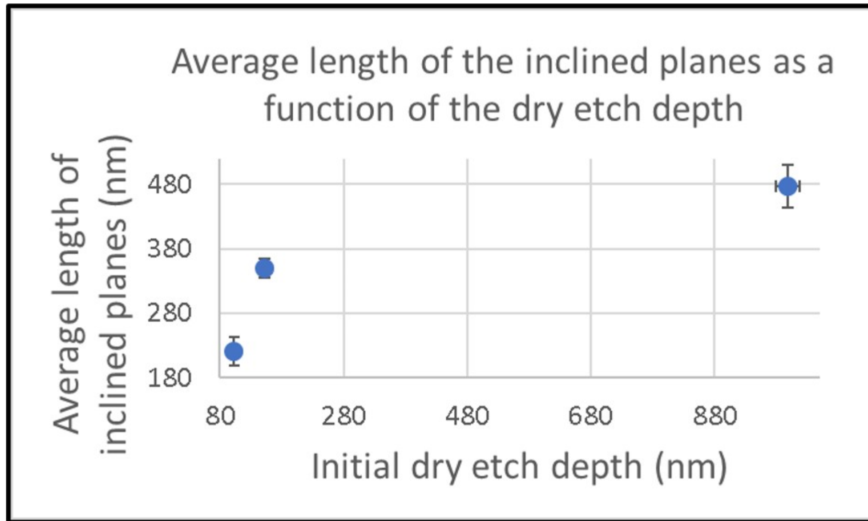

Figure 5-4: In this figure, a plot of the average length of the inclined planes as a function of initial dry etch depth is shown. The length of these planes were calculated by measuring the horizontal length of the planes and dividing this by the cosine of the average angle of the planes. The error bars in x represent the standard deviation of 10 measured values of the initial dry etch depth. The error bars in y represent the standard deviation of 10 measurements of the horizontal length of the planes.

In order to gain an insight into the nature of the inclined planes in these wet etched nanohole samples, AFM scans of all three samples (Figures 5-3 (d) - (f)) were performed, in Appendix 2, Figure 8-5 (a) - (c)). The angles of the planes were extracted along with the lengths of the planes. More details can be found in the Appendix 2. The angles of the inclined planes (data not shown) do not show any real correlation between a change in dry etch depth and change in the inclined plane angles. Hence, there does not seem to be any relation of the dry etch depth and the angle of inclined planes.

The triangle top c-plane material holds promise to house quantum dots. Hence, it was desirable to find the relation of the size of these triangles with respect to initial dry etch depth, to see if they could be tuned. The length between the triangles in between the nanohole structures were extracted from the SEM images shown in Figure 5-3. There is a correlation between the dry etch depth of the nanoholes and the altitude of the top c-plane triangles (data not shown). The deeper the initial dry etch, the shorter the altitude of the triangles (and indeed the size of the triangles as a whole). The length of the bottom c-plane was also measured from the SEM images shown in Figure 5-3 (data not shown). There is also a a correlation with increased dry etch depth and a reduction in the diameter of the bottom c-plane.

A plot of the average lengths of the inclined planes is presented in Figure 5-4. It was found that the length of the inclined planes increased with increasing initial dry etch depth. It should be noted that although estimating etch depth via dimensions shown in an SEM cross-section is unreliable, as one does not know if the cleave is directly through the centre of the hole, it can give some coarse estimate of the trend present. This is especially so when considering the stark contrast in aspect ratio's present between the features in Figures 5-3 (d) or (e) compared to (f).

In summary, the size of the bottom c-plane of these nanohole structures (in Figure 5-3) and the altitude of the top, in-between, c-plane can both be controlled by the initial starting vertical dry etch depth. Potentially, a sharp inverse apex may be realisable via increased dry etch depth or by using a tapered, but also deep, dry etch to reduce the starting bottom diameter of the holes. Additionally, a deeper dry etch may realise sharp features at the top c-plane material. Both could potentially be suitable for quantum dot sites. This was investigated and is shown in the next sub-section.

5.4.2 Study of the effect of wet etching on deliberately tapered dry etched nanoholes

By deliberately performing a deep dry etch (more than 500 nm) that heavily tapers the nanohole, it may be possible to form a sharp inverse apex. The reasoning behind this was that if the bottom c-plane was small to begin with, in addition to a deep etch, this may allow for a sharp inverse pyramid to be formed with effectively no bottom c-plane after wet etching. A number of dry etching conditions were investigated in order to try and create this structure. The dry etch parameters chosen to manipulate to achieve this tapered profile will now be discussed.

5.4.2.1 Tapered dry etching of nanoholes

The plasma based etching used here utilised a gas chemistry of 50 sccm of Cl_2 and 10 sccm of Ar. The chemical component of the etch was provided from active species formed in the plasma from the Cl_2 gas. The Ar component provided ions to enhance the dry etch process via ion bombardment in addition to contributing to the efficient decomposing and ionising the chlorine feed gas. Furthermore, Ar ions play an important role in the removal of etch by-products [231]. The three parameters investigated here in order to try and achieve a tapered dry etched hole were the dry etch pressure, the RF power and the etch temperature. Both the pressure, and particularly the RF power,

Table 5.1: Etch details of the tapered nanohole samples and the corresponding estimates of the dimensions. All etching was performed with a Cl_2/Ar gas chemistry with flow rates of 50 and 10 sccm respectively. All etching was performed at room temperature (other than the no taper sample which was etched at 150 ^{o}C). All dimension estimates were performed by measuring dimensions of cross-sectional SEM images via ImageJ.

Table of tapered nanohole samples.											
	Dry etching details					Structure Dimensions					
Sample	RF power (W)	ICP power (W)	DC Bias (V)	Pressure (mTorr)	Time (minutes:seconds)	Depth (nm)*	Top diameter (nm)*	Bottom diameter (nm)*	Tapering (nm)*	Figure
No taper	80	800	364-362	14	10:00	998	354	223	131	5-3 (c)
A	100	800	417-403	12	06:30	915	309	110	199	5-6 (a)
B	120	800	456-443	12	08:00	1362	300	27	273	5-6 (b)
C	80	800	369-354	12	07:00	890	341	131	210	5-6 (c)
E	100	800	374-354	6	04:00	989	319	177	142	5-6 (d)

*These quantities are only rough estimates. They are taken from cross-sectional SEM images, meaning that they would only be truly correct if the cleave had perfectly gone through the centre of the structures.

have an impact on the DC bias during the etch. The DC bias is important as this has a major influence on the ion energy and therefore the level of physical sputtering taking place. We were aiming to have a large amount of physical sputtering as this would help realise a tapered etch as more material would be removed at the center of the hole compared to closer to the sides. Thus, we wanted a higher DC bias during our dry etch.

A reduction in etch pressure should increase the ion energy due to the ions possessing a large mean free path. This essentially means there will be fewer collisions, which the ions take part in, which would act to reduce the ion energy, before bombarding the etch target [231]. Additionally, a reduction in etch pressure results in less off-angle ions being incident upon the etch target improving the etch anisotropy. At lower etch pressure there is an inhibition of the lateral etching of the nanoholes due to less sputtering of sidewall passivants. Oppositely, an increase in pressures leads to more off-angle ions incident on the etch target. Thus, at a higher etch pressure there will be more sputtering of etch by-products deposited on the sidewalls of the holes that act as passivation [231].

What is can be seen from Table 5.1 is that comparing recipes A with E, more tapering of the nanohole occurs at higher etch pressure. Additionally, the etch depth of E is greater than A. As in the work of Coluon et al. [231], an increase in etch pressure results in a reduction in the mean free path of the ions, meaning more ion collisions and so lower average ion energy. As the etch gas used here was Cl_2 and Ar, the Ar ions act to enhance the Cl based chemical etch. Lower ion energy therefore means less enhancement of the chemical etch by the Ar ions and thus a lower etch rate, as is observed (comparing the etch depths of sample A and E). In the work by Coulon et al. [231], a higher etch pressure was found to lead to less tapered nanorods as there are more off angle ions. This was because there were then more ions able to sputter away etch by-products on the sidewalls of the rods that would normally act to passivate these sidewalls, hindering etching, thus leading to tapering. In the case here, a higher etch pressure leads to a more tapered nanohole. A higher pressure means fewer ions will enter the nanohole and reach the bottom of the hole during the etch, especially as the nanohole gets deeper, as there are more off angle ions. This will likely mean that fewer ions will impinge near the edges of the base of the holes compared to the centre. Thus, the centre of the hole will etch more than the edge, leading to tapering. Additionally, as is revealed in column 4 of Table 5.1, the recipe in A also has a significantly larger DC bias during the etch than that of recipe E. It is know that a higher DC bias leads to higher ion energy and therefore more physical sputtering [231]. This would likely lead to more tapered nanoholes, as is observed. This is discussed in the section below in more detail with regards to the RF power.

The RF power is a critical parameter one can use to control the etch profile. An increase in the RF power would typically also lead to an increase the DC bias. A higher bias would then increase the energy of the incident ions on the etch target, due to the a greater electron charging of the electrode surface. This will contribute to the chemical etching component of the etch, as a larger ion energy would greater enhance the chemical reactions and assisting in increased bond breaking [231]. Not only would this result in a greater etch rate as a whole but the physical etching component would increase. The physical sputtering is typically highly anisotropic. This is due to both greater ion irradiance on surfaces normal to the accelerating electric field rather than inclined planes and the much lower sputtering efficiency for ions incident at glancing angles [315]. This would lead to greater etching in the centre of the hole compared to closer to the edges. Thus, when nanoholes are etched at a higher RF power this would lead to a higher DC bias and would subsequently promote tapering of the structures. In addition, an increase in etch rate would also occur. As can be seen from Table 5.1, when one compares sample B with either samples A or C, this is exactly what is

observed, in both respects.

The choice of a low temperature Cl_2/Ar based dry etch is also an important factor when trying to achieve tapered sidewalls. It was found that the tapering of GaN nanorods was heavily dependent on the dry etch temperature when utilising a Cl_2/Ar gas chemistry [315]. This can be explained based on the passivation layer mentioned earlier. At higher temperature this passivation layer can more readily be removed via evaporation combined with physical sputtering [316]. Conversely, a lower etch temperature, such as 300 K, only physical sputtering can contribute to the removal of this layer. Therefore, as the sidewalls, and indeed the edges of the exposed etch target, are bombarded by less energetic ions, and there is much less thermal evaporation, less of this layer is removed. This is additive to the fact that glancing ions have much lower sputtering efficiency. Therefore, as the physical sputtering is weak on the tapered sidewalls, the removal of the passivisation layer in this region does not occur readily. The tapered profile is protected as the etch progresses allowing for only the most energetic ions, incident closer to the centre of the etch window, to readily sputter the target material or enhance chemical etching in this region. Whilst the structures being etched here were AlN and not GaN, the results shown in the previous chapter (Chapter 4) suggest that high temperature dry etching ($\sim$ 150 ^oC) also leads to relatively straighter nanostructure profiles in AlN.

The most successfully tapered nanohole sample was recipe B, with a higher RF power than any of the other samples combined with a high etch pressure and a low, room temperature, etch temperature. One thus would expect sample B to be the most promising sample to achieve a sharp inverse apex upon wet etching. However, this was only an initial prediction based on the dry etch profile. It cannot really be assumed that this structure would render the desired, inverse nanopyramidal pit after wet etching without performing the experiment. Thus, the effects of wet etching on all 4 of the tapered holes was investigated for comparison.

5.4.2.2 Wet etching of the tapered nanoholes

One can visually see the tapering profile after dry etching of sample A (Table 5.1) in Figure 5-6 (a). There is $\sim$ 200 nm tapering (from the top to the bottom of the hole), also visible from the SEM image is that the bottom of the hole isn't particularly sharp (it is $\sim$ 220 nm in diameter). After wet etching, see Figure 5-6 (e), large six-sided hexagonal inclined planes are visible with a small c-plane at the centre of the structures. Similar to Figure 5-3 (f), the corners of the inclined planes are misaligned

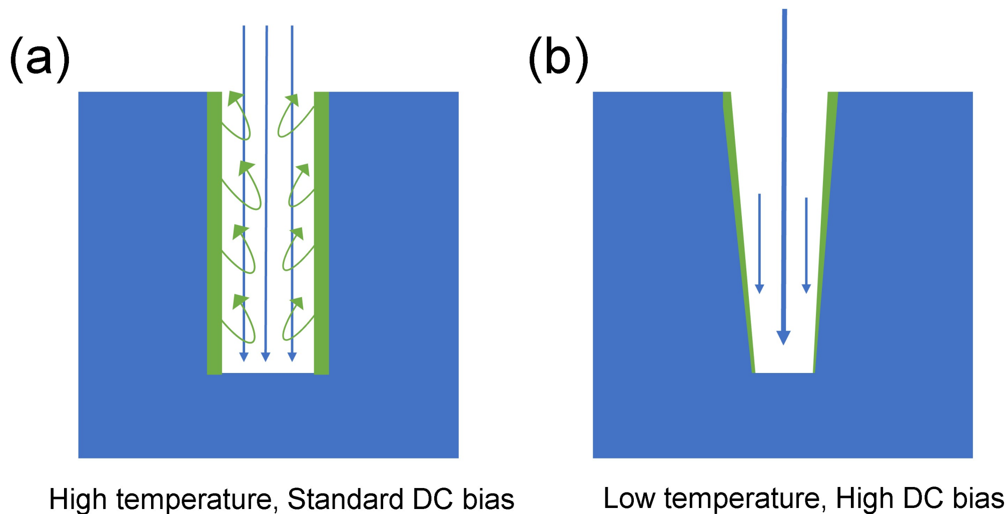

Figure 5-5: Figure (a) shows Cl_2 based dry etching of AlN nanoholes at high etch temperature and standard DC bias. In (b) Cl_2 dry etching of AlN nanoholes is shown at low temperature with a high DC bias. The blue material represents the AlN. The green material represents etch by-products that passivate the sidewalls of the holes. The green arrows show if this layer is likely to evaporate. The blue arrows show the direction of the ions incident on the nanoholes. A thicker longer arrow represents a greater concentration of ions.

leading to a small triangular top c-plane between the structures. The source of this misalignment is from the lithography step. The wafer's crystal orientation was slightly misaligned during the lithography step, meaning that any faceted structures would be at an angle to a parallel line through the wafer. This is as the wafer was not positioned with the flat of the wafer exactly horizontally during the UV exposure. More details of how lithographic wafer orientation affect faceting orientation (such as edge-to-edge or point-to-point in rods) can be seen in Appendix 1.

The tapering profile of sample B (Table 5.1), can be seen in Figure 5-6 (b). Here, one can see the deepest etch compared to other samples with significant tapering such that the bottom c-plane appears to have been etched out to almost a point. After wet etching (Figure 5-6 (f)) for 1 minute, a void can be observed in the centre of the structure. This is also present after only 30 seconds (inset (i)) but after 120 seconds of etching (inset (ii)) the uniform array of nanostructures appear to be etched away with only a remnant pattern remaining. It appears that the sharp tapering effect has not been successful for forming a sharp inverse apex. The presence of the void appears to be related primarily to the initial etch depth. There is some critical dry etching depth above which, after a small amount of wet etching, a void will result at the center of the

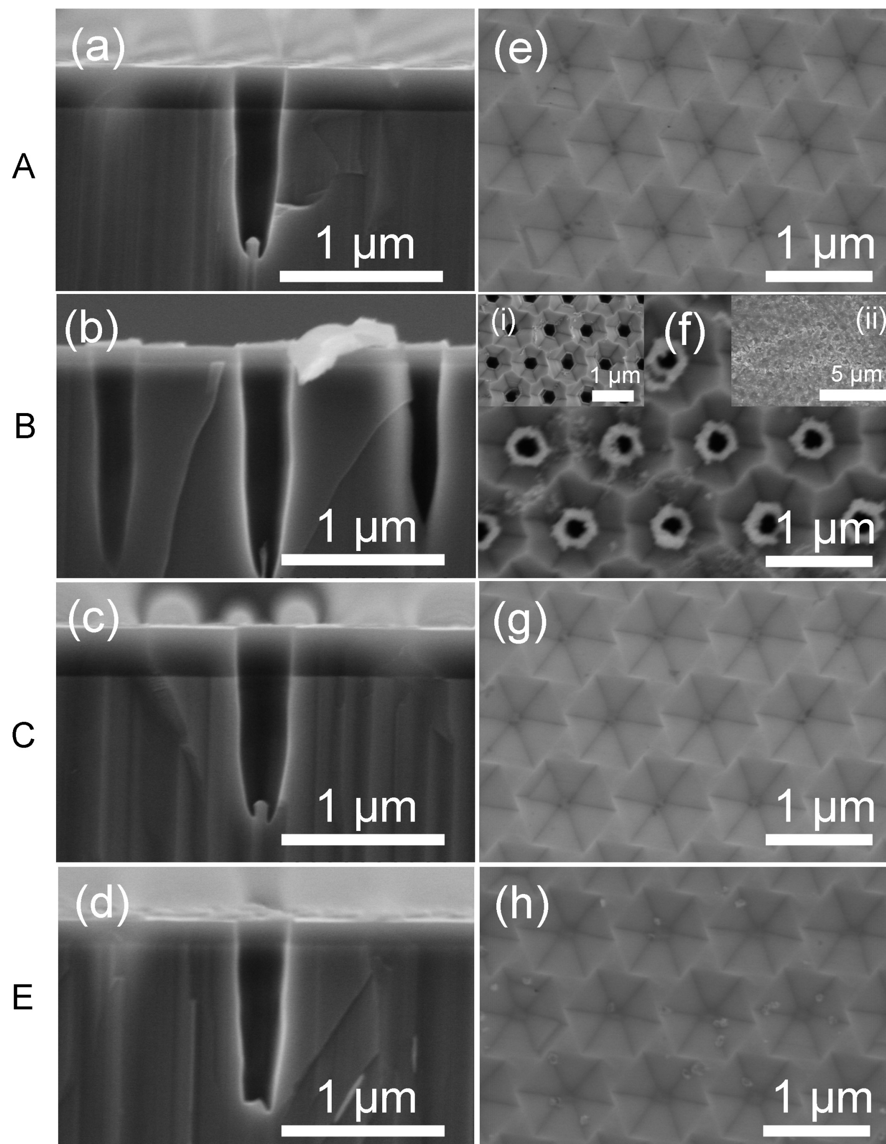

Figure 5-6: Figures (a) - (d) show SEM cross-sections of samples A, B, C and E respectively. Figures (e) - (h) show a planar SEM images of samples A - E respectively after 2 minutes of wet etching with KOH at 150 ^oC unless otherwise specified. The main image of Figure (f) shows a planar SEM image of sample B after a 1 minute KOH wet etch at 150 ^oC. Inset (i) shows the sample after 30 seconds wet etch and sample (ii) after 2 minutes wet etch under the same conditions as the main image. In all cases if the SiN_x mask had been present before the wet etch, it would have rapidly etched away, not affecting the morphology of the AlN nanostructures.

*These images must be taken with caution as one cannot say for certain that the cleave, and therefore the cross-sectional SEM image is directly through the centre of the holes in (a) - (d).

inclined planes. Interestingly, the top triangle c-plane regions between the structures are non-existent. In its place are sharp regions where three inclined planes from three planes meet. It is likely that the void, beneath the inclined planes, itself etches laterally as etch time progresses, effectively resulting in the etching away of the structure after a certain amount of time (as is observed in Figure 5-6 inset (ii)).

Samples C (Table 5.1) and E are shown before wet etching in Figures 5-6 (c) and (d) respectively. Sample C has similar tapering to that of sample A, and sample E has less than that of samples C or A. The diameter of the bottom c-plane of E, after wet etching, is larger than either that of C or A. Whilst one could argue there appears to be some correlation between amount of tapering and diameter of bottom c-plane (graph not shown), the error in these measurements is very large. This is even more apparent when considering that the cleave in all samples to provide the cross-section may not be perfectly through the centre. The sample standard deviation is defined as:

$$SD = \sqrt{\frac{1}{N-1}\sum_{i=1}^{N}(x_i - \overline{x})^2} \quad [317] \tag{5.5}$$

This definition of the standard deviation was chosen as the sum of squares multiplied by a $\frac{1}{N-1}$ term instead of just $\frac{1}{N}$ provides a better estimate of the standard deviation [317]. This standard deviation was primarily used as an estimate of the error of the measurements of the dimensions extracted from various SEM and AFM images/maps. In Figure 5-7 (b) the diameter of the bottom c-plane as a function of the dry etch depth for the tapered nanoholes is shown. It appears that there is likely a trend similar to that of Figure 5-3 where as etch depth increases c-plane diameter decreases but sample E is an outlier to this behaviour.

The altitude of the c-plane triangles (length of the triangle peak to the centre of the flat base) appear to reduce with increased dry etch depth, Figure 5-7 (a). From samples A, C, E in (a), the tapering appears to have had no real difference on the altitude of the triangles in these samples. This is evident from the very similar measured altitudes across these three samples. It is important to point out again that the errors in the measurements presented in Figure 5-7 are large when considering the spread of data point and so it is difficult to reliably deduce too much information here.

AFM maps of each of the samples were taken (see Appendix 2, Figure 8-6). From these maps the average angles of the facets were extracted. The result of this can be seen in Figure 5-7 (c). As can be seen in this plot, there seems to be some correlation between

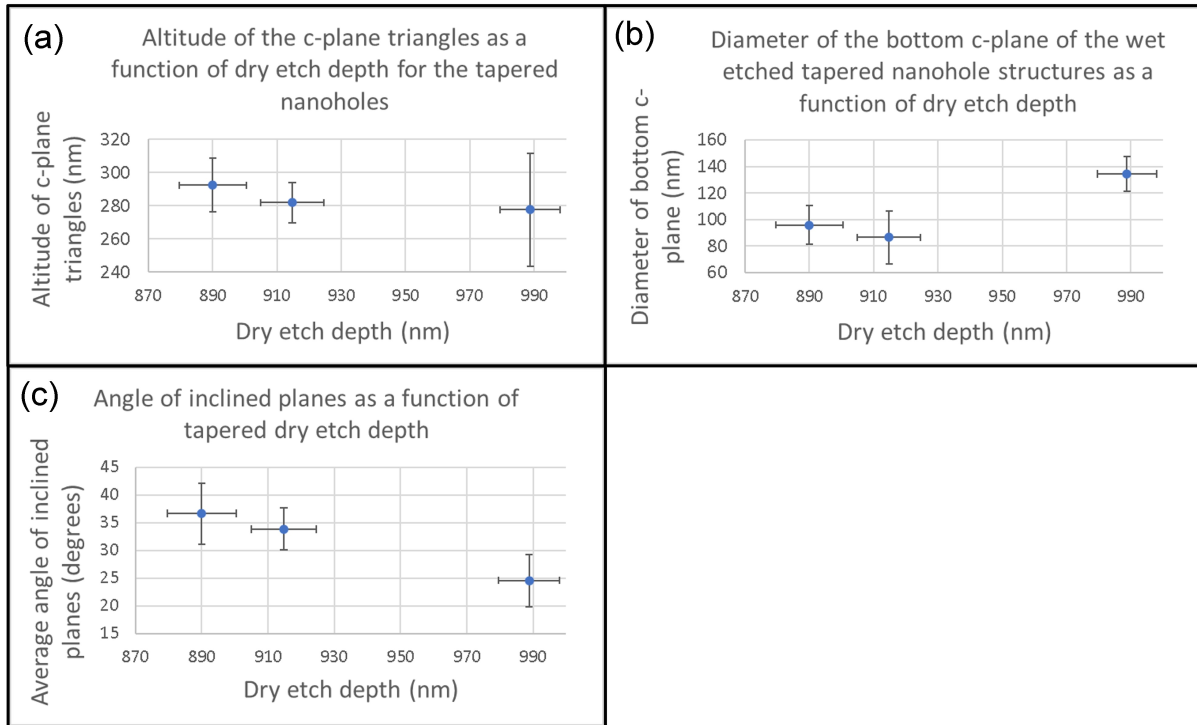

Figure 5-7: Figure (a) shows a plot of the c-plane triangle altitudes in as a function of the initial dry etch depths. Figure (b) shows a plot of the diameter of the bottom c-plane as a function of initial dry etch depth. Figure (c) shows a plot of the angle of the inclined planes as a function of the dry etch depth. All three plots show samples A, C and E. In (a)-(c) the dry etch depths and other feature dimensions were measured from cross-sectional SEM images. In (c) the angles of the planes were extracted from AFM maps of the samples (see Appendix 2).

The data in (a) and (b) must be taken with caution as it was extracted from cross-sectional SEM images.

increasing tapered dry etch depth and reduction in angle of the inclined planes. Sample B is an exception to this and has been omitted from the plot for better clarity on any trend present in the other samples. The errors are very large, and coincide with other measurements so it is difficult to reliably extract information from this data.

Overall, it appears the tapering plays only a small role in determine the size of the bottom c-plane. The size of the top c-plane triangles in-between the structures and the bottom c-plane diameters of the structures are largely determined from the initial dry etch depth, especially when considering the results of both Figures 5-3 and 5-6. The mechanism of the nanohole etching process from a geometrical standpoint will now be discussed.

5.4.3 Wet etching dynamics of the nanohole structures

It seems evident that the initial dry etch depth of the nanohole structures is a major determining factor in the resultant morphology of the wet etched structures. If we make two fairly sensible assumptions about the system being wet etched this can provide one possible explanation of what is observed. First, we could assume that the dry etch depth does not increase by anything more than a nominal amount during the wet etching process. Secondly, considering that the structures all have well defined hexagonal symmetry, the inclined planes that are formed are those of a semi-polar plane. These planes are either conventional or more exotic.

If we now consider a triangle, see Figure 5-8 (b), with an opposite plane which represents the dry etch depth of the nanohole and some hypotenuse which is at a given angle to the adjacent (this angle corresponds to a semi-polar plane). If the angle of the hypotenuse is assumed to remain similar or the same and we increase the length of the opposite plane (the dry etch depth), then both the length of the hypotenuse and adjacent planes will increase in size to accommodate this increase in opposite plane height.

Now if we apply this to the nanoholes in this chapter, we would expect that when the dry etch depth is larger the length of the semi-polar planes will be greater (Figure 5-8 (a)). This is what is observed and manifests itself as the observed reduced sizes in the bottom c-plane and top c-plane triangles as dry etch depth is increased.

With a very deep hole, such as sample B (Figure 5-6 (b)), a void is formed at the centre. This is as only a semi-polar plane of a certain maximum angle can form. The pitch is fixed at 1 μm. The total possible length of this semi-polar plane is now limited by the pitch of the hole array. As the dry etch depth is very large, the semi-polar planes expand as much as possible, joining to meet those of another hole and forming a sharp

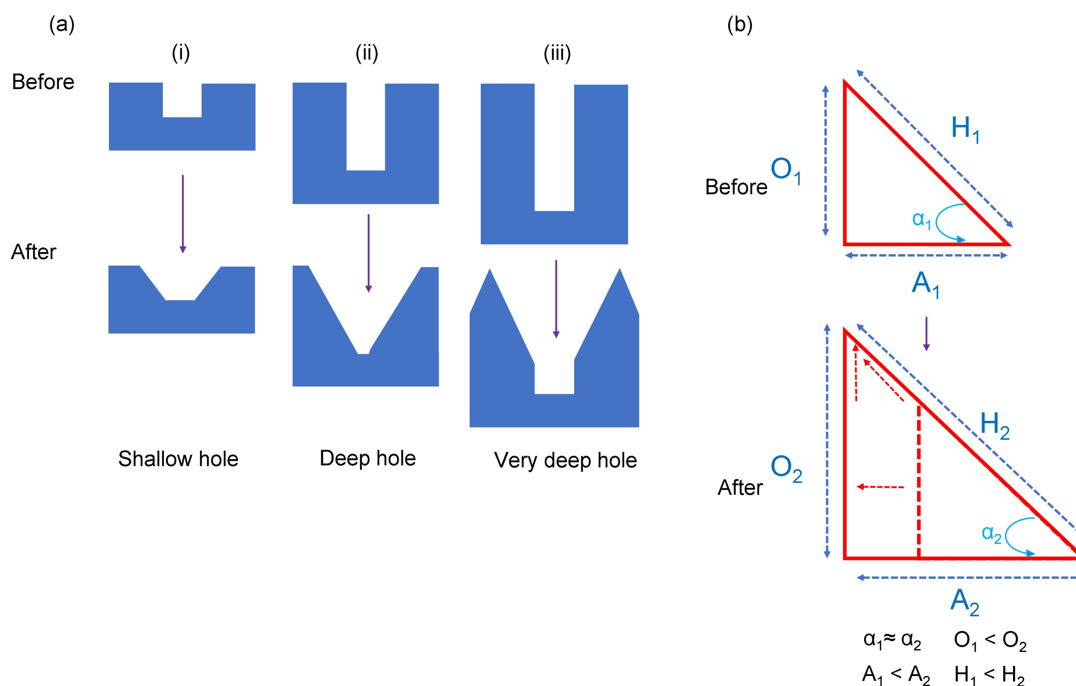

Figure 5-8: In (a) three dry etch nanohole schematics are shown. Before indicates prior to wet etching, after indicates after wet etching. (i) is shallow such as the sample in Figures 5-3 (a) and (d), (ii) is deep such as the sample in Figures 5-3 (c) and (f), and (iii) is very deep such as sample B (Figures 5-6 (b) and (f)). Figure (b) shows the increase in the semi-polar plane size as dry etch depth increases, from the argument perspective of a triangle. Before indicates, before an increase in the dry etch depth and after refers to after an increase in the dry etch depth. All sides after are longer than before whilst the angle remains roughly the same.

feature at the join. If the pitch of these structures was large enough, these semi-polar planes would also end up being larger and extend down to the bottom of the nanohole. However, as this is not the case the semi-polar planes, with a certain maximum angle, extend only part of the way down the hole. Hence, what is left is a void at the centre of the structure where the semi-polar planes terminate.

The same scenario with sample B could therefore be achieved with a structure that has a shallower etch depth with a smaller pitch. Conversely, structures with a base similar to samples A, C, and E could be achieved with sample B if the pitch was large enough. It is likely that a remaining small c-plane at the bottom of the wet etched structures is preferential, from the data presented in this chapter. It may be that a perfect inverse apex without bottom c-plane is a thermodynamically unfavourable structure and so is unlikely to be formed. If this structure is actually achievable, it would require perfect

tuning of the dry etch depth. This depth is difficult to estimate accurately with the data collected here. It is interesting to note that this is a similar result to that of growth upon dry etched nanoholes, presented in the previous chapter (Chapter 4).

On the atomic level the mechanism is similar to that reported for Ga-polar and N-polar GaN in [53]. The OH^- ions can readily attack the sidewalls of the nanoholes as there are less dangling bonds here relative to the c-plane. This allows for the rapid etching of these sidewalls to realise semi-polar planes. Whilst there are convex-concave region at the tops of inclined planes where they meet the c-plane, these do not appear to etch away as one would expect from a 'corner' that may be more easily attacked by the OH^- ions than the c-plane. Thus, the structures appears to self-limit, with the final exact geometry based on the discussion above. Further, excessive etching, appears to remove the nanostructures and, eventually, the epilayer as a whole.

Other nanostructures were explored for wet etching other than dry etched nanoholes. Specifically, wet etching of dry etched nanorods was also studied. The next sub-sections presents the results of the investigation into these nanostructures.

5.4.4 Wet etching of dry etched shallow nanorod samples

Whilst the nanohole structures resulted in some interesting morphologies after wet etching, no inverse apex geometry was created. The most promising feature was indeed the sharp features formed by the joining of inclined planes as seen in Figure 5-6 (f). The fact that this top c-plane region between the nanoholes shrunk upon wet etching is an interesting result. By using the inverse structure to a nanohole, a nanorod, there could certainly be the potential to create sharp features, as the top c-plane of such a rod may also etch away to a point. This structure could then be used to act as a site for quantum dot growth.

The starting material for all wet etched nanostructures shown in Figures 5-9 (a) - (f) was a $\sim$ 100 nm dry etch nanorod. A planar image of this starting material is shown in the inset of Figure 5-9 (a). This precursor structure can be seen in more detail Figure 4-1 in Chapter 4. In the main image of Figure 5-9 (a), an SEM image of the dry etched nanorod sample after 30 seconds KOH etching at 120 ^{o}C is shown. As is revealed in the AFM image in 5-9 (d), the structures still have a sizable c-plane which is a fraction of the size of the original starting diameter.

After a further 30 seconds of wet etching (Figure 5-9 (b)) the nanopyramids appear to be difficult to see in the SEM image compared to that of (a). This suggests that more material has been 'etched away' than in (a). What is revealed from the AFM image (e) is that the nanopyramids have sharp tips with no real visible c-plane remaining. What is visible from (d) and (e) is that whilst the top of the nanorod etches to a sharp tip as the etching progresses, the base does not change significantly in diameter.

Figure 5-9 (c) shows precursor nanorods after etching for a total of 120 seconds at 120 ^{o}C in KOH. The structures are barely visible in the SEM image. What is revealed in the AFM image in (f) is that the uniform hexagonal pyramid structures no longer remain. Instead, only slightly raised features of nonuniform height and with no well defined facets/planes are present. This made determining the average angles of the features rather difficult as there were no well defined planes to measure across. This AFM image confirms the previous observation from (b), that with increasing etch time the nanopyramid structures 'etch away' leaving little to no features remaining. Etching for 120 s at 150 ^{o}C (data not shown) results in complete removal of the nanostructures.

The average angles of the inclined planes were determined from the AFM scans in (d) - (f) and were plotted as a function of etch time (see Figure 5-9 (g)). Indeed, what is observed is that the angle of the planes decreases as etch time increases. In (h) the average height of the pyramids of each sample as a function of etch time is shown. A

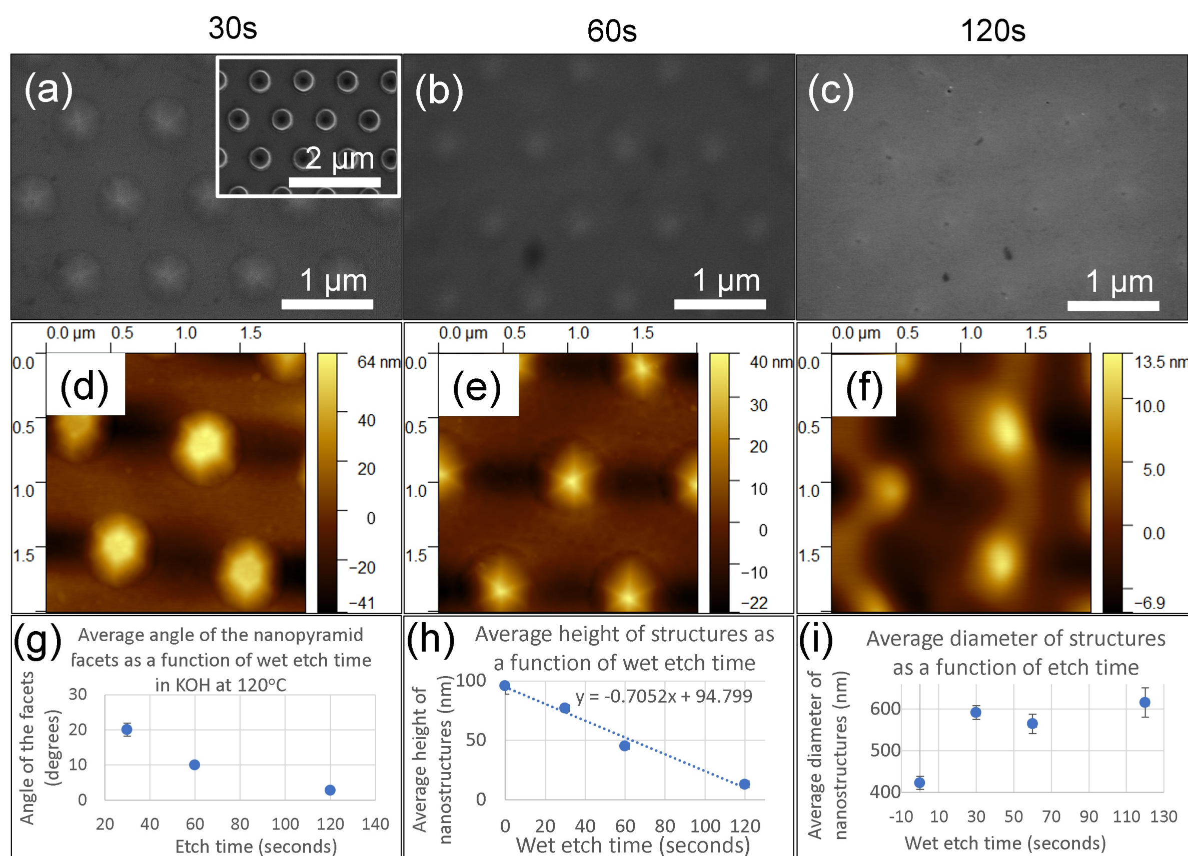

Figure 5-9: In (a), an SEM image of a dry etched ∼ 100 nm tall nanorod after undergoing a 30 second etch with KOH at 120 ^{o}C is presented. The inset in (a) is an SEM image of the rods prior to wet etching. In (b) the same as in (a) is presented but this time the wet etch was for a total of 60 seconds. In (c) the same as (a)/(b) is presented but with a wet etch time of 120 seconds. In (d) an AFM image of the sample presented in (a) is displayed. In (e) an AFM image of the sample presented in (b) is displayed. In (f) an AFM image of the sample presented in (c) is displayed. In (g) the average angle of the nanopyramid semi-polar facets as a function of etch time is presented. In (h) a plot of the average height of the nanopyramids as a function of etch time is presented. In (i) a plot of the average diameter of the nanopyramids as a function of etch time is presented.

Figure (i) - Measuring the dimensions of the diameters however was extremely challenging and as such this plot should only be taken as a rough estimate.

linear reduction in height is found as etch time increases. Conversely, little change in the diameters of the structures is found as a function of etch time (Figure 5-9 (i)). What can be discerned is that the height of the structures reduces much more rapidly than the diameters. This, therefore, leads to a a reduction in the angle of the inclined planes. The fact that the angle of the inclined planes can be tuned via the etch time is an interesting result. It also raises the question of the nature of the faceting in this experiment. The planes appear uniform and the pyramids are hexagonal in structure but do not necessarily correspond to a conventional semi-polar facet. They may correspond to an unconventional, exotic semi-polar facet.

5.4.5 Wet etching of dry etched nanorods of different aspect ratios

In order to determine a more general model for the wet etching dynamics, rods of different aspect ratios were etched in order to study the impact of both the starting diameters of the rods and the starting dry etch heights.

The same wet etching process as in Figure 5-9 at a temperature of 120 ^oC was applied to a number of wet etched nanorods with different aspect ratios. Figure 5-10 shows three sets of dry etched rods with different aspect ratios, shown before and after wet etching. The diameters, and pitch, were all larger than previous rod samples, such as those in Figure 5-9. The key observations from the morphology revealed in the AFM maps in Figures 5-10 will now be discussed.

The rods shown in Figures 5-10 (a) - (c) were fabricated from the same template via a lift-off process followed by ICP dry etching. Hence the diameters of the hard mask upon the template for all the samples shown in (a) - (c) were the same, prior to dry etching, see Table 5.2. The diameters of the rods were not the same however, after dry etching, as the metal mask reduced in diameter as the dry etch time increased. Thus, the diameters of the tops of the rods are smaller with increased dry etch time. This has been highlighted to show that the rods are not exactly the same in diameter even though they are taken from the original template.

When comparing the rods in Figures 5-10 (a) - (c) after wet etching ((d) - (f), respectively), one can observe that in all cases nanopyramids are formed. It is interesting to see that no 'pyramid-on-rod' structure is created in the 30 s wet etch duration presented here. Hence, it appears that a nanopyramid is the most stable structure to be realised after the initial duration of wet etching. Thus, when speaking generally about the resulting morphology of the rods after wet etching, the increase in aspect ratio of

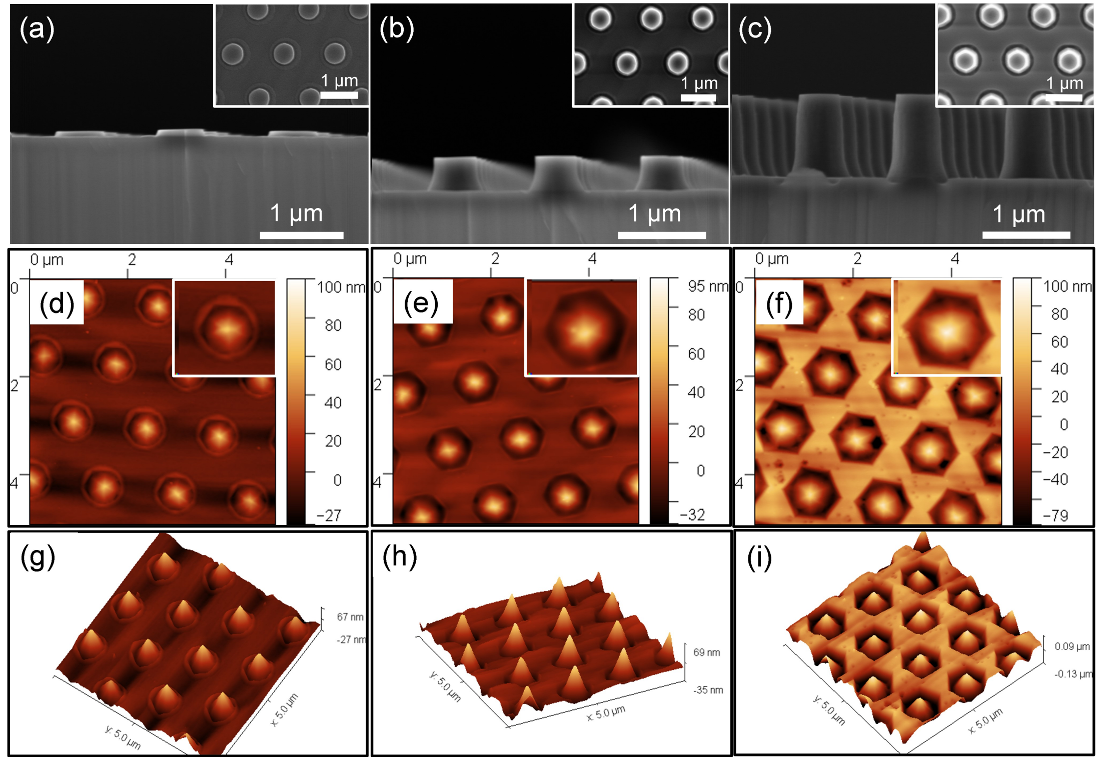

Figure 5-10: In (a) – (c) cross-sectional SEM images of nanorods after dry etching, mask removal and cleaning from nanorod samples fabricated at a 1.5 μm pitch are shown for 70 s, 240 s and 540 s of dry etching duration respectively. The insets are the corresponding planar SEM images of each sample. Figures (d) – (f) show AFM maps of the nanopyramidal structures revealed after KOH based wet etching of the samples shown in (a) – (c) respectively. The insets in (d) - (f) are magnified images of a single nanopyramid from the main figures of each map. In (g) - (i) tilted maps of the AFM maps shown in (d) - (f) respectively are presented.

Table 5.2: Diameters of the 1.5 μm pitch rods for different dry etch durations. The diameters of the rods were measured at the top of the rods. Measurements were performed upon cross-sectional SEM images

Diameter of the rods (1.5 μm pitch) as a function of dry etch duration	
Dry Etch Duration (seconds)	Diameter of 1.5 μm pitch rods (nm)
70	620 ±64
240	470 ±29
540	444 ±48

the rods appears to have little effect.

Height dimensions of the nanostructures after wet etching are summarised in Table 5.3 for all rods created with a 1.5 μm pitch at wet etch times of 30, 60 and 120 seconds. There is a clear reduction in total structure height of all three dry etched structures as wet etch duration increases from 30 to 120 seconds. Additionally, whilst the height dimensions of the 70 s and 240 s dry etched structures after equivalent wet etch duration appear similar, the total height of the sample dry etched for 540 s is noticeably higher. Considering the sample dry etched for 540 s starts off much taller than the samples etched for either 70 or 240 s this result is an expected one. This can be seen more clearly in Figure 5-11 (a).

After the dry etch process, trenches are formed around the rod structures, which have a greater depth than the surrounding c-plane. On further inspection of the data in Table 5.3, one can see that the trenches of the three rods remain roughly the same in depth during each of the three wet etch durations. What does appear stark is that these trenches increase in depth significantly as dry etch time increases. Interestingly, in rods of all three aspect ratios, in most cases, as wet etch time increases the height of the nanopyramid structure decreases compared the the unpatterned c-plane. Thus, from this we can further confirm that generally the height of the nanopyramid structure itself decreases as wet etch time increases in all three samples. This is without exception when comparing 30 s wet etch time to 120 s wet etch time.

Table 5.3: This table shows the structure height dimensions for the 1.5 μm pitch pyramid samples after wet etching

Height dimensions of 1.5 μm pitch pyramids after wet etching				
Dry Etch Duration (seconds)	Wet Etch Time (seconds)	Height of c-plane to pyramid apex (nm)	Trench Depth (nm)	Total Structure Height (nm)
70	30	73 $\pm$4.7	3 $\pm$1.4	75 $\pm$4.8
70	60	50 $\pm$2.5	5 $\pm$3.8	56 $\pm$2.6
70	120	55 $\pm$5	3 $\pm$1.8	58 $\pm$4.3
240	30	63 $\pm$5.3	16 $\pm$4.0	79 $\pm$6.7
240	60	52 $\pm$3.4	26 $\pm$4.8	78 $\pm$6.2
240	120	39 $\pm$5.1	14 $\pm$4.1	52 $\pm$8.2
540	30	41 $\pm$8.5	80 $\pm$4.8	122 $\pm$9.3
540	60	4 $\pm$6.1	76 $\pm$11.6	80 $\pm$11.0
540	120	-33 $\pm$11.6	84 $\pm$10.0	51 $\pm$11.1

In order to give more information on the nature of the inclined planes of the pyramids, the angles of these planes were extracted in the same manner as that performed for the data in Figure 5-9. This data is presented in Table 5.4, for the pyramids with a 1.5 μm pitch. See Figure 5-11 (b) for a plot of the angle of the inclined planes as a function of

Table 5.4: This table shows the average angles of the inclined planes of the 1.5 μm pitch pyramids extracted from AFM maps.

Average angles of inclined planes for 1.5 μm pitch pyramids		
Dry Etch Duration (seconds)	Wet Etch Time (seconds)	Mean Angle of Inclined Planes (degrees)
70	30	13.5 ±0.8
70	60	11.4 ±0.6
70	120	9.8 ±0.6
240 (top) *	30	15.3 ±1.6
240 (bottom) *	30	11.7 ±1.3
240	60	13.6 ±0.5
240	120	10.2 ±0.7
540	30	18.7 ±0.8
540	60	11.9 ±0.9
540	120	9.3 ±0.7

* This indicates the top and bottom of the pyramids. It appeared from the data that for these pyramids there may have been different gradients at different regions of the pyramid, although this is inconclusive. This was not taken into account for any other sample only the 1.5 μm pitch pyramid dry etched for 240 s and wet etched for 30 s.

dry etch duration and wet etch time.

As can be seen from Table 5.4 and Figure 5-11 (b), in most cases as wet etching time increases, the angle of the inclined planes reduces. In most samples, this is only a relatively shallow decrease in angle. However, for the sample dry etched for 540 s this is more dramatic. Additionally, samples with taller starting rod heights appear to have more steeply inclined planes after 30 s of wet etching. This suggests a taller initial rod leads to an initially taller nanopyramid with sharper inclined planes.

5.4.6 Wet etching dynamics of nanorod structures

Considering the data presented in Figure 5-9, the sidewalls of the nanorod, with less dangling bonds than the c-plane, etch more readily. Similar to the model described in [50], the OH^- ions are repelled by the dangling bonds present on the structure. Whilst the model presented in [50] concerned itself with polarity selective etching, some of the principles can still be applied here. As there are less dangling bonds oriented perpendicular to the c-direction, on the sidewalls, the OH^- ions are repelled more weakly than the c-plane, leading to the rapid lateral, inward etching of the sidewalls to form inclined planes. This results in the etching away of the top c-plane to realise a sharp apex at the centre of the rod. The inclined planes then etch away to those of shallower and shallower angles.

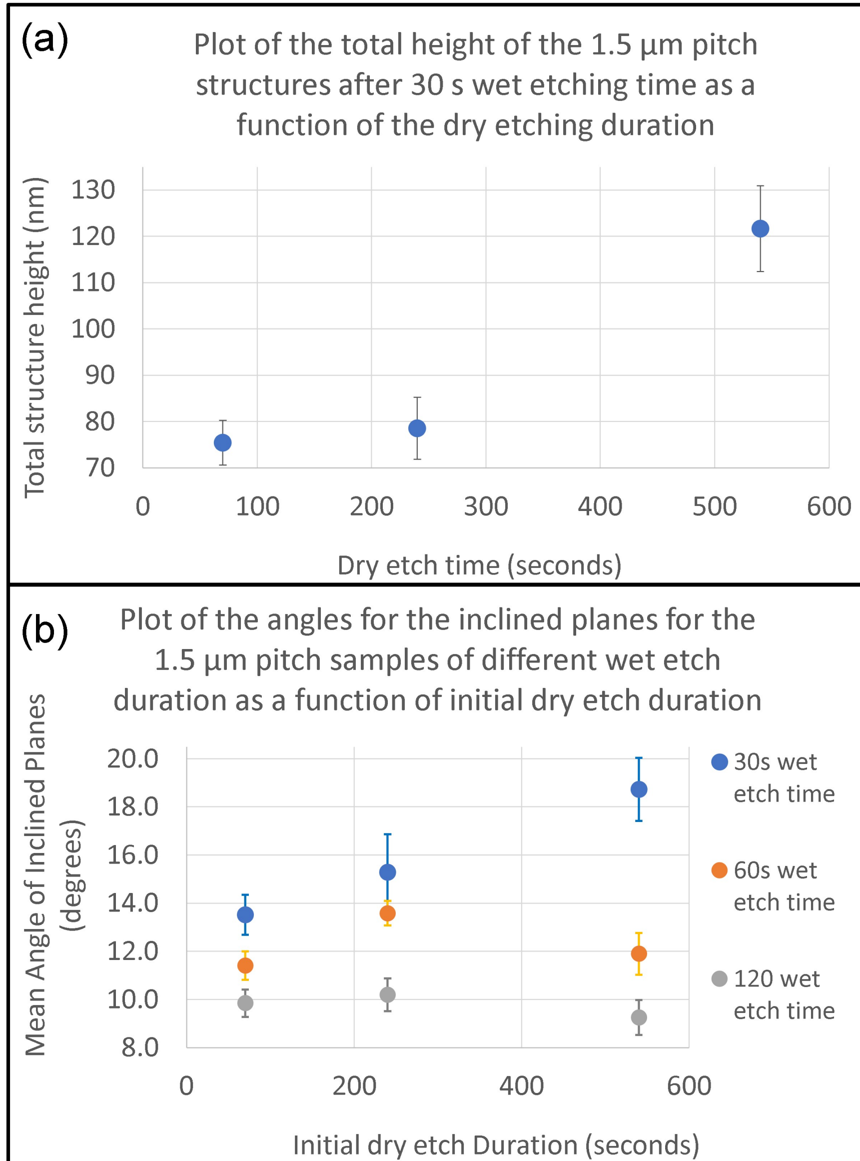

Figure 5-11: In (a) a plot of the total height of the 1.5 μm pitch rods wet etched for 30 s as a function of the initial dry etched depth is shown. In (b) a plot of the mean angles of the inclined planes of the 1.5 μm pitch nanopyramids are shown as a function of the dry etch time for all three wet etch durations.

At the base of the nanorod the higher number of dangling free bonds, due to the surrounding c-plane material, repel the OH^- ions. Whilst there is the formation of inclined planes at this base, there is not the significant rapid etching to a point that is observed at the top of the rods. This results in the base diameter of the structure barely changing, although there is faceting of the base, see Figure 5-12 (a).

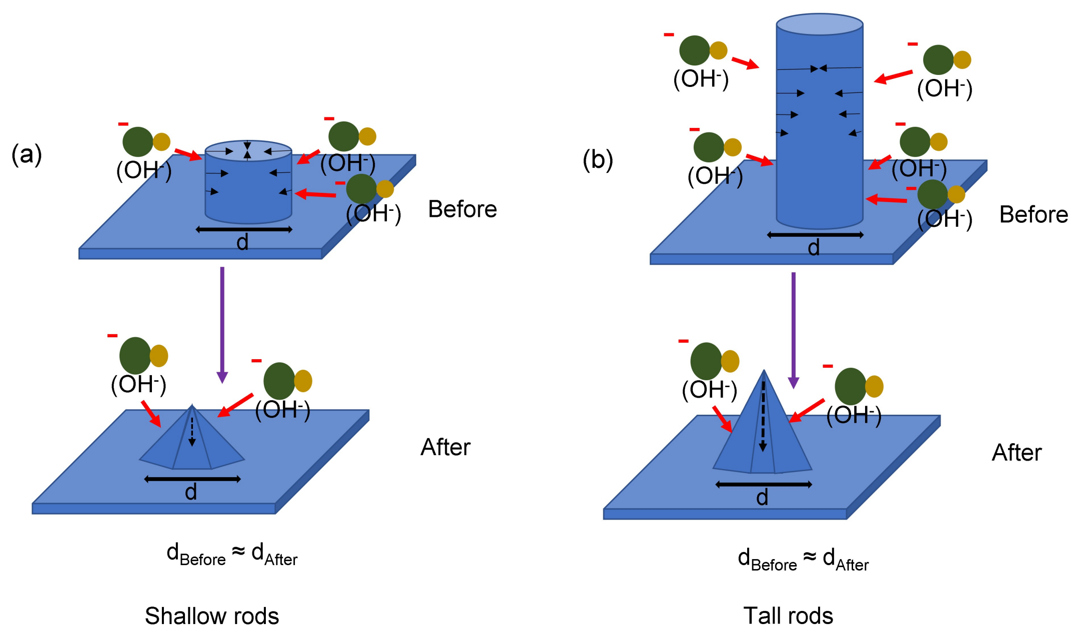

Figure 5-12: In (a) wet etching of the shallow dry etched nanorod. Top before/at the start of wet etching, bottom after a given amount of wet etching such as 30 s at 120 ^{o}C. Figure (b) shows the wet etching of a tall nanorod, again into a nanopyramid. Again the top is before/at the start of etching. The bottom is after a short period of wet etching such as 30 s at 120 ^{o}C. This nanopyramid is taller than in (a), in reality this is only slight but has been exaggerated in this figure for clarity.

As etch time progresses, lateral etching does not occur much on the base of the nanostructures but etching, causing a reduction in the height of the pyramids, does occur. This manifests itself in a reduction in pyramid height relative to pyramid diameter as etch time increases. Thus, there is a reduction in inclined plane angle as etch time progresses.

What is observed in Section 5.4.5 is that even relatively tall rods etch into a nanopyramid structure, albeit with initially taller height than the shallower counterparts. Additionally, the starting diameter does not appear to have a very critical impact on the resulting morphology of the structure after wet etching, when comparing the data in Figures 5-9 and 5-10. Finally, a key element to consider in all of the wet etched

nanorod data is the very well defined and faceted hexagonal symmetry present in all but one (Figure 5-9 (f)) of the rod structures. Based on this information, a clearer picture can be discerned.

Whilst the above mentioned impact of dangling bond geometry is important, it is likely that the observed hexagonal symmetry is a result of the formation of rather exotic semi-polar planes. The differences in height of the pyramid structures and the corresponding differences in inclined facet angle, especially on increased wet etch time will now be explained. It is likely that steeper, exotic semi-polar planes are first formed in the early stages of wet etching after the consumption of the top c-plane. These steeper, exotic semi-polar planes are likely stable for a short amount of time before rapid etching to another, shallower exotic semi-polar plane, which then is also stable for a short amount of time. This also leads to a reduction in total pyramid height, whilst keeping the well defined hexagonal symmetry. Eventually, the hexagonal symmetry is lost as is shown in Figure 5-9 (f), before removal of the structures completely. This occurs similarly for the taller nanorods as the dry etched sidewalls can also be easily attacked resulting in the formation of a pyramid rather than pyramid-on-rod structure (see Figure 5-12 (b)). It is likely that a pure pyramid is a more thermodynamically stable than a pyramid-on-rod structure and so etching into this former structure directly is more preferential. This means that as the structure will assume the lowest possible surface energy [318], suggesting a nanopyramid structure, as opposed to a nanopyramid-on-rod structure, has a lower surface energy. Hence, this the the general morphology assumed by the nanostructure before full removal of the feature by the wet etch.

5.5 Conclusions

In conclusion, two different nanostuctures have been realised with the potential to house site-controlled quantum dots. The sharp join between the nanohole inclined planes being the first and the apices of the wet etched nanopyramids being the second. The former was a largely unexpected result as we expected the formation of arrays of inverse nanopyramids. The latter is particularly promising for site-controlled quantum dot growth considering the wealth of previous literature on growth of InGaN quantum dots at the apices of GaN nanopyramids ([41], [43], [45]).

In Chapter 7, the effect of the growth conditions are explored in regards to trying to form a GaN quantum dot at the apex of some of these nanopyramids. Before visiting attempted GaN growth on these nanopyramid structures, an investigation of thermal etching of GaN to realise sites for InGaN quantum dots will be presented in the next chapter.

Chapter 6

Selective area sublimation of GaN as a route towards site-controlled quantum dots

6.1 Introduction to selective area thermal etching and its advantages

Whilst high quality GaN nanostructures can be realised by selective area growth (SAG), such nanostructures have lateral dimensions limited by the resolution of the lithography technique employed to pattern the mask upon the GaN layer itself [319]. Many previous reports have shown the growth of site-controlled InGaN quantum dots upon SAG upon GaN micro/nano-pyramids ([41], [43], [270], [45]). However, residual contamination resulting from the fabrication processes and/or air exposure remains a problem in SAG [319]. Moreover, bottom-up growth of nanowires often result in incorporation of high concentrations of impurities and defects due to the non-ideal growth conditions which need to be employed [320].

By employing a purely subtractive process to create high quality, high resolution nanostructure features, these problems can be avoided. Selective area thermal etching or selective area sublimation of GaN can be described as a simple subtractive process which is thermally activated. Compared to dry etching, thermal etching does not generate any ion-induced surface defects which could affect the optical properties of a device [55]. In addition, the lack of these defects would allow, in theory, an active region grown within these thermally etched structures to be of a higher quality. This is as there,

ideally, would be a damage and defect free interface between the thermally etched GaN nanostructure and the subsequently grown active region. Optoelectronic benefits of such an interface would be a reduction in the likelihood of non-radiative recombination, current leakage and/or increased sheet resistance, as would be problematic with GaN based nanostructures created via ICP-based dry etching [321]. A structural benefit would be a likely crystallographic higher quality active region grown within the thermally etched GaN as a result of the lack of defect surface GaN states. As thermal etching is not believed introduce any nonradiative defects into the nanostructures which have been created, this can lead to material with more intense optical emission compared to that of purely planar material [320]. Evidence of this can be seen in the work by Fernandez-Garrido et al. [320], where it was shown that the cathodoluminescence (CL) emission is greater for GaN nanowires created by thermal etching compared to the original planar layer demonstrated in [320].

In the work by Coulon et al. [55], it was found that arrays of very small nanoholes could be produced within openings of a dielectrically masked GaN sample after selective area sublimation (see Figure 6-1 (a)). This result could be achieved when subliming using purely N_2 carrier gas, a small flow of ammonia (10 sccm), a reactor chamber pressure of 100 mbar, a set temperature of 875 ^{o}C (true temperature $\sim$ 950 ^{o}C) for a time of 60 minutes [55]. Upon reproduction, a novel application of such a structure would be to grow an individual InGaN quantum dot within each small opening. This chapter is dedicated to the study of the reproduction of this structure as shown in Figure 6-1 (a) and (b), and the subsequent growth of InGaN quantum dots within the nanohole structures.

Using the same fabricated wafer as that used by Coulon et al in [55], sublimation experiments were repeated with all conditions remaining the same except a change in set temperature. The morphology of the GaN at a set temperatures of 875 ^{o}C and 925 ^{o}C are shown in Figures 6-1 (b) and (c), respectively. Several notable observations can be made.

Firstly, temperature drastically affects the etch depth. In more detail, the morphology presented in Figure 6-1 (b) is more desirable for site controlled quantum dots growth. The 'pin-hole like' features at the centre of each window appear to have lateral dimensions comfortably less than 50 nm potentially . The exact size is hard to measure from the data shown in Figure 6-1 (b) however. It is likely these features are small enough to house quantum dots. Even if the hole features are larger than quantum dot dimensions, a small amount of growth at the centre of each hole should realise quantum dot growth at the inverse apex. Alternatively, inverse pyramid and holes are formed at

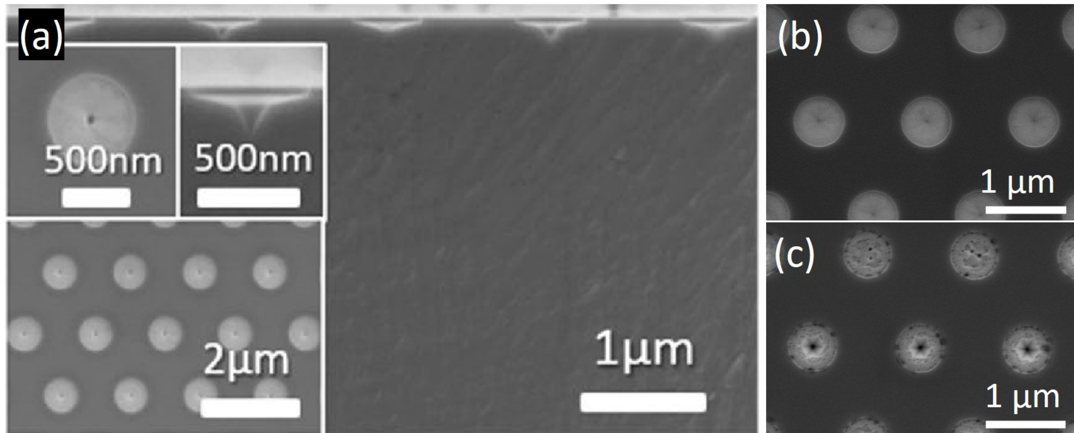

Figure 6-1: In (a) sublimation of GaN under an N_2 atmosphere performed by Coulon et al. [55] is presented (Figure (a) is reproduced and cropped from [55] under Creative Commons Attribution 4.0 International License, http://creativecommons.org/licenses/by/4.0/). In (b) and (c) reproductions of this work from the same original template as that in (a) are presented at sublimation set temperatures of 875 ^oC and 925 ^oC respectively. All other sublimation conditions were the same as in Figure 6-1 (a).

higher sublimation temperature (Figure 6-1 (c)). Not all windows have these features at this temperature. Some have a 2-layer structure with a thicker layer of material near the edges of the window. In addition, windows with pitted surfaces among the central features are also present in Figure 6-1 (c). Sasaki demonstrated that when GaN was grown at too high a temperature, re-evaporation caused a thermally-pitted surface [322]. This appears to also be the case in these purely sublimated templates, the occurrence of which is to a lesser extent at the centre of the sample.

From the raw SEM data image in Figure 6-1 (c), 7 windows were analysed to obtain an estimate of the number of pits per unit area. 10 measurements of the diameters of the windows were measured and an average extracted. Where a central sublimation feature existed, the average diameter (from 10 measurements) of this was determined. The feature was approximated to be circular, and when present the area of this feature extracted from the total window area. The number of pits were then manually counted. Summing the total number of pits and the area of each window (subtracting the sublimed central feature area where present), a density of pits per unit are was calculated. This crude estimate of the pit density was found to be in the region of 7 x 10^9 cm^{-2}. The template was a commercially sourced 7 μm GaN wafer grown upon a sapphire substrate [55]. Dislocation densities quoted by the supplier for these templates are in the region of $\sim$ 5 x 10^8 cm^{-2}. This is an order of magnitude smaller than the densities

estimated from the SEM image in Figure 6-1 (c). When comparing dislocation densities of GaN grown upon sapphire in the literature some interesting comparisons were found. Some historical values for some typical dislocation densities on GaN grown on sapphire substrates have been reported to range from 10^{10} - 10^{8} cm^{-2} [323] and on the order of 10^{8} when using micropatterned sapphire substrates [324]. Considering the crude estimate of the pit density of 7 x 10^{9} cm^{-2} it is debatable that the pits observed in the SEM image correspond to preferentially thermally etched threading dislocations. This is as there is an order of magnitude difference between the estimated density of pits and the typical quoted value from the supplier. However, there is likely a large degree of error in the pit density estimation presented here.

Phenomenologically, it is likely a potential minimum exists at the centre of the GaN windows where it is preferential for more material to be thermally etched. Considering that the main pit features are at the centre of the windows in Figures 6-1 (a) - (c), it is likely that the mask plays a key role in defining this minimum, as the centre of the windows is the furthest region away from the mask in all directions. This makes the centre the easiest place for sublimation of material without re-incorporation. Re-incorporation then gradually increases as one moves from the centre of the window closer to the mask-GaN interface.

Several attempts to reproduce the results by Coulon et al. (in Figure 6-1 (a) and (b)) were made. The key information concerning fabrication and cleaning procedures on every sample are presented in Table 6.1. Further details can be found in Appendix 3. On all samples the first fabrication step was to deposit a $\sim$ 35 nm SiN_x mask layer via PECVD (Plasma Enhanced Chemical Vapour Deposition) (see Figure 6-2) for a schematic of the fabrication process. This was followed by the spin coating of back antireflection coating (BARC) and photoresist, with appropriate baking steps. Displacment Talbot Lithography (DTL) was then used to expose the reist followed by development in MF-CD26 photoreisist developer. This patterned resist was then used as an etch mask in order to transfer the pattern in the resist into the SiN_x mask below. Finally, appropriate cleaning steps were performed. The sublimation conditions for these thermal etching experiments were as follows, unless specified: pure N_2 carrier gas, reactor chamber pressure of 100 mbar, NH_3 flow of 10 sccm and a 60 minutes thermal etch time. A set temperature chosen to be either 875 or 900 ^{o}C, and is specified when the particular results are presented.

In this chapter, initial reproduction attempts of the samples shown in Figures 6-1 (a) and (b) were undertaken. This proved challenging and there could have been a num-

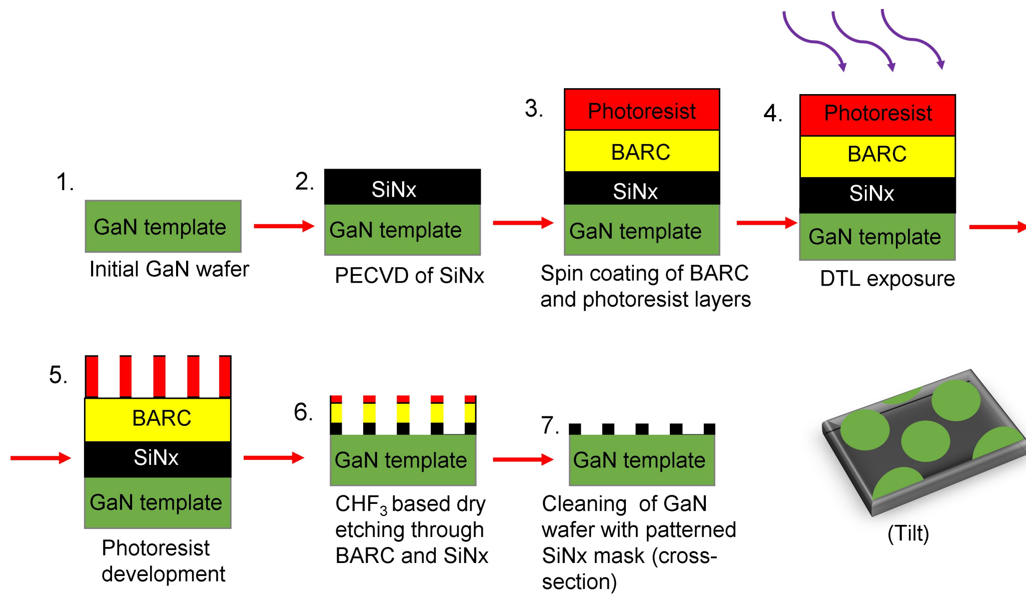

Figure 6-2: Here a schematic of the fabrication process is presented. The planar GaN template is the starting wafer in 1. In 2, PECVD is used to deposit a ~ 35 nm thick layer of SiN_x. In 3, BARC and photo-resist are spin coated upon the template with appropriate baking steps. In 4, DTL is used to expose the resist with a specific periodic pattern. In 5, the resist is developed to reveal a hole array within the resist. In 6, CHF_3 based ICP dry etching is performed to transfer the pattern in the resist into the SiN_x hard mask. In 7, appropriate cleaning steps are taken to remove any remaining BARC, photoresist and oxides.

Table 6.1: Fabrication and cleaning details of all samples within this study. Samples taken from the same initial wafer are denoted with the same letter. Those with different numbers have different fabrication/cleaning conditions applied to them.

Table of sample processing					
	Patterning Processes	Cleaning Processes			
Sample	ICP CHF_3 etch time (minutes)	Piranha (3:1 ratio, cyclesxtime (minutes)	O_2 descum - gentle/very gentle, time (minutes))	BOE clean in seconds (100:1 = blue, 5:1 = red)	Other Comments
A1	10	1x3	None.	None.	Cleaning = only piranha.
A2	A1	None	Gentle, 15	10	A1 + additional cleaning steps incl. 10 s AZ400K
A3	A1	1x5	Gentle	15	A2 + additional cleaning steps
G1	11	4x5	None.	40	1 piranha clean then BOE 100:1, repeated 4x ensuring thoroughly clean sample.
G2	G1	2x5	Gentle, 10	10	2x piranha cleans, O_2 descum, then BOE 100:1. On G1 sample.
G3	G1	1x5	Gentle, 1	10	1x piranha clean, O_2 descum, then BOE 100:1 on G1 sample.
B1	8	2x5	None.	10	2x piranha cleans, then BOE 100:1.
B2	B1	2x5	Gentle, 10	10	2x piranha cleans, O_2 descum, then BOE on part of B1 sample.
B3	B1	1x5	Gentle, 2	10	1x piranha clean, O_2 descum, then BOE 100:1 on part of B1 sample.
B4	7 CHF_3 + 1 minutes O_2 + calibrated BOE 5:1	2x5	None.	10	2x piranha then BOE 100:1 on part of B1 sample after optimised etch through SiN_x.
B5	B4	2x5	Very Gentle, 3	10	2x piranha, O_2 descum, then BOE 100:1 on part of B1 after optimised etch through SiN_x.
B6	6(05:20) for minimal GaN exposure to CHF_3 plasma.	2x5	None.	10	2x piranha then BOE 100:1 B1 after optimised etch through SiN_x.
B7	B6	2x5	Very Gentle, 3 minutes	10	2x piranha, O_2 descum then BOE 100:1 on B1 after optimised etch through SiN_x.
B8A (B8B)	8(09:30) for minimal GaN exposure to CHF_3 plasma.	Acetone rinse, 1x5	Very gentle, 3 minutes	10	1x acetone, 1x piranha clean, O_2 descum, then BOE 100:1 after calibrated CHF_3 etch on part of B1.
B9	8	1x1	No.	20	1x piranha then BOE 5:1 only.
B10	B9	1x1	Gentle, 1	20	1x piranha, O_2 descum then BOE 5:1.
B11	B9	1x2	No.	20	1x piranha then BOE 5:1 only.
B12	B9	1x2	Gentle, 1	20	1x piranha, O_2 descum then BOE 5:1.
B13	B9	1x3	No.	20	1x piranha then BOE 5:1 only.
B14	B9	1x3.	Gentle, 1	20	1x piranha, O_2 descum then BOE 5:1.

ber of reasons for the difficulties encountered. In order to determine the source of poor morphology encountered in Section 6.2, a detailed investigation of the fabrication and sublimation conditions was undertaken. In terms of fabrication, both patterning conditions and the effects of sample cleaning were studied in detail. A mechanism is proposed for selective area sublimation under the conditions employed here in addition to the underlying cause of the poor morphology observed in unoptimised samples. Finally, optimisation of the fabrication process and sublimation conditions was employed to realise arrays of sites suitable to house InGaN or InN quantum dots.

6.2 Initial reproduction attempts of reproducing sublimation sites

Sample A1 from template A can be seen in Figure 6-3 (a), after the fabrication steps elaborated in Table 6.1. This same sample after sublimation at set temperatures of 875 ^{o}C and 900 ^{o}C can be seen in Figures 6-3 (b) and (c) respectively. Whilst there are central hole features in both (b) and (c), there appears to be some undesirable central growth features in the holes. This is more prevalent in (c) compared to (b). In addition, the holes themselves are not particularly uniform in shape, and, to some extent, size. This lack of uniformity of the central holes appears to be more accentuated at higher sublimation temperature. This demonstrates, due to the variation between Figures 6-3 (b) and (c) that sublimation temperature is a critical parameter in determining the resultant morphology of the GaN windows as was also observed in Figure 6-1 (b) and(c). Thus, this is key to realise sites for quantum dot growth.

This lack of uniformity and the presence of central growth features required investigation and as the only cleaning process performed on the sample was a 3:1 ratio $\sim$ 3 minute piranha clean, further cleaning steps were performed (see sample A2 in Table 6.1). The sample surface of the GaN windows looks relatively clean with only differing contrast observed within a fraction of the windows. The surface after sublimation at 875 ^{o}C is shown in Figure 6-3 (e). There is a large amount of undesirable growth-like structures at the centre of each hole; a phenomenon which is enhanced in magnitude and tendency after further cleaning compared to the morphology shown in Figure 6-3 (b). This suggests that the extra cleaning steps have had a detrimental effect on achieving the desired morphology of the structures.

There are a number of possible reasons for the observed poor morphology of sample

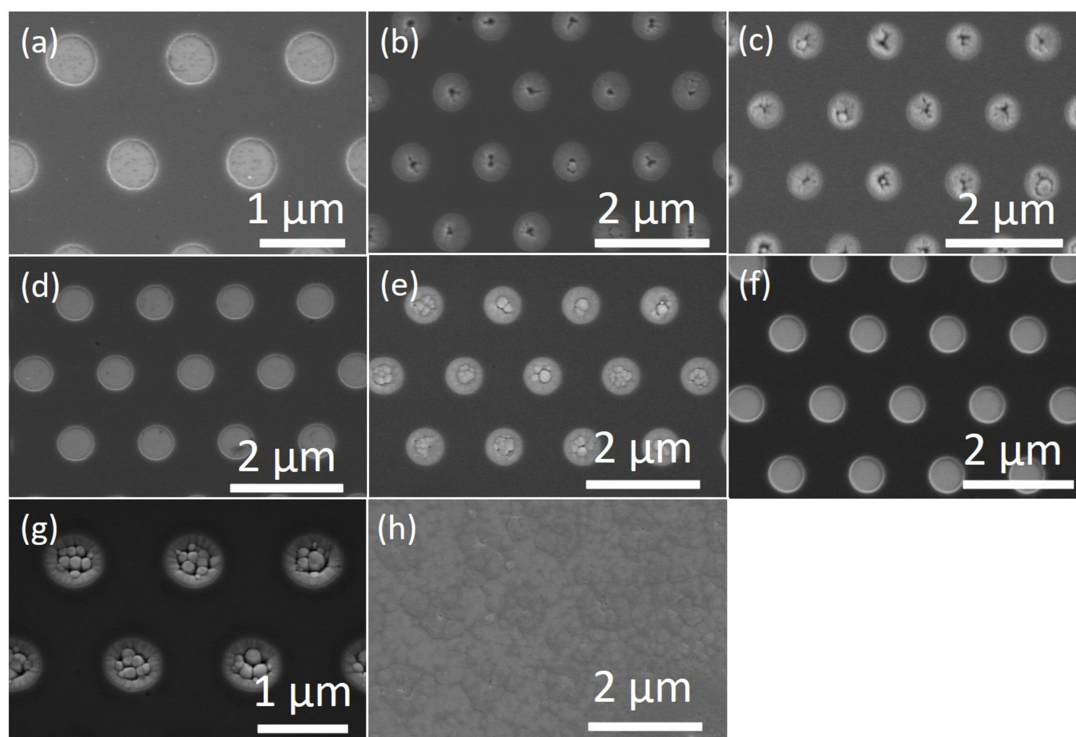

Figure 6-3: In (a) a planar SEM image of sample A1 (see Table 6.1) sample after initial cleaning is presented. In (b) and (c) initial sublimation tests are presented, at a set temperature of 900 ^{o}C in the latter. In (d) a planar image of the sample is shown after the second cleaning process (A2 in Table 6.1). In (e) sublimation upon sample A2 is shown. In (f) a planar image of the sample surface after the third cleaning process is shown (A3 in Table 6.1). In (g) a corresponding sublimation upon A3 is presented. Figure (h) shows the results of sublimation on a sample from A3 with the SiN_x mask stripped off via a BOE 5:1 treatment. All samples were sublimed at a set temperature of 875 ^{o}C unless otherwise specified.

A2 (Figure 6-3 (e)). The responsible cause for this poor morphology required further investigation. The potential causes of this poor morphology are listed below and summarised in Figure 6-4:

1. The long (15 minute), excessive O_2 descum has severely oxidised the surface. These surface oxides have not been fully removed by the BOE 100:1 10 second dip. This may then have caused the accumulation of some compound of GaO_x at the centre of the windows. Hence these central 'lump' features would actually be GaO_x compounds. This oxidation theory, if it is purely just a surface effect, could potentially be tested by exposing the sample to a chemical treatment to significantly reduce any excessive surface oxides present prior to sublimation.

2. Processing has physically damaged the surface. This has then led to a rougher or defective surface which may have led to non-uniform thermal etching and could inhibit the movement of material across the surface, either in the form of gaseous GaN (or Ga and N) or liquid Ga droplets. This reduced movement of species would then result in some material accumulation at the center of the windows instead of the central hole within each window as material finds it more difficult to travel away from the center of the window. This hypothesis can be tested by fabricating new templates with a significantly reduced O_2 descum step and optimisation of other fabrication/cleaning processes.

3. The choice of a 10 second AZ400K dip has had a very detrimental effect on the surface of the GaN. In particular, it may have caused a surface reconstruction, resulting in a rougher surface, inhibiting the migration of material. This may result in less diffusion across the GaN window and incorporation at the center instead of effective diffusion from the center. The remedy for this would be the fabrication of new samples, avoiding an AZ400K process on the sample.

4. The reactor chamber is dirty and thus contamination has caused this unusual morphology at the centre of the windows. This can be solved, to some extent, via cleaning of the internal quartz parts of the reactor chamber. However, cleaning of the separation plate (due to the difficulty of it's removal) and the reactor walls themselves presents a large challenge which may not be realistically achievable without irreversible damage to the reactor itself.

5. The sample is simply not properly clean. This can be tested by preforming further cleaning steps upon the sample.

Sample A3 was a sample from A2 with additional cleaning in order to test hypothesis

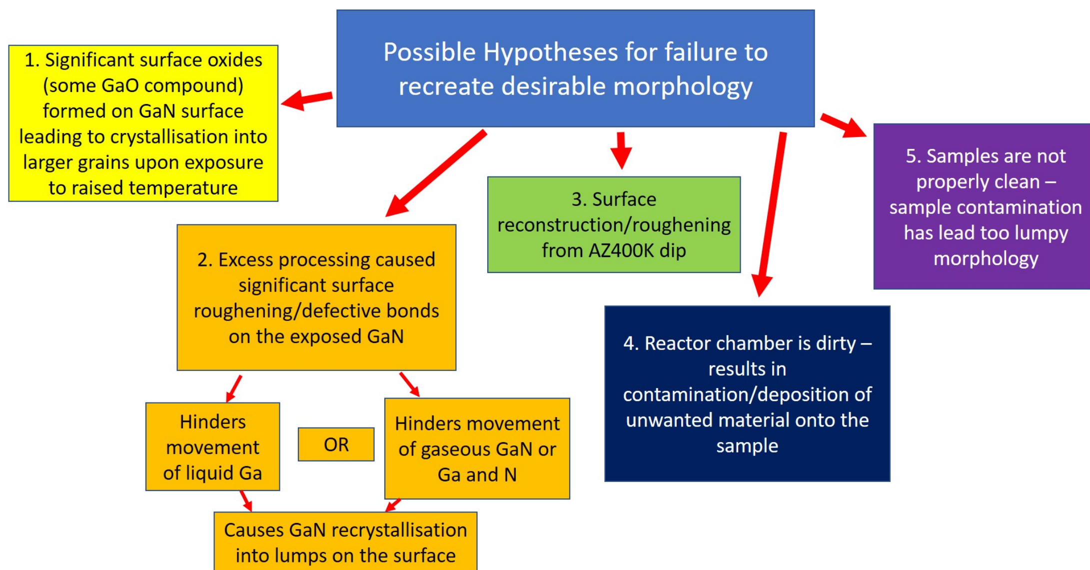

Figure 6-4: This figure shows a summary of the possible hypotheses for the failure of sample A and in particular A2 and A3 to recreate the results presented in Figures 6-1 (a) and (b).

5. The surface of sample A3 before sublimation can be seen in Figure 6-3 (f). As can be seen the sample surface of the GaN windows looks very clean with minimal differing contrast observed in the windows. The surface after sublimation at 875 ^{o}C is shown in Figure 6-3 (g). The further cleaning steps have degraded the surface morphology further, leading to this undesirable lumpy and very rough surface morphology across the majority of the GaN window compared to only the center of the window in Figure 6-3 (e). As this has had a negative impact on the morphology of the sublimed sample, this confirms that hypothesis 5 is not correct. Indeed, this result indicates that the processing steps upon the sample may have a very influential impact on the morphology of the sample after sublimation. A study into the effect of the fabrication and cleaning processes themselves required investigation, in particular, this included an exclusion of the AZ400K treatment step that was performed upon sample A2.

To further confirm that processing has had a significant impact on the GaN surface, sublimation after stripping the SiN_x mask with BOE 5:1 was performed as shown in Figure 6-3 (h). A remaining, somewhat, periodic pattern corresponding to the location of the mask openings is visible, providing fairly solid evidence that processing has impacted the exposed GaN window regions. Another interesting observation is that there is a central pit within some of the lumpy features.

Whilst it is apparent that processing and potentially contamination has had a profound

impact on the resulting morphology of the sample after sublimation, it remains unclear what the exact cause has resulted in the lumpier, less desirable morphology observed in Figures 6-3 (e) and (g). As processing steps have appeared to have caused irreversible damage to the sample surface, new templates required patterning in order to investigate the impact of fabrication and cleaning processes upon the sublimation of GaN windows.

6.3 Study of the impact of fabrication/processing and reactor cleanliness

Fabrication of new template without AZ400K step

Figure 6-5 (a) inset shows a planar image of sample G1 after 4 cycles of cleaning (as detailed in Table 6.1). This image is representative of the entire sample. As can be seen the GaN windows appear very clean. It is however difficult to see if the processing has roughened the surface of the exposed GaN to some extent, as this is beyond the resolution limit of the SEM.

6.3.1 Temperature study on sample G1

An investigation on the impact of sublimation temperature was performed on sample G1 (data not presented here), but this did not result in any profound impact on the surface morphology of the majority of the samples. No central hole features in any of the samples were observed. This seems to indicate that a property of the sample itself is the source of this lack of central hole feature (as can also be seen in Figure 6-5 (a) main figure).

6.3.2 Effect of reduction of contamination via cleaning of reactor parts on sample G1

The quartz components of the reactor chamber were removed and replaced, after thorough cleaning with KOH solution. Comparison of a sublimed G1 sample before and after quartz component cleaning can be seen in Figures 6-5 (a) and (b) respectively. As can be observed in the figures, there has been no significant impact on the morphology of these sublimed samples after component cleaning. This suggests that contamination from the rector chamber components is not the source of the lack of a central hole feature.

6.3.3 Deep etch study (N_2:H_2 carrier gas)

As a test to see if surface contamination or damage had taken place on the G1 sample a deep thermal etch using a 1:1 mixture of H_2:N_2 carrier gas was performed, this is shown in Figure 6-5 (c). As can be seen in the inset of (c) whilst there has been some deep thermal etching, it is by no means uniform as one would expect (such as similar

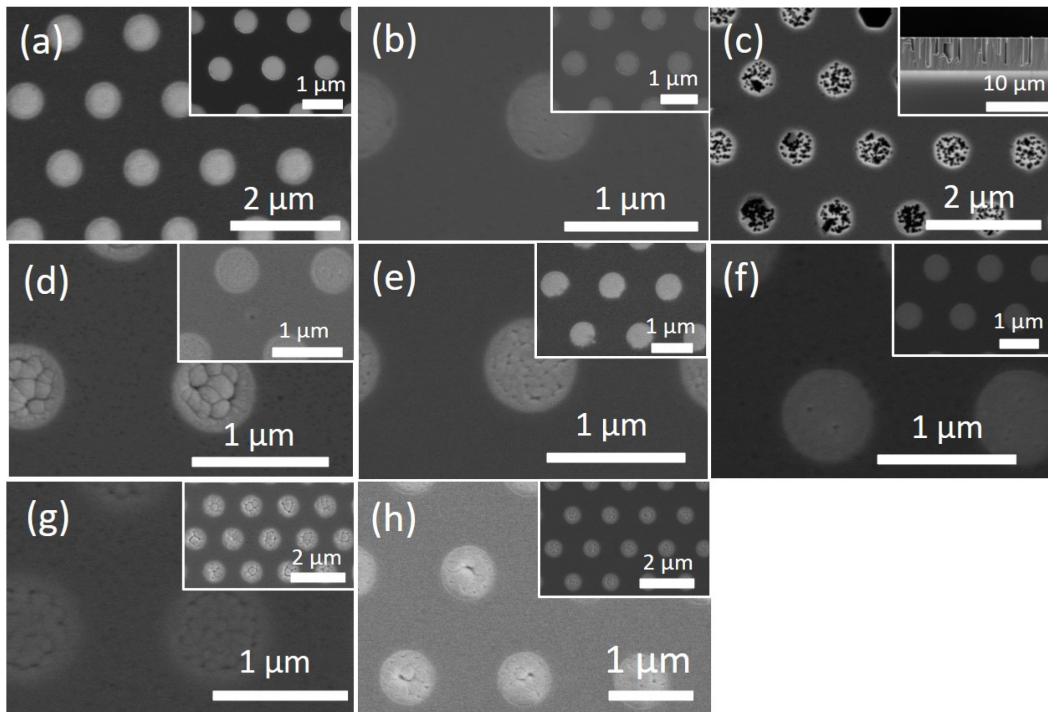

Figure 6-5: In the main figure of (a) sublimation upon a sample from G1 (shown prior to sublimation in the inset) is presented. In (b) sublimation upon a sample from G1 is shown after a thorough cleaning of the reactor chamber quartz components and replacement of susceptors and covering sapphire wafers. The main image is the centre of the sample whilst the inset is that of the edge of the sample. In (c) planar (main image) and cross-sectional (inset) SEM images are presented after a sublimation of a sample from G1 with a mix of H_2 and N_2 carrier gas (1:1). In the main figure of (d), sublimation of sample G2 is shown. In the inset, sublimation of sample G3 is shown. In the main figure of (e), sublimation of sample B2 is presented. In the inset, sublimation of sample B1 is presented. In (f), sublimation of sample B3 is shown. The main image is taken at the centre of the sample and the inset at the edge. In the main figure of (g), sublimation of sample B4 is presented. In the inset, sublimation of sample B5 is presented. In the main figure of (h), sublimation of sample B6 is presented. In the inset, sublimation of sample B7 is presented. All samples were sublimated at 900 ^{o}C set temperature.

results by Coulon et al. [55]). In addition, the planar image shows that whilst there has been considerable thermal etching vertically beneath the GaN windows, many have a very thin top layer of unetched material. This is observed in the contrast difference in the windows in the main image of (c) with the lighter contrast being the thin top layer and the dark regions being holes to the deep etched material underneath. This indicates that the surface of the windows have either been contaminated (such as with large amounts of oxides) or damaged in a way such that they do not thermally etch as readily as the material underneath. This is interesting as it suggests that the sample itself (Figure 6-5 (a) and (b)) is the source of the unsuccessful reproduction of Figure 6-1 (a) and (b). Thus, processing plays a key role in the ability to reproduce Figures 6-1 (a) and (b) and hence a detailed investigation of the impact of fabrication and cleaning on the sublimation of the GaN windows is necessary. Another possibility is that the original template itself, before processing was contaminated to some extent which resulted in the unsuccessful morphology observed.

6.3.4 Fabrication of a new template

After fabrication of a new sample (B1 in Table 6.1), the subsequent sublimation reveals a sample with no central hole features. Thus, we can likely rule out that the lack of central hole features in the G1 template (Figures 6-5 (a), (b)) is due to the initial template itself, before processing. This is as the results in Figures 6-5 (a) and (b), from the previous sample, G, has effectively been reproduced in the new sample, B, in Figure 6-5 (e) inset. This again demonstrates that the impact of the fabrication and cleaning is a likely source of poor sample morphology.

6.3.5 Further cleaning with long O_2 descum

Samples G2 and B2 were taken from the B1 and G1 templates but with additional cleaning steps preformed on them, as detailed in Table 6.1. Comparing G1, (a), to the sample with further cleaning processes, including a 10 minute O_2 descum, (d) main image, one can see that the additional cleaning steps have led to a much rougher, 'lumpier' morphology. Similarly, comparing B1, (e) inset, to that of B1 with the additional cleaning steps (B2, Figure (e) main image) the morphology here is also rougher, with a 'brain-like' structure across the whole window. Comparatively, B1 appears less rough than that of G2, which has similar morphology to A3. However, both have undesirable features without a singular uniform feature in each window, as is required for

site-controlled quantum dot growth. It is apparent that the additional cleaning steps have had a negative impact in the subsequent morphology after sublimation. New samples taken from the G1 and B1 templates were taken and the cleaning steps repeated with a much shorter O_2 descum time (1 minute) to give an indication if reducing this step has a large impact in the resulting morphology.

6.3.6 Further cleaning with a short O_2 descum

Comparing the G3 (Table 6.1) sample in Figure 6-5 (d) inset to that of G1 (a) one can see that again the additional cleaning, even with a reduced O_2 descum time has not resulted in any real morphological improvement. Specifically, the G3 is still very rough and 'lumpy', however, the lumps themselves seem to be smaller in size than that observed in G2 (d) main image. This represents a small improvement in the morphology of the sample. Similarly, B3 (F) has also seen some improvement in morphology compared to that of B2 (e). However there still appears to be some roughness to the windows although this is hard to see. Importantly neither the B3 or G3 samples, undergoing the additional cleaning, have successfully reproduced the results in Figures 6-1 (a), and (b). So, whilst the length of the O_2 descum does have a small impact on the morphology of the windows, it does not appear to be a particularly vital step, and, in fact, may have a negative impact on the samples themselves.

6.3.7 Effect of reactor pressure

The impact of the reactor pressure (during sublimation) on the sublimation process under N_2 carrier gas was also investigated but this had very little impact on the success of recreating the morphology of Figure 6-1 or in a change in the morphology itself at all. For this reason these results won't be presented here.

6.3.8 Effect of the CHF_3 dry etching

The impact of processing on the morphology of the sublimed samples is stark. For this reason optimised etching through the SiN_x mask was investigated in order to see if exposure of the GaN surface to the CHF_3 dry etch had had a negative impact on the surface morphology after sublimation.

Thus, this exposure was minimised by two methods. The first, B4 and B5 (with O_2 descum) in Table 6.1 etched up to the mask and then through the mask with BOE 5:1.

The second, B6 and B7 (with O_2 descum) (Table 6.1) used a carefully optimised etch time such that there was limited exposure of the GaN surface to the dry etch.

Sample B4 (Figure 6-5 (g) main image) has rough lumpy features across the whole window. With the addition of an O_2 descum (B5, Figure 6-5 (g) inset) the lumpiness observed appears slighly more centralised. In sample B6 (Figure (h) main image), there appears to be the same slight sign of central features with cracking and lumpiness that seems to occur across the entire GaN window. Similarly with B5, B7 (Figure (h) inset) offers a minimal improvement with more well defined localisation of lump features towards the centre of the GaN windows.

Overall, the windows of all samples B4-B7 are rather lumpy and undulating. There may be some, marginal, improvement with the addition of an O_2 descum (B5, B7) but this is minimal. The same is true with the minimisation of the GaN window to contact with the CHF_3 plasma in general. Thus, controlling this fabrication parameter extremely carefully is not particularly important.

The investigations into reactor cleanliness, sublimation conditions and processing parameters in this section (6.3) have not rendered any significant improvement in the morphology of the sublimed samples samples. In all cases, uniform ‘pin-hole-like’ central features, such as those in Figures 6-1 (a) and (b) were not realised. Indeed, in most samples lumpy, undulating morphology across the majority of the GaN window was observed. Thus, it appears the parameters examined in this section (6.3) did not drastically alter the GaN window morphology. Hence, it is unlikely the parameters investigated here were responsible for the lumpy, undulating features in the majority of GaN windows. Investigation into other areas of the sublimation recipe and fabrication process was therefore required.

6.4 Initial study into the effect of sublimation time on the morphology of the samples

Initial attempts to tune the fabrication/cleaning steps to improve the GaN morphology after sublimation were rather fruitless. A study of the impact of the growth conditions, specifically the growth time, was employed in order to determine if the sublimation recipe itself required optimisation to reveal successful structures.

For B5, after 30 minutes etch time (Figure 6-6 (a)) the morphology of the sample is very promising, especially in the centre of the sample where there are some central holes. The majority of the holes have unwanted deposition/growth at the centre but this sample is promising nonetheless. However, after 60 minutes (d) the sample appears rough with large features compared to those in (a). The same is true after 120 minutes, shown in (g), where the mask also appears to have degraded after this etch time (see inset). Thus, for this sample, sublimation time is shown to be a critical parameter to optimise in order to realise small central hole structures, especially homogeneously.

Similar results can be found for B7 after 30 minutes etch time (Figure 6-6 (b)) albeit less successful. As can be seen from the inset in (b) there is the occasional central hole but most have central growth within the window where the central hole would have been located. Again, as with B5 (a), as time is increased to 60 minutes (e) and 120 minutes (h) to morphology becomes considerably worse.

The fabrication details of B8 was designed in order to follow the process of Coulon et al. [55] more closely (see B8 in Table 6.1) than that of any of the B or G samples presented so far (G1-G3, B1-B7 in Table 6.1). Specifically this processes utilised only one piranha clean to minimise surface oxidisation and surface damage.

The B8 (see Table 6.1) sample is shown for 30, 60 and 120 minutes sublimation time in Figures 6-6 (c), (f) and (i), respectively. This sample appears to be the most successful across all three etch times. In (c) there is an overall majority of successful windows, with central hole features, in both the centre and edge of the sample. As sublimation time increases to 60 (f) and 120 (i) minutes, the size of the hole features in both the centre and the edges of the samples appear to increase in size. In addition, there appears to be the formation of 'channels/cracks' across the window regions propagating out from the central holes. These appear to also increase in width and number as growth time is increased from 60 to 120 minutes.

Samples G1 and B2 were also investigated, but very little change was observed across the sublimation time range investigated. Whilst this shows that sublimation time alone

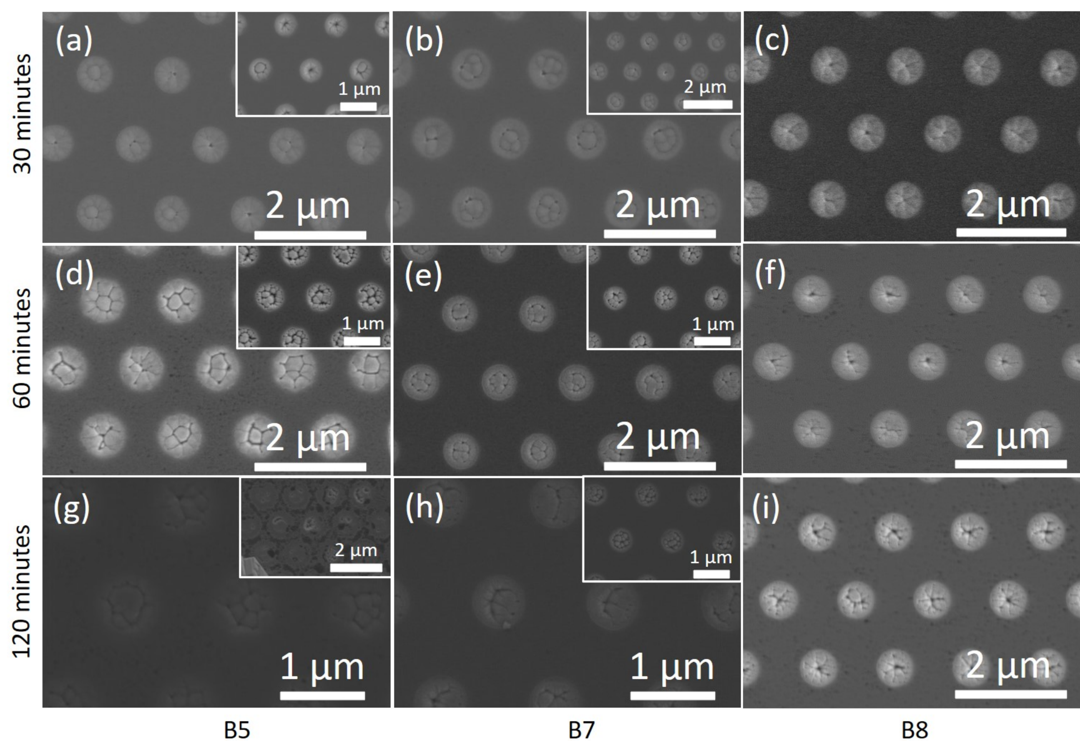

Figure 6-6: This figure shows the results for the initial sublimation time study. 30 minutes sublimation time is shown for samples B5, B7, B8 in (a), (b) and (c) respectively. 60 minutes sublimation time is shown for samples B5, B7, B8 in (d), (e) and (f) respectively. 120 minutes sublimation time is shown for samples B5, B7, B8 in (g) and (i) respectively. All main figures are images of the centres of the samples and the insets are those of the sample edges.

cannot be the only factor required to achieve the desired morphology, these samples were rather insignificant. For this reason these samples are not shown.

The success of the window morphology after sublimation is clearly dependent on time for B5, B7 and B8. This is therefore a critical parameter that may need further tuning to avoid unwanted central lumpy growth in the GaN windows. Additionally, it appears from B8 that the sublimation time can be used to tune the size of the central hole openings.

6.5 Impact of oxidisation on the sample surface and resulting sublimation

In order to test the impact of surface oxidation on the sample morphology after 30 minutes sublimation time, a BOE 5:1 treatment was applied to a selection of samples prior to thermal etching. This was performed for $\sim$ 30 seconds in order to have enough of a deoxidising impact on the samples such that a change in sublimation morphology with respect to untreated samples can be easily discerned. The BOE 5:1 treatment was limited to $\sim$ 30 seconds in order to limit the removal of the thin, $\sim$ 35 nm, mask. The etch rate of a SiN_x layer on a silicon substrate in BOE 5:1 was calibrated to be 30 - 40 nm/min.

In Figure 6-7 (a), a sample from the A3 template presented at the beginning of this chapter is shown after a BOE 5:1 treatment and 30 minute sublimation. The combination of the BOE 5:1 treatment and the shortened sublimation time has led to a sample with some potentially usable hole features at the centre of some of the GaN windows. However, there are many windows with undesirable growth in the central region. This result overall is surprising as it shows that the A3 sample is potentially salvageable and usable even after the excessive processing steps performed upon it.

In Figure 6-7 (b), the B8 sample after 30 minutes of sublimation is presented. The sample has arrays of windows with many of them possessing central hole features without unwanted deposition/growth. There is still the presence in some windows of this unwanted deposition/growth. In addition, the hole structures themselves are irregular, many with shapes deviating from that of a perfect circle. Even with these issues, this result is still promising for the growth of InGaN quantum dots within the holes themselves. The homogeneity and regularity of the hole structures may be improved upon further by fine tuning the sublimation temperature and, in particular,

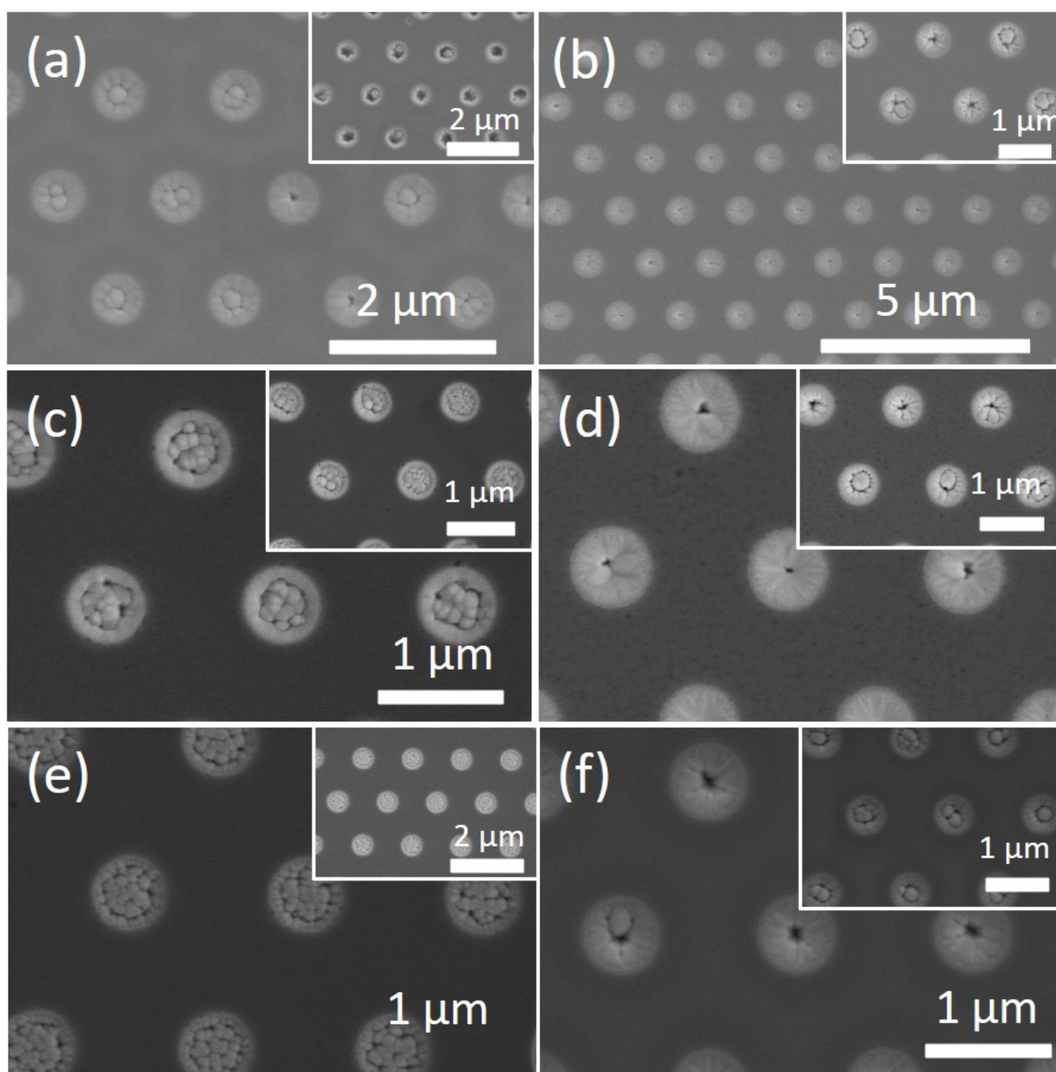

Figure 6-7: In this figure, samples have undergone sublimation for 30 minutes at a set temperature of 900 ^{o}C after a BOE 5:1 treatment, unless otherwise specified. In (a), sample A3 is presented. In (b), sample B8 is presented. In (c), sample A3 without a BOE 5:1 treatment and with the HCl:D.I. water treatment is shown. In (d), sample B8 without a BOE 5:1 treatment and with the HCl:D.I. water treatment is shown. In (e), sample A3 is presented but this sample, critically, has not undergone any BOE 5:1 treatment. In (f), sample A3 with a BOE 5:1 treatment and with the HCl:D.I. water treatment is shown. All main images show the centre of the samples, the insets show the edges of the samples.

the sublimation time.

As another test a sublimation process was performed on an A3 sample without such a BOE 5:1 treatment, the results of which are shown in Figure 6-7 (e). As can be seen from (e) there is a rough, lumpy morphology which appears to be present across the entire sample as has been seen previously in Figure 6-3 (g). This shows that by applying a BOE 5:1 treatment on sample A3 is a critical process required for salvaging the A3 sample (comparing (e) without, to (a) with a BOE 5:1 treatment).

Samples B1, B2, G1 and B7 were also investigated (not shown). All of these samples showed a very marginal improvement. This was certainly not significant enough to constitute a useful surface morphology after sublimation.

To determine more conclusively if the removal of oxides has a significant, positive impact in the resultant sublimation morphology of the samples another chemical treatment was performed using a 1:1 ratio of concentrated HCl:D.I. water for a duration of ~ 5 minutes. This treatment was chosen as it has been shown to remove oxides effectively from GaN in previous literature [325], [326]. Moreover, a longer cleaning time could be used for a more thorough oxide removal as HCl is unlikely attack the SiN_x mask. The results of this are shown in Figures 6-7 (c) and (d).

The HCl:D.I. treatment on samples for ~ 5 minutes at room temperature has not had a significantly beneficial impact on the morphologies of any of the surfaces after sublimation if at all ((c) and (d)). The simplest explanation of this observation is that oxide removal has not had a major impact on the surface of the samples. This would then suggest the mechanism behind the rough, lumpy surface morphology which has been observed is not as a result of surface oxides. It can however, be discerned that a BOE 5:1 treatment has a significantly beneficial impact on the A3 sample with or without the HCl:D.I. water treatment ((b) and (f)). It is likely that surface roughness/defects on this sample is somehow reduced.

6.6 Further optimisation of the sublimation time

In this section a closer inspection of the effect of sublimation time on the B8 and A3 samples which had undergone a BOE 5:1 treatment was performed. In Figure 6-8, an additional time study for the B8 and A3 samples, both with a BOE 5:1 treatment, is shown.

After 10 minutes sublimation (Figures 6-8 (a) and (b)), it appears that not enough material has migrated across the GaN window. This has led to a lumpy morphology without revealing properly formed central holes, especially in sample B8. Similar is observed in A3 with a rough, lumpy morphology in most windows.

Sublimation after a duration of 20 minutes reveals small central holes in both samples in most windows (see Figures 6-8 (c) and (d)). This looks to be a good balance between enough sublimation to realise relatively uniform central holes and, in addition, to keep the holes reasonably small.

40 minutes of sublimation is shown in Figures 6-8 (e) and (f). In sample B8, (e), excessive material removal has led to less uniform holes with the start of sublimed channels propagating out from the central holes. As a result the features are less uniform. Sample A3, (f), has remained similar to that of 20 minutes sublimation time, (d). The results in this figure further suggests that the sublimation time is critical to the formation of relatively uniform central holes withing the GaN windows. In particular, 20 minutes is the most successful time. This is as at 20 minutes the central holes are fully formed but there has not been too much material removal such that the holes have become more irregular with 'channels' appearing in the rest of the window, as is the case for B8 after 40 minutes sublimation time.

6.7 Study of the effect of the piranha clean duration

A study of the effect of piranha clean time on samples from the B template (see samples B9-B14 in Table 6.1) and the resulting morphology after sublimation was investigated in the section.

It seems evident from all the data presented so far that not only the sublimation recipe employed but also the processing steps have a significant impact on the success of the formation of central holes within the GaN windows. One processing parameter which has not yet been investigated thoroughly is the impact of the piranha clean step.

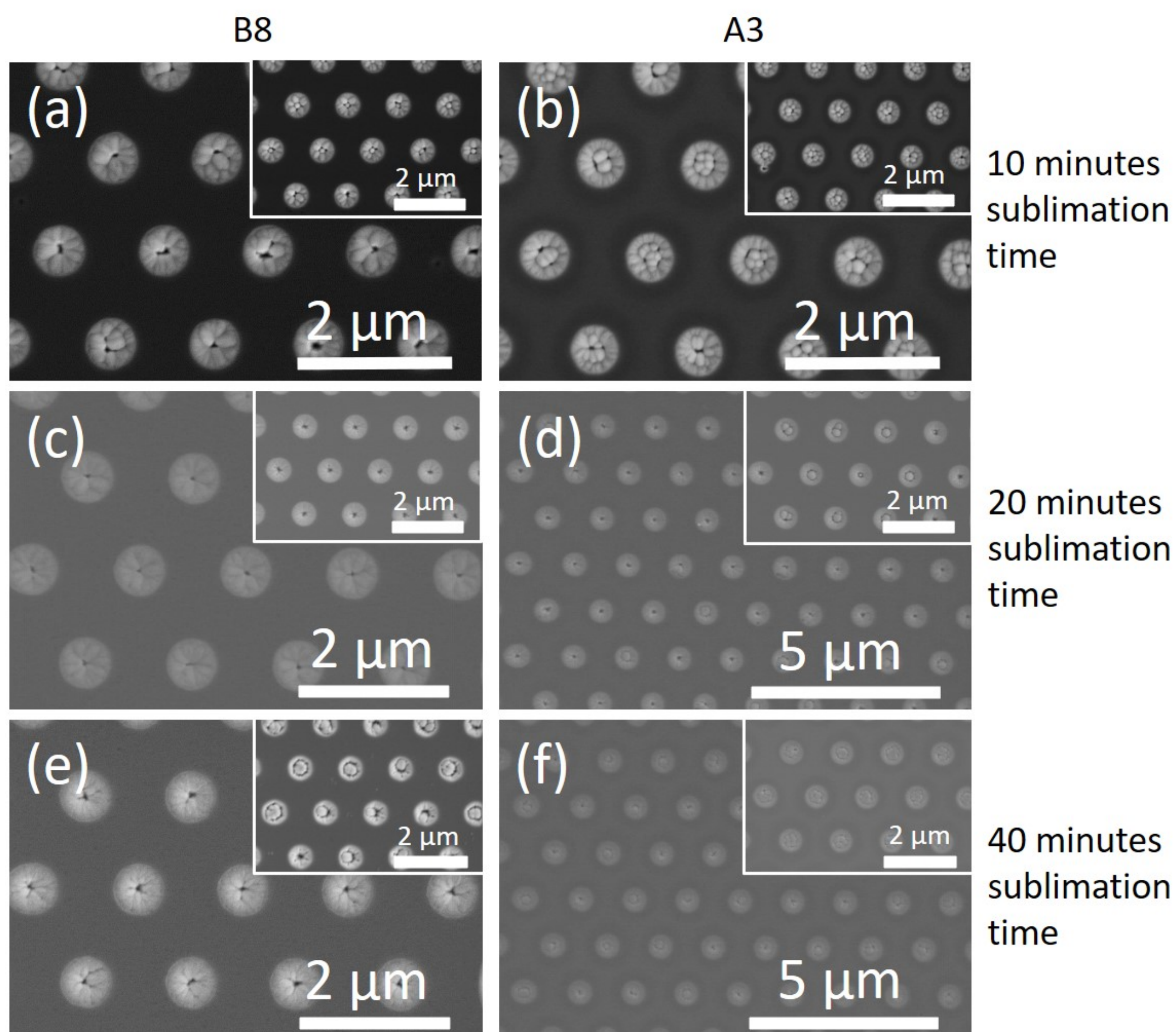

Figure 6-8: In (a) sample B8 is shown after sublimation at for 10 minutes. In (b) sample A3 is shown after sublimation at for 10 minutes. In (c) sample B8 is shown after sublimation at for 20 minutes. In (d) sample A3 is shown after sublimation for 20 minutes. In (e) sample B8 is shown after sublimation at for 40 minutes. In (f) sample A3 is shown after sublimation at for 40 minutes. All samples underwent a BOE 5:1 treatment prior to sublimated at 900 ^{o}C set temperature. For images (a), (b) (c), (e), the main image is at the centre of the sample and the inset is at the sample edge. For figures (d) and (f) the main image is the most successful region of the sample. The inset is a less successful edge of the sample.

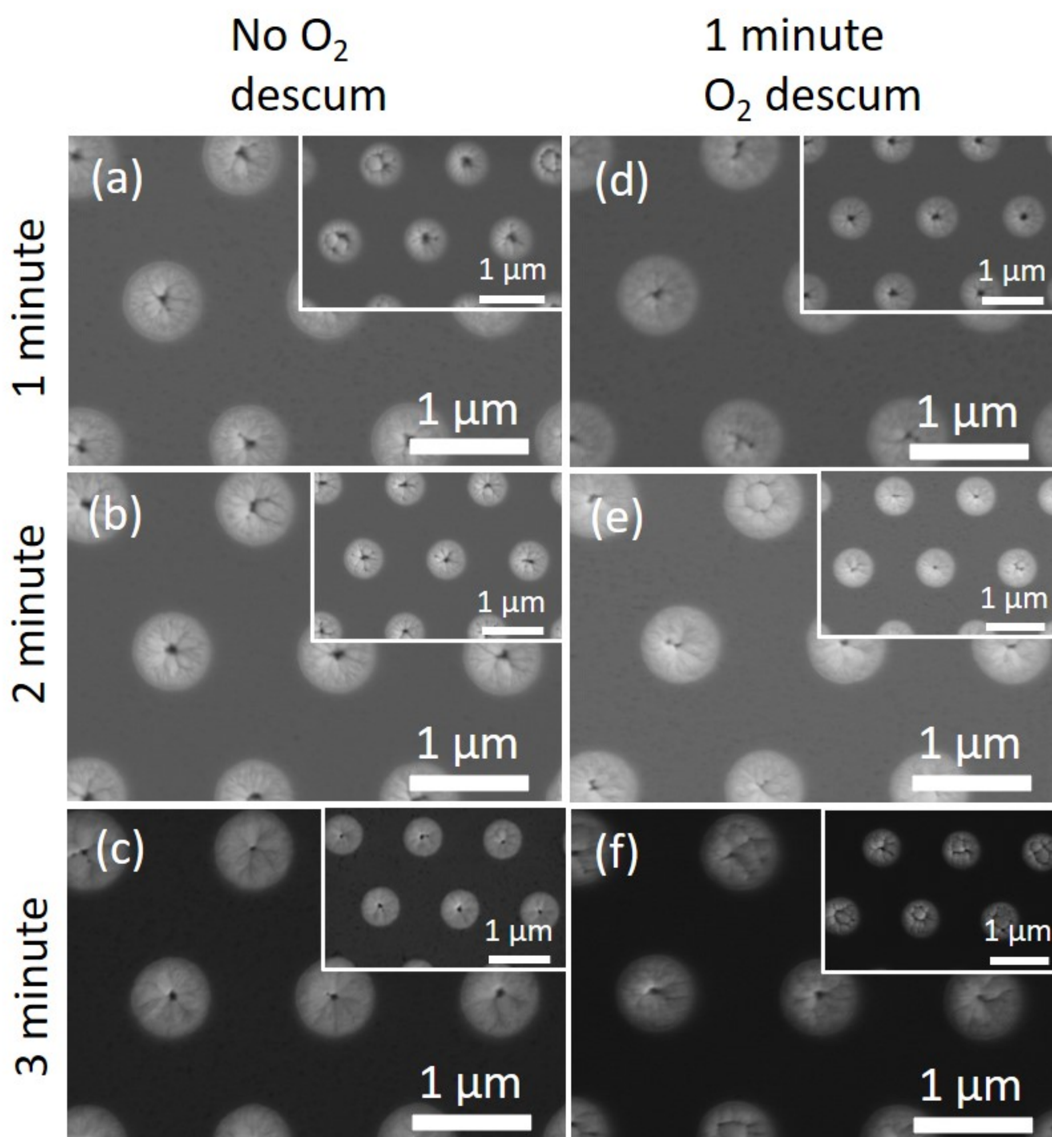

Figure 6-9: In (a), sublimation of sample B9 is shown. In (b), sublimation of sample B11 is shown. In (c), sublimation of sample B13 is shown. In (d), sublimation of sample B10 is shown. In (e), sublimation of sample B12 is shown. In (f), sublimation of sample B14 is shown. None of the samples (a) – (f) had a BOE 5:1 treatment, only a BOE 100:1 $\sim 20-30$ second dip. All samples were sublimated for 30 minute at a set temperature of 900 ^{o}C.

Indeed, whilst a piranha clean of a 3:1 ratio is an effective way of removing organic material, it is a rather aggressive cleaning process. It is certainly conceivable that excessive piranha cleaning could lead to significant surface damage of the underlying GaN. This could then impact the effectiveness of the sublimation process on the GaN window. For this reason, a piranha clean study was performed. Here, piranha cleans of different time durations on the GaN templates followed by sublimation are presented. Some samples also underwent an O_2 descum after the piranha clean and all had a ~ 20 second 100:1 ratio BOE performed upon them just prior to sublimation.

From Figure 6-9 the following can be determined. The O_2 descum step doesn't make much of a difference. If anything it has a slight negative impact. It appears that the samples which were cleaned for 1 and 2 min with piranha 3:1 had the most consistent topology with holes in the centre of most windows with central growth features a rarity. Thus, the piranha clean duration is then a critical processing factor. 2 minutes of piranha cleaning or less is the most desirable duration.

A BOE 5:1 treatment was also performed on second halves of all of the samples prior to sublimation (not shown) but this seemed to give no beneficial impact on the subsequent morphology and, in fact, appeared to have a slightly detrimental effect. Overall it can be discerned that piranha clean duration has a greater impact on the final morphology of the sublimed samples, compared to many of the other fabrication process parameters explored.

6.8 Mechanism of GaN sublimation under N_2

From the evidence collected from the experiments presented in this chapter, it is clear that processing, and in particular, the cleaning of the GaN samples plays a significant role in the morphology obtained after sublimation. Section 1.5 demonstrated that surface oxides were unlikely to be the cause of poor, rough morphology observed across a number of samples. The final cleaning stage of the AZ400K dip on sample A2 will have likely had a detrimental impact in realising a central small pit structure in the centre of the GaN windows after sublimation to some extent. However, as there were also issues in reproducing this morphology in newly fabricated templates, which also exhibited lumpy morphology, this is not the main source of the undesirable morphology. Moreover, some of the A3 template could be salvaged with a BOE 5:1 treatment. Whilst it is still certainly possible that there could be reactor chamber contamination, no noticeable change in surface morphology of the sublimed samples before and after extensive reactor chamber quartz component cleaning was observed. Hence, this hypothesis is also unlikely. Furthermore, contamination of the samples themselves was ruled out by the extensive and excessive cleaning upon some of the studied samples. Therefore, a rough, 'lumpy' surface morphology is very likely to be caused by surface roughening and damage created in the GaN windows during processing.

In order to further investigate the source of the lumpy surface after sublimation, AFM scans of the G1 sample prior to sublimation were performed. These can be seen in Figures 6-10 (a) and (b). As can be seen in (a) whilst there is some minor contrast differences within the windows, this is not especially prominent. One would expect a greater range of colour or at least more of a variation in the observed blue if there was large rough, lumpy features across the window prior to sublimation. There is some contrast differences between the centre and top and bottom of the windows but this is likely a scan artefact as it is also present across the SiN_x mask too, observed as the orange streaks present. There does appear to be some slight other colour differences within some of the windows however this is difficult to see in the 5x5 μm scan. Thus a 1x1 μm scan was performed (see (b)) to more closely inspect a window's features.

In Figure 6-10 (b), one can see a single GaN window surrounded by SiN_x mask. Very few large roughness features can be seen within the window other than the slight pit offset to the left from the centre of the window. Whilst the scale is roughly 50 nm in total height one would still expect to see some larger rough features if they were present as a 5 nm change in height gives a easily noticeable colour change with the

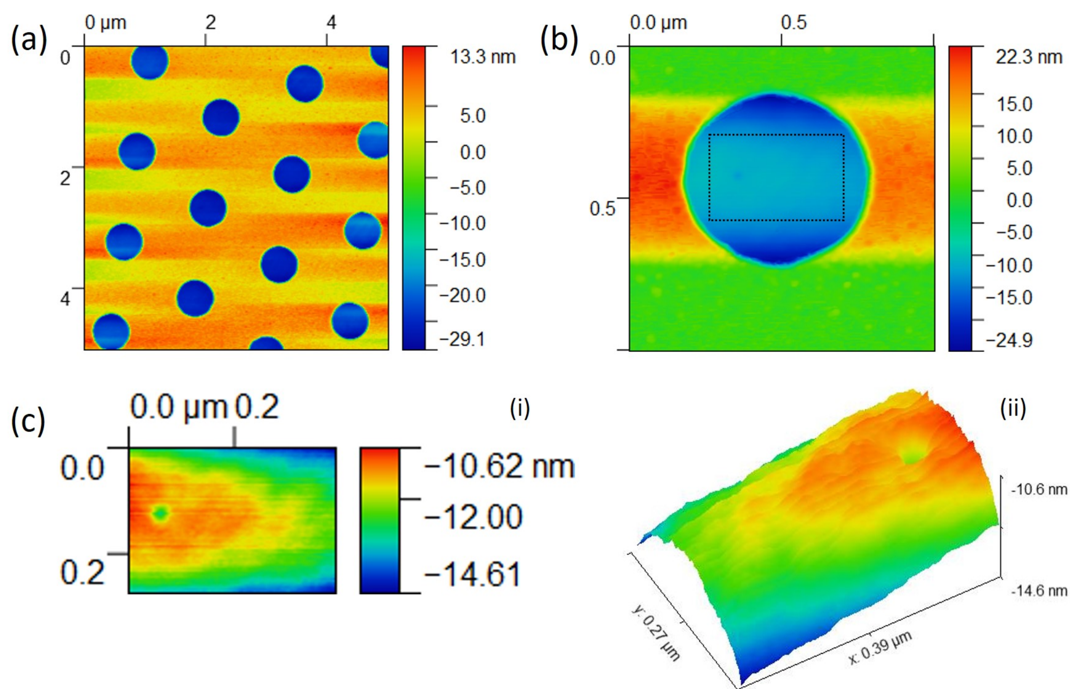

Figure 6-10: Figure 12 shows an AFM scan of part of the G1 sample, prior to sublimation (see Table 6.1). In (a) a 5x5 μm AFM map of the sample is shown. In (b) a 1x1 μm AFM map of the sample is shown. In (c) a zoom of a region of the AFM map shown in the dashed rectangle in (b) is presented. In (i) the planar AFM image is shown and in (ii) a 3D map of the image in (ii) is shown.

colour scheme used. For instance, larger rough features are observable on the SiN_x mask itself.

In order to explore this more fully, a crop of the figure in (b) was taken in order to view the GaN window surface independently of the SiN_x mask. This is shown in (c) (i) (planar) and (ii) (3D). The total height change in (c) (i) from left to right and top to bottom is an artefact of the scan in addition to the observed scan lines across the window. However, there does appear to be some small undulation across the window, especially visible in the 3D image in (ii), other than the obvious pit. It is also possible that the observed small undulations could also be some form of artefact but as they are present across most of the image in (c) (ii) this seems unlikely.

Thus, from this data it can be concluded that there are only undulations which are small in height. After sublimation however, a severely rough surface present in the GaN windows is observed. It is likely that, due to the initial undulations prior to sublimation being small in magnitude, that small scale roughness may be responsible for the lumpy morphology observed after sublimation. What is meant by this is that, a very small scale, undulating, rough morphology may be present on the GaN surface that is present as result of surface damage, and would not be present in undamaged c-plane GaN. It is likely that the small scale roughness leads to extra nucleation sites that allows more easy nature of the GaN or Ga and N adatoms travelling across the GaN window to bond to, compared to the normal free bonds present on an undamaged c-plane GaN layer. Thus, these new nucleation sites, as a result of surface damage, act as sinks for reincorporation of material during the sublimation process leading to the rough lumpy grains observed on the surface.

It was found that a piranha clean duration of over 2 minutes piranha leads to a poor surface morphology after sublimation. It is likely, due to this being a very aggressive cleaning process, that this causes the formation of small roughness features on the GaN surface when the clean time is long enough. This rough, damaged surface limits the mobility of sublimed species across the GaN window and restricts the movement of material away from the centre of the windows. Additionally, this allows for more reincorporation of material. This results in successful windows having smaller holes at the centre as less material has migrated effectively from the centre of the window. There are far more windows with central growth features, compared to piranha cleans of shorter times, where material has not migrated effectively from the centre of the window.

Thus, the cleaning processes and in particular the duration and number of piranha

cleans is a critical factor. This is summarised in Figure 6-11 (a). A rough, damaged surface would hinder species migration in the form of either liquid Ga or gaseous GaN or gaseous Ga and N across the window. It is desirable to determine if the material migrating across the window is indeed liquid GaN or gaseous GaN or Ga and N. According to Coulon et al. [55] and Koleske et al. [327] liquid Ga droplet formation does not occur for thermal etching in a nitrogen atmosphere. Therefore, it is most likely that it is gaseous GaN, gaseous Ga and N or a combination of the two which sublimes and then diffuses across the GaN window. To further corroborate this, as it is known that HCl effectively dissolves liquid Ga droplets [328], a sample with a large amount of lumpy features, post sublimation, was immersed in HCl:D.I. water at a 1:1 ratio for 30 minutes at ambient conditions. After this process (data not shown) no noticeable change in the sample surface occurred. This is as the lump features in the centres of the windows, thought to possibly be Ga droplets, remained after the HCl treatment. This then provides further evidence that the transport of material across the surface is not in the form of liquid Ga. Thus, the material diffusion across the sample after it has been thermally etched will be either gaseous Ga and N or GaN. Some of the gaseous species appears to accumulates near the mask-window interface, leading to a gradient from the mask region to the inner region of the window, finally with a sharp small hole at the centre. A schematic of the process is shown in Figures 6-11 (b) and (c).

When one considers the ability to salvage the A3 sample via a BOE 5:1 treatment, a possible explanation can be proposed. First it is important to consider than the only sample where a BOE 5:1 clean significantly improved the surface morphology was that of A3. It is likely the AZ400K dip actually had a beneficial impact on the surface morphology when combined with a BOE 5:1. A previously rough and damaged surface could have had this roughness etched away by the short AZ400K exposure which would react with the GaN via the formation of GaO_x [53]. The remaining GaO_x could then have been removed via the BOE 5:1 clean, leaving a very smooth surface, allowing for the formation of small central holes upon sublimation. Some of these oxides could be more readily attacked by BOE than HCl:D.I. water. The reason behind this is unknown but it may be as a result of generation of subsurface oxides which HF may remove more easily than HCl:D.I. water. This would require further investigation to determine if this was indeed the case. It is worth noting that a G1 sample was also able to be salvaged (data not shown) via the use of a 10 second AZ400K dip followed by a 40 second BOE 100:1 treatment. This further supports that the AZ400K dip is key to salvaging the samples.

Using the understanding of the likely mechanism of sublimation and the results from

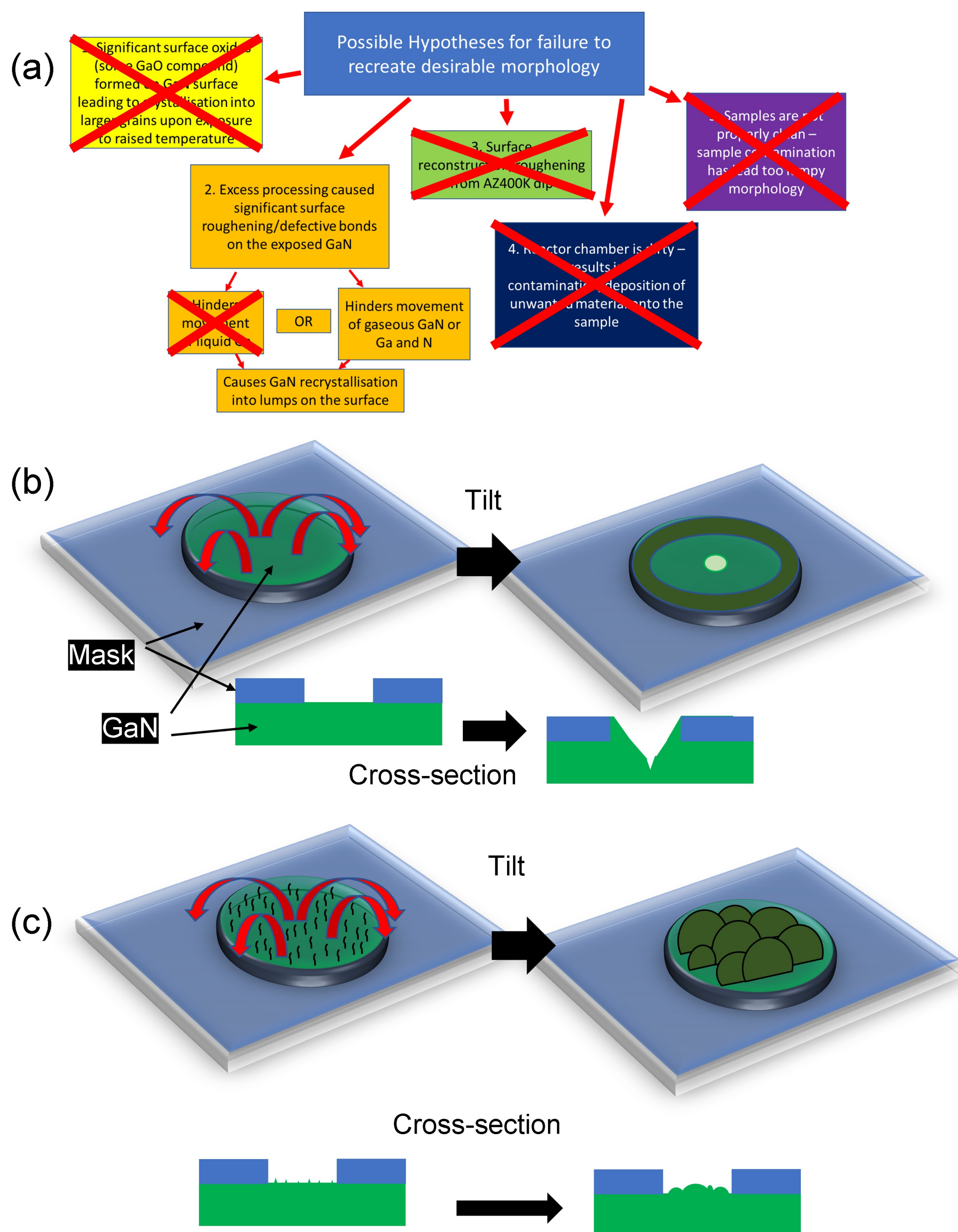

Figure 6-11: In (a) the diagram of Figure 6-4 is shown with the incorrect possible explanations for the poor morphology observed in the A3 sample crossed through. From the experiments preformed the most likely mechanism to explain the morphology of A3 is left without a red cross through. In (b) the mechanism of surface migration of sublimated species is shown, resulting in more material near the edge of the window and a hole at the centre of the window (right) after sublimation. This corresponds to an initially smooth, minimally damaged, GaN surface (left). In (c) the surface of the GaN window is roughened and damaged by over processing (black lines on window of left figure). This then leads to a lumpy, rough morphology after sublimation (right figure). In (b) and (c) both tilted and cross-sectional diagrams are shown.

previous sections, optimised growth conditions were preformed on the fabricated samples which have rendered the best results. The results of these final optimisations are shown in the next section.

6.9 Conclusions of the sublimation investigation and final optimisations

In order to achieve the aim set out at the start of this chapter of growing InGaN quantum dots within uniform arrays of holes, of quantum dot dimensions, at the centre of the GaN windows the sublimation process needed to be optimised. The small hole dimensions realised in Figure 6-1 (b) when subliming at a temperature of 875 ^{o}C in addition to those realised after a sublimation time of only 20 minutes in Figure 6-8 provide good conditions for quantum dot sites. Thus, this set temperature and sublimation time was chosen in addition to all the other standard conditions used throughout the rest of the sublimation experiments presented here. This was performed upon some of the most successful samples (B13, B8, A3 with BOE 5:1 treatment and B9) and can be seen in Figure 6-12.

As can be seen in Figure 6-12 (a) only minimal success is achieved with sample B13, although there were the presence of some very small central hole features. Thus, this sample is an unlikely candidate to produce InGaN quantum dot sites. In (b), showing sample B8, there is moderate success across most of the sample with over 50% of the windows (estimated from image of lower magnification, this is not shown here) showing successful small central hole openings. Sample A3, in (c), is also less successful with a large inhomogeneity across the sample. The edge (not shown) shows moderate success, whereas the centre of the sample is far less successful. Sample B9, in (d), shows the most successful sample. As can be observed in (d) the sublimation is largely successful across the majority of the sample with the majority of windows displaying the desirable morphology. This demonstrates that careful optimisation of the processing parameters and growth conditions can be utilised to realise successfully sublimed small hole openings, across the majority of the sample, suitable for InGaN quantum dot growth.

Whilst suitable sites for InGaN quantum dots were created, the growth of site-controlled InGaN quantum dot structures was not investigated in much depth. Thus the results of attempted InGaN quantum dot growth has not been presented in this thesis as we chose to concentrate on GaN site-controlled quantum dot growth on the AlN nanostructures, created in the previous two chapters. The results of the attempted site-controlled GaN quantum dot growth will now be presented in Chapter 7.

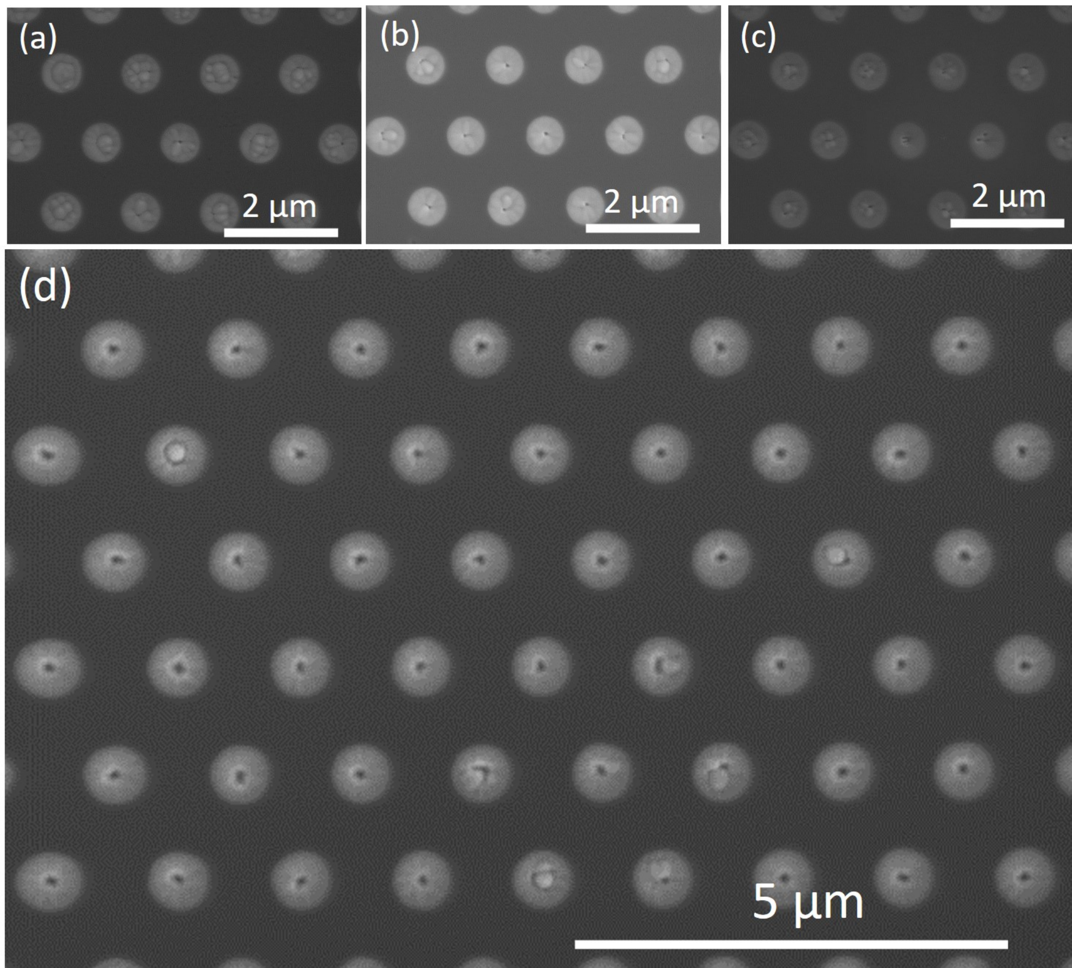

Figure 6-12: In (a), sample B13 is shown. In (b), sample B8 is shown. In (c), sample A3, after a BOE 5:1 treatment, is shown. All main figures in (a)-(c) are that of the centre of the sample, the insets are that of the edge. In (d) sample B9 is shown. All images show samples after sublimation with optimised conditions.

Chapter 7

Attempted site-controlled GaN quantum dot growth

7.1 Introduction

The target of this thesis was to grow a single GaN quantum dot on sharp, periodic AlN nanofeatures. A review of the literature is an important starting point in order to chose some suitable starting growth conditions from which site-controlled GaN quantum dot growth can be attempted. Self-assembled GaN/AlN quantum dots are grown via the Stranski-Krastanov (SK) growth mode. This can be achieved with MOVPE. The GaN layer is typically grown under a very low V/III ratio of input precursors [96]. Quantitatively, this V/III ratio is usually below 100 and can be as low as 30 or even lower [329], [330], [331]. This is especially true if one wants to grow quantum dots with relatively small dimensions [332], [330]. Such Ga-rich conditions are used in order to decrease the surface energy of the planar AlN layer [330] allowing the build-up of strain during heteroepitaxial growth to be the dominant factor between compensating for the the strain and minimising the surface energy. This then allows for the formation of SK quantum dots via a 2D-3D morphological transition. Self-assembled quantum dots can also be grown at higher V/III ratios, but this leads to larger dots [332], [333]. GaN growth pressures have been reported to be in the range of 200 mbar [332], [96] - 133 mbar [330]. GaN quantum dot growth temperatures have been reported to be in the range of 860 ^{o}C [330] - 990 ^{o}C [334], [96].

Choi et al. [273] grew GaN quantum dots at the apices of AlGaN nanorods, utilising a very high V/III ratio to promote faster growth in the c-direction compared to other

Table 7.1: Initial quantum dot growth conditions identified from the literature.

Initial GaN quantum dot growth conditions			
Growth temperature (^oC) (set)*	V/III ratio	Growth pressure (mbar)	Growth time (seconds)
820	20,000	300	?

*True temperature, as measured by pyrometry, has an off-set from the set temperature. In this case the true temperature is higher than the set temperature by ~ 100 ^oC.

facets. The specific TMGa and NH_3 flow rates used in [273] were 0.13 μmol/min and 60 sccm, respectively. This corresponds to a V/III ratio of $\sim 20,000$. The growth temperature utilised to grow site-controlled GaN quantum dots upon AlGaN was of 880 ^oC.

What can be seen from the information above is that there are two different growth conditions, and, in particular, V/III ratios, that are utilised depending on if one wants to grow Stranski-Krastanov GaN/AlN quantum dots or GaN/AlGaN nanorod site-controlled quantum dots. Whilst we will be growing GaN/AlN quantum dots they do indeed intend to be grown at the apices of AlN nanorods. For that reason it seems most logical to attempt to reproduce the GaN growth conditions reported by Choi et al. in [273] as opposed to those conditions reported in the self-assembled GaN/AlN quantum dot literature. Concerning the V/III ratio, and considering our systems limitations, the above precursor flows are particularly low. Our MOVPE system had mass flow controllers for the precursor flows that were unable to accurately replicate such low flow rates. We can, however, recreate roughly the same V/III ratio with our reactor albeit with higher precurosr flow rates. For our reactor this corresponds to a flow rate of 1 sccm of TMGa and a flow rate of 1800 sccm for NH_3 in order to realise a V/III ratio of $\sim 20,000$. Whilst a growth temperature of 880 ^oC was used in the work by Choi [273], there is no mention of if this was measured via pyrometry or by their growth reactors internal temperature monitoring apparatus. Thus, there is no mention of the magnitude of any off-set, if present, of this growth temperature value. Hence, this value can only be taken with caution, and it was decided to target a true growth temperature of ~ 920 ^oC (corresponding to a set temperature of 820 ^oC). As growth pressure was not specified in the work by Choi [273], other literature for the growth of GaN/AlN systems was consulted and was found to be in the range of 100 [335] - 267 [336] mbar. For this reason a growth pressure of 300 mbar was chosen as a starting point. Table 7.1 summarises these growth conditions. In order to determine a suitable growth time, the growth rate was investigated utilising these conditions.

7.2 GaN growth rate

The growth rate of GaN using the growth conditions specified in Table 7.1 was required in order to select an appropriate deposition duration for quantum dot growth. As we were aiming to grow a thin layer of GaN on the remaining c-plane of a sharp feature, such as a nanopyramid or rod apex, calibration of the growth rate of c-plane GaN was therefore appropriate. In order to do this in-situ monitoring of the growth was harnessed via the use of pyrometry/spectroscopic reflectometry.

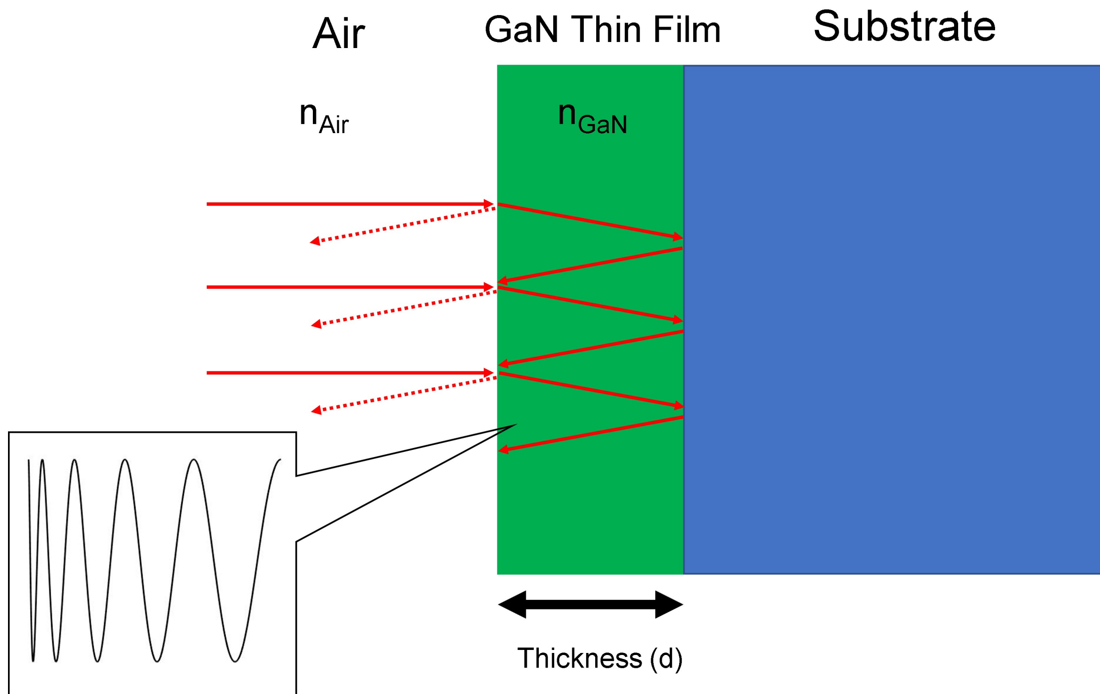

Figure 7-1: This figure shows a diagram of interference effects within a GaN thin film leading to Fabry-Perot fringes, as diagrammatically represented in the box to the bottom left. This figure is diagrammatically only and not to scale.

In-situ monitoring of growth via spectroscopic reflectometry allows for measurement of the true temperature of the sample during MOVPE growth [337]. Additionally, one can use this measurement tool in order to measure the amount of growth which has occurred [338]. The background of how this can take place will be now briefly presented followed by the calculation of the growth rate.

Fabry-Perot fringes originate from multiple interferences between beams transmitted and partially reflected from the thin film-air and thin film-substrate interfaces [339], see Figure 7-1. The resultant constructive and destructive interference of the beams leads

to the the formation of peaks and troughs in the detected signal. The positions of the peaks and troughs in the fringe pattern are determined by the Fabry-Perot relationship:

$$m \cdot \lambda = 2n \cdot d \quad [339] \tag{7.1}$$

where λ is wavelength, m is an integer corresponding to the number of successive peaks (i.e. a nearest neighbour peak-to-peak value would have m = 1), n is the refractive index and d is the thickness [339]. Hence, as the peaks and troughs at a given wavelength is dependent on the thickness for the thin film, the change in position of these peaks and troughs can give an indication of the corresponding change in the thickness of the film.

In-situ monitoring of the changes in location of peaks and troughs present in the spectroscopic reflectometry signal can give a measure of the growth thickness deposited and, therefore, the growth rate. The growth rate can be calculated using the below equation from [338], this is a modified version of the equation shown above from [339]. In this case, m is effectively taken as a half. When considering movement of the spectra to the left from a peak to a trough (or vice-versa) in the reflectometry signal, one can determine the growth rate from the following:

$$Growth\ rate = \frac{\lambda}{4 \cdot n} \cdot \frac{1}{\Delta t} \quad [338] \tag{7.2}$$

Here λ is the wavelength at which the peak/trough shift is being measured, n is the refractive index of GaN, and Δt is the time elapsed during the movement from a peak to trough (or vice versa). This measurement of the change in peak/trough position can be seen in Figure 7-2. In this figure the spectral reflected signal from the sample is plotted in black after a recipe run time of 3338 seconds. In blue the spectra is shown after 6238 seconds. Using the red vertical line at 500 nm as a reference point one can see the spectra has effectively shifted to the left after by a distance of ~ 1 trough to peak.

Extracting the refractive index of GaN at ~ 900 ^oC from [337], this is found to be a value of 2.4. If we look at the shift to the left of a trough to peak at 500 nm in Figure 7-2, this occurs in ~ 2900 seconds. Thus, we can calculate the growth rate as:

$$\approx 1 \text{ nm/min.}$$

Thus, from this measurement an approximate growth rate of 1 nm/min has been extracted. It is worth mentioning that this is the growth rate across a planar GaN

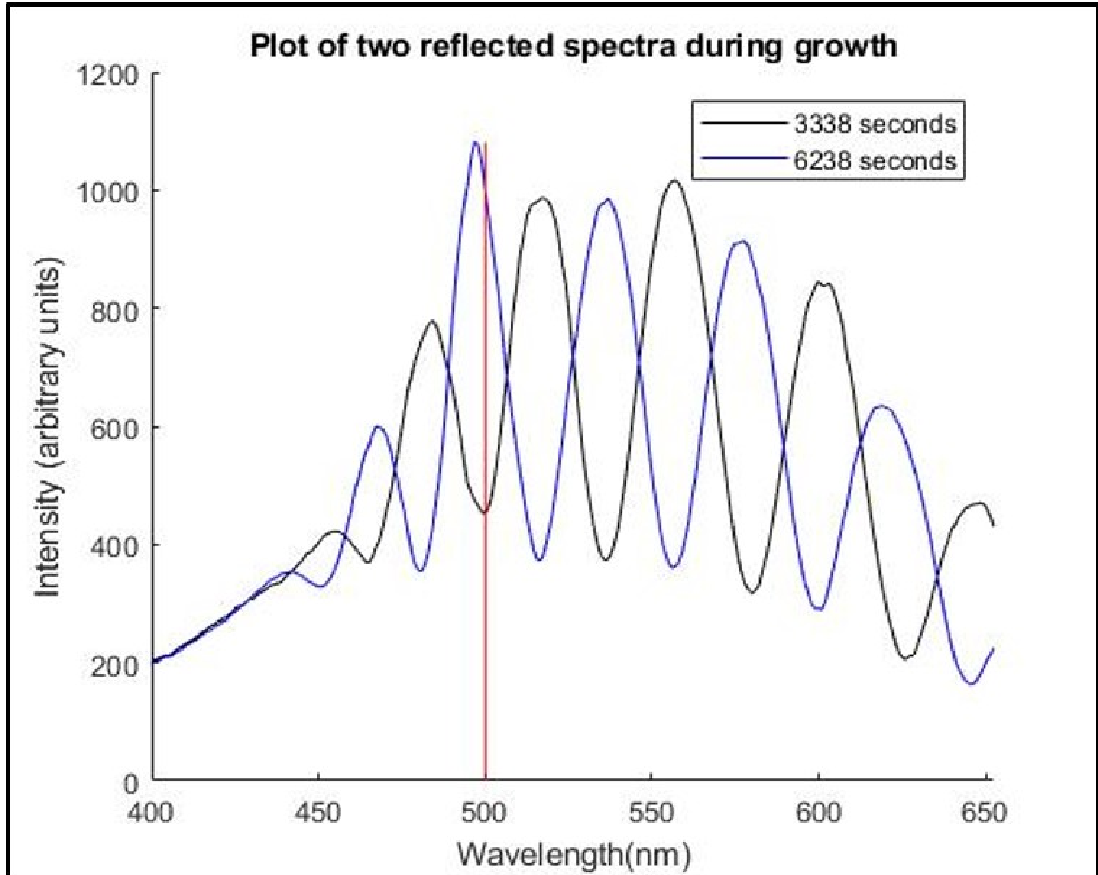

Figure 7-2: In this figure, the black line shows a plot of the reflected pyrometry signal from the in-situ growth monitoring system after 3338 seconds recipe run time. In blue the signal is again presented but after 6238 seconds run time. The red line at 500 nm is shown as a reference point from which to see the evolution of the plot in black to the plot in blue. This data was extracted from the 'Laytec Episense' software and plotted using MATLAB.

sample. The growth in this chapter intends to be localised to a small nanostructure c-plane apex. Hence, one would expect that a shorter growth time would be required to create a small localised region of GaN growth of height of 1 or a few nanometers. This supposition is further supported by the short growth time, 8 seconds, and low flow rates presented in the work by Choi [273]. Whilst this is a rather crude measurement and calculation, it does give an indication of the order of growth time that is required.

7.3 GaN growth on AlN nanopyramids

As was determined in the previous sections, some sensible growth conditions for the site-controlled growth of c-plane GaN quantum dots have been found. The aim was now to attempt growth upon a sharp AlN nanofeature. One array of promising structures realised in a previous chapter were the AlN nanopyramids formed by combining dry and wet etching. These appear to have very sharp apices, which could potentially house a single quantum dot. As the conditions determined in the previous section favour c-plane growth, it may be possible to grow a small amount of GaN at this apex, if there is a small c-plane, without also growing on the semi-polar planes.

It is worth mentioning that a very sharp apex is not necessarily an absolute requirement for growth of a 3-dimensionally confined system at a rod apex. A continuous quantum wire layer could be grown across a nanorod that would be thicker at the apex leading to a different ground state energy at this apex region compared to the rest of the wire [340]. According to Inoshita and Sakaki [340], this thicker channel at the ridge top of the rod would lead to stronger carrier confinement in this region [340]. This would then result in some 3D confinement at this apex. However, we chose to aim for very sharp features to grow our active regions upon as the level on confinement via a small region of material at a sharp apex encapsulated purely by the barrier material would likely be greater than that of a thickness variation of a wire. In the latter structure, carriers may be able to more easily excite, via thermal effects, into regions of lower quantum confinement compared to barrier capped growth at purely localised sharp features, which we aimed to create. Such an architecture would then lead to a QD device which would not be able to operate at as high a temperature as a QD device (such as the device we intended to create) fully encapsulated by a higher bandgap barrier layer.

Whilst the pyramids look exceptionally sharp see Figure 7-3 (a), a small top c-plane, beyond the resolution of the AFM tip, may still be present. Additionally, after a short anneal only, the nanopyramid peaks appear blunter, see Figure 7-3 (b). Considering

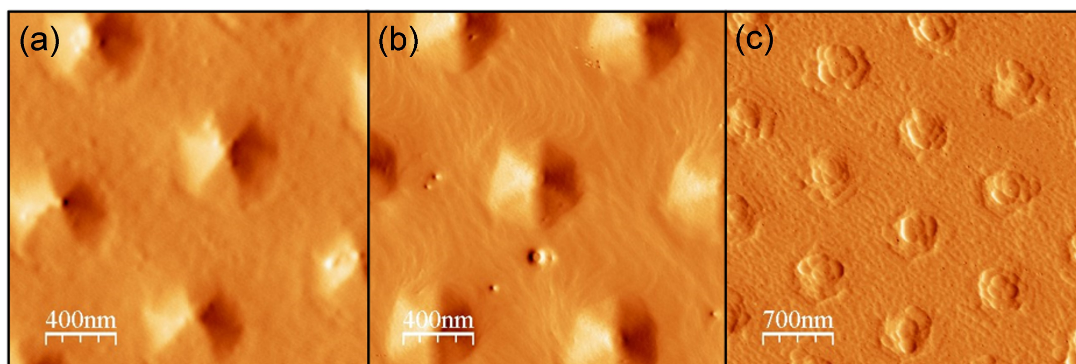

Figure 7-3: In (a) a nanopyramid sample is shown after wet etching and prior to any growth/anneal. In (b) shows a nanopyramid sample after a short anneal. In (c) shows a nanopyramid sample after 1 minute of GaN growth without an AlN cap. All the images were amplitude-retrace maps as this aids the viewing of the sharpness of the apices. This data was extracted via the WXsM software [56]

this anneal was merely a temperature ramp step which would be required in order to grow GaN in any case, this does offer promise that there should be some amount of small c-plane at the apex upon which to grow the quantum dot.

In order to gain a greater appreciation of the amount of GaN deposited after 1 minute and, if indeed, it would growth preferentially at the top c-plane, an uncapped sample was grown. This sample after growth can be seen in Figure 7-3 (c). As can be seen in this figure, there is a sizable amount of GaN growth visible across the sample signified by this 'lumpy' morphology. It does however seem to have some slight localisation to the AlN nanopyramid as a whole. Thus, it seemed sensible to grow for a shorter growth time to try and achieve small amounts of localised growth at the apices.

Two samples were deposited with GaN for two different growth times, followed by AlN caps. A summary of the growth conditions for these two samples and the uncapped and annealed samples is presented in Table 7.2. SEM images of these two samples, 5401, and 5402, can be seen in Figures 7-4 (a) and (b) respectively. The GaN growth time in Figure 7-4 (a) was 10 s and in (b) was 30 s. As can be seen in (a) there seems to be some dark features at the apices of the pyramids and a rough texturing to the c-plane between the nanopyramids. Similar is also observed in (b), where, in this case, there are lighter regions at the apices of the pyramids in addition to rough texturing of the c-plane between structures. It is worth noting that the majority of the sample did not have this morphology and had a morphology closer to that of (a).

When we now consider both panchromatic CL images in (c) and (d), what is immedi-

Table 7.2: Summary of conditions of attempted GaN quantum dot growth on AlN nanopyramids.

Attempted GaN quantum dot growth on AlN nanopyramids					
Sample	Growth temperature (^oC) (set)*	V/III ratio	Growth pressure (mbar)	Growth time (seconds)	AlN cap
Anneal only	850	NH_3 only	100	60	No
5399	820	20,000	300	60	No
5401	820	20,000	300	10	Yes
5402	820	20,000	300	30	Yes

*True temperature, as measured by pyrometry, has an off-set from the set temperature. In this case the true temperature is higher than the set temperature by $\sim$ 100 ^oC.

ately clear is that dark regions are localised to the nanopyramid regions. Additionally, it appears that some of the semi-polar planes are darker than others, and this seems similar for all pyramids in a given image. What is also of note is the lack of any bright localised emission, especially at the apices of the pyramids.

Turning to the mean CL spectra in (e) and (f), both are largely very similar. There is a large defect band from $\sim$ 290 nm to $\sim$ 510 nm in both spectra. This originates from the defects inherent in the AlN template. The periodic modulation of these defect bands is likely due to Fabry-Perot oscillations within the AlN template. There is again no evidence of quantum dot signatures or any visible GaN signature at all. A weak GaN signal could have been masked by the large, strong defect band in the spectra however. After performing both room temperature and low temperature ($\sim$ 77 K) photoluminescence on sample 5402 (data not shown), no other features of any interest are revealed and the PL spectra is largely similar to that of the CL in Figure 7-4 (f).

It is difficult to see from the CL (Figures 7-4 (c) - (f)) any sign of active region luminescence. There could be a number of reasons for this. Whilst it appears there may have been some deposition from the SEM images, especially in (b), this may in fact be contamination. Hence, it is possible that both 10 s and 30 s growth time are not long enough for the nucleation of GaN to occur on these structures, especially at the apices. This is supported form the lack of any real GaN signature in either of the samples as seen in (c) - (f).

Another possibility, is that GaN growth has occurred but is so defective this just appears as dark regions on the CL images shown in (c) and (d). In highly defective material, the majority of recombination would be via nonradiative routes, therefore

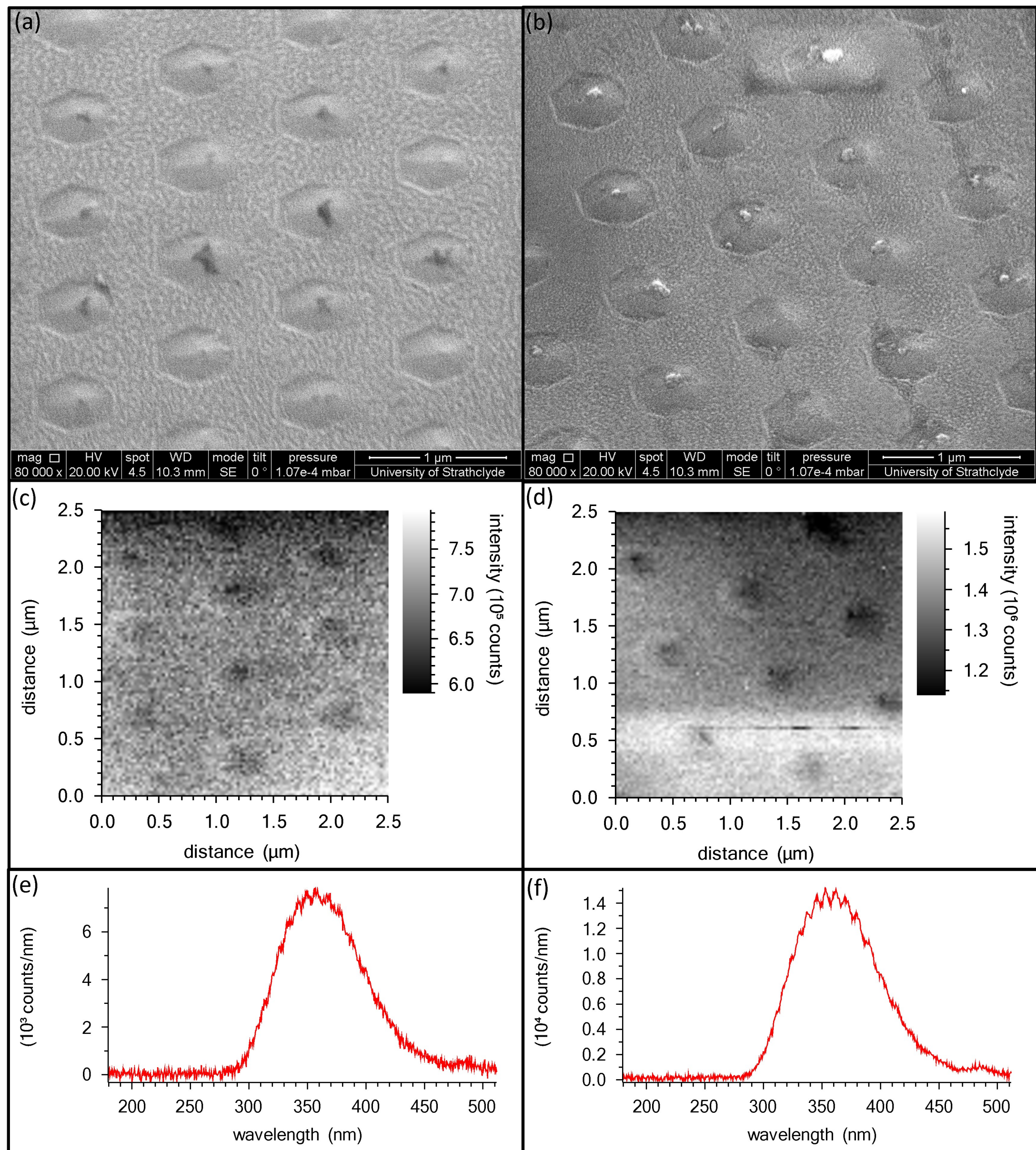

Figure 7-4: Figure (a) shows an SEM image of sample 5401. In (b) and SEM image of 5402 is presented. Figure (c) shows a panchromatic CL image of the sample presented in (a). In (d) shows a panchromatic CL image of the sample presented in (b). In (e) a mean CL spectrum of the sample, and region, shown in (a) is presented. In (f) a mean CL spectrum of the sample, and region, shown in (b) is shown. This data was taken by Dr Jochen Bruckbauer, University of Strathclyde. These measurements were performed at room temperature and under vacuum. The electron beam acceleration voltage used was 20 kV.

this would show up as dark regions in the panchromatic CL map.

Alternatively, the orientation of the CL detection source with respect to the detector could hinder the detection of an optical signal from these nanopyramids. This is supported to some extent by the darker regions observed from different semi-polar planes of the pyramids. It may be easier for photons to escape certain planes more easily, and be subsequently detected. This would manifest itself in darker planes where photons are more difficult to be detected from, which is what is observed.

Another hypothesis is that the growth conditions used are not suitable for growing localised GaN material at the apices of the pyramids. Finally, the fact that the perturbation of the c-plane layer is minimal could mean that there is no preferential growth at the apices of the structures and just conformal deposition of material. This material could then, additionally, be either is highly defective or difficult to detect considering the detection geometry of the system and the shallow nature of the pyramids. Both these latter points would result in little or no GaN signal being detected.

7.4 Initial Investigation of GaN growth on AlN nanorods

The attempted growth of GaN QD's upon the nanopyramid nanostructures, in the previous section, was not successful. There are a lot of possibilities for why this was the case. If it is assumed that this is as a result of the sample itself, and not as a result of the growth conditions employed, a sensible route forward can be made. The shallow and minimal perturbation of the c-plane AlN, in these nanopyramid structures, may have led to no real preferential incorporation at the apices of the pyramids. Thus, it is pertinent to investigate the growth of GaN on AlN nanostructures with much more drastic aspect ratios and hence perturbation, from the flat c-plane. The 'top-down bottom-up' AlN nanorods presented in Chapter 4 are one such suitable structure.

Dry-etched $\sim 1\ \mu m$ AlN rods first underwent faceted regrowth to realise hexagonal rods with pyramidal heads and sharp apices. GaN growth was then performed for 10 and 60 seconds, followed by an AlN cap. More details of the growth conditions can be seen in Table 7.3.

SEM images of samples 5415 and 5412 are shown in Figures 7-5 (a) and (b) respectively. As can be seen in both (a) and (b) hexagonal nanorods with pyramidal heads and sharp apices have been realised after the AlN faceted growth step, GaN deposition and AlN cap. Both arrays of rods are almost fully faceted, except for an incomplete

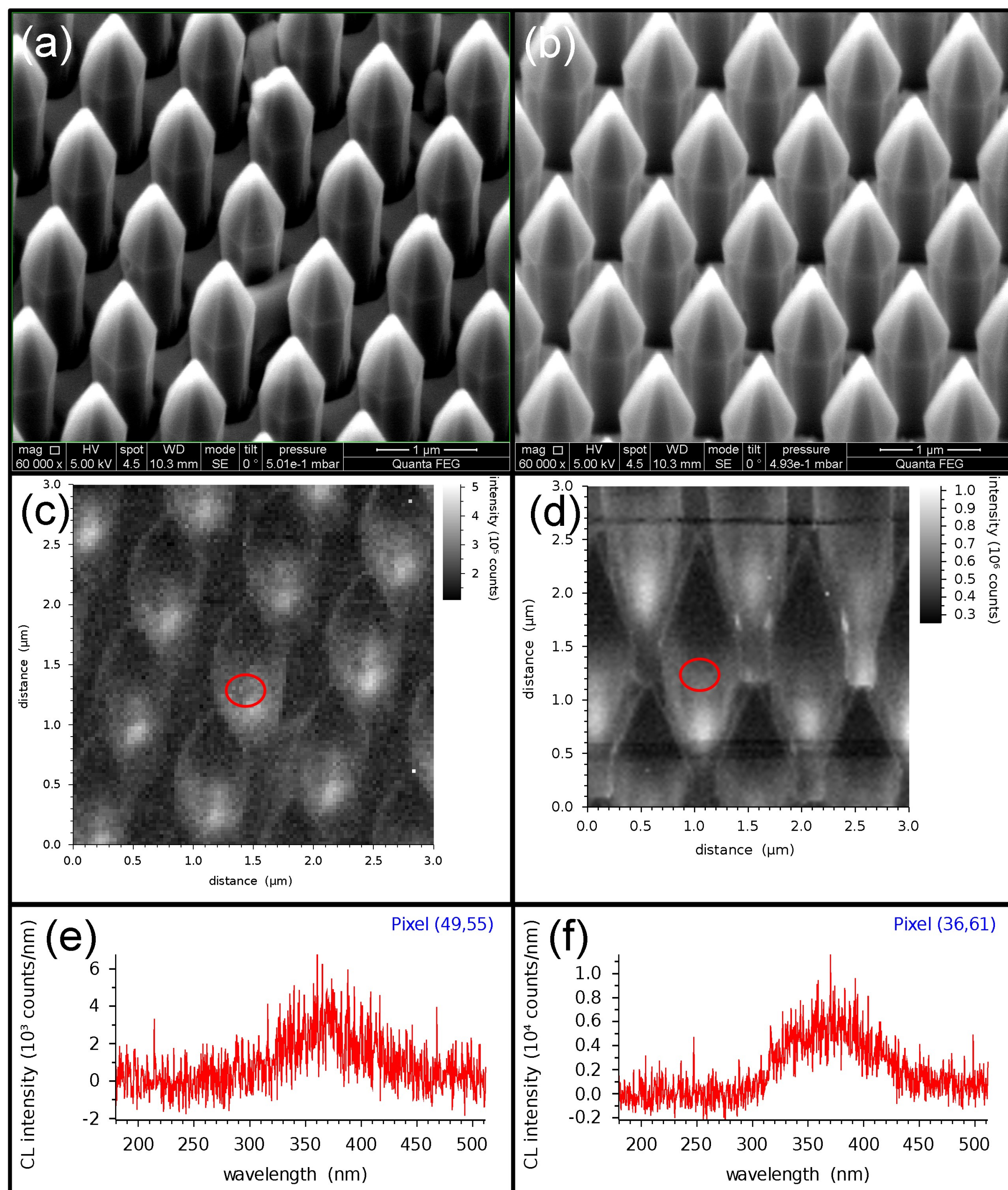

Figure 7-5: Figure (a) shows an SEM image of sample 5415 and in (c) the corresponding panchromatic CL map of the same area. Figure (b) shows an SEM image of sample 5412 and in (d) a panchromatic CL map of the same area. In (e) and (f) are two example spectra from the centres of two rods from the panchromatic CL images in (c) and (d) respectively. The red circles on (c) and (d) show the approximate area within which the spectra in (e) and (f) were taken. This data was taken by Dr Jochen Bruckbauer, University of Strathclyde. These measurements were performed at room temperature and under vacuum. An acceleration voltage of 5 kV was used.

Table 7.3: Summary of conditions of attempted GaN quantum dot growth on AlN nanorods.

Stage 1 - AlN faceted regrowth				
Sample	Growth temperature (^oC) (set)*	V/III ratio	Growth pressure (mbar)	Growth time
5412/5415	960	19,000	20	150 minutes
Stage 2 - GaN growth				
5412	820	20,000	300	60 seconds
5415	820	20,000	300	10 seconds
Stage 3 - AlN cap				
5412/5415	820	7,600	20	8 minutes

*True temperature, as measured by pyrometry, has an off-set from the set temperature. In this case the true temperature is higher than the set temperature by $\sim 100\ ^oC$.

m-plane near the base of the rods. The rods are known to have m-plane facets as the slowest growing, and therefore dominant, non-polar facets from the evidence presented in Chapter 4. Although these rods were dry etched in a different batch to those shown in Chapter 4, they were from the same originally patterned template and so from the same argument in Chapter 4, they display m-planes when in point-to-point geometry. As can be seen in the panchromatic CL in (c) there are not many interesting features and little sign of localised emission. There are two bright pixels but these correspond to cosmic rays. In (d) however, there does seem to be some features of note. In particular, there appears to be regions of localised bright emission near the corners of the pyramid sections of some of the rods. In order to ascertain the nature these bright regions, individual pixels at these positions were inspected more closely.

As can be seen in Figure 7-6 (a), (c) and (e), individual pixels were inspected in more detail and their corresponding emission spectra extracted, Figures 7-6 (b), (d) and (f) respectively. What is immediately striking from these spectra, and not observed in other regions, are the sharp emission peaks centered at ~ 280, ~ 300 and ~ 290 nm for (b), (d) and (f) respectively. As can be seen from all three spectra these peaks appear to be the dominant luminescent feature in these specific locations. It is not entirely clear from this figure where exactly the luminescence source is spatially located. What is apparent is that these sharp luminescence features do not originate from the apices of the rods as one intended. It was unclear what regions of the rod these emission features were localised at or if they were located at some point on the bottom c-plane of the sample, between the rods. Hence, another CL map was taken of this sample, but at an edge which had been cleaved post-growth in order to get a semi-cross-sectional

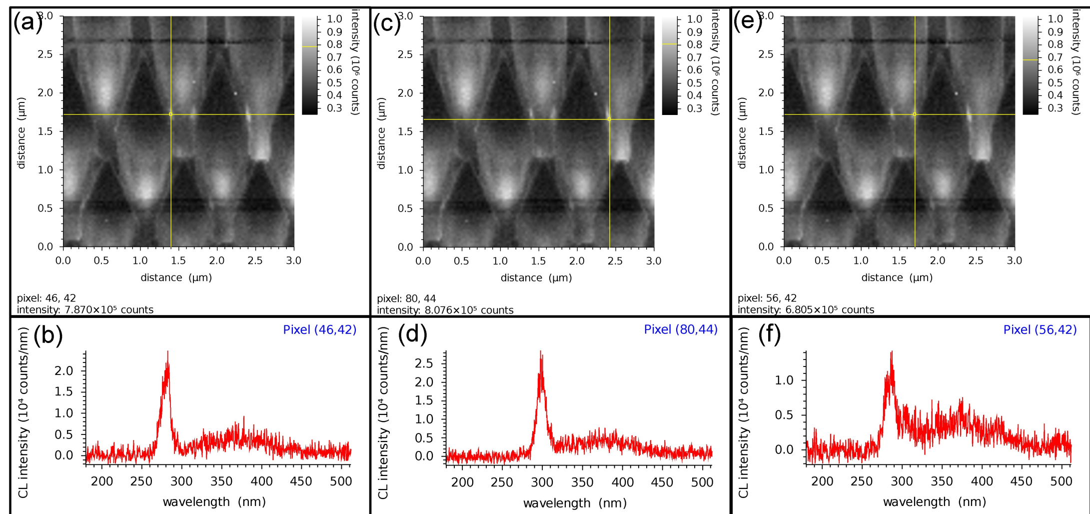

Figure 7-6: Figures (a), (c) and (e) show 3 targeted pixels from the panchromatic CL map shown in Figure 7-5 (d). The corresponding CL spectra for these three pixel are presented in Figures (b), (d) and (f) respectively. This data was taken by Dr Jochen Bruckbauer, University of Strathclyde. These measurements were performed at room temperature and under vacuum. An acceleration voltage of 5 kV was used.

view on the rods themselves.

The SEM image in Figure 7-7 (a) shows a post-growth cleaved-edge from sample 5412. As can be seen fromm the image, nearly the entire length of the nearest most rods can be seen. Hence, if any interesting luminescent data was observed along the length of these rods, its spatial location on the rod could be easily identified. A corresponding panchromatic CL image of the region shown in (a) is shown in (c), with a specific pixel highlighted. As can be seen from the spectra associated in this pixel, in (d), a sharp luminescence peak can be observed centred on $\sim$ 290 nm. Similarly in (e) another region of the panchromatic CL map is selected with the corresponding spectra in (f) also showing a sharp peak. This latter peak was also centred at $\sim$ 290 nm. When comparing with the SEM image in (a) it appears that the localised sharp emission features arise from near the bottom of the rods, but crucially, not at the base. There seems to be a correlation with these sharp emission features and the top of the regions where there is still some a-plane non-polar facet remaining.

What is believed to be occurring, as can be seen from the schematic in Figure 7-7 (b), is that after the AlN faceted regrowth stage, near the bottom of the rods, the m-plane has not fully formed with the a-plane not being fully extinguished. A triangular region of remaining a-plane is subsequently remaining near the lower part of the rod, prior to

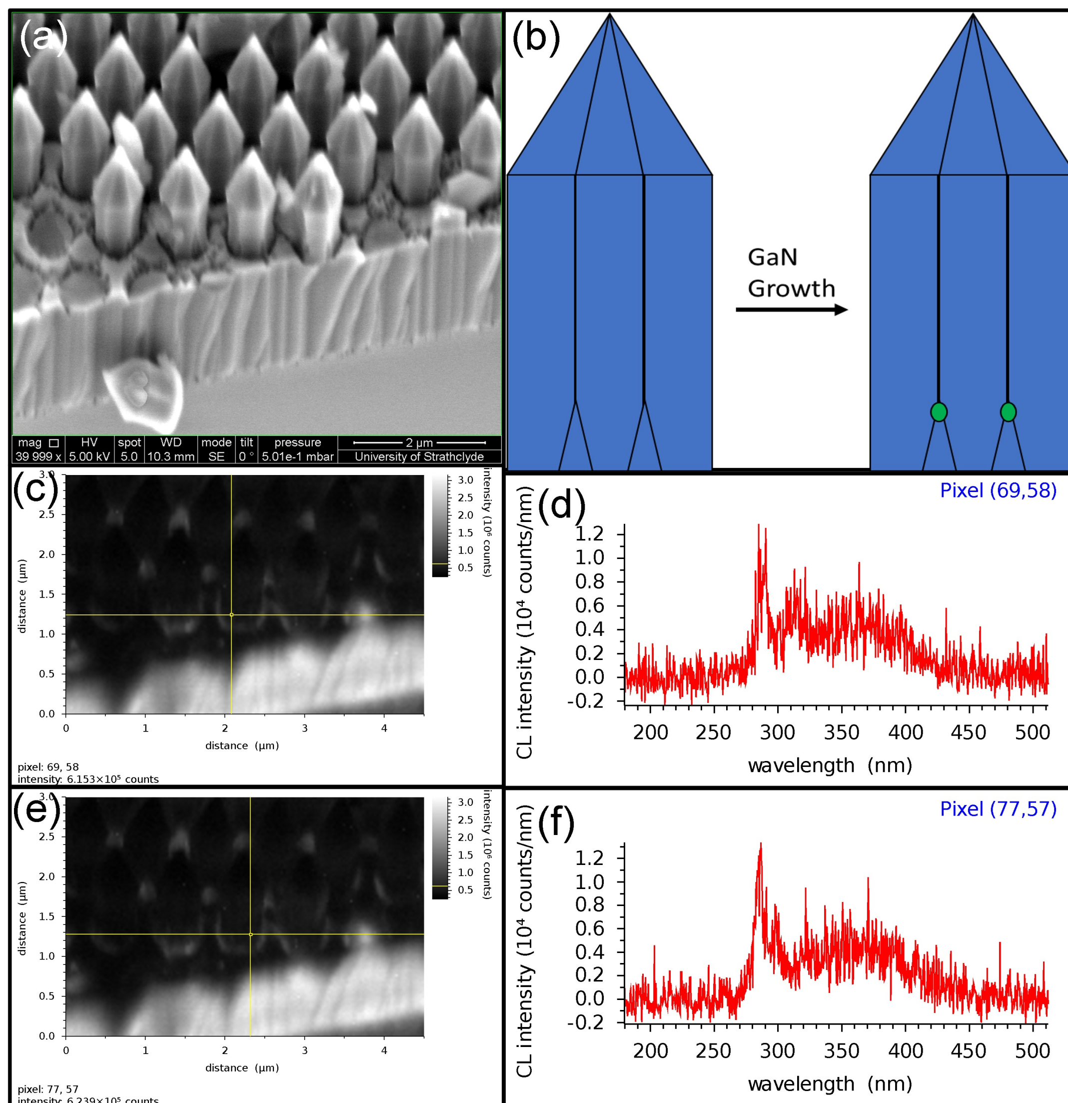

Figure 7-7: Figure (a) shows an SEM image of sample 5412 near the cleaved edge. In (b) a schematic of the growth occurring on 5412 is presented. In (c) a specific pixel of the panchromatic CL image which corresponds to the same location as shown in (a) is presented. The corresponding detected CL spectrum of the pixel highlighted in (c) is shown in (d). In (e) another pixel (different to (c)) in the panchromatic CL image is selected. The corresponding detected CL spectrum for the pixel in (e) is shown in (f). This data was taken by Dr Jochen Bruckbauer, University of Strathclyde. These measurements were performed at room temperature and under vacuum. An acceleration voltage of 5 kV was used.

GaN growth. Under the GaN growth conditions employed, there is preferential incorporation of material at the top of this triangle region where the fast growing a-plane is being extinguished and grown out leaving only the m-plane. Hence, GaN accumulates at this region as this area/facet of the rod is fast growing. This then leads to localisation of emission in these regions, which show sharp emission peaks, especially considering the measurements were performed at room temperature.

It cannot be said for certain if the emission features present in Figures 7-6 and 7-7 correspond to non-polar GaN quantum dots close to the bottom of the rods. In order to give a better indication of this, the FWHM of each of the sharp spectra presented in these figures were extracted and compared to those reported in other literature. The data can be seen in Table 7.4. This data was taken from the CL spectra in its raw form and then smoothed before calculating the FWHM of the sharp peak regions. Thus, these extracted linewidths can only be taken as estimates of the true linewidths of the sharp emission features. As a reference point some room temperature linewidth FWHM's of GaN/AlN or GaN/AlGaN quantum dots are also presented in Table 7.4.

As one can see from Table 7.4, the FWHM's of the sharp features in the CL data presented in Figure 7-6 and 7-7 have rather broad linewidths, $\sim 309 - 104$ meV, compared to some results from the literature. In most of the literature the linewidths are measured from PL data, whereas our data was collected via CL. Even considering this it is still useful to survey and compare the literature with our data.

In the work by Choi et al. [273], the PL linewidths of single GaN quantum dots are $\sim$ 10 meV. This data was collected at 4 K. In the works by Yang et al. [331] and Peres et al. [341], PL of ensembles of self-assembled quantum dots was performed. Whilst PL performed in the work by Yang et al. was performed at 300 K the work by Peres et al. was performed at 14 K. Yang et al. found a linewidth of 153 meV and Peres et al. found a linewidth of $\sim$ 300 meV. In the works by Holmes et al. [15] and Deng et al. [274] PL spectra was measured at or above room temperature. In the former, a linewidth of 33 meV (350 K) is reported and in the latter a linewidth of 58 meV is reported (300 K).

Whilst Choi et al. [273] found very narrow linewidths of $\sim$ 10 meV, these measurement were performed at 4 K. This is significant as it is known that at higher measurement temperatures, PL measurements suffer from to spectral linewidth broadening. This is as a result of thermal population of higher energy levels and coupling to phonons

Table 7.4: Measured linewidths of sharp peaks observed in CL spectra.

FWHM of sharp peaks from CL spectra			
Sample	Emission wavelength (peak centre) (nm)	FWHM (meV)	FWHM (nm)
1 (Figure 7-6 (a), (b))	279	308.6	18.3
2 (Figure 7-6 (c), (d))	298	217.4	17.8
3 (Figure 7-6 (e), (f))	284	233.3	20.4
4 (Figure 7-7 (c), (d))	290	120.6	8.07
5 (Figure 7-6 (a), (b))	284	103.9	13.4
Averages and Standard deviations			
Mean linewidth (meV)	Standard deviation (meV)	Mean linewidth (nm)	Standard Deviation (nm)
196.8	84.7	15.6	4.9
Linewidth data from the literature			
Linewidth (meV)	Measurement Temperature (K)	Emission wavelength (nm)	Source Material
7-9	4	$\sim 310 - 290$	Nanowire AlGaN/GaN QD's [273]
153	300	~ 310	Self-assembled AlGaN/GaN/AlN QD's [331]
~ 300	14	$\sim 520 - 320$	Stacks of SK GaN/AlN quantum dots [341]
33	350	290	AlGaN/GaN nanowire QD [15]
58	300	322.5	AlN/GaN dot-in-self-assembled wire [274]

* The experimental values are not too accurate as the data was quite noisy. One would expect a relatively large error in these measurements.

[248]. In addition, there would likely be greater degrees of spectral diffusion at higher measurement temperatures, which would further broaden the detected linewidths [342]. Hence, although our linewidths are much broader, it is difficult for us to compare our results with that found by this group. For the works by Yang et al. [331] and Peres et al. [341] it can be seen that our CL linewidths appear in the same broad range of the PL linewidths measured in both [331] and [341]. Indeed, the results by Peres et al. reveals a larger linewidth value than for our sample. However, this data also cannot be directly compared to our own. This is as ensembles of self-assembled quantum dots are probed in both these publications as opposed to the single feature probed via our CL measurements. It is known that self-assembled quantum dots have a distribution in shape and size [110], corresponding to slightly differing energetic structures [114] [115]. Thus, one would expect the PL linewidths of these samples to be broader than a single QD, especially in the case of the work of Peres et al., where stacks of many quantum dots were probed.

The quantum dots measured in the works by Holmes et al. [15] and Deng et al. [274] are much more comparable to our own data. This is as both measured single GaN quantum dots at at above room temperature albeit via PL. These values do appear to be smaller than our average linewidth of $\sim$ 197 meV by a noticeable amount. This could be due to the structures reported in [15] and [274] being quantum confined in more dimensions than ours. Alternatively, it is also possible that both our structures and those from the literature have the same level of quantum confinement (i.e. 3D quantum confinement), but the grown material quality surrounding our structures is noticeable poorer. This is as a greater incorporation of defects in the material surrounding the quantum dots could lead to a larger amount of spectral diffusion, subsequently leading to a broadening of the emission linewidth [249], [250]. This would not be unexpected, as was argued in Chapter 5, the AlN regrowth step for these nanorods could be largely defective.

In more detail, point defects, such as interstitials, vacancies and impurities could be introduced during the AlN faceted regrowth step of the rods [267]. This would then provide a defective material, with poorer crystallographic quality, on the non-polar planes upon which the GaN quantum dot growth nucleates. In turn, this would lead to the growth of a GaN region in the vicinity of a barrier region, of a poorer crystallographic quality compared to those grown in some of the literature (such as [273], [15], [274]). Poor crystal quality of the AlN barrier region would lead to a broader emission linewidth of the quantum dot due to a greater contribution to the emission spectra from spectral diffusion. Spectral diffusion is a linewidth broadening phenomenon whereby

an optical transition between two states suffers from inhomogenous broadening as a result of Coulomb interactions with a fluctuating electronic environment [249]. This essentially means that there will be a strong Coulomb interaction between the quantum dot confined charges and the charges present in the surrounding barrier material [343]. Such charges in the barrier material can arise due to charge traps originating from the occurrence of point defects in the barrier material [249]. These charge traps in the vicinity of the quantum dot cause emission shifts of the energy of the quantum dot when the traps change their charging status [343]. Thus, this leads to a variation in the emission wavelength of the quantum dot as different traps change their charge status, resulting in an overall broader emission linewidth.

In the work by Deng et al. [274], both GaN quantum dots in self-assembled AlN structures, and GaN quantum dots in SAG AlN nanowires were presented. Both structures were grown via plasma-assisted MBE. The quoted linewidth, (58 meV), in Table 7.4 is that of a GaN QD-in-self-assembled-AlN rod. On inspection of the data presented in [274], the linewidth of the QD in self-assembled structure appears considerably narrower than that of the compared selective area grown GaN/AlN site-controlled quantum dot also presented in the work. This latter linewidth is not reported in the publication, but on inspection of the data can be estimated to be $\sim$ 200 meV. Taking this into account, the suggestion from this data and the arguments above are that there is a reasonably high chance of emission features we observe on the non-polar planes of our rods being ascribed to GaN quantum dots.

Importantly, it is also worth noting that whilst the FWHM's in our samples were taken across the entire smoothed peak, many of the peaks in their raw form appear to be double-peaked in nature. This could either be as a result of noise in the data or the presence of two sharper peaks in very close proximity. Two sharp peaks in proximity could indicate the presence of two quantum confined GaN structures, such as quantum dots, with very similar properties in close proximity. Alternatively, these double peaks could be the sign of both exciton and biexciton transitions from a single quantum dot.

If we now compare the emission wavelength of our structures with those of the literature an interesting observation is found. For all but the work in [341], our emission wavelengths, 279-290 nm, are very similar to those of the literature. This indicates that the sharp peaks in our structures arise from a highly confined GaN region. Additionally, our spectra appear much brighter than the defect band which dominates spectra obtained from other areas (Figure 7-5 (f) for comparison). Considering these last two points, along with the linewidth data just mentioned and the possible double-peaked nature of our emission profiles, some conclusions can be drawn. As the emission

wavelengths are similar to those of the literature for known quantum dots, one would assume that there is a similar amount of quantum confinement in our structures to that of the literature. This, however, does not take into account that our structures are on the non-polar planes of the rods, whereas the QD's in the literature mentioned are all c-plane structures. It is known that the internal fields present in polar III-N structures can lead to a red shifting of the emission spectra [173]. However, it is also the case that the Quantum Confined Stark Effect (QCSE) in c-plane GaN/AlN quantum dots which are shallow in height is largely suppressed [274]. Hence, if our structures were also c-plane, we would expect them to have an emission wavelength slightly longer than that we observe here. The nature and general emission wavelength of our structures do imply a high degree of quantum confinement. Whilst, the emission peaks are generally broader than those most similar in the literature, it is not out of the question that our structures are indeed quantum dots, especially if the peaks are double-peaked in nature and represent more than one QD or if the double peaks are a sign of both exciton and biexciton transitions. This is not conclusive evidence that we have grown some non-polar quantum dots but the evidence presented here certainly suggests that it could indeed be the case.

7.5 Further investigation of GaN growth on AlN rods – room temperature and low temperature PL

From the last section we have found that sample 5412 certainly has some interesting features. We decided to explore the growth conditions around those used for 5412 in order to try and promote growth of localised emission features at the apices of the rods, where we initially intended. In order to do this we wanted to investigate an attempt to further promote top c-plane growth of GaN upon the AlN structures. Table 7.5 summarises the differing growth conditions explored. The choice of these growth conditions will now be discussed and justified in more detail.

As can be seen from Section 7.4 localisation of GaN growth has been achieved, but not at the regions of the rods initially intended. In order to promote growth of GaN at the apex of the AlN nanorod, the growth conditions for sample 5412 (Table 7.3) were tuned. In all cases one growth condition was changed whilst the rest remained the same in order to gain a direct comparison with 5412.

The GaN growth step for sample 5419 was performed at higher temperature. The motivation behind this was that this higher growth temperature would provide the

Table 7.5: Further exploration of GaN quantum dot growth conditions on AlN nanorods.

GaN growth conditions				
Sample	AlN faceted regrowth**, growth time (minutes)	GaN growth set temperature* (^{o}C)	GaN V/III ratio	GaN growth pressure (mbar)
5411	150	none	none	none
5412	150	820	20,000	300
5419	150	900	20,000	300
5420	150	820	20,000	30
5421	150	820	60,000	300
5422	120	820	20,000	300

*True temperature, as measured by pyrometry, has an off-set from the set temperature. In this case the true temperature is higher than the set temperature by $\sim 100\ ^{o}C$. **All samples had an AlN cap grown upon them after the GaN growth stage. The growth conditions for both the AlN regrowth stage and the AlN cap of all samples are specified in Table 7.3. In 5419 of Table 7.5 the growth temperature was increased from a set temperature of 820 to 900 ^{o}C. The intention was that by increasing the growth temperature, adatom migration would increase as the adatoms would have more energy at this higher temperature. This then may allow for more migration of the adatoms on the surface of the rod allowing for nucleation and incorporation of GaN at the apex regions of the rods.

adatoms with more energy, increasing their average migration length. This then may allow for more migration of adatoms to the apex regions of the rods where it is hoped growth should be preferential.

The GaN layer in sample 5420 was grown at a significantly lower pressure, an order of magnitude less than 5412 (Table 7.5). It was the hope that this would also lead to better adatom migration due to fewer collisions with gas phase atoms and the migrating surface adatoms. Additionally, fewer gas phase collisions at lower pressure, before adatom adsorption would allow for higher energy adatoms adsorbing on the surface, also increasing the migration length. Finally, this would also allow for more desorption of adatoms allowing for less GaN incorporation as a whole and incorporation to be likely only in the most preferential regions. Hence, if the other growth conditions promoted c-plane growth it should be more likely that growth occurs preferentially in this region at lower growth pressure.

Sample 5421 was grown at an even higher V/III ratio than 5412. The V/III ratio used was 60,000. This was performed as a high V/III ratio is known to promote c-plane growth [273]. By increasing the V/III ratio from 20,000 to 60,000 it was thought that

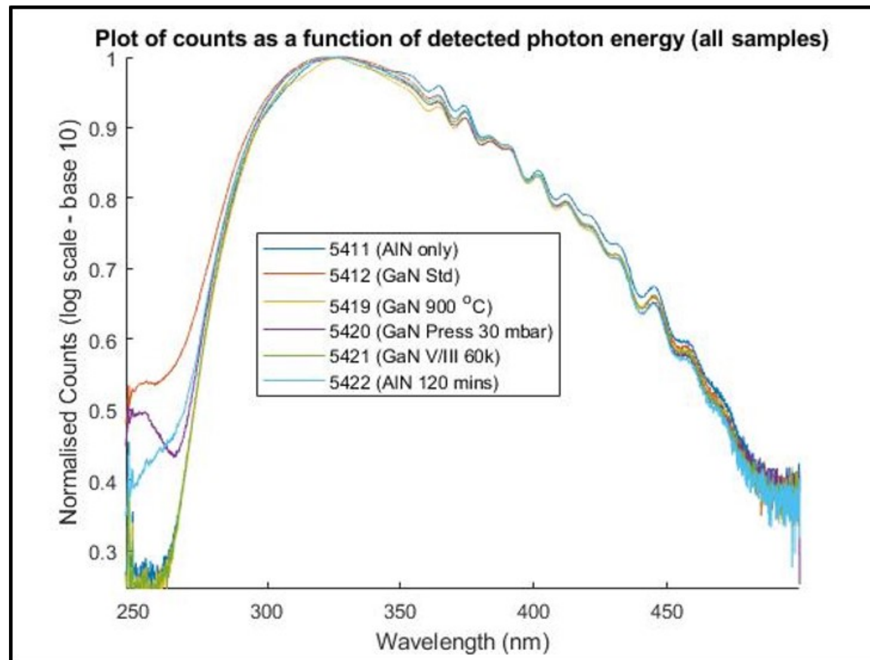

Figure 7-8: This figure shows a plot of the room temperature PL measurements for all the samples presented in Table 7.5.

this could lead to conditions which would promote c-plane GaN growth more than 5412 and so lead to incorporation of GaN at the apices of the rods.

Finally, sample 5422 was grown with the same conditions during the GaN step as of 5412 but the initial AlN faceted regrowth step was shorter by 30 minutes. As can be seen in Figure 7-5 (b) the apices of the rods from batch 5412 appear very sharp. It is possible that these structures are in fact too sharp, after the first AlN growth stage, to allow for growth at the apices as there may be no remaining c-plane. Hence, utilising a shorter AlN faceted regrowth step would lead to a greater c-plane truncation at the top of the rod prior to GaN growth. This may then allow for incorporation of GaN at the top of the rods which was not observed in 5412.

Micro-PL was performed upon the samples at room temperature to see if there were any features of interest. The wavelength of the laser used for the Micro-PL experiments was 244 nm and the spot size was at least $\sim 3.5\ \mu m$. This was additionally undertaken with sample 5412 and a control sample with only the AlN faceted regrowth step to allow for direct comparison with a sample known to have sharp emission features and a sample known to have no GaN growth whatsoever. A plot of all 6 samples (all the samples in Table 7.5) are shown in Figure 7-8. This plot is displayed on a log scale (base 10) to better reveal any luminescent features of interest considering the large and very

luminescent defect band present in all samples. On inspection of sample 5412 what is immediately apparent, other than the large AlN defect band, is the luminescence at short wavelength at $\sim 260 - 270$ nm. No sharp features, such as those observed in the CL data from Figures 7-6 and 7-7 are observed however. Additionally, the short wavelength luminescence in the PL does not correspond to the wavelength range of the sharp emission in the CL. It is unclear why this is. It could be that the source of this luminescence is not the same as that observe in the CL. Alternatively, there could be some blue shifting of the emission wavelength in the PL compare to that of the CL but the author is unaware of a mechanism that would cause this.

Sample 5419, grown at higher temperature, in the plot in Figure 7-8 shows very little features of interest. There certainly does not appear to be any sign of confined GaN luminescence in the wavelength region $\sim 300 - 250$ nm. One possible reason for this observation is that the growth temperature was too high leading to too much adatom desorption during growth. This renders growth of GaN under these conditions either not possible or requiring longer than the 60 seconds growth time for nucleation and further incorporation. Interestingly, what is observed for sample 5420, grown at lower pressure, in Figure 7-8 is that there is a noticeable luminescence feature centered at ~ 260 nm. It is rather broad but relatively bright, even considering this plot is on a log scale. It is certainly the most dominant luminescence feature not ascribed to the defect band across all of the samples presented.

In contrast to 5420, what was observed from the PL data in Figure 7-8 for sample 5421, grown at a higher V/III ratio, is very little except for the large AlN defect band. This suggests that there are no quantum confined GaN regions under the growth conditions used in sample 5421. It is possible that as the V/III ratio here is so large that the ratio of Ga to N is such that very little growth occurs at all. Sample 5422, with shorter AlN refaceting time, also possesses some interesting features at short wavelength. There appears to be some sign of some broad luminescence which appears to have some shallow oscillatory nature to it.

Overall what seems most obvious from Figure 7-8 is that samples 5412, 5420 and 5422 are the most promising, showing signs of short wavelength luminescence. As this was the case, measurements of these samples were performed at liquid nitrogen temperatures within a cryostat. This data is shown in Figure 7-9 (b). In order to view a like-for-like comparison a room temperature measurement was also taken with the samples mounted in the cryostat. This data can be seen in Figure 7-9 (a).

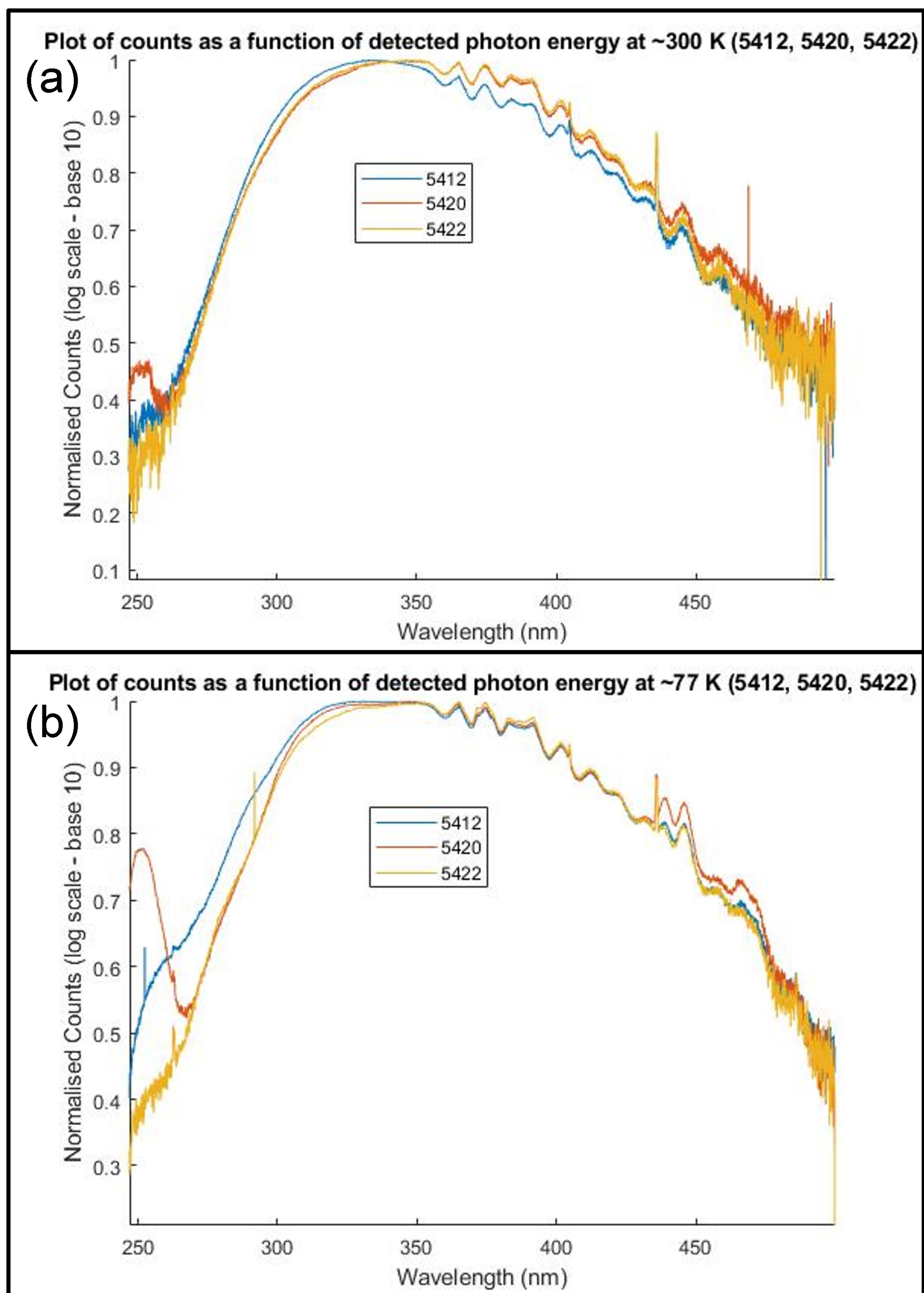

Figure 7-9: Figure (a) shows a plot of the room temperature PL of samples 5412, 5420 and 5422 whilst house in the cryostat. Figure (b) shows a plot of the PL of 5412, 5420, 5422 whilst housed in the cryostat at a temperature of $\sim$ 77 K.

When one compares Figures 7-9 (a) and (b) what appears most striking is the significant increase in luminescence of the band in sample 5420 at short wavelength ($\sim 250 - 270$ nm). There also appears to be a shoulder on the defect band emission at $\sim$ 280 nm which is not present at room temperature (in (a)). There may also be another shoulder at slightly longer wavelength of $\sim$ 300 nm.

Similarly, sample 5412 shows an increase in the relative brightness of the band at short wavelength (centred at $\sim$ 255 nm). As with 5420 there appears to be a shoulder on the defect band at $\sim 280 - 290$ nm, which is not visible at room temperature.

In 5422, there is perhaps a slight increase in luminescence in the short wavelength region, more prominently observed in the other two samples. Additionally, there is also a shoulder present on the defect band at low temperature, again at $\sim$ 280 nm. The sharp peaks observed in all three spectra at $\sim$ 270 nm are as a result of the ambient lighting in the laboratory. This was confirmed by taking a spectra with the lights off (data not shown) which resulted in this peak being no longer present in the spectra.

When one compares the results in the CL data for 5412 (Figures 7-6 and 7-7) with the PL data at low temperature (Figure 7-9 (b)) a few conclusions can be drawn. From what has been observed in the CL maps of 5412, the shoulder around $\sim$ 290 nm in the PL spectra for 5412 likely arises from the sharp emission peaks observed near the lower regions of the rods. This shoulder is also present in 5420 and 5422 and thus it is likely that these two samples would reveal similar features if probed with CL. The rather weak, broad emission in 5412, centered at $\sim$ 260 nm in Figure 7-9 (b) is rather intriguing. This feature is not observed in the CL and its origin is unknown. This could be a signature of some quantum confined GaN as the PL will excite an ensemble of nanorods and perhaps reveal information difficult to observe with CL when considering the geometry of both the CL excitation source and detector. When considering sample 5420 this is much more prominent. There is a large relative increase in the brightness of the luminescence band centred at $\sim$ 260 nm at low temperature compared to room temperature. It is unknown what the source of this luminescence band is. It is a rather broad band to be a quantum dot signature. However, the shoulders of the defect band, which likely correspond to the sharp luminescence features in the CL, also appear somewhat broad. Thus, this sample requires further investigation in order to determine the source of this short wavelength luminescence feature.

7.6 Sample 5420 in more detail

The interesting luminescence feature centred at $\sim$ 260 nm in 5420 (see Figure 7-9 (b)) appears to have a large temperature dependence. This interesting behaviour justifies further investigation considering how bright this feature appears on the log scale of Figure 7-9. To gain a greater appreciation of the brightness of this feature, the spectra was plotted without use of a log scale. This can be seen in Figure 7-10 (a).

What appears a bit more clearly on this plot is a possible shoulder on the defect band centred around $\sim$ 300 nm. Additionally, when comparing the short wavelength luminescence at room and low temperature the dramatic increase in brightness is also visible. At 77 K the brightness of the emission centered at $\sim$ 260 nm is greater than 10% that of the defect band. This is significantly more than any other sample, and a clear view of this UV luminescence is visible without the use of a log scale. As was discussed in the previous section the origin of this luminescence is unknown. Cathodoluminescence of this sample would be an attractive proposition in order to identify the source of the bright UV luminescence feature.

In order to gain a better insight into the evolution of the brightness of the feature at $\sim$ 260 nm, a plot of this peak as a function of measurement temperature is presented in Figure 7-10 (b). At 77 and 100 K the magnitude of the brightness of the luminescence is rather similar. This is not entirely unexpected as there is not too big a difference in these two temperatures. What is observed as the sample heats from 150 K - 300 K is a sizeable reduction in the relative luminescence of the feature, where at 300 K it is less than $\sim$ 10% that of 77 K. One cannot estimate the IQE of this feature as 77 K is not a low enough temperature to assume all the non-radiative centres are completely frozen out. Typically one would require temperatures accessible via liquid helium to do this. It is however interesting to see that the brightness of this luminescence is very temperature dependent. Comparatively, the work by Choi et al. [47] also shows a temperature dependence in the intensity of the PL spectrum of a GaN quantum dot. The emission features they detected, also increased in linewidth as measurement temperature increased. This is not so obvious in the data shown in Figure 7-10 (b). However, the data presented by Choi el al. [47] was of a single quantum dot and the data shown in Figure 7-10 (b) may be that of an ensemble of quantum dots. This is as the spot-size of the laser was at least ~ 3.5 μm and nanorod pitch of 1 μm. Thus we can assume more than one quantum dot would be excited. Additionally, if this emission were to originate from a number of c-plane quantum dots at the apex, spectral diffusion could significantly broaden a polar QD emission linewidth. This is as it is

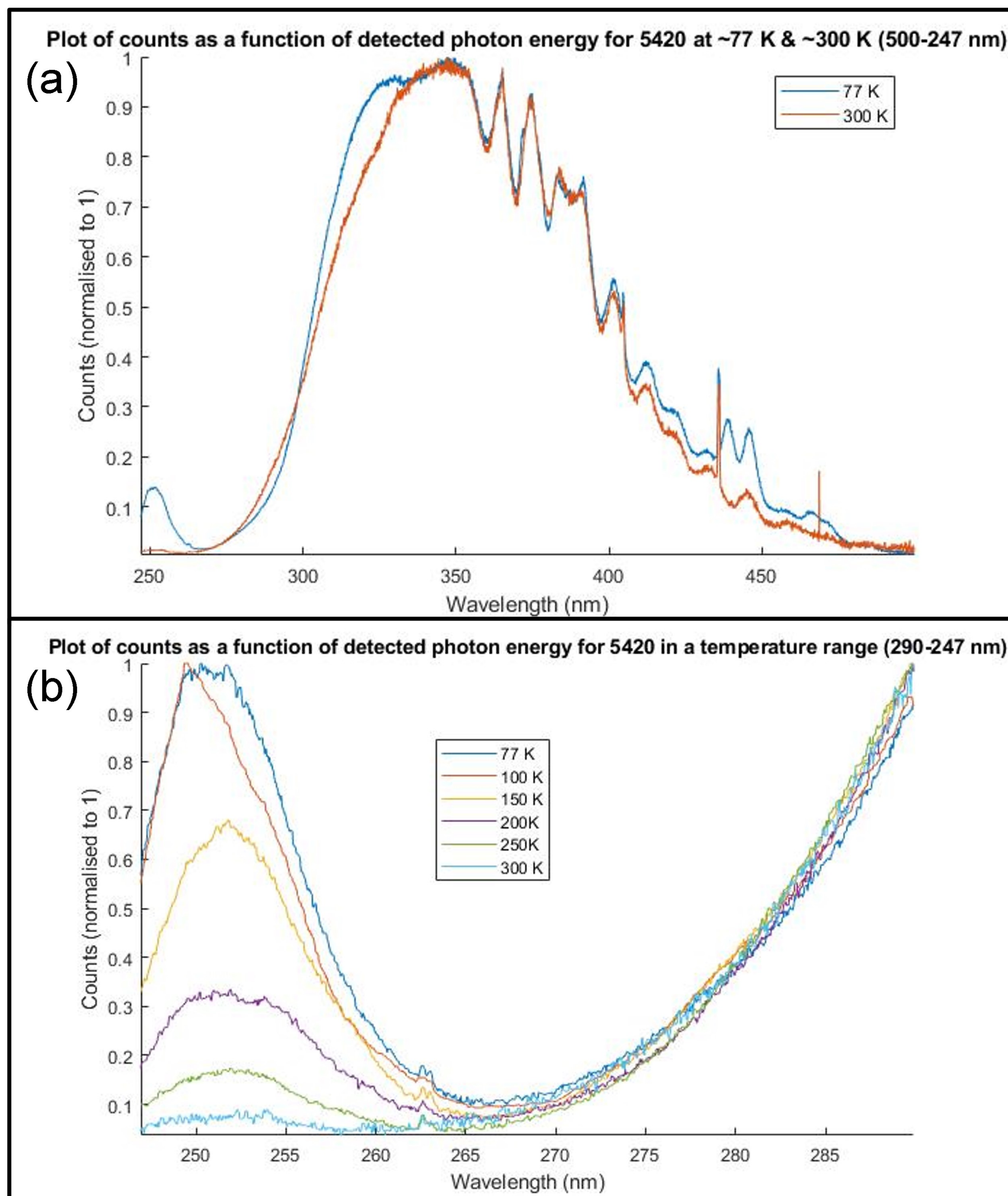

Figure 7-10: In (a) a plot of the entire PL spectra for samples 5420 is plotted at both room temperature and 77 K. No log scale has been used on the data, although cosmic ray removal has been performed via a mean function and the data is normalised to 1. In (b) a plot of the evolution of the peak centred at $\sim$ 260 nm as a function of measurement temperature is presented.

know that the presence of the in-plane internal electric fields in c-plane GaN quantum dots can cause significantly worse spectral diffusion compared to non-polar QDs. The reason for this is that the internal electric field enhances the effect of the electrostatic environment fluctuations on the QD transition [344]. However, considering this, and although it is interesting nonetheless that a similar behaviour in the emission intensity shown in Figure 7-10 (b) is also observed in the work by Choi et al. [47], ultimately further investigation is required in order to determine the nature of this luminescence feature.

7.7 Conclusion

Whilst the AlN nanopyramid samples were not particular successful regarding growing quantum confined GaN, the AlN rod samples were much more promising. Sharp emission features were realised closer to the bottom of the rods (5412). The sharp nature of these emission features suggest that they could arise from quantum dots localised at where the m- and a-planes meet on the AlN rods. Whilst the GaN growth conditions were employed to try and promote top c-plane growth it was interesting to observe that these features grew on the non-polar planes. It is likely that, due to the fact that the m-plane was not fully formed near the bottom of the rods, preferential incorporation of GaN here occurred as the system drives towards a shape of low surface energy. We know from Chapter 4 that this corresponds to a fully formed m-plane with an extinguished a-plane. In addition, compared to the literature, the emission wavelength of these features appear sensible on the assumption that they arise from quantum dots, albeit that they are non-polar. If these structures are indeed non-polar GaN quantum dots this an interesting result. This is as non-polar III-N quantum dots are particularly desirable for quantum information science applications. The reason for this is because the orientation of non-polar quantum dots with respect to the internal fields avoids a spatial separation of the electron and hole wavefunctions, as is found with polar quantum dots. This leads to shorter excitonic lifetimes and thus faster repetition rates in devices such as single photon emitters [345]. Further GaN growth would likely lead to a quantum well or wire like structure extending to the base the rod, extinguishing the remaining a-plane.

The nature of the bright feature centered at $\sim$ 260 nm in sample 5420 is also very intriguing. It shows strong temperature dependence and further investigation of this luminescence would be interesting. Specifically, CL would be a promising avenue to explore this sample in order to gain information on the spatial location of this emission

on the AlN rod itself. A feature of this brightness is not observed in the other samples so it would be reasonable to assume that the CL map of 5420 would reveal additional features to that of 5412 presented in Figures 7-5 - 7-7.

Chapter 8

Summary, Conclusion, Future Exploration and Outlook

8.1 Introduction

Quantum information science (QIS) can be described as 'involving the encoding, communication, manipulation and measurement of information using quantum mechanical objects' [346]. Photons are a good choice of quantum mechanical objects for QIS applications. This is as they travel at the speed of light and only weakly interact with their environment, meaning that they suffer lower noise and loss during transit compared to other quantum mechanical objects [346]. Often, for QIS applications, one requires a single photon emitter (SPE). Quantum dots are useful structures for generating single photons on demand as they can more easily be integrated into existing semi-conductor technology compared to other SPE devices [342].

In terms of the III-N's, as has been mentioned previously, single photon emission has been recorded up to 350 K [15]. When this is compared to the typical operating temperatures of III-As quantum to single photon emitters, requiring cryogenic temperatures [13], this is rather astounding. Even if, in real devices, high operation temperatures such as these are not achieved, with the III-N's, operational temperatures accessible via thermoelectric cooling should be possible, avoiding the use of cryogenics [342]. There has been quite a lot of research conducted on self-assembled GaN/AlN quantum dots grown by the Stranski-Krastanov growth mode [329], [330], [332], [331], [96]. However, such quantum dots are not spatially predetermined and have a distribution in shape and size and therefore energetic structure. This would mean that one quantum dot may

have different luminescent properties from another because they may possess different properties, such as the ground state energy [114], [115].

III-N site-controlled quantum dots (SCQDs) are grown at specific spatially predetermined sites and have uniform shape and size. Hence, integration into real world devices is far more practical. GaN/AlN III-N SCDQs grown via MOVPE have been rarely reported on. This is largely due to the difficulty creating uniform arrays of AlN nanostructures suitable to house GaN quantum dots. One reason for this is the failure, thus far, to perform selective area growth via MOVPE with AlN [49]. The work in this thesis presents some different avenues in order to realise periodic arrays of uniform AlN nanostructures, suitable for housing GaN quantum dots. Additionally, an investigation of an unexplored route to create periodic sites in GaN for quantum dot growth was undertaken. An exploration of attempted growth of GaN SCQDs on AlN nanostructures is also performed.

8.2 Summary and conclusions of research completed

The work in this thesis showed that AlN nanostructures could be created by a number of routes by combining dry etching with either selective additive regrowth or subtractive wet etching. The mechanisms of the growth or wet etching processes were explored. Structures created by both methods appeared suitable to house quantum dots.

In Chapter 4, an exploration of the creation of uniform spatially predetermined AlN nanorod and holes was performed via the top-down bottom-up approach. This involves combining top-down dry etching with bottom-up MOVPE regrowth. As is presented in this chapter, whilst the creation of inverse apex nanopyramidal pits was challenging, nanorods with complete non-polar m-plane facets and sharp apices were realised. These rod structures held promise in housing GaN quantum dots, specifically at the sharp apices where a small amount of GaN growth could be localised [49].

An alternative approach, presented in the next chapter, Chapter 5, was to employ wet etching on dry etched AlN nanostructures. Initially etching of a planar AlN template with a pattered dielectric mask to try and create inverse pyramids was explored. This was not found to be successful and so the wet etching of more complex, dry etched structures was undertaken. The wet etching of nanorod and nanohole arrays realised some interesting features. In particular, the AlN nanopyramid array created via the wet etching of shallow rods showed particular promise as sites to house GaN quantum dots. Sharp features were also realised between faceted nanohole structures.

Moving away from AlN, quantum dot sites in a GaN template were realised in Chapter 6. Here, selective area thermal etching of GaN windows exposed through a patterned dielectric mask was performed. By carefully controlling the processing parameters to avoid surface damage small 'pin-hole' like features were realised at the centres of each exposed GaN window.

En-route to achieving this a thorough investigation into the process parameter effects on the formation of a small hole at the centre of GaN windows via thermal etching was performed. The result of this investigation and optimisation was the realisation of sites for InGaN quantum dots with an understanding of parameters that need to be carefully controlled to successfully thermally etch small central holes in the GaN windows. This study highlighted the importance of the sensitivity of the exposed GaN surface if one wants to selectively thermal etch GaN. The dimensions of these features were on the order of that of quantum dots.

Hence, it should be possible to grow InGaN quantum dots within these openings if the growth conditions are carefully optimised. As this thermal etching avoids subsurface damage compared to dry etching techniques, and defective material, with weaker bonds, would be more easily etched away by this technique, this should realise sites with good crystallographic quality.

Finally, attempted site-controlled GaN quantum dot growth was performed. This was undertaken on both the wet etched AlN nanopyramid samples and also on the top-down bottom-up AlN faceted regrown rods. This was not successful on the nanopyramid samples, or at the apices of the top-down bottom-up AlN rods. This did highlight the challenge in trying to grow localised regions of GaN on features that were as sharp as those at the apices of the rods or pyramids. Overall, further optimisation of the growth conditions would be required to achieve this combined with ensuring there is a large enough c-plane at this apex upon which to grow the GaN.

Sharp emission features were detected on other locations of the AlN nanorods. These sharp emission features were however, located on the non-polar planes rather than the intended sites at the rod apices. Whilst the evidence from the CL and PL is not conclusive, the nature of the sharp emission lines at room temperature suggest that these could be ascribed to non-polar GaN quantum dots. Non-polar III-N quantum dots are attractive for QIS applications as they do not suffer from the in-built spontaneous electric fields that polar III-N quantum dots suffer from which leads to the quantum confined stark effect (QCSE) [345]. This means that non-polar quantum dots do not suffer from the large spatial separation of the electron and hole wavefunctions that

occurs with polar III-N quantum dots [345]. This could therefore allow for a device with shorter exciton lifetimes and thus, a faster repetition rate if one uses non-polar as opposed to polar quantum dots [345].

On further exploration of the growth conditions it was found that, in one sample, a bright emission feature at ~ 260 nm was detected via PL. This emission feature in the UV is an interesting observation, however the origin of which is not fully understood.

8.3 Possible future exploration

Considering the work presented in this thesis, whilst there has been some success, further exploration, particularly of the quantum dot growth conditions would be desirable. Further study and optimisation of the growth conditions of the GaN active region to ensure apex GaN quantum dots would be an attractive exploration. Additionally, it may be possible to control the location of the quantum dots, either the apex, pyramid corners of the rods, or at a specific point down the non-polar plane by control of the AlN regrowth step. The lack of success of growth of GaN quantum dots at the apices bring into question either the AlN nanostructures used for this endeavour or the GaN growth conditions employed. The sharp apex features realised for both the pyramids and rods could be in-fact too sharp for the nucleation of any GaN material. This does suggest that if one were to optimised the AlN regrowth step of the nanorods suitable sites for GaN quantum dots may be achieved at the apices.

Avoiding the defective AlN regrowth step in the top-down bottom-up approach could lead to higher quality AlN sites for QDs. This may then, in addition to optimisation of the GaN growth conditions, allow for higher quality GaN quantum dot growth. The possibility of optimising the morphology of the AlN nanopyramids seems less promising when compared to the AlN rods, however. One could carefully tune wet etch rate to realise a top c-plane truncation. Unfortunately, it is likely that precisely tuning the wet etching process may be difficult to do accurately and reproducibly. If one were to undertake this, a very long wet etch at, or close to, room temperature would probably be the best route to allow for the greatest degree of control.

Additionally, utilising the sharp features in the inclined plane joins of the wet etched nanoholes for GaN quantum dot growth would also be attractive. This could allow for some more fundamental studies of III-N quantum dots as these sites should have 3-fold, rather than 6-fold symmetry. Ultimately, optimisation of both the wet etch process in addition to the GaN growth conditions would present a rather lengthy body of work

for both AlN wet etched structures.

The growth of InGaN in thermally etched GaN windows would be a novel route towards InGaN site-controlled quantum dots. The nature of thermal etching may lead to GaN sites with higher crystallographic therefore allowing for the growth of higher quality InGaN quantum dots. Further investigation of the process could allow for thermal etching of a n-type GaN template followed by InGaN quantum dot growth and a p-type top layer in order to create an electrically injected quantum dot device. Optimisation of InGaN quantum dot growth conditions would likely be rather challenging as one would want to enable enough adatom migration for preferential InGaN formation within the central pits. One is limited in the range of growth temperatures one could use as InN has a low thermal decomposition temperature [347]. This makes growing InGaN quantum dots at anything but relatively low growth temperatures compared to pure GaN or AlN impossible if one wants to have a relatively high In content in the InGaN QDs.

Finally, further characterisation of sample 5420 in Chapter 7 via CL would be an attractive proposition in order to identify the source of the bright luminescence feature observed at $\sim$ 260 nm in the PL spectra. Such a bright emission could be the signature of quantum dot arrays. Further work with AlGaN rods as opposed to purely AlN rods could allow for the creation of AlGaN/GaN/AlGaN quantum dot architectures that could be electrically injected. This latter investigation would comprise a very large body of work however.

8.4 Outlook and final comments

The work in this thesis provided investigation into areas of uniform, wafer scale AlN nanostructuring that were previously unexplored. The process impact of GaN sublimation has also been explored in detail. It is arguable that site-controlled GaN quantum dots have been realised on one of the AlN structures created. This work therefore offers a route to the creation of non-polar AlN/GaN/AlN site-controlled quantum dots. Further optimisation of the top-down bottom-up AlN nanorods and GaN quantum dot growth to form apex quantum dots would be the most attractive avenue of exploration. This is as this area of investigation seems to be more well developed than that of the other routes for sites for quantum dots. Optimisation of the wet etched structures would likely be challenging and time consuming. Additionally, the sublimed GaN samples presented their own issues with regards to homogeneity and full optimisation of

this process to the wafer scale in addition to site-controlled InGaN quantum dot growth presents a sizable undertaking.

When referring back to the original aims and objectives of this project at the start of Chapter 1, the aims of this project have only partially been fulfilled, with the original aims being rather ambitious. Three methods were developed to create suitable sites to house SCQDs. It is arguable (although certainly not conclusive) that GaN/AlN site-controlled quantum dots have been created albeit not in the specific regions of the nanostructures intended. The creation of a single photon source was not achieved however. It may be possible for another researcher to build upon the results in this thesis to achieve this final aim in the future.

Considering these conclusions, is still the authors hope, that with further work and optimisation, even higher temperature SPE than that reported by Holmes et al. [15] could be achieved with the top-down bottom-up AlN rod architectures, within a feasible investigation time scale. This may then allow for a further step forward in III-N QIP technology.

Bibliography

[1] Wojs. A Jacak. L, Hawrylak. P. *Quantum Dots.* Sringer-Verlag Berlin Heidelberg, Berlin Heidelberg, 1st edition, 1998.

[2] M. A. Reed. Spatial quantization in GaAs–AlGaAs multiple quantum dots. *Journal of Vacuum Science & Technology B: Microelectronics and Nanometer Structures*, 4(1):358, 1986.

[3] Xing Lin, Xingliang Dai, Chaodan Pu, Yunzhou Deng, Yuan Niu, Limin Tong, Wei Fang, Yizheng Jin, and Xiaogang Peng. Electrically-driven single-photon sources based on colloidal quantum dots with near-optimal antibunching at room temperature. *Nature Communications*, 8(1):1–7, 2017.

[4] Mark A. Reed. Quantum Dots. *Scientific American*, 268(1):118–123, 1993.

[5] R. C. Ashoori, H. L. Stormer, J. S. Weiner, L. N. Pfeiffer, S. J. Pearton, K. W. Baldwin, and K. W. West. Single-electron capacitance spectroscopy of discrete quantum levels. *Phys. Rev. Lett.*, 68:3088–3091, 1992.

[6] B. J. Riel. An introduction to self-assembled quantum dots. *American Journal of Physics*, 76(8):750–757, 2008.

[7] B. Daudin, F. Widmann, G. Feuillet, Y. Samson, M. Arlery, and J. Rouvière. Stranski-Krastanov growth mode during the molecular beam epitaxy of highly strained GaN. *Physical Review B - Condensed Matter and Materials Physics*, 56(12):R7069–R7072, 1997.

[8] C. Tessarek, S. Figge, and D. Hommel. Colour and multicolour tuning of InGaN quantum dot based light-emitting diodes. *Journal of Physics D: Applied Physics*, 47(5), 2014.

[9] Meng Zhang, Animesh Banerjee, Chi Sen Lee, John M. Hinckley, and Pallab Bhattacharya. A InGaN/GaN quantum dot green (λ=524 nm) laser. *Applied Physics Letters*, 98(22), 2011.

[10] A. J. Shields, R. M. Stevenson, R. M. Thompson, M. B. Ward, Z. Yuan, B. E. Kardynal, P. See, I. Farrer, C. Lobo, K. Cooper, and D. A. Ritchie. Self-assembled quantum dots as a source of single photons and photon pairs. *Physica Status Solidi (B) Basic Research*, 238(2):353–359, 2003.

[11] T. Nakaoka, S. Kako, Y. Arakawa, and S. Tarucha. Coulomb blockade in a self-assembled GaN quantum dot. *Applied Physics Letters*, 90(16):1–4, 2007.

[12] Johannes D. Plumhof, Rinaldo Trotta, Armando Rastelli, and Oliver G. Schmidt. Experimental methods of post-growth tuning of the excitonic fine structure splitting in semiconductor quantum dots. *Nanoscale Research Letters*, 7(336), 2012.

[13] Lei Zhang, Chu Hsiang Teng, Tyler A. Hill, Leung Kway Lee, Pei Cheng Ku, and Hui Deng. Single photon emission from site-controlled InGaN/GaN quantum dots. *Applied Physics Letters*, 103(19):1–6, 2013.

[14] Hsiang Szu Chang, Chieh Ming Hsu, Ming Hui Yang, Tung Po Hsieh, Jen Inn Chyi, and Tzu Min Hsu. Site-controlled InGaAs quantum dots grown on a GaAs multi-faceted microstructure for single photon emissions. *Physica Status Solidi (C) Current Topics in Solid State Physics*, 5(9):2713–2715, 2008.

[15] Mark J. Holmes, Satoshi Kako, Kihyun Choi, Munetaka Arita, and Yasuhiko Arakawa. Single Photons from a Hot Solid-State Emitter at 350 K. *ACS Photonics*, 3(4):543–546, 2016.

[16] Ian M. Watson. Metal organic vapour phase epitaxy of AlN, GaN, InN and their alloys: A key chemical technology for advanced device applications. *Coordination Chemistry Reviews*, 257(13-14):2120–2141, 2013.

[17] Dabing Li, Ke Jiang, Xiaojuan Sun, and Chunlei Guo. AlGaN photonics: recent advances in materials and ultraviolet devices. *Advances in Optics and Photonics*, 10(1):43, 2018.

[18] Ueda. D. *'Properties and Advantages of Gallium Nitride', Power GaN Devices Materials, Applications and Reliability.* Springer International Publishing, Switzerland, 1st edition, 2017.

[19] Tanya Paskova. Development and prospects of nitride materials and devices with nonpolar surfaces. *Physica Status Solidi (B) Basic Research*, 245(6):1011–1025, 2008.

[20] P Li and ZF Zhang. Standing wave effect and fractal structure in dislocation evolution. *Scientific reports*, 7(1):1–6, 2017.

[21] Friedel. J. *Dislocations.* Pergamon Press Ltd, Oxford, 1st edition, 1964.

[22] Harun H. Solak, Christian Dais, and Francis Clube. Displacement Talbot lithography: a new method for high-resolution patterning of large areas. *Opt. Express*, 19(11):10686–10691, 2011.

[23] Kazuo Nojiri. *Dry Etching Technology for Semiconductors.* Springer International Publishing : Imprint: Springer, Cham, 1st ed. edition, 2015.

[24] Goodhew.P & Humphreys. F. J. *Electron Microscopy and Analysis.* Taylor & Francis Ltd, London, 2nd edition, 1988.

[25] Reimer. L. *Transmission Electron Microscopy Physics of Image Formation and Microanalysis.* Springer-Verlag Berlin Heidelberg, Berlin, 1st edition, 1984.

[26] Shaoyang Liu and Yifen Wang. Application of AFM in microbiology: a review. *Scanning*, 32(2):61–73, 2010.

[27] D. Simeonov, E. Feltin, J. F. Carlin, R. Buttá, M. Ilegems, and N. Grandjean. Stranski-Krastanov GaNAlN quantum dots grown by metal organic vapor phase epitaxy. *Journal of Applied Physics*, 99(8), 2006.

[28] Pierre Lefebvre and Bruno Gayral. Optical properties of GaN/AlN quantum dots. *Comptes Rendus Physique*, 9(8):816–829, 2008. Recent advances in quantum dot physics / Nouveaux développements dans la physique des boîtes quantiques.

[29] Thierry Bretagnon, Pierre Lefebvre, Pierre Valvin, Richard Bardoux, Thierry Guillet, Thierry Taliercio, Bernard Gil, Nicolas Grandjean, Fabrice Semond, B Damilano, et al. Radiative lifetime of a single electron-hole pair in GaN/AlN quantum dots. *Physical Review B*, 73(11):113304, 2006.

[30] Pierre Marie Coulon, Gunnar Kusch, Robert W. Martin, and Philip A. Shields. Deep UV Emission from Highly Ordered AlGaN/AlN Core-Shell Nanorods. *ACS Applied Materials and Interfaces*, 10(39):33441–33449, 2018.

[31] P. R. Edwards, R. W. Martin, I. M. Watson, C. Liu, R. A. Taylor, J. H. Rice, J. H. Na, J. W. Robinson, and J. D. Smith. Quantum dot emission from site-controlled InGaN/GaN micropyramid arrays. *Applied Physics Letters*, 85(19):4281–4283, 2004.

[32] Gordon Schmidt, Christoph Berger, Peter Veit, Sebastian Metzner, Frank Bertram, Jürgen Bläsing, Armin Dadgar, André Strittmatter, Jürgen Christen, Gordon Callsen, Stefan Kalinowski, and Axel Hoffmann. Direct evidence of single quantum dot emission from GaN islands formed at threading dislocations using nanoscale cathodoluminescence: A source of single photons in the ultraviolet. *Applied Physics Letters*, 106(25):252101, 2015.

[33] J.P. Garayt, J.M. Gérard, F. Enjalbert, L. Ferlazzo, S. Founta, E. Martinez-Guerrero, F. Rol, D. Araujo, R. Cox, B. Daudin, B. Gayral, Le Si Dang, and H. Mariette. Study of isolated cubic GaN quantum dots by low-temperature cathodoluminescence. *Physica E: Low-dimensional Systems and Nanostructures*, 26(1):203–206, 2005. International Conference on Quantum Dots.

[34] S. Ohkouchi, Y. Nakamura, H. Nakamura, and K. Asakawa. Indium nano-dot arrays formed by field-induced deposition with a Nano-Jet Probe for site-controlled InAs/GaAs quantum dots. *Thin Solid Films*, 464-465:233–236, 2004.

[35] J. Tommila, A. Tukiainen, J. Viheriälä, A. Schramm, T. Hakkarainen, A. Aho, P. Stenberg, M. Dumitrescu, and M. Guina. Nanoimprint lithography patterned GaAs templates for site-controlled InAs quantum dots. *Journal of Crystal Growth*, 323(1):183–186, 2011.

[36] Bhattacharya. S Basu. A. K. Tatiya. S, Bhatt. G. *'Fabrication Processes for Sensors for Automotive Applications: A Review', Sensors for Automotive and Aerospace Applications*. Springer Nature Singapore Pte. Ltd, Singapore, 1st edition, 2019.

[37] P. Atkinson, M. B. Ward, S. P. Bremner, D. Anderson, T. Farrow, G. A.C. Jones, A. J. Shields, and D. A. Ritchie. Site control of InAs quantum dot nucleation by ex situ electron-beam lithographic patterning of GaAs substrates. *Physica E: Low-Dimensional Systems and Nanostructures*, 32(1-2 SPEC. ISS.):21–24, 2006.

[38] Brandon Demory, Tyler A. Hill, Chu Hsiang Teng, Lei Zhang, Hui Deng, and Pei Cheng Ku. Plasmonic Enhancement of Single Photon Emission from a Site-Controlled Quantum Dot. *ACS Photonics*, 2(8):1065–1070, 2015.

[39] Lei Zhang, Chu Hsiang Teng, Pei Cheng Ku, and Hui Deng. Charge-tunable indium gallium nitride quantum dots. *Physical Review B*, 93(8):1–7, 2016.

[40] Shota Kitamura, Kazumasa Hiramatsu, and Nobuhiko Sawaki. Fabrication of GaN hexagonal pyramids on dot-patterned GaN/sapphire substrates via selective metalorganic vapor phase epitaxy. *Japanese journal of applied physics*, 34(9B):L1184, 1995.

[41] V Perez-Solorzano, A Groning, H Schweizer, and M Jetter. Evidence of different confinement regimes in site-controlled pyramidal InGaN structures. *physica status solidi (b)*, 242(12):R97–R99, 2005.

[42] V. Perez-Solorzano, A. Groning, M. Jetter, T. Riemann, and J. Christen. Near-red emission from site-controlled pyramidal InGaN quantum dots. *Applied Physics Letters*, 87(16):1–3, 2005.

[43] A. F. Jarjour, T. J. Parker, R. A. Taylor, R. W. Martin, and I. M. Watson. Two-photon absorption in single site-controlled InGaN/GaN quantum dots. *Physica Status Solidi C: Conferences*, 2(11):3843–3846, 2005.

[44] Su-Hyun Gong, Sejeong Kim, Je-Hyung Kim, Jong-Hoi Cho, and Yong-Hoon Cho. Site-Selective, Two-Photon Plasmonic Nanofocusing on a Single Quantum Dot for Near-Room-Temperature Operation. *ACS Photonics*, 5(3):711–717, 2018.

[45] Chih Wei Hsu, Anders Lundskog, K. Fredrik Karlsson, Urban Forsberg, Erik Janzén, and Per Olof Holtz. Single excitons in InGaN quantum dots on GaN pyramid arrays. *Nano Letters*, 11(6):2415–2418, 2011.

[46] Anders Lundskog, Chih Wei Hsu, K. Fredrik Karlsson, Supaluck Amloy, Daniel Nilsson, Urban Forsberg, Per Olof Holtz, and Erik Janzén. Direct generation of linearly polarized photon emission with designated orientations from site-controlled InGaN quantum dots. *Light: Science and Applications*, 3(September 2013), 2014.

[47] Kihyun Choi, Satoshi Kako, Mark J. Holmes, Munetaka Arita, and Yasuhiko Arakawa. Strong exciton confinement in site-controlled GaN quantum dots embedded in nanowires. *Applied Physics Letters*, 103(17), 2013.

[48] Žarko Gačević, Mark Holmes, Ekaterina Chernysheva, Marcus Müller, Almudena Torres-Pardo, Peter Veit, Frank Bertram, Jürgen Christen, José María González Calbet, Yasuhiko Arakawa, Enrique Calleja, and Snežana Lazić. Emission of Linearly Polarized Single Photons from Quantum Dots Contained in Nonpolar, Semipolar, and Polar Sections of Pencil-Like InGaN/GaN Nanowires. *ACS Photonics*, 4(3):657–664, 2017.

[49] R. Armstrong, P-M. Coulon, P. Bozinakis, R.W. Martin, and P.A. Shields. Creation of regular arrays of faceted AlN nanostructures via a combined top-down, bottom-up approach. *Journal of Crystal Growth*, 548:125824, 2020.

[50] Dongsheng Li, M. Sumiya, S. Fuke, Deren Yang, Duanlin Que, Y. Suzuki, and Y. Fukuda. Selective etching of GaN polar surface in potassium hydroxide solution studied by x-ray photoelectron spectroscopy. *Journal of Applied Physics*, 90(8):4219–4223, 2001.

[51] Hock M Ng, Nils G Weimann, and Aref Chowdhury. GaN nanotip pyramids formed by anisotropic etching. *Journal of applied physics*, 94(1):650–653, 2003.

[52] D. Zhuang, J.H. Edgar, B. Strojek, J. Chaudhuri, and Z. Rek. Defect-selective etching of bulk AlN single crystals in molten KOH/NaOH eutectic alloy. *Journal of Crystal Growth*, 262(1):89–94, 2004.

[53] W. Guo, J. Xie, C. Akouala, S. Mita, A. Rice, J. Tweedie, I. Bryan, R. Collazo, and Z. Sitar. Comparative study of etching high crystalline quality AlN and GaN. *Journal of Crystal Growth*, 366:20–25, 2013.

[54] I Cimalla, Ch Foerster, V Cimalla, V Lebedev, D Cengher, and O Ambacher. Wet chemical etching of AlN in KOH solution. *physica status solidi c*, 3(6):1767–1770, 2006.

[55] Pierre-Marie Coulon, Peng Feng, Benjamin Damilano, Stéphane Vézian, Tao Wang, and Philip A Shields. Influence of the reactor environment on the selective area thermal etching of GaN nanohole arrays. *Scientific reports*, 10(1):1–9, 2020.

[56] Ignacio Horcas, Rs Fernández, JM Gomez-Rodriguez, JWSX Colchero, JWSXM Gómez-Herrero, and AM Baro. WSXM: A software for scanning probe microscopy and a tool for nanotechnology. *Review of scientific instruments*, 78(1):013705, 2007.

[57] Caroline A Schneider, Wayne S Rasband, and Kevin W Eliceiri. NIH Image to ImageJ: 25 years of image analysis. *Nature methods*, 9(7):671–675, 2012.

[58] Tomas Jemsson, Houssaine Machhadani, K. Fredrik Karlsson, Chih Wei Hsu, and Per Olof Holtz. Linearly polarized single photon antibunching from a site-controlled InGaN quantum dot. *Applied Physics Letters*, 105(8), 2014.

[59] Marco Felici, Pascal Gallo, Arun Mohan, Benjamin Dwir, Alok Rudra, and Eli Kapon. Site-controlled InGaAs quantum dots with tunable emission energy. *Small*, 5(8):938–943, 2009.

[60] Alberto Pimpinelli and Jacques Villain. *Physics of Crystal Growth*. Collection Alea-Saclay: Monographs and Texts in Statistical Physics. Cambridge University Press, Cambridge, 1998.

[61] Pawel Hawrylak. Single-electron capacitance spectroscopy of few-electron artificial atoms in a magnetic field: Theory and experiment. *Phys. Rev. Lett.*, 71:3347–3350, Nov 1993.

[62] Jana Drbohlavova, Vojtech Adam, Rene Kizek, and Jaromir Hubalek. Quantum dots—characterization, preparation and usage in biological systems. *International journal of molecular sciences*, 10(2):656–673, 2009.

[63] David Sands. *Diode lasers*. IOP Publishing Ltd, London, 2005.

[64] Hau-Vei Han, Huang-Yu Lin, Chien-Chung Lin, Wing-Cheung Chong, Jie-Ru Li, Kuo-Ju Chen, Peichen Yu, Teng-Ming Chen, Huang-Ming Chen, Kei-May Lau, and Hao-Chung Kuo. Resonant-enhanced full-color emission of quantum-dot-based micro LED display technology. *Optics Express*, 23(25):32504, 2015.

[65] Julien Brault, Benjamin Damilano, Borge Vinter, Philippe Vennégués, Mathieu Leroux, Abdelkarim Kahouli, and Jean Massies. AlGaN-based light emitting diodes using self-assembled GaN quantum dots for ultraviolet emission. *Japanese Journal of Applied Physics*, 52(8 PART 2):08JG01, 2013.

[66] Satoshi Kako, Mark Holmes, Sylvain Sergent, Matthias Bürger, Donat J. As, and Yasuhiko Arakawa. Single-photon emission from cubic GaN quantum dots. *Applied Physics Letters*, 104(1):2012–2015, 2014.

[67] Chu Hsiang Teng, Lei Zhang, Tyler A. Hill, Brandon Demory, Hui Deng, and Pei Cheng Ku. Elliptical quantum dots as on-demand single photons sources with deterministic polarization states. *Applied Physics Letters*, 107(19), 2015.

[68] Mark J. Holmes, Kihyun Choi, Satoshi Kako, Munetaka Arita, and Yasuhiko Arakawa. Room-temperature triggered single photon emission from a III-nitride site-controlled nanowire quantum dot. *Nano Letters*, 14(2):982–986, 2014.

[69] Aditya Sharma, Gajjala Sumana, Sameer Sapra, and Bansi Dhar Malhotra. Quantum dots self assembly based interface for blood cancer detection. *Langmuir*, 29(27):8753–8762, 2013.

[70] Xiaohu Gao, Yuanyuan Cui, Richard M. Levenson, Leland W.K. Chung, and Shuming Nie. In vivo cancer targeting and imaging with semiconductor quantum dots. *Nature Biotechnology*, 22(8):969–976, 2004.

[71] Tomah Sogabe, Qing Shen, and Koichi Yamaguchi. Recent progress on quantum dot solar cells: a review. *Journal of Photonics for Energy*, 6(4):040901, 2016.

[72] Cherie R. Kagan, Efrat Lifshitz, Edward H. Sargent, and Dmitri V. Talapin. Building devices from colloidal quantum dots. *Science*, 353(6302), 2016.

[73] Zhongsheng Luo, Jesse Manders, and Jeff Yurek. Television's Quantum dots will be the next darling of TV manufacturers. *IEEE Spectrum*, 55(3):28–53, 2018.

[74] Daniel Huber, Marcus Reindl, Yongheng Huo, Huiying Huang, Johannes S. Wildmann, Oliver G. Schmidt, Armando Rastelli, and Rinaldo Trotta. Highly indistinguishable and strongly entangled photons from symmetric GaAs quantum dots. *Nature Communications*, 8(May):15506, 2017.

[75] RC Ashoori. Electrons in artificial atoms. *Nature*, 379(6564):413, 1996.

[76] Jonathan Owen and Louis Brus. Chemical Synthesis and Luminescence Applications of Colloidal Semiconductor Quantum Dots. *Journal of the American Chemical Society*, 139(32):10939–10943, 2017.

[77] E. M. Clausen, H. G. Craighead, J. M. Worlock, J. P. Harbison, L. M. Schiavone, L. Florez, and B. Van der Gaag. Determination of nonradiative surface layer thickness in quantum dots etched from single quantum well GaAs/AlGaAs. *Applied Physics Letters*, 55(14):1427–1429, 1989.

[78] Tijana Rajh, Olga I. Micic, and Arthur J. Nozik. Synthesis and characterization of surface-modified colloidal cadmium telluride quantum dots. *The Journal of Physical Chemistry*, 97(46):11999–12003, 2005.

[79] Graham H. Carey, Ahmed L. Abdelhady, Zhijun Ning, Susanna M. Thon, Osman M. Bakr, and Edward H. Sargent. Colloidal Quantum Dot Solar Cells. *Chemical Reviews*, 115(23):12732–12763, 2015.

[80] A.I. Ekimov, Al.L. Efros, and A.A. Onushchenko. Quantum size effect in semiconductor microcrystals. *Solid State Communications*, 56(11):921 – 924, 1985.

[81] S. Watanabe, E. Pelucchi, K. Leifer, A. Malko, B. Dwir, and E. Kapon. Patterning of confined-state energies in site-controlled semiconductor quantum dots. *Applied Physics Letters*, 86(24):1–3, 2005.

[82] Debajyoti Das and Arup Samanta. Photoluminescent silicon quantum dots in core/shell configuration: Synthesis by low temperature and spontaneous plasma processing. *Nanotechnology*, 22(5), 2011.

[83] Lichan Chen, Nengna Xu, Haiyan Yang, Chen Zhou, and Yuwu Chi. Zinc oxide quantum dots synthesized by electrochemical etching of metallic zinc in organic electrolyte and their electrochemiluminescent properties. *Electrochimica Acta*, 56(3):1387–1391, 2011.

[84] Shunsuke Ohkouchi, Yusui Nakamura, Hitoshi Nakamura, and Kiyoshi Asakawa. InAs nano-dot array formation using nano-jet probe for photonics applications. *Japanese Journal of Applied Physics, Part 1: Regular Papers and Short Notes and Review Papers*, 44(7 B):5777–5780, 2005.

[85] Yen Sheng Lin, Kung Jen Ma, C. C. Yang, and Thomas E. Weirich. Effects of post-growth thermal annealing on the indium aggregated structures in InGaN/GaN quantum wells. *Journal of Crystal Growth*, 242(1-2):35–40, 2002.

[86] Yen-Sheng Lin, Kung-Jen Ma, Cheng Hsu, Yi-Yin Chung, Chih-Wen Liu, Shih-Wei Feng, Yung-Chen Cheng, C. C. Yang, Ming-Hua Mao, Hui-Wen Chuang, Cheng-Ta Kuo, Jian-Shihn Tsang, and Thomas E. Weirich. Quasiregular quantum-dot-like structure formation with postgrowth thermal annealing of InGaN/GaN quantum wells. *Applied Physics Letters*, 80(14):2571–2573, 2002.

[87] Munetaka Arita, Florian Le Roux, Mark J. Holmes, Satoshi Kako, and Yasuhiko Arakawa. Ultraclean Single Photon Emission from a GaN Quantum Dot. *Nano Letters*, 17(5):2902–2907, 2017.

[88] Raja S. R. Gajjela and Paul M. Koenraad. Atomic-Scale Characterization of Droplet Epitaxy Quantum Dots. *Nanomaterials*, 11(1), 2021.

[89] Suwit Kiravittaya, Armando Rastelli, and Oliver G Schmidt. Advanced quantum dot configurations. *Reports on Progress in Physics*, 72(4):046502, 2009.

[90] Jiang Wu and Zhiming M Wang. Droplet epitaxy for advanced optoelectronic materials and devices. *Journal of Physics D: Applied Physics*, 47(17):173001, 2014.

[91] Rachel A. Oliver, G. Andrew D. Briggs, Menno J. Kappers, Colin J. Humphreys, Shazia Yasin, James H. Rice, Jonathon D Smith, and Robert A. Taylor. InGaN quantum dots grown by metalorganic vapor phase epitaxy employing a post-growth nitrogen anneal. *Applied Physics Letters*, 83(4):755–757, 2003.

[92] Anas F. Jarjour, Rachel A. Oliver, and Robert A. Taylor. Nitride-based quantum dots for single photon source applications. *physica status solidi (a)*, 206(11):2510–2523, 2009.

[93] Rachel A. Oliver, Haitham A.R. El-Ella, Daniel P. Collins, Benjamin Reid, Yucheng Zhang, Fiona Christie, Menno J. Kappers, and Robert A. Taylor. Growth of InGaN quantum dots with AlGaN barrier layers via modified droplet epitaxy. *Materials Science and Engineering: B*, 178(20):1390–1394, 2013.

[94] Nobuyuki Koguchi, Satoshi Takahashi, and Toyohiro Chikyow. New MBE growth method for InSb quantum well boxes. *Journal of Crystal Growth*, 111(1):688–692, 1991.

[95] F. Widmann, B. Daudin, G. Feuillet, Y. Samson, J. L. Rouvière, and N. Pelekanos. Growth kinetics and optical properties of self-organized GaN quantum dots. *Journal of Applied Physics*, 83(12):7618–7624, 1998.

[96] K. Hoshino and Y. Arakawa. Formation of high-density GaN self-assembled quantum dots by MOCVD. *Journal of Crystal Growth*, 272(1-4 SPEC. ISS.):161–166, 2004.

[97] M Copel, MC Reuter, Efthimios Kaxiras, and RM Tromp. Surfactants in epitaxial growth. *Physical review letters*, 63(6):632, 1989.

[98] Konrad Bellmann. *Epitaxial growth of GaN quantum dots on smooth AlN.* PhD thesis, Technischen Universität Berlin, February 2018.

[99] Tao Yang, Shigeru Kohmoto, Hitoshi Nakamura, and Kiyoshi Asakawa. Effects of lateral quantum dot pitch on the formation of vertically aligned InAs site-controlled quantum dots. *Journal of Applied Physics*, 93(2):1190–1194, 2003.

[100] F. Widmann, J. Simon, B. Daudin, G. Feuillet, J. Rouvière, N. Pelekanos, and G. Fishman. Blue-light emission from GaN self-assembled quantum dots due to giant piezoelectric effect. *Physical Review B - Condensed Matter and Materials Physics*, 58(24):R15989–R15992, 1998.

[101] Konrad Bellmann, Farsane Tabataba-Vakili, Tim Wernicke, Andre Strittmatter, Gordon Callsen, Axel Hoffmann, and Michael Kneissl. Desorption induced GaN quantum dots on (0001) AlN by MOVPE. *Physica Status Solidi - Rapid Research Letters*, 9(9):526–529, 2015.

[102] Satoru Tanaka, Sohachi Iwai, and Yoshinobu Aoyagi. Self-assembling GaN quantum dots on $Al_xGa_{1-x}N$ surfaces using a surfactant. *Applied Physics Letters*, 69(26):4096–4098, 1996.

[103] M. Miyamura, K. Tachibana, and Y. Arakawa. High-density and size-controlled GaN self-assembled quantum dots grown by metalorganic chemical vapor deposition. *Applied Physics Letters*, 80(21):3937–3939, 2002.

[104] J Brault, M Al Khalfioui, S Matta, B Damilano, M Leroux, S Chenot, M Korytov, J E Nkeck, P Vennéguès, J–Y Duboz, J Massies, and B Gil. UVA and UVB light emitting diodes with $Al_yGa_{1-y}N$ quantum dot active regions covering the 305-335 nm range. *Semiconductor Science and Technology*, 33(7):075007, 2018.

[105] Jai Verma, Prem Kumar Kandaswamy, Vladimir Protasenko, Amit Verma, Huili Grace Xing, and Debdeep Jena. Tunnel-injection GaN quantum dot ultraviolet light-emitting diodes. *Applied Physics Letters*, 102(4), 2013.

[106] P Bhattacharya, S Ghosh, and AD Stiff-Roberts. Quantum dot opto-electronic devices. *Annu. Rev. Mater. Res.*, 34:1–40, 2004.

[107] D. L. Huffaker, G. Park, Z. Zou, O. B. Shchekin, and D. G. Deppe. 1.3 μm room-temperature GaAs-based quantum-dot laser. *Applied Physics Letters*, 73(18):2564–2566, 1998.

[108] P. Michler, A. Kiraz, C. Becher, W. V. Schoenfeld, P. M. Petroff, L. Zhang, E. Hu, and A. Imamoğlu. A quantum dot single-photon turnstile device. *Science*, 290(5500):2282–2285, 2000.

[109] Richard Nötzel. Self-organized growth of quantum-dot structures. *Semiconductor Science and Technology*, 11(10):1365–1379, 1996.

[110] E Pelucchi, S Watanabe, K Leifer, B Dwir, and E Kapon. Site-controlled quantum dots grown in inverted pyramids for photonic crystal applications. *Physica E: Low-Dimensional Systems and Nanostructures*, 23(3-4 SPEC. ISS.):476–481, 2004.

[111] Saniya Deshpande, Thomas Frost, Arnab Hazari, and Pallab Bhattacharya. Electrically pumped single-photon emission at room temperature from a single InGaN/GaN quantum dot. *Applied Physics Letters*, 105(14), 2014.

[112] W. Unrau, D. Quandt, J. H. Schulze, T. Heindel, T. D. Germann, O. Hitzemann, A. Strittmatter, S. Reitzenstein, U. W. Pohl, and D. Bimberg. Electrically driven single photon source based on a site-controlled quantum dot with self-aligned current injection. *Applied Physics Letters*, 101(21), 2012.

[113] A. Lochmann, E. Stock, O. Schulz, F. Hopfer, D. Bimberg, V. A. Haisler, A. I. Toropov, A. K. Bakarov, M. Scholz, S. Büttner, and O. Benson. Electrically driven quantum dot single photon source. *Physica Status Solidi (C) Current Topics in Solid State Physics*, 4(2):547–550, 2007.

[114] Ephriam Chukwuocha, Michael Onyeaju, and Taylor S T Harry. Theoretical Studies on the Effect of Confinement on Quantum Dots Using the Brus Equation. *World Journal of Condensed Matter Physics*, 2:96–100, 01 2012.

[115] Vladimir A. Fonoberov and Alexander A. Balandin. Excitonic properties of strained wurtzite and zinc-blende GaN/Al_xGa_1-xN quantum dots. *Journal of Applied Physics*, 94(11):7178–7186, 2003.

[116] T. Tran, A. Muller, C. K. Shih, P. S. Wong, G. Balakrishnan, N. Nuntawong, J. Tatebayashi, and D. L. Huffaker. Single dot spectroscopy of site-controlled InAs quantum dots nucleated on GaAs nanopyramids. *Applied Physics Letters*, 91(13):38–41, 2007.

[117] K. D. Jöns, P. Atkinson, M. Müller, M. Heldmaier, S. M. Ulrich, O. G. Schmidt, and P. Michler. Triggered indistinguishable single photons with narrow line widths from site-controlled quantum dots. *Nano Letters*, 13(1):126–130, 2013.

[118] S Sergent, M Arita, S Kako, S Iwamoto, and Y Arakawa. High-Q ($>$ 5000) AlN nanobeam photonic crystal cavity embedding GaN quantum dots. *Applied Physics Letters*, 100(12):121103, 2012.

[119] B. Fain, D. Elvira, L. Le Gratiet, L. Largeau, G. Beaudoin, D. Troadec, I. Abram, A. Beveratos, I. Robert-Philip, G. Patriarche, and I. Sagnes. Structural analysis of site-controlled InAs/InP quantum dots. *Journal of Crystal Growth*, 334(1):37–39, 2011.

[120] H. Z. Song, T. Usuki, T. Ohshima, Y. Sakuma, M. Kawabe, Y. Okada, K. Takemoto, T. Miyazawa, S. Hirose, Y. Nakata, M. Takatsu, and N. Yokoyama. Site-controlled quantum

dots fabricated using an atomic-force microscope assisted technique. *Nanoscale Research Letters*, 1(2):160–166, 2006.

[121] A Surrente, P Gallo, M Felici, B Dwir, A Rudra, and E Kapon. Dense arrays of ordered pyramidal quantum dots with narrow linewidth photoluminescence spectra. *Nanotechnology*, 20(41), 2009.

[122] M. Calic, P. Gallo, M. Felici, K. A. Atlasov, B. Dwir, A. Rudra, G. Biasiol, L. Sorba, G. Tarel, V. Savona, and E. Kapon. Phonon-mediated coupling of InGaAs/GaAs quantum-dot excitons to photonic crystal cavities. *Physical Review Letters*, 106(22):1–4, 2011.

[123] Jesus Herranz, Lukasz Wewior, Benito Alen, David Fuster, Luisa Gonzalez, and Yolanda Gonzalez. Role of re-growth interface preparation process for spectral line-width reduction of single InAs site-controlled quantum dots. *Nanotechnology*, 26(19), 2015.

[124] K. G. Lagoudakis, P. L. McMahon, C. Dory, K. A. Fischer, K. Müller, V. Borish, D. Dalacu, P. J. Poole, M. E. Reimer, V. Zwiller, Y. Yamamoto, and J. Vuckovic. Ultrafast coherent manipulation of trions in site-controlled nanowire quantum dots. *Optica*, 3(12):1430, 2016.

[125] Christoph Simon. Photonic quantum information processing: From quantum memories to photon-photon gates. *2011 ICO International Conference on Information Photonics, IP 2011*, pages 1–2, 2011.

[126] Ágoston Schranz, Eszter Udvary, and Zsolt Kis. Photon statistics determination for single photon based quantum key distribution. *International Conference on Transparent Optical Networks*, 2016-August(1):2–5, 2016.

[127] E. B. Fel'dman, A. N. Pyrkov, and A. I. Zenchuk. Solid-state multiple quantum NMR in quantum information processing: exactly solvable models. *Philosophical Transactions of the Royal Society A: Mathematical, Physical and Engineering Sciences*, 370(1976):4690–4712, 2012.

[128] Stefan Kremling, Christian Tessarek, Heiko Dartsch, Stephan Figge, Sven Höfling, Lukas Worschech, Carsten Kruse, Detlef Hommel, and Alfred Forchel. Single photon emission from InGaN/GaN quantum dots up to 50 K. *Applied Physics Letters*, 100(6):1–4, 2012.

[129] Igor Aharonovich, Dirk Englund, and Milos Toth. Solid-state single-photon emitters. *Nature Photonics*, 10(10):631–641, 2016.

[130] Stefan Scheel. Single-photon sources-an introduction. *Journal of Modern Optics*, 56(2-3):141–160, 2009.

[131] Charles Santori, David Fattal, Jelena Vučković, Glenn S. Solomon, and Yoshihisa Yamamoto. Indistinguishable photons from a single-photon device. *Nature*, 419(6907):594–597, 2002.

[132] Y. Yamamoto. Quantum communication and information processing with quantum dots. *Quantum Information Processing*, 5(5):299–311, 2006.

[133] J L O'Brien. Optical Quantum Computing. *Science*, 318(5856):1567–1570, 2007.

[134] C. L. Salter, R. M. Stevenson, I. Farrer, C. A. Nicoll, D. A. Ritchie, and A. J. Shields. An entangled-light-emitting diode. *Nature*, 465(7298):594–597, 2010.

[135] Daniel Huber, Marcus Reindl, Johannes Aberl, Armando Rastelli, and Rinaldo Trotta. Semiconductor quantum dots as an ideal source of polarization-entangled photon pairs on-demand: A review. *Journal of Optics (United Kingdom)*, 20(7), 2018.

[136] Mishra. V. *An Introduction to Quantum Communication*. Momentum Press LLC, New York, 1st edition, 2016.

[137] L. O. Mereni, O. Marquardt, G. Juska, V. Dimastrodonato, E. P. O'Reilly, and E. Pelucchi. Fine-structure splitting in large-pitch pyramidal quantum dots. *Physical Review B - Condensed Matter and Materials Physics*, 85(15):1–13, 2012.

[138] Ranber Singh. Tuning fine structure splitting and exciton emission energy in semiconductor quantum dots. *Journal of Luminescence*, 202(February):118–131, 2018.

[139] Simone Birindelli, Marco Felici, Johannes S. Wildmann, Antonio Polimeni, Mario Capizzi, Annamaria Gerardino, Silvia Rubini, Faustino Martelli, Armando Rastelli, and Rinaldo Trotta. Single photons on demand from novel site-controlled GaAsN/GaAsN:H quantum dots. *Nano Letters*, 14(3):1275–1280, 2014.

[140] M. Facão, A. Lopes, A. L. Silva, and P. Silva. Computer simulation for calculating the second-order correlation function of classical and quantum light. *European Journal of Physics*, 32(4):925–934, 2011.

[141] Hans A. Bachor and Timothy C. Ralph. *Quantum Models of Light*, pages 93–137. Wiley-VCH, 2019.

[142] Mark J Holmes, M Arita, and Y Arakawa. III-nitride quantum dots as single photon emitters. *Semiconductor Science and Technology*, 34(3):033001, feb 2019.

[143] T. Braun, V. Baumann, O. Iff, S. Höfling, C. Schneider, and M. Kamp. Enhanced single photon emission from positioned InP/GaInP quantum dots coupled to a confined Tamm-plasmon mode. *Applied Physics Letters*, 106(4), 2015.

[144] R. Hanbury Brown and R. Q. Twiss. A test of a new type of stellar interferometer on Sirius. *Nature*, 178(4541):1046–1048, 1956.

[145] Giorgio Pettinari, Marco Felici, Francesco Biccari, Mario Capizzi, and Antonio Polimeni. Site-controlled quantum emitters in dilute nitrides and their integration in photonic crystal cavities. *Photonics*, 5(2):10, 2018.

[146] J. Martin-Sanchez, G. Muñoz-Matutano, J. Herranz, J. Canet-Ferrer, B. Alen, Y. Gonzalez, P. Alonso-Gonzalez, D. Fuster, L. Gonzalez, J. Martinez-Pastor, and F. Briones. Single Photon Emission from Site-Controlled InAs Quantum Dots Grown on GaAs(001) Patterned Substrates. *ACS Nano*, 3(6):1513–1517, 2009.

[147] S.N Mohammad and H Morkoç. Progress and prospects of group-III nitride semiconductors. *Progress in Quantum Electronics*, 20(5-6):361–525, 1996.

[148] Sarad Bahadur Thapa. *Studies of AlN grown by MOVPE for Electronic and Optoelectronic Applications*. PhD thesis, Faculty of Engineering and Computer Sciences Ulm University, July 2010.

[149] A. Khaledi-Nasab, M. Sabaeian, M. Rezaie, and M. Mohammad-Rezaee. Linear and nonlinear tunable optical properties of intersubband transitions in GaN/AlN quantum dots in presence and absence of wetting layer. *Journal of the European Optical Society*, 9, 2014.

[150] David Holec and Paul H. Mayrhofer. Surface energies of AlN allotropes from first principles. *Scripta Materialia*, 67(9):760–762, 2012.

[151] S. C. Jain, M. Willander, J. Narayan, and R. Van Overstraeten. III-nitrides: Growth, characterization, and properties. *Journal of Applied Physics*, 87(3):965–1006, 2000.

[152] O. Ambacher. Growth and applications of group III-nitrides. *Journal of Physics D: Applied Physics*, 31(20):2653–2710, 1998.

[153] S. Strite. GaN, AlN, and InN: A review. *Journal of Vacuum Science & Technology B: Microelectronics and Nanometer Structures*, 10(4):1237, 1992.

[154] Andrew McAllister, Dylan Bayerl, and Emmanouil Kioupakis. Radiative and Auger recombination processes in indium nitride. *Applied Physics Letters*, 112(25):1–6, 2018.

[155] Chuanle Zhou, Amirhossein Ghods, Vishal G. Saravade, Paresh V. Patel, Kelcy L. Yunghans, Cameron Ferguson, Yining Feng, Bahadir Kucukgok, Na Lu, and Ian T. Ferguson. Review—the current and emerging applications of the III-nitrides. *ECS Journal of Solid State Science and Technology*, 6(12):Q149–Q156, 2017.

[156] Margarita P. Thompson, Gregory W. Auner, Tsvetanka S. Zheleva, Kenneth A. Jones, Steven J. Simko, and James N. Hilfiker. Deposition factors and band gap of zinc-blende AlN. *Journal of Applied Physics*, 89(6):3331–3336, 2001.

[157] Y Goldberg, Michael Levinshtein, and Sergey Rumyantsev. *Properties of advanced semiconductor materials: GaN, AIN, InN, BN, SiC, SiGe.* John Wiley & Sons, New York, 1st edition, 2001.

[158] Poppy Siddiqua, Walid A. Hadi, Amith K. Salhotra, Michael S. Shur, and Stephen K. O'Leary. Electron transport and electron energy distributions within the wurtzite and zinc-blende phases of indium nitride: Response to the application of a constant and uniform electric field. *Journal of Applied Physics*, 117(12), 2015.

[159] Morkoc. H. *'Forward', Properties of Group III Nitrides.* INSPEC, the Institute of Electrical Engineers, London, 1st edition, 1994.

[160] Meng. W. *'Crystal structure, mechanical properties, thermal properties and refractive index of AlN', Properties of Group III Nitrides.* INSPEC, the Institute of Electrical Engineers, London, 1st edition, 1993.

[161] Amano. H Akasaki. I. *'Crystal structure, mechanical properties, thermal properties and refractive index of AlN', Properties of Group III Nitrides.* INSPEC, the Institute of Electrical Engineers, London, 1st edition, 1994.

[162] Tansley. T. *'Crystal structure, mechanical properties, thermal properties and refractive index of AlN', Properties of Group III Nitrides.* INSPEC, the Institute of Electrical Engineers, London, 1st edition, 1993.

[163] Ichiro Yonenaga, Yasushi Ohkubo, Momoko Deura, Kentaro Kutsukake, Yuki Tokumoto, Yutaka Ohno, Akihiko Yoshikawa, and Xin Qiang Wang. Elastic properties of indium nitrides grown on sapphire substrates determined by nano-indentation: In comparison with other nitrides. *AIP Advances*, 5(7), 2015.

[164] Jinlong Ma, Wu Li, and Xiaobing Luo. Intrinsic thermal conductivities and size effect of alloys of wurtzite AlN, GaN, and InN from first-principles. *Journal of Applied Physics*, 119(12):125702, 2016.

[165] Quay. R. *Gallium Nitride Electronics.* Springer-Verlag Berlin Heidelberg, Berlin, 1st edition, 2008.

[166] Popovici. G. *'Deposition and properties of group III nitrides by molecular beam epitaxy' Group III Nitride Semiconductor Compounds.* Oxford University Press, Oxford, 1st edition, 1998.

[167] M. L. Glasser. Symmetry properties of the wurtzite structure. *Journal of Physics and Chemistry of Solids*, 10(2-3):229–241, 1959.

[168] D. Zhuang and J. H. Edgar. Wet etching of GaN, AlN, and SiC: A review. *Materials Science and Engineering R: Reports*, 48(1):1–46, 2005.

[169] D. Zhuang, J.H. Edgar, Lianghong Liu, B. Liu, and L. Walker. Wet Chemical Etching of AlN Single Crystals. *MRS Internet Journal of Nitride Semiconductor Research*, 7:e4, 2002.

[170] Daisuke Muto, Tsutomu Araki, Hiroyuki Naoi, Fumie Matsuda, and Yasushi Nanishi. Polarity determination of InN by wet etching. *physica status solidi (a)*, 202(5):773–776, 2005.

[171] Feiliang Chen, Qian Li, Mo Li, Hui Zhang, Feng Huang, and Jian Zhang. Grating-patterned hyperbolic metamaterials for InGaN/GaN nanowire quantum dots single photon source. *Proceedings of the International Conference on Numerical Simulation of Optoelectronic Devices, NUSOD*, pages 99–100, 2017.

[172] Charlotte Rothfuchs, Fabrice Semond, Marc Portail, Olivier Tottereau, Aimeric Courville, Andreas D. Wieck, and Arne Ludwig. Ion-induced interdiffusion of surface GaN quantum dots. *Nuclear Instruments and Methods in Physics Research, Section B: Beam Interactions with Materials and Atoms*, 409:107–110, 2017.

[173] J. Renard, R. Songmuang, G. Tourbot, C. Bougerol, B. Daudin, and B. Gayral. Evidence for quantum-confined Stark effect in GaN/AlN quantum dots in nanowires. *Physical Review B - Condensed Matter and Materials Physics*, 80(12):2–5, 2009.

[174] Bruno Daudin. Polar and nonpolar GaN quantum dots. *Journal of Physics Condensed Matter*, 20(47), 2008.

[175] Xiaojing Gong, Ke Xu, Jianfeng Wang, Hui Yang, Lifeng Bian, Jingping Zhang, and Zijian Xu. Growth behavior of GaN film along non-polar [1 1 -2 0] directions. *Physica B: Condensed Matter*, 406(1):36–39, 2011.

[176] N. Kriouche, P. Venéngués, M. Nemoz, G. Nataf, and P. De Mierry. Stacking faults blocking process in (1 1 -2 2) semipolar GaN growth on sapphire using asymmetric lateral epitaxy. *Journal of Crystal Growth*, 312(19):2625–2630, 2010.

[177] M. A. Moram and M. E. Vickers. X-ray diffraction of III-nitrides. *Reports on Progress in Physics*, 72(3), 2009.

[178] H. Wang, S. L. Li, H. Xiong, Z. H. Wu, J. N. Dai, Y. Tian, Y. Y. Fang, and C. Q. Chen. The effect of AlN nucleation temperature on the growth of AlN films via metalorganic chemical vapor deposition. *Journal of Electronic Materials*, 41(3):466–470, 2012.

[179] Keller. S. *'Substrates and Materials', Power GaN Devices Materials, Applications and Reliability*. Springer International Publishing, Switzwerland, 1st edition, 2017.

[180] Ponce. F. *'Structural defects and materials performance of the III-V nitrides', Group III Nitride Semiconductor Compounds*. Oxford University Press, Oxford, 1st edition, 1998.

[181] Cracknell. A. *Crystals and their structures*. Pergamon Press Ltd., Oxford, 1st edition, 1969.

[182] Henderson. B. *Defects in Crystalline Solids*. Edward Arnold Ltd, London, 1st edition, 1972.

[183] Tilley. R. *Defect Crystal Chemistry and Its Applications*. Blackie & Son Ltd., London, 1st edition, 1987.

[184] Cottrell. A. *Theory of Crystal Dislocations*. Blackie & Son Ltd., London, 1st edition, 1964.

[185] Groves. G Kelly. A. *Crystallography and Crystal Defects*. Longman Group Ltd, London, 1st edition, 1970.

[186] I. Demir, H. Li, Y. Robin, R. McClintock, S. Elagoz, and M. Razeghi. Sandwich method to grow high quality AlN by MOCVD. *Journal of Physics D: Applied Physics*, 51(8), 2018.

[187] H. Behmenburg, C. Giesen, R. Srnanek, J. Kovac, H. Kalisch, M. Heuken, and R. H. Jansen. Investigation of AlN buffer layers on 6H-SiC for AlInN HEMTs grown by MOVPE. *Journal of Crystal Growth*, 316(1):42–45, 2011.

[188] C. Rawn and Jharna Chaudhuri. Lattice parameters of gallium nitride at high temperatures and resulting epitaxial misfits with alumina and silicon carbide substrates, JCPDS-International Centre for Diffraction Data. *Adv. X-ray Anal.*, 43:338–343, 01 2000.

[189] C. J. Lu, L. A. Bendersky, Hai Lu, and William J. Schaff. Threading dislocations in epitaxial lnN thin films grown on (0001) sapphire with a GaN buffer layer. *Applied Physics Letters*, 83(14):2817–2819, 2003.

[190] M. Amirhoseiny, Z. Hassan, and S. S. Ng. Comparative study on structural and optical properties of nitrogen rich InN on Si(110) and 6H-SiC. *Surface Engineering*, 29(7):561–565, 2013.

[191] Daniel Feezell and Shuji Nakamura. Invention, development, and status of the blue light-emitting diode, the enabler of solid-state lighting. *Comptes Rendus Physique*, 19(3):113–133, 2018.

[192] J W Orton and C T Foxon. Group III nitride semiconductors for short wavelength light-emitting devices. *Reports on Progress in Physics*, 61(1):1–75, jan 1998.

[193] Haoning Li, Thomas C. Sadler, and Peter J. Parbrook. AlN heteroepitaxy on sapphire by metalorganic vapour phase epitaxy using low temperature nucleation layers. *Journal of Crystal Growth*, 383:72–78, 2013.

[194] M. Alizadeh, B. T. Goh, A. K. Pandey, C. F. Dee, and S. A. Rahman. Low-RF-power growth of InN thin films by plasma-assisted reactive evaporation with a localized ion source. *Materials Chemistry and Physics*, 199:408–415, 2017.

[195] J. Mickevičius, D. Dobrovolskas, R. Aleksiejūnas, K. Nomeika, T. Grinys, A. Kadys, and G. Tamulaitis. Influence of growth temperature on carrier localization in InGaN/GaN MQWs with strongly redshifted emission band. *Journal of Crystal Growth*, 459:173 – 177, 2017.

[196] N. B. Hannay, editor. *Semiconductors*. American Chemical Society monograph series ; no.140. Chapman and Hall, London, 1959.

[197] R.A Stradling & P.C Klipstein, editor. *Growth and characterisation of semiconductors*. CRC Press, 1990.

[198] Rajappan Radhakrishnan Sumathi. Status and Challenges in Hetero-epitaxial Growth Approach for Large Diameter AlN Single Crystalline Substrates. *ECS Journal of Solid State Science and Technology*, 10(3):035001, 2021.

[199] R. Dwiliński, R. Doradziński, J. Garczyński, L.P. Sierzputowski, A. Puchalski, Y. Kanbara, K. Yagi, H. Minakuchi, and H. Hayashi. Excellent crystallinity of truly bulk ammonothermal GaN. *Journal of Crystal Growth*, 310(17):3911–3916, 2008. Special issue IWBNS-5.

[200] O. Kovalenkov, V. Soukhoveev, V. Ivantsov, A. Usikov, and V. Dmitriev. Thick AlN layers grown by HVPE. *Journal of Crystal Growth*, 281(1):87–92, 2005. The Internbational Workshop on Bulk Nitride Semiconductors III.

[201] K. Kamei, Y. Shirai, T. Tanaka, N. Okada, A. Yauchi, and H. Amano. Solution growth of AlN single crystal using Cu solvent under atmospheric pressure nitrogen. *physica status solidi c*, 4(7):2211–2214, 2007.

[202] Jaime A Freitas. Properties of the state of the art of bulk III–V nitride substrates and homoepitaxial layers. *Journal of Physics D: Applied Physics*, 43(7):073001, 2010.

[203] Dupuis. R Ryou. J-H, Kanjolia. R. *'Chapter 6 CVD of III-V Compound Semiconductors', Chemcial Vapour Depostion: Precursors, Processes and Applications.* Royal Society of Chemistry, Cambridge, 1st edition, 2009.

[204] Volker Hessel. *Micro process engineering : a comprehensive handbook.* Wiley-VCH, Berlin, 2009.

[205] Peter G Mahaffy, RB Bucat, Roy Tasker, John C Kotz, Paul Treichel, Gabriela C Weaver, and John McMurry. *Chemistry: Human activity, chemical reactivity.* Nelson Education Toronto, Toronto, 2011.

[206] Ludmila Eckertova. *Physics of thin films.* Plenum Press, New York ; London, 1st ed. edition, 1977.

[207] Alan G. Thompson. MOCVD technology for semiconductors. *Materials Letters*, 30(4):255 – 263, 1997.

[208] M. Balaji, R. Ramesh, P. Arivazhagan, M. Jayasakthi, R. Loganathan, K. Prabakaran, S. Suresh, S. Lourdudoss, and K. Baskar. Influence of initial growth stages on AlN epilayers grown by metal organic chemical vapor deposition. *Journal of Crystal Growth*, 414:69–75, 2015.

[209] Pierre-Marie Coulon, Gunnar Kusch, Robert W. Martin, and Philip A. Shields. Deep UV Emission from Highly Ordered AlGaN/AlN Core–Shell Nanorods. *ACS Applied Materials & Interfaces*, 10(39):33441–33449, 2018. PMID: 30188116.

[210] M. R. Goulding. The selective epitaxial growth of silicon. *Materials Science and Engineering B*, 17(1-3):47–67, 1993.

[211] R. A. Taylor, J. H. Rice, J. H. Na, J. W. Robinson, R. W. Martin, P. R. Edwards, I. M. Watson, and C. Liu. Quantum dot emission from selectively-grown InGaN/GaN micropyramid arrays. *AIP Conference Proceedings*, 772(2004):865–866, 2005.

[212] Marc Madou and Chunlei (Peggy) Wang. Photolithography. In *Encyclopedia of Nanotechnology*, pages 3157–3166. Springer Netherlands, Dordrecht, 2016.

[213] M. J. (Mike J) Cooke. *Semiconductor devices.* Prentice Hall, London, 1990.

[214] M.J. Madou. *Fundamentals of Microfabrication.* CRC-Press, Boca Raton, 1997.

[215] Ionut Gîrgel, Paul R. Edwards, Emmanuel Le Boulbar, Pierre-Marie Coulon, Suman Lata Sahonta, Duncan W. E. Allsopp, Robert W. Martin, Colin J. Humphreys, and Philip A. Shields. Investigation of indium gallium nitride facet-dependent nonpolar growth rates and composition for core–shell light-emitting diodes. *Journal of Nanophotonics*, 10(1):1 – 11, 2016.

[216] E. D. Le Boulbar, P. J. P. Chausse, S. Lis, and P. A. Shields. Displacement Talbot lithography: an alternative technique to fabricate nanostructured metamaterials. In Ion M. Tiginyanu, editor, *Nanotechnology VIII*, volume 10248, pages 83 – 92. International Society for Optics and Photonics, SPIE, 2017.

[217] Alongkorn Pimpin and Werayut Srituravanich. Review on micro-and nanolithography techniques and their applications. *Engineering Journal*, 16(1):37–56, 2012.

[218] Lorenz Stuerzebecher, Frank Fuchs, Uwe D. Zeitner, and Andreas Tuennermann. High-resolution proximity lithography for nano-optical components. *Microelectronic Engineering*, 132:120–134, 2015. Micro and Nanofabrication Breakthroughs for Electronics, MEMS and Life Sciences.

[219] Richard A. Lawson and Alex P.G. Robinson. Chapter 1 - Overview of materials and processes for lithography. In Alex Robinson and Richard Lawson, editors, *Materials and Processes for Next Generation Lithography*, volume 11 of *Frontiers of Nanoscience*, pages 1–90. Elsevier, 2016.

[220] C Gomez-Reino. *Gradient-Index Optics : Fundamentals and Applications*. Springer Berlin, Heidelberg, Berlin, Heidelberg, 1st ed. edition, 2002.

[221] Li Wang, Francis Clube, Christian Dais, Harun H Solak, and Jens Gobrecht. Sub-wavelength printing in the deep ultra-violet region using Displacement Talbot Lithography. *Microelectronic Engineering*, 161:104–108, 2016.

[222] PJP Chausse, ED Le Boulbar, SD Lis, and PA Shields. Understanding resolution limit of displacement Talbot lithography. *Optics express*, 27(5):5918–5930, 2019.

[223] Pierre Chausse, Emmanuel Le Boulbar, Pierre-Marie Coulon, and Philip A Shields. "Double" displacement Talbot lithography: fast, wafer-scale, direct-writing of complex periodic nanopatterns. *Optics express*, 27(22):32037–32046, 2019.

[224] Jogender Singh and Douglas Edward Wolfe. Review Nano and macro-structured component fabrication by electron beam-physical vapor deposition (EB-PVD). *Journal of materials Science*, 40(1):1–26, 2005.

[225] K.S. Sree Harsha. Chapter 5 - Thermal Evaporation Sources. In K.S. Sree Harsha, editor, *Principles of Vapor Deposition of Thin Films*, pages 367–452. Elsevier, Oxford, 2006.

[226] Michael Huff. Recent Advances in Reactive Ion Etching and Applications of High-Aspect-Ratio Microfabrication. *Micromachines*, 12(8), 2021.

[227] Anthony C. Jones and Michael L. Hitchman. 1.1 Basic Definitions. In *Chemical Vapour Deposition - Precursors, Processes and Applications*. Royal Society of Chemistry, 2009.

[228] Mohd Y Lone, Avshish Kumar, Samina Husain, Mohammad Zulfequar, and Mushahid Husain. Growth of carbon nanotubes by PECVD and its applications: a review. *Current Nanoscience*, 13(5):536–546, 2017.

[229] Yue Shi, Liang He, Fangcao Guang, Luhai Li, Zhiqing Xin, and Ruping Liu. A review: preparation, performance, and applications of silicon oxynitride film. *Micromachines*, 10(8):552, 2019.

[230] Eugen Stamate and Geun Young Yeom. *Dry Etching*, pages 871–882. Springer Berlin Heidelberg, Berlin, Heidelberg, 2012.

[231] Pierre-Marie Coulon, Gunnar Kusch, Emmanuel D Le Boulbar, Pierre Chausse, Christopher Bryce, Robert W Martin, and Philip A Shields. Hybrid Top-Down/Bottom-Up Fabrication of Regular Arrays of AlN Nanorods for Deep-UV Core–Shell LEDs. *physica status solidi (b)*, 255(5):1700445, 2018.

[232] Jiandong Hu, Wei Li, Jian Chen, Xiaohui Zhang, and Xiangyang Zhao. Novel plating solution for electroless deposition of gold film onto glass surface. *Surface and Coatings Technology*, 202(13):2922 – 2926, 2008.

[233] Rennie. R & Law. J. *A Dictionary of Chemistry*. Oxford University Press, Online, 7th edition, 2016.

[234] Wolf. S & Tauber. R.N. *Silicon Processing for the VLSI era Volume 1: Process Technology*. Lattice Press, California, 1st edition, 1986.

[235] McCoy. J. W. *Industrial Chemical Cleaning*. Chemical Publishing Co., New York, 1st edition, 1984.

[236] Y.B Hahn, J.W Lee, K.D Mackenzie, D Johnson, S.J Pearton, and F Ren. Effect of deposition condition on wet and dry etch rates of device quality inductively coupled plasma-chemically vapor deposited SiN_x. *Solid-State Electronics*, 42(11):2017 – 2021, 1998.

[237] Ul-Hamid. A. *A Beginners' Guide to Scanning Electron Microscopy*. Springer Nature Switzerland, Switzerland, 1st edition, 2018.

[238] Herle.J.W.S & Sparrow. S. T & Cross. P. M. *The use of scanning electron microscope*. Pergamon Press Ltd, Oxford, 1st edition, 1972.

[239] D.E. & Joy D.C. & Lyman C.E. & Echlin P. & Lifshin E.& Sawyer L.& Michael J.R. Goldstein J. & Newbury. *Scanning Electron Microscope and X-ray Microanalysis*. Plenum Press, New York, 1st edition, 1981.

[240] Magonov. S & Whangbo. M-H. *Surface Analysis with STM and AFM*. VCH Verlagsgesellschaft mbH & VCH Publishers Inc., Weiheim, New York, 1st edition, 1966.

[241] Haugstad. G. *Atomic Force Microscopy: Understanding Basic Modes and Advanced Applications*. VCH Verlagsgesellschaft mbH & VCH Publishers Inc., Weiheim, New York, 1st edition, 1966.

[242] Gunning. A. P Morris. V. J, Kirby. A. R. *Atomic Force Microscopy for biologists*. Imperial College Press, London, 2nd edition, 2010.

[243] C Adelmann, E Martinez Guerrero, F Chabuel, J Simon, B Bataillou, G Mula, Le Si Dang, N.T Pelekanos, B Daudin, G Feuillet, and H Mariette. Growth and characterisation of self-assembled cubic GaN quantum dots. *Materials Science and Engineering: B*, 82(1):212 – 214, 2001.

[244] Parker. C. A. *Photoluminescence of Solutions with applications to Photochemistry and Analytical Chemistry*. Elsevier Publishing Company, Amsterdam, 1st edition, 1968.

[245] G.D. Gilliland. Photoluminescence spectroscopy of crystalline semiconductors. *Materials Science and Engineering: R: Reports*, 18(3):99 – 399, 1997.

[246] L.Peraldo Bicelli. A review on photoluminescence and electroluminescence of semiconductors for photoelectrochemical cells. *Surface Technology*, 26(2):93 – 105, 1985.

[247] Zhiqiang Liu, Yang Huang, Xiaoyan Yi, Binglei Fu, Guodong Yuan, Junxi Wang, Jinmin Li, and Yong Zhang. Analysis of photoluminescence thermal quenching: guidance for the design of highly effective p-type doping of nitrides. *Scientific reports*, 6:32033, 2016.

[248] JVD Veliadis, JB Khurgin, YJ Ding, AG Cui, and DS Katzer. Investigation of the photoluminescence-linewidth broadening in periodic multiple narrow asymmetric coupled quantum wells. *Physical Review B*, 50(7):4463, 1994.

[249] M. Holmes, S. Kako, K. Choi, M. Arita, and Y. Arakawa. Spectral diffusion and its influence on the emission linewidths of site-controlled GaN nanowire quantum dots. *Physical Review B - Condensed Matter and Materials Physics*, 92(11):1–7, 2015.

[250] Mark J. Holmes, M. Arita, and Y. Arakawa. III-nitride quantum dots as single photon emitters. *Semiconductor Science and Technology*, 34(3), 2019.

[251] Claire Kammerer, Guillaume Cassabois, C Voisin, M Perrin, C Delalande, Ph Roussignol, and JM Gérard. Interferometric correlation spectroscopy in single quantum dots. *Applied Physics Letters*, 81(15):2737–2739, 2002.

[252] A. F. Jarjour, R. A. Oliver, and R. A. Taylor. Progress in the optical studies of single InGaN/GaN quantum dots. *Philosophical Magazine*, 87(13):2077–2093, 2007.

[253] T. V. Hakkarainen, A. Schramm, E. Luna, J. Tommila, and M. Guina. Temperature dependence of photoluminescence for site-controlled InAs/GaAs quantum dot chains. *Journal of Crystal Growth*, 378:470–474, 2013.

[254] A. J.C. Hogg, E. Sellier, and A. J. Jourdan. Cathodoluminescence of quartz cements in Brent Group sandstones, Alwyn South, UK North Sea. *Geological Society Special Publication*, 61(1):421–440, 1992.

[255] Tomoyuki Tanikawa, Kazuki Ohnishi, Masaya Kanoh, Takashi Mukai, and Takashi Matsuoka. Three-dimensional imaging of threading dislocations in GaN crystals using two-photon excitation photoluminescence. *Applied Physics Express*, 11(3), 2018.

[256] K Kusakabe, T Furuzuki, and K Ohkawa. Cathodoluminescence characterization of 11-20-oriented InGaN/GaN thin films grown on r-plane sapphire substrates by metalorganic vapor-phase epitaxy. *physica status solidi c*, 4(7):2544–2547, 2007.

[257] Gunnar Kusch, Michele Conroy, Haoning Li, Paul R Edwards, Chao Zhao, Boon S Ooi, Jon Pugh, Martin J Cryan, Peter J Parbrook, and Robert W Martin. Multi-wavelength emission from a single InGaN/GaN nanorod analyzed by cathodoluminescence hyperspectral imaging. *Scientific reports*, 8(1):1742, 2018.

[258] Paul R Edwards and Robert W Martin. Cathodoluminescence nano-characterization of semiconductors. *Semiconductor Science and Technology*, 26(6):064005, 2011.

[259] Nobuyuki Koguchi, Keiko Ishige, and Satoshi Takahashi. New selective molecular-beam epitaxial growth method for direct formation of GaAs quantum dots. *Journal of Vacuum Science & Technology B: Microelectronics and Nanometer Structures Processing, Measurement, and Phenomena*, 11(3):787–790, 1993.

[260] Zhou. W. *Nanoimprint Lithography: An Enabling Process for Nanofabrication.* Spinger-Verlag Berlin Heidleberg, Heidelberg, 1st edition, 2013.

[261] Lei Zhang, Chu Hsiang Teng, Pei Cheng Ku, and Hui Deng. Site-controlled InGaN/GaN single-photon-emitting diode. *Applied Physics Letters*, 108(15), 2016.

[262] Yu. B & Pan. D. Z. *Design for Manufacturing with Advanced Lithography.* Springer International Publishing Switzerland, Cham, Switzerland, 1st edition, 2016.

[263] Danxu Du, David J. Srolovitz, Michael E. Coltrin, and Christine C. Mitchell. Systematic prediction of kinetically limited crystal growth morphologies. *Physical Review Letters*, 95(15):1–4, 2005.

[264] Yoshiki Kato, Shota Kitamura, Kazumasa Hiramatsu, and Nobuhiko Sawaki. Selective growth of wurtzite GaN and $Al_xGa1-xN$ on GaN/sapphire substrates by metalorganic vapor phase epitaxy. *Journal of Crystal Growth*, 144(3-4):133–140, 1994.

[265] Seung-Chang Lee, Kevin J Malloy, and SRJ Brueck. Nanoscale selective growth of GaAs by molecular beam epitaxy. *Journal of Applied Physics*, 90(8):4163–4168, 2001.

[266] Zarko Gacevic, Daniel Gomez Sanchez, and Enrique Calleja. Formation mechanisms of GaN nanowires grown by selective area growth homoepitaxy. *Nano letters*, 15(2):1117–1121, 2015.

[267] Pierre-Marie Coulon, Gunnar Kusch, Philip Fletcher, Pierre Chausse, Robert W. Martin, and Philip A. Shields. Hybrid Top-Down/Bottom-Up Fabrication of a Highly Uniform and Organized Faceted AlN Nanorod Scaffold. *Materials*, 11(7), 2018.

[268] Mohammed Zeghouane, Geoffrey Avit, Thomas W Cornelius, Damien Salomon, Yamina André, Catherine Bougerol, Thierry Taliercio, Ariane Meguekam-Sado, Pierre Ferret, Dominique Castelluci, et al. Selective growth of ordered hexagonal InN nanorods. *CrystEngComm*, 21(16):2702–2708, 2019.

[269] Andreas Winden, Martin Mikulics, Toma Stoica, Martina von der Ahe, Gregor Mussler, Anna Haab, Detlev Grützmacher, and Hilde Hardtdegen. Site-controlled growth of indium nitride based nanostructures using metalorganic vapour phase epitaxy. *Journal of crystal growth*, 370:336–341, 2013.

[270] Sejeong Kim, Su Hyun Gong, Jong Hoi Cho, and Yong Hoon Cho. Unidirectional Emission of a Site-Controlled Single Quantum Dot from a Pyramidal Structure. *Nano Letters*, 16(10):6117–6123, 2016.

[271] Jong-Hoi Cho, Youngmin M Kim, Seung-Hyuk Lim, Hwan-Seop Yeo, Sejeong Kim, Su-Hyun Gong, and Yong-Hoon Cho. Strongly coherent single-photon emission from site-controlled InGaN quantum dots embedded in GaN nanopyramids. *ACS Photonics*, 5(2):439–444, 2017.

[272] Tomas Jemsson, Houssaine Machhadani, Per Olof Holtz, and K. Fredrik Karlsson. Polarized single photon emission and photon bunching from an InGaN quantum dot on a GaN micropyramid. *Nanotechnology*, 26(6), 2015.

[273] Kihyun Choi, Munetaka Arita, Satoshi Kako, and Yasuhiko Arakawa. Site-controlled growth of single GaN quantum dots in nanowires by MOCVD. *Journal of Crystal Growth*, 370:328–331, 2013.

[274] Jun Deng, Jiadong Yu, Zhibiao Hao, Jianbin Kang, Boyang Lu, Lai Wang, Changzheng Sun, Yanjun Han, Bing Xiong, Jian Wang, et al. Disk-Shaped GaN Quantum Dots Embedded in AlN Nanowires for Room-Temperature Single-Photon Emitters Applicable to Quantum Information Technology. *ACS Applied Nano Materials*, 2022.

[275] V.B. Verma and V.C. Elarde. Nanoscale selective area epitaxy: From semiconductor lasers to single-photon sources. *Progress in Quantum Electronics*, 75:100305, 2021.

[276] Bin Wang, Yugang Zeng, Yue Song, Ye Wang, Lei Liang, Li Qin, Jianwei Zhang, Peng Jia, Yuxin Lei, Cheng Qiu, Yongqiang Ning, and Lijun Wang. Principles of Selective Area Epitaxy and Applications in III-V Semiconductor Lasers Using MOCVD: A Review. *Crystals*, 12(7), 2022.

[277] R. R. Li, P. D. Dapkus, M. E. Thompson, W. G. Jeong, C. Harrison, P. M. Chaikin, R. A. Register, and D. H. Adamson. Dense arrays of ordered GaAs nanostructures by selective area growth on substrates patterned by block copolymer lithography. *Applied Physics Letters*, 76(13):1689–1691, 2000.

[278] Jehong Oh, Jungel Ryu, Duyoung Yang, Seungmin Lee, Jongmyeong Kim, Kyungwook Hwang, Junsik Hwang, Dongho Kim, Yongjo Park, Euijoon Yoon, and Ho Won Jang. Selective Area Growth of GaN Using Polycrystalline γ-Alumina as a Mask for Discrete Micro-GaN Array. *Crystal Growth & Design*, 22(3):1770–1777, 2022.

[279] Max Strauß, Arsenty Kaganskiy, Robert Voigt, Peter Schnauber, Jan Hindrik Schulze, Sven Rodt, André Strittmatter, and Stephan Reitzenstein. Resonance fluorescence of a site-controlled quantum dot realized by the buried-stressor growth technique. *Applied Physics Letters*, 110(11), 2017.

[280] T. H. Chung, G. Juska, S. T. Moroni, A. Pescaglini, A. Gocalinska, and E. Pelucchi. Selective carrier injection into patterned arrays of pyramidal quantum dots for entangled photon light-emitting diodes. *Nature Photonics*, 10(12):782–787, 2016.

[281] Wei Zhang, Zhenwu Shi, Dayun Huo, Xiaoxiang Guo, Feng Zhang, Linsen Chen, Qinhua Wang, Baoshun Zhang, and Changsi Peng. In-situ laser nano-patterning for ordered InAs/GaAs(001) quantum dot growth. *Applied Physics Letters*, 112(15):1–5, 2018.

[282] Michael Kneissl, Tae-Yeon Seong, Jung Han, and Hiroshi Amano. The emergence and prospects of deep-ultraviolet light-emitting diode technologies. *Nature Photonics*, 13(4):233–244, 2019.

[283] Kazuhito Ban, Jun ichi Yamamoto, Kenichiro Takeda, Kimiyasu Ide, Motoaki Iwaya, Tetsuya Takeuchi, Satoshi Kamiyama, Isamu Akasaki, and Hiroshi Amano. Internal Quantum Efficiency of Whole-Composition-Range AlGaN Multiquantum Wells. *Applied Physics Express*, 4(5):052101, 2011.

[284] S Zhao, AT Connie, MHT Dastjerdi, XH Kong, Q Wang, M Djavid, S Sadaf, XD Liu, I Shih, H Guo, et al. Aluminum nitride nanowire light emitting diodes: Breaking the fundamental bottleneck of deep ultraviolet light sources. *Scientific reports*, 5:8332, 2015.

[285] Christoph Reich, Martin Guttmann, Martin Feneberg, Tim Wernicke, Frank Mehnke, Christian Kuhn, Jens Rass, Mickael Lapeyrade, Sven Einfeldt, A. Knauer, Viola Kueller, Markus Weyers, Rüdiger Goldhahn, and Michael Kneissl. Strongly transverse-electric-polarized emission from deep ultraviolet AlGaN quantum well light emitting diodes. *Applied Physics Letters*, 107, 10 2015.

[286] X. J. Chen, T. J. Yu, H. M. Lu, G. C. Yuan, B. Shen, and G. Y. Zhang. Modulating optical polarization properties of Al-rich AlGaN/AlN quantum well by controlling wavefunction overlap. *Applied Physics Letters*, 103(18):181117, 2013.

[287] Dong Yeong Kim, Jun Hyuk Park, Jong Won Lee, Sunyong Hwang, Seung Jae Oh, Jungsub Kim, Cheolsoo Sone, E Fred Schubert, and Jong Kyu Kim. Overcoming the fundamental light-extraction efficiency limitations of deep ultraviolet light-emitting diodes by utilizing transverse-magnetic-dominant emission. *Light: Science & Applications*, 4(4):e263, 2015.

[288] Michele Conroy, Vitaly Z Zubialevich, Haoning Li, Nikolay Petkov, Sally O'Donoghue, Justin D Holmes, and Peter J Parbrook. Ultra-high-density arrays of defect-free AlN nanorods: A "space-filling" approach. *ACS nano*, 10(2):1988–1994, 2016.

[289] S Walde, S Hagedorn, P-M Coulon, A Mogilatenko, C Netzel, J Weinrich, N Susilo, E Ziffer, L Matiwe, C Hartmann, et al. AlN overgrowth of nano-pillar-patterned sapphire with different offcut angle by metalorganic vapor phase epitaxy. *Journal of Crystal Growth*, 531:125343, 2020.

[290] Yu Kee Ooi, Cheng Liu, and Jing Zhang. Analysis of polarization-dependent light extraction and effect of passivation layer for 230-nm AlGaN nanowire light-emitting diodes. *IEEE Photonics Journal*, 9(4):1–12, 2017.

[291] Jinwan Kim, Uiho Choi, Jaedo Pyeon, Byeongchan So, and Okhyun Nam. Deep-ultraviolet AlGaN/AlN core-shell multiple quantum wells on AlN nanorods via lithography-free method. *Scientific reports*, 8(1):935, 2018.

[292] Yanan Guo, Jianchang Yan, Yun Zhang, Junxi Wang, and Jinmin Li. Enhancing the light extraction of AlGaN-based ultraviolet light-emitting diodes in the nanoscale. *Journal of Nanophotonics*, 12(4):1 – 12, 2018.

[293] Chirantan Singha, Sayantani Sen, Pallabi Pramanik, Mainak Palit, Alakananda Das, Abhra Shankar Roy, Susanta Sen, and Anirban Bhattacharyya. Growth of AlGaN alloys under excess group III conditions: Formation of vertical nanorods. *Journal of Crystal Growth*, 481:40 – 47, 2018.

[294] L.H. Shen, X.F. Li, J. Zhang, Y.M. Ma, F. Wang, G. Peng, Q.L. Cui, and G.T. Zou. Synthesis of single-crystalline wurtzite aluminum nitride nanowires by direct arc discharge. *Applied Physics A*, 84(1):73–75, Jul 2006.

[295] Qiang Wu, Zheng Hu, Xizhang Wang, Yinong Lu, Kaifu Huo, Shaozhi Deng, Ningsheng Xu, Bo Shen, Rong Zhang, and Yi Chen. Extended vapor–liquid–solid growth and field emission properties of aluminium nitride nanowires. *Journal of Materials Chemistry*, 13(8):2024–2027, 2003.

[296] Shih-Chen Shi, Surojit Chattopadhyay, Chia-Fu Chen, Kuei-Hsien Chen, and Li-Chyong Chen. Structural evolution of aln nano-structures: Nanotips and nanorods. *Chemical Physics Letters*, 418(1):152 – 157, 2006.

[297] V. Cimalla, Ch. Foerster, D. Cengher, K. Tonisch, and O. Ambacher. Growth of AlN nanowires by metal organic chemical vapour deposition. *physica status solidi (b)*, 243(7):1476–1480, 2006.

[298] Elena Alexandra Serban, Justinas Palisaitis, Per Ola Åke Persson, Lars Hultman, Jens Birch, and Ching-Lien Hsiao. Site-controlled growth of GaN nanorod arrays by magnetron sputter epitaxy. *Thin Solid Films*, 660:950–955, 2018.

[299] Pierre-Marie Coulon, Blandine Alloing, Virginie Brändli, Denis Lefebvre, Sébastien Chenot, and Jesús Zúñiga-Pérez. Selective area growth of Ga-polar GaN nanowire arrays by continuous-flow MOVPE: A systematic study on the effect of growth conditions on the array properties. *physica status solidi (b)*, 252(5):1096–1103, 2015.

[300] Ryan G. Banal, Mitsuru Funato, and Yoichi Kawakami. Surface diffusion during metalorganic vapor phase epitaxy of AlN. *physica status solidi c*, 6(2):599–602, 2009.

[301] George T. Wang, Qiming Li, Jonathan J. Wierer, Daniel D. Koleske, and Jeffrey J. Figiel. Top–down fabrication and characterization of axial and radial III-nitride nanowire LEDs. *physica status solidi (a)*, 211(4):748–751, 2014.

[302] Yingdong Tian, Jianchang Yan, Yun Zhang, Yonghui Zhang, Xiang Chen, Yanan Guo, Junxi Wang, and Jinmin Li. Formation and characteristics of AlGaN-based three-dimensional hexagonal nanopyramid semi-polar multiple quantum wells. *Nanoscale*, 8(21):11012–11018, 2016.

[303] C G Bryce, E D Le Boulbar, P-M Coulon, P R Edwards, I Gîrgel, D W E Allsopp, P A Shields, and R W Martin. Quantum well engineering in InGaN/GaN core-shell nanorod structures. *Journal of Physics D: Applied Physics*, 50(42):42LT01, sep 2017.

[304] Pierre-Marie Coulon, Benjamin Damilano, Blandine Alloing, Pierre Chausse, Sebastian Walde, Johannes Enslin, Robert Armstrong, Stéphane Vézian, Sylvia Hagedorn, Tim Wernicke, Jesús Zúñiga-Pérez, Markus Weyers, Michael Kneissl, and Philip Shields. Displacement Talbot Lithography for nano-engineering of III-nitride materials. *Microsystems & Nanoengineering*, 8 2019.

[305] Vibhu Jindal and Fatemeh Shahedipour-Sandvik. Theoretical prediction of GaN nanostructure equilibrium and nonequilibrium shapes. *Journal of Applied Physics*, 106(8), 2009.

[306] Fangzheng Li, Lianshan Wang, Weizhen Yao, Yulin Meng, Shaoyan Yang, and Zhanguo Wang. Analysis of growth rate and crystal quality of AlN epilayers by flow-modulated metal organic chemical vapor deposition. *Superlattices and Microstructures*, 137:106336, 2020.

[307] Ryota Ishii, Mitsuru Funato, and Yoichi Kawakami. Huge electron-hole exchange interaction in aluminum nitride. *Phys. Rev. B*, 87:161204, Apr 2013.

[308] Hua-Chi Cheng. Wet Etching. In *Handbook of Visual Display Technology*, pages 1331–1341. Springer International Publishing, Cham, 2016.

[309] Gottlieb S. Oehrlein. Dry etching damage of silicon: A review. *Materials Science and Engineering: B*, 4(1):441–450, 1989.

[310] Stella W. Pang. Chapter 11 - Dry Etching Technology for Optical Devices. In Achyut K. Dutta, Niloy K. Dutta, and Masahiko Fujiwara, editors, *WDM Technologies*, pages 533–562. Academic Press, San Diego, 2002.

[311] W Guo, R Kirste, I Bryan, Z Bryan, L Hussey, P Reddy, J Tweedie, R Collazo, and Z Sitar. KOH based selective wet chemical etching of AlN, $Al_xGa_{1-x}N$, and GaN crystals: A way towards substrate removal in deep ultraviolet-light emitting diode. *Applied Physics Letters*, 106(8):082110, 2015.

[312] JR Mileham, SJ Pearton, CR Abernathy, JD MacKenzie, RJ Shul, and SP Kilcoyne. Wet chemical etching of AlN. *Applied physics letters*, 67(8):1119–1121, 1995.

[313] CB Vartuli, SJ Pearton, JW Lee, CR Abernathy, JD MacKenzie, JC Zolper, RJ Shul, and F Ren. Wet chemical etching of AlN and InAlN in KOH solutions. *Journal of the Electrochemical Society*, 143(11):3681, 1996.

[314] Min Sun, Yuhao Zhang, Xiang Gao, and Tomas Palacios. High-performance GaN vertical fin power transistors on bulk GaN substrates. *IEEE Electron Device Letters*, 38(4):509–512, 2017.

[315] E.D. Le Boulbar, C.J. Lewins, D.W.E. Allsopp, C.R. Bowen, and P.A. Shields. Fabrication of high-aspect ratio GaN nanostructures for advanced photonic devices. *Microelectronic Engineering*, 153:132–136, 2016.

[316] Philip Shields, Maxime Hugues, Jesus Zúñiga-Pérez, Mike Cooke, Mark Dineen, Wang Wang, Federica Causa, and Duncan Allsopp. Fabrication and properties of etched GaN nanorods. *physica status solidi c*, 9(3-4):631–634, 2012.

[317] Homer Thornton Hayslett and Patrick J. Murphy. *Statistics made simple*. W.H. Allen, London, 2nd edition, 1971.

[318] Edward Bormashenko and Viktor Valtsifer. Interfacial crystallization at the intersection of thermodynamic and geometry. *Advances in Colloid and Interface Science*, 296:102510, 2021.

[319] B Damilano, S Vézian, J Brault, B Alloing, and J Massies. Selective area sublimation: a simple top-down route for GaN-based nanowire fabrication. *Nano letters*, 16(3):1863–1868, 2016.

[320] Sergio Fernández-Garrido, Thomas Auzelle, Jonas Lähnemann, Kilian Wimmer, Abbes Tahraoui, and Oliver Brandt. Top-down fabrication of ordered arrays of GaN nanowires by selective area sublimation. *Nanoscale Advances*, 1(5):1893–1900, 2019.

[321] Ryo Kita, Ryo Hachiya, Tomoya Mizutani, Hiroki Furuhashi, and Akihiko Kikuchi. Characterization of hydrogen environment anisotropic thermal etching and application to GaN nanostructure fabrication. *Japanese Journal of Applied Physics*, 54(4):046501, 2015.

[322] T. Sasaki. Surface morphology of MOVPE-grown GaN on (0001) sapphire. *Journal of Crystal Growth*, 129(1):81–90, 1993.

[323] P Vennéguès, B Beaumont, S Haffouz, M Vaille, and P Gibart. Influence of in situ sapphire surface preparation and carrier gas on the growth mode of GaN in MOVPE. *Journal of Crystal Growth*, 187(2):167–177, 1998.

[324] Guoqiang Li, Wenliang Wang, Weijia Yang, Yunhao Lin, Haiyan Wang, Zhiting Lin, and Shizhong Zhou. GaN-based light-emitting diodes on various substrates: a critical review. *Reports on Progress in Physics*, 79(5):056501, apr 2016.

[325] SW King, JP Barnak, MD Bremser, KM Tracy, C Ronning, RF Davis, and RJ Nemanich. Cleaning of AlN and GaN surfaces. *Journal of Applied Physics*, 84(9):5248–5260, 1998.

[326] LL Smith, SW King, RJ Nemanich, and RF Davis. Cleaning of GaN surfaces. *Journal of electronic materials*, 25(5):805–810, 1996.

[327] DD Koleske, AE Wickenden, RL Henry, JC Culbertson, and ME Twigg. GaN decomposition in H_2 and N_2 at MOVPE temperatures and pressures. *Journal of crystal growth*, 223(4):466–483, 2001.

[328] T. Hurlen, T. Vland, and G. Lunde. Anodic dissolution of liquid gallium. *Electrochimica Acta*, 9(11):1433–1437, 1964.

[329] S Kako, K Hoshino, S Iwamoto, S Ishida, and Y Arakawa. Exciton and biexciton luminescence from single hexagonal GaN/AlN self-assembled quantum dots. *Applied physics letters*, 85(1):64–66, 2004.

[330] JC Zhang, B Meyler, A Vardi, G Bahir, and J Salzman. Stranski–Krastanov growth of GaN quantum dots on AlN template by metalorganic chemical vapor deposition. *Journal of Applied Physics*, 104(4):044307, 2008.

[331] Weihuang Yang, Jinchai Li, Yong Zhang, Po-Kai Huang, Tien-Chang Lu, Hao-Chung Kuo, Shuping Li, Xu Yang, Hangyang Chen, Dayi Liu, et al. High density GaN/AlN quantum dots for deep UV LED with high quantum efficiency and temperature stability. *Scientific reports*, 4(1):1–5, 2014.

[332] D Simeonov, E Feltin, J-F Carlin, R Butté, M Ilegems, and N Grandjean. Stranski-Krastanov GaN/AlN quantum dots grown by metal organic vapor phase epitaxy. *Journal of applied physics*, 99(8):083509, 2006.

[333] D. Simeonov, E. Feltin, F. Demangeot, C. Pinquier, J.-F. Carlin, R. Butté, J. Frandon, and N. Grandjean. Strain relaxation of AlN epilayers for Stranski–Krastanov GaN/AlN quantum dots grown by metal organic vapor phase epitaxy. *Journal of Crystal Growth*, 299(2):254–258, 2007.

[334] S Kako, M Miyamura, K Tachibana, K Hoshino, and Y Arakawa. Size-dependent radiative decay time of excitons in GaN/AlN self-assembled quantum dots. *Applied physics letters*, 83(5):984–986, 2003.

[335] Yasuo Ohba Yasuo Ohba and Ako Hatano Ako Hatano. Growth of high-quality AlN and AlN/GaN/AlN heterostructure on sapphire substrate. *Japanese journal of applied physics*, 35(8B):L1013, 1996.

[336] Diethard Marx, Zempei Kawazu, Takeshi Nakayama, Yutaka Mihashi, Tetsuya Takami, Masahiro Nunoshita, and Tatsuo Ozeki. Selective area growth of GaN/AlN heterostructures. *Journal of Crystal Growth*, 189-190:87–91, 1998.

[337] C. Liu, S. Stepanov, A. Gott, P. A. Shields, E. Zhirnov, W. N. Wang, E. Steimetz, and J. T. Zettler. High temperature refractive indices of GaN. *physica status solidi c*, 3(6):1884–1887, 2006.

[338] C. Liu, S. Stepanov, P. A. Shields, A. Gott, W. N. Wang, E. Steimetz, and J.-T. Zettler. In situ monitoring of GaN epitaxial lateral overgrowth by spectroscopic reflectometry. *Applied Physics Letters*, 88(10):101103, 2006.

[339] Zhijie Wang, Xinwei Xu, Jinghua Gong, Jinghong Ma, and Jian Xu. Structure and fabry-pérot fringes of polymer-boehmite hybrid thin film by sol–gel dip-coating. *Journal of Sol-Gel Science and Technology*, 73(1):154–160, 2015.

[340] T. Inoshita and H. Sakaki. Electronic structure of the ridge quantum wire based on an analytic confinement model. *Journal of Applied Physics*, 79(1):269–272, 1996.

[341] M. Peres, A. J. Neves, T. Monteiro, S. Magalhães, E. Alves, K. Lorenz, H. Okuno-Vila, V. Fellmann, C. Bougerol, and B. Daudin. Influence of thermal annealing on the structural and optical properties of GaN/AlN quantum dots. *physica status solidi (b)*, 247(7):1675–1678, 2010.

[342] Tong Wang, Tim J Puchtler, Saroj K Patra, Tongtong Zhu, John C Jarman, Rachel A Oliver, Stefan Schulz, and Robert A Taylor. Deterministic optical polarisation in nitride quantum dots at thermoelectrically cooled temperatures. *Scientific Reports*, 7(1):1–9, 2017.

[343] Kang Gao, Helen Springbett, Tongtong Zhu, Rachel A. Oliver, Yasuhiko Arakawa, and Mark J. Holmes. Spectral diffusion time scales in InGaN/GaN quantum dots. *Applied Physics Letters*, 114(11):112109, 2019.

[344] F. Rol, B. Gayral, S. Founta, B. Daudin, J. Eymery, J.-M. Gérard, H. Mariette, Le Si Dang, and D. Peyrade. Optical properties of single non-polar GaN quantum dots. *physica status solidi (b)*, 243(7):1652–1656, 2006.

[345] Tongtong Zhu, Fabrice Oehler, Benjamin P. L. Reid, Robert M. Emery, Robert A. Taylor, Menno J. Kappers, and Rachel A. Oliver. Non-polar (11-20) InGaN quantum dots with short exciton lifetimes grown by metal-organic vapor phase epitaxy. *Applied Physics Letters*, 102(25):251905, 2013.

[346] M. D. Eisaman, J. Fan, A. Migdall, and S. V. Polyakov. Invited Review Article: Single-photon sources and detectors. *Review of Scientific Instruments*, 82(7):071101, 2011.

[347] Kripasindhu Sardar, Meenakshi Dan, Birgit Schwenzer, and C. N. R. Rao. simple single-source precursor route to the nanostructures of AlN, GaN and InN. *J. Mater. Chem.*, 15:2175–2177, 2005.

Appendix 1

In this appendix, extra details and data regarding the AFM measurements and *c*-plane growth rate mentioned in Chapter 4 is provided. All data in this appendix was collected with a Bruker multimode IIIA AFM system. High resolution silicon AFM tips (supplied from Nunano) with a tip radius of curvature of < 10 nm were used. Other specifications of the tips include a spring constant of 42 N/m, resonant frequency of 350 kHz, cantilever dimensions of 125 µm, 30 µm and 4.5 µm for the length, width and thickness of the cantilever, respectively. The tips had a high aspect ratio with a cone angle $< 15°$ over the last 1 µm. All AFM data was analysed with the freely available Gwyddion software package. The AFM raw data of all of the samples was distorted to some extent in terms of the lengths scales of the x and y axis measured. All the samples were fabricated with a 1 μm pitch; therefore by measuring the pitch of the structures in the x and y directions, one could obtain the level of distortion (see black lines in Figure 8-1). From the obtained dimension measurements the length of the x and y axes were re-scaled. This process was performed iteratively until the correct pitch between the structures was obtained. It was often observed that only the y-direction was distorted and not that of the x. This calibration step was performed on scan sizes of either 2x2 or 5x5 μm and then applied to 1x1 μm scans under the assumption that the distortion remains constant across all scan sizes. Using this calibration, the pixel ratios of the AFM scans were also adjusted accordingly. From this, profile slices perpendicular to the facets were taken in order to extract the angles of the semi-polar facets present and thus identify their nature. As all of the samples have edge-to-edge morphology, it is assumed that the semi-polar facets are a-plane in type $\{xx\bar{2}xy\}$.

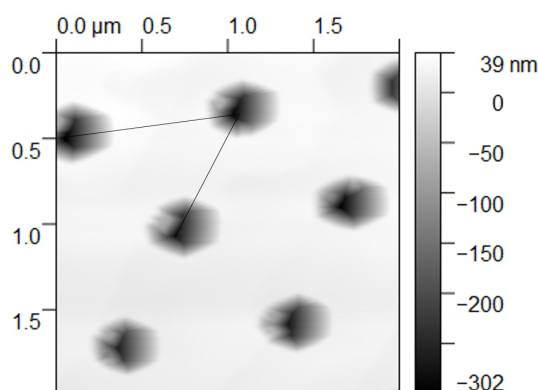

Figure 8-1: Calibration image of the AFM data. The black lines indicate measurement lines from which the difference between the know size of 1 μm and the measure size is obtained.

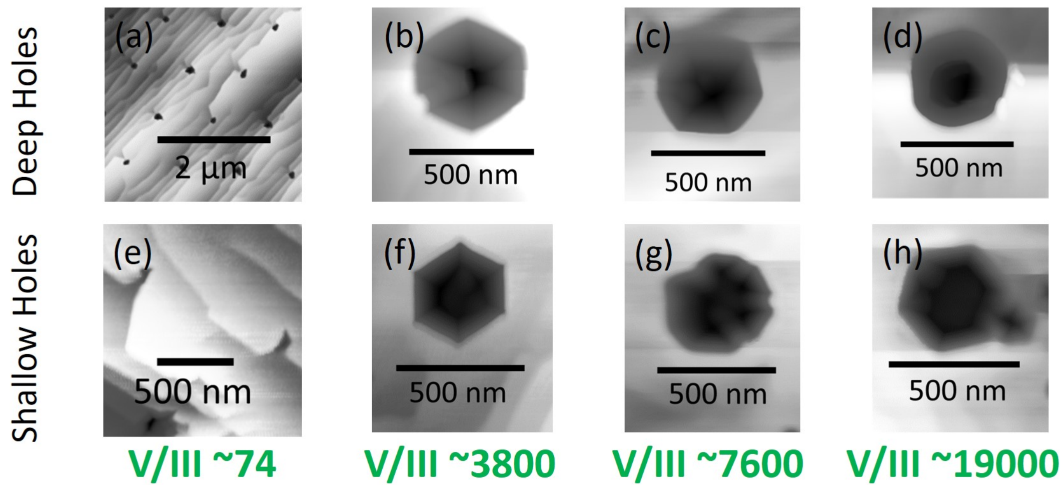

Figure 8-2: AFM data of the deep (a - d) and shallow (e - h) holes grown at different V/III ratios.

The AFM scans of single faceted nanohole structures are shown in Figure 8-2. The angles extracted from the planes are given in Table 8.1. Any misoriented growth observed in the AFM images are neglected and omitted from Table 8.1 as they do not provide a true representation of the semi-polar facets present. The error is estimated to be quite large considering that a reasonable amount of calibratory changes have been made to the AFM scans which has had an effect on the angles extracted comparatively between the raw and adjusted data. Considering that the error is likely to be on the order of $\pm 3 - 4°$ and the samples exhibit edge-to-edge morphology, it is very likely that the semi-polar facets of samples 1, 2, 4 and 6 (in Table 8.1) are that of $\{11\bar{2}2\}$. Whilst sample 3 has facet angles similar to that of the other samples, due to the circularity of this sample is is difficult to definitively identify the semi-polar facets present. Indeed, the circularity could mean that a mixture of $\{11\bar{2}2\}$ and $\{10\bar{1}1\}$ facets are present.

Figure 8-3 shows the AFM data corresponding to the prolonged growth time study upon the deep hole structures. As above, the angles of the semi-polar planes were extracted (see Table 8.2). The angles of samples 1-3 all resided between 59 and 62°. Considering that all the structures have edge-to-edge morphology this data suggests that the semi-polar facets present are again $\{11\bar{2}2\}$. Sample 4 of Table 8.2 has a lot of facet competition and misoriented growth present. Subsequently the extraction of reliable angles from this structure is not possible. This does however suggest that after a given, prolonged growth time, facet competition arises which is not present in samples grown for a lesser amount of time (comparing Figures 8-3 (c) and (d)). Thus, this data

Table 8.1: This table provides the semi-polar facet angles measured for the deep and shallow hole structures grown at different V/III ratios.

Sample Number	Sample	V/III Ratio	Facet Angle Measured	Comments
1	Deep Holes	~ 3800	61-62°	Some misoriented growth
2	Deep Holes	~ 7600	58-62°	some misoriented growth
3	Deep Holes	~ 19000	60-62°	Circular morphology, likely a lot of mixed, competing faceting
4	Shallow Holes	~ 3800	59-62°	Some misoriented growth at centre of hole
5	Shallow Holes	~ 7600	N/A	A lot of facet competition, cannot really extract angle date from this sample
6	Shallow Holes	~ 19000	58-59°	Some misoriented growth

Table 8.2: This table provides the semi-polar the facet angles measured for the deep hole structures grown at a V/III ratio of ~ 7600 for prolonged growth times.

Sample Number	Growth Time (Minutes)	Facet Angle Measured	Comments
1	60	61-62°	Some misoriented growth
2	120	59-61°	Well faceted structure
3	150	60-61°	Well faceted structure
4	180	N/A	A lot of misoriented growth and facet competition

suggests that the observed inverse pyramid with channel structure (Figure 8-3 (a) -(c)) is not a stable one after prolonged growth.

When considering the quantitative growth rates of the nanostructures, estimation of the *c*-plane growth rate is very difficult due to a lack of contrast difference in homoepitaxial regrowth. This is especially the case when considering the nanorod samples where only the relative growth between the top *c*-plane and bottom *c*-plane in between the rod can be compared. This difficulty is further compounded by the large variation in total AlN wafer thickness across the original template, making estimation of the *c*-plane growth rate via inspection of the total height of the AlN layer impossible. Nevertheless, in analysing cross-sectional images of some of the deep hole samples under different growth conditions and comparing that to the initial dry etched sample, one can estimate the growth rate of the *c*-plane. This is possible as it is observed that very little growth

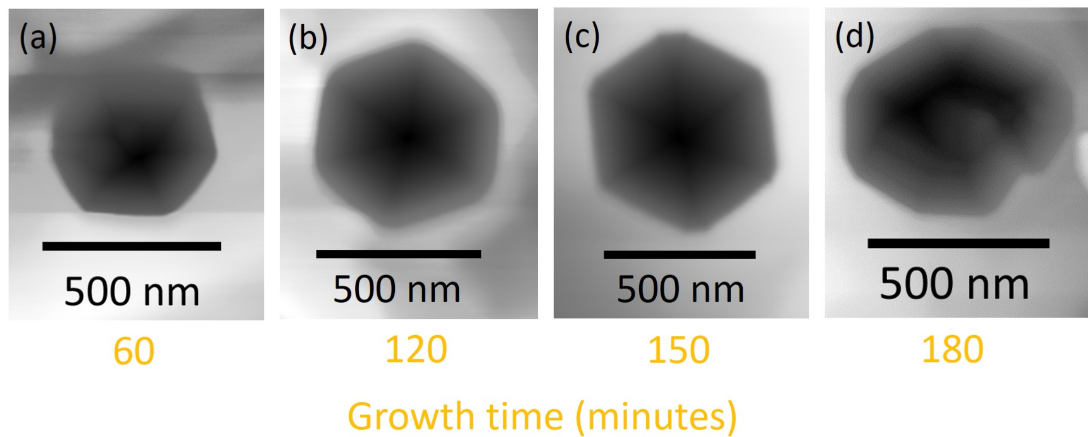

Figure 8-3: AFM data of the growth time study of the deep holes at a V/III ratio of ~ 7600.

occurs at the bottom of the holes due to very limited gas species travelling the full depth of the hole structure. We assume that this growth rate can then be used as an estimate for the different AlN nanostructures such as the AlN nanorods.

The depth of the nanohole structures was extracted using the ImageJ software in order to measure length scales on cross-sectional SEM images. This was performed for both the deep hole structures at a V/III ratio of ~ 74 and ~ 7600 (see Figure 8-4). 10 measurements were made via ImageJ for each sample allowing us to find a average value for each sample plotted. This also allowed us to extract an error which was determined to be the greatest deviation from the average within these 10 measurements taken. We justify this because the only error of any significance in this process was the physical human error of using the ImageJ software for the hole structure depth determination. The *c*-plane growth rate per hour was determined from the average difference between the total depth after a given growth time compared to that of the initial dry etch depth. This can be extracted from the gradient of the fitted lines in Figure 8-4.

The average *c*-plane growth rate for a V/III ratio of ~ 74 was calculated to be ~ 430 nm/hour. The average *c*-plane growth rate for a V/III ratio of ~ 7600 was calculated to be ~ 280 nm/hour. Thus, this shows that the V/III ratio has a significant impact on the rate of c-plane growth such that as the V/III ratio is increased the c-plane growth rate decreases. This is likely due to a reduction in the total amount of growth as V/III ratio increases when considering the slow *c*-plane growth comparative to that of other planes as observed in Figure 4-5 (a).

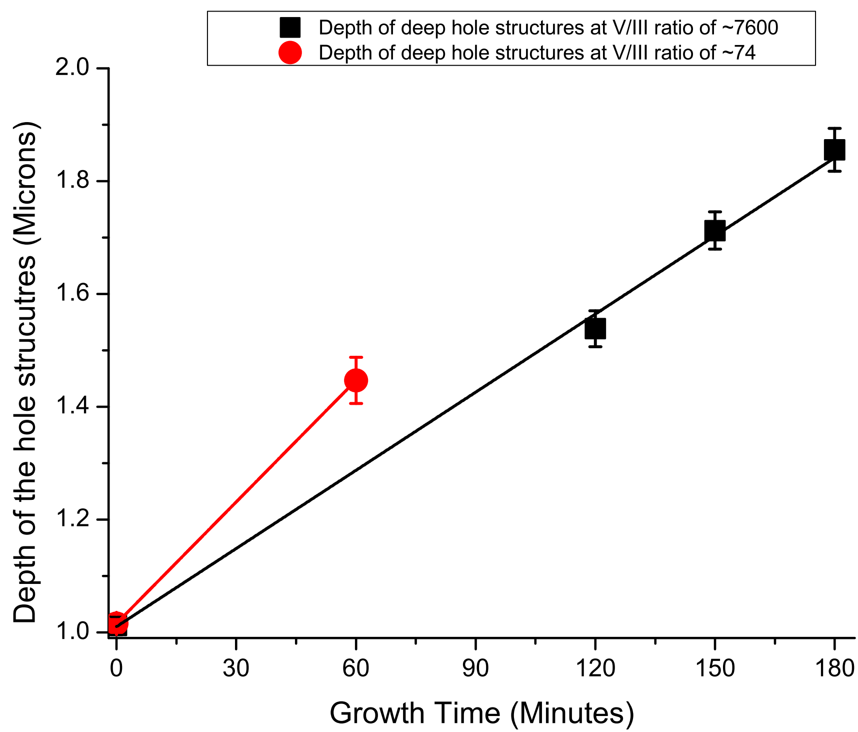

Figure 8-4: Plot of the height of the nanohole structures from the initial dry etch depth as a function of growth time for V/III ratios of ~ 74 and ~ 7600.

Appendix 2

Measurements of the mask opening changes and hexagonal etch features in Figure 5-2

For the data presented in Table 8.3 dimensions were extracted from SEM images. The pitch of the patterned structures (Figures 5-2 (a) and (b)) were measured 10 times and the average compared to the known pitch of the pattern from the lithography step. Five measurement were taken in each direction to make a total of 10 measurements. A correction value was thus obtained, and whilst there was some difference from the measured pitch to the true pitch it was relatively small. This was performed as charging effects can distort the dimensions observed on the SEM image. This would then incur spurious measurements when extracting values for the diameters of the hole openings from such an SEM image. The hole openings at the AlN mask interface can be reasonably estimated to be the same as that at the top of the mask. This is justified from the almost unobservable tapering as seen in the cross-sectional inset of Figure 5-2 (a). The diameters of 10 of the nanoholes was measured. The average of these values were determined with and without the correction as mentioned above. When measuring the diameters of the holes every measurement was on a new hole and 50% of measurements were taken in the y-direction and the other 50% in the perpendicular x-direction (this method was applied to all measurements presented in Table 8.3). This was performed to minimise spurious lengthening or widening of the holes as a result of charging effects. All of these dimensions were extracted from the main Figure in 5-2 (a). The diameter of the mask openings after wet etching and the hexagonal etched structures were extracted from Figure 5-2 (b). After multiple measurements of the pitch present on this image, it was determined that no correction was required. All of the data extracted and the standard deviations of the 10 measurements of the corresponding features are presented in Table 8.3. All dimensions were extracted from SEM images via the ImageJ software.

Table 8.3: Measurements of features (mask opening size and etched hexagon size) present in Figures 5-2 (a) and (b). Measurements were performed upon SEM images using the ImageJ software package [57].

Feature Measured	Mask Openings Before Wet Etching	Openings Before Wet Etching - With Correction	Openings After Wet Etching	Etched Hexagon
Diameter (nm)	343 ±21.1	353 ±21.7	754 ±15.3	372 ±26.8

AFM maps of the samples presented in Figure 5-3

In Figure 8-5 below, the corresponding AFM maps of the three samples shown in Figure 5-3 are presented. In Figure 8-5 (a), (b) and (c) an AFM maps of the samples shown in Figures 5-3 (d), Figure 5-3 (e) and Figure 5-3 (f) are shown, respectively. It is from these three 5x5 μm maps that the facet angle data was extracted. In all cases 10 measurements (five in each x/y pitch direction) were made first in order confirm that the pitch was correct and hence that there had been no x or y dimension scaling/stretching artefacts introduced. The pitches of all three AFM maps were found to be free from such stretching artefacts.

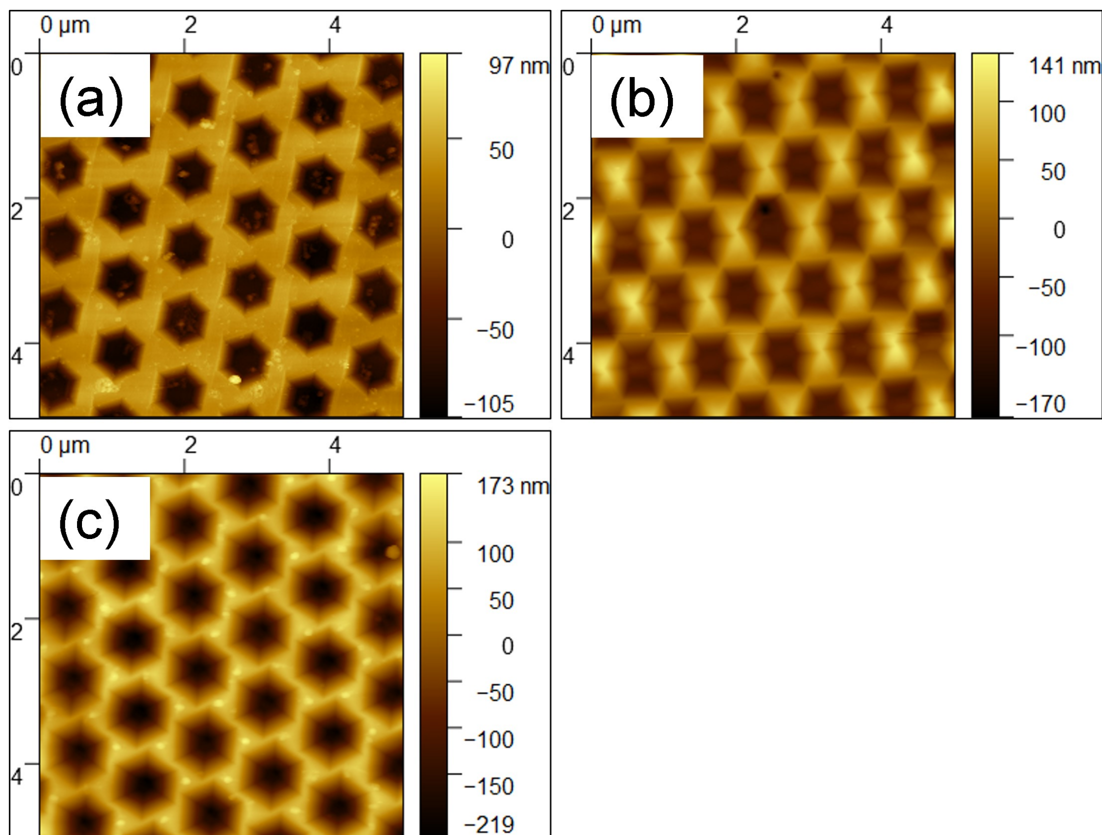

Figure 8-5: In (a) a 5x5 um AFM scan of a nanohole array sample with an initial dry etch depth of ~ 100 nm is shown after 2 minutes of KOH wet etching at 150 ^{o}C (same sample as that shown in Figure 5-3 (d)). In (b) a 5x5 um AFM scan of a nanohole array sample with an initial dry etch depth of ~ 150 nm is shown after 2 minutes of KOH wet etching at 150 ^{o}C (same sample as that shown in Figure 5-3 (e)). In (c) a 5x5 um AFM scan of a nanohole array sample with an initial dry etch depth of ~ 1000 nm is shown after 2 minutes of KOH wet etching at 150 ^{o}C (same sample as that shown in Figure 5-3 (f)).

AFM maps of samples and data presented in Figure 5-6

Figures 8-6 (a), (c) and (d) shows AFM maps of the sample presented in Figure 5-6 (e), (g) and (h) respectively. In Figure 8-6 (b) an AFM map of a similar sample (which has been etched for 15 seconds longer) to that in Figure 5-6 (f) is presented. The AFM maps in Figures 8-6 (b), (e) and (f) make up the data of the samples from which the plot in Figure 5-6 (l) was derived. All of the AFM maps in Figures 8-6 (a) - (f) were used to extract inclined plane angles via the Gwyddion software package. As with Figure 8-5 the pitch was checked in both the x and y directions to ensure no stretching artefacts were present in the AFM maps. This would lead to spurious data being extracted from the maps, however, these artefacts were not found to be present here.

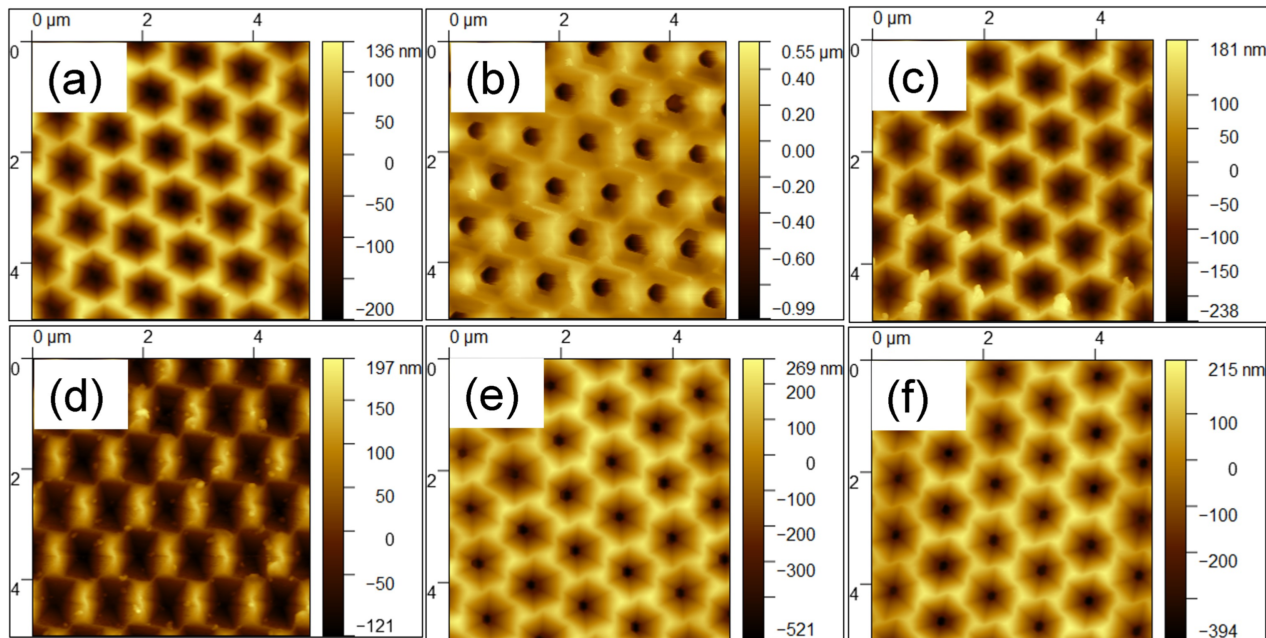

Figure 8-6: In (a) and AFM map of sample A (Figure 5-6 (a)) after wet etching in KOH at 150 ^{o}C for 120 seconds is presented. In (b) an AFM map of sample B (Figure 5-6 (b)) after wet etching in KOH at 150 ^{o}C for 75 seconds is presented. In (c) and AFM map of sample C (Figure 5-6 (c)) after wet etching in KOH at 150 ^{o}C for 120 seconds is presented. In (d) and AFM map of sample E (Figure 5-6 (d)) after wet etching in KOH at 150 ^{o}C for 120 seconds is presented. In (e) an AFM map of sample B after wet etching in KOH at 150 ^{o}C for 90 seconds is presented. In (f) an AFM map of sample B after wet etching in KOH at 150 ^{o}C for 105 seconds is presented.

Appendix 3

Here more details concerning the cleaning a fabrication details of all of the samples mentioned in Chapter 6 are tabulated.

More details about the fabrication process:

Sample and Spinning - all samples used wide 30W BARC baked at 80 ^oC for 60 s and then 200 ^oC for 90 s. All samples had resist baked at 90 ^oc for 90 seconds.

DTL - all samples were exposed using a 1.5 μm hexagonal periodic mask, $\sim$ 150 μm gap, with 120 ^oC 90 s post exposure bake, allowed to cool for 10 mins, developed in MFCD-26 developer for 01:30 mins.

Table 8.4: Fabrication details of a number of samples within this study. Samples taken from the same initial wafer are denoted with the same letter. Those with different numbers have different fabrication/processing conditions applied to them. On all samples the first fabrication step was to deposit a ~ 35 nm SiN_x mask layer via PECVD.

Table of sample processing							
	Patterning Processes			Cleaning Processes			
Sample	Spinning (all samples used wide 30W BARC baked at 80 ^oC for 60 s and then 200 ^oC for 90 s. All samples had resist bake at 90 ^oc for 90 seconds)	DTL (all samples - 1.5 μm hexagonal periodic mask, $\sim$ 150 μm gap, with 120 ^oC 90 s post exposure bake, allowed to cool for 10 mins, developed in MFCD-26 developer for 01:30 mins)	CHF_3 etch (ICP) (all samples had CHF_3 flow 25 sccm, RF power 50 W, ICP power 300 W, Chamber pressure 6.5 mTorr)	Piranha (all samples cleaned with a 3:1 ratio)	O_2 descum (O_2 flopw 50 sccm, RF power 40 W, ICP power 500 W, pressure 20 mTorr, unless otheriwise specified)	BOE (100:1 10 second dip unless otherwise specified)	Other Comments
A1 (GaN Alpha 1)	BARC (Wide 30W) + bake. Diluted Ultra I-123 photoresist + bake.	180 mJ exposure dose.	Temperature 45-66 ^{o}C. DC bias 272-274 V. Time 10 mins.	1x for $\sim$ 3 minutes.	None.	None.	This sample only had a piranha clean as part of the cleaning process.
A2 (Alpha 2nd clean)					Temperature 20 ^{o}C. DC bias 256-257 V. Time 15 minutes.	Yes.	Sample A1 with additional cleaning steps. Also had AZ400K dip for 10 seconds after BOE 100:1 10 second dip.
A3 (Alpha 3rd clean)				Piranha clean $\sim$ 5 minutes.	Temperature 20 ^{o}C. DC bias 255-253 V.	BOE 100:1 15 second dip.	This clean performed on sample A2.
G1 (Gamma no O_2)	BARC (Wide 30W) + bake. Undiluted PFI-88 photoresist + bake.	Exposure dose 160 mJ.	Temperature 62-63 ^{o}C. DC bias 283-286 V. Time 11 minutes.	Piranha clean $\sim$ 5 minutes. 4x cycles with BOE 100:1.	None.	4x cycles.	1 Piranha clean followed by BOE 100:1 dip repeated 4x to ensure sample surface was thoroughly clean.
G2 (Gamma 10 min O_2)				2x piranha cleans $\sim$ 5 minutes each.	Temperature 23-24 ^{o}C. DC bias 261-260 V. 10 minutes.	Yes.	2x Piranha cleans first, then O_2 descum and finally BOE 100:1 dip. All performed on G1 sample.
G3 (Gamma 1 min O_2)				1x Piranha clean $\sim$ 5 mins.	Temperature 24-25 ^{o}C. DC bias 257-259 V. 1 minute.	Yes.	1x piranha clean, O_2 descum and BOE 100:1 dip in that order to G1 sample.
B1 (beta no O_2)	BARC (Wide 30W) + bake. Undiluted PFI-88 + bake.	Exposure dose 180 mJ.	Temperature 42-43 ^{o}C. DC bias 287-288 V. Etch time 8 minutes.	2x Piranha clean $\sim$ 5 minutes each.	None.	1x Yes.	2x piranha cleans first, BOE 100:1 dip then performed.
B2 (Beta 10 mins O_2)				2x Piranha cleans $\sim$ 5 minutes each.	Temperature 23-24 ^{o}C. DC bias 261-260 V. 10 minutes.	1x Yes.	2x Piranha cleans first, O_2 descum, then BOE on a B1 sample.
B3 (2 min O_2)				1x Piranha clean $\sim$ 5 mins.	Temperature 24-25 ^{o}C. DC bias 258-259 V. 2 minutes.	Yes.	Piranha clean first, O_2 descum and then BOE 100:1 in order to the B1 sample.
B4 (Beta A no O_2)	B1.	B1.	Temperature 24-25 ^{o}C. DC bias 285-281 V. 7 minutes in total. Etched up until the SiN_x mask. O_2 etch then performed. Same conditions as O_2 descum, with RF power 50 W. Temperature 24-25 ^{o}C. DC bias 291-290 V. Time 1 minute. Calibrated BOE 5:1 used to etch through the remaining SiN_x mask.	2x piranha clean $\sim$ 5 minutes.	None.	1x Yes.	2x piranha then BOE on part of wafer B1 after optimised etching through SiN_x.
B5 (Beta A 3 min O_2)	B1.	B1.	B4.	2x piranha clean $\sim$ 5 minutes.	RF power 25 W, ICP power 300 W. Pressure 10 mTorr. Temperature 24-25 ^{o}C. DC bias 196-197 V. 3 minutes.	1x Yes.	2x piranha, O_2 descum then BOE on part of B1 after optimised etching through SiN_x.

Table 8.5: Fabrication details of samples not presented in Table 8.4 in this study. Samples taken from the same initial wafer are denoted with the same letter. Those with different numbers have different fabrication/processing conditions applied to them. On all samples the first fabrication step was to deposit a $\sim$ 35 nm SiN_x mask layer via PECVD.

Table of sample processing							
	Patterning Processes			Cleaning Processes			
Sample	Spinning (all samples used Wide 30W BARC baked at 80 ^oC for 60 s and then 200 ^oC for 90 s. All samples had resist bake at 90 ^oC for 90 seconds)	DTL (all samples - 1.5 μm hexagonal periodic mask, $\sim$ 150 μm gap, with 120 ^oC 90 s post exposure bake, allowed to cool for 10 mins, developed in MFCD-26 developer for 01:30 mins)	CHF_3 etch (ICP) (all samples had CHF_3 flow 25 sccm, RF power 50 W, ICP power 300 W, Chamber pressure 6.5 mTorr)	Piranha (all samples cleaned with a 3:1 ratio)	O2 descum (O_2 flow 50 sccm, RF power 40 W, ICP power 500 W, pressure 20 mTorr, unless otheriwise specified)	BOE (100:1 10 second dip unless otherwise specified)	Other Comments
B6 (Beta B/(C) no O_2)	B1.	B1.	Temperature 23-24 ^{o}C. DC bias 280-282 (278-280) V 6 mins (5 mins, 20 seconds). Calibrated to etch through SiN_x mask with minimal exposure of GaN to plasma.	2x piranha clean $\sim$ 5 minutes each.	None.	1x Yes.	2x piranha then BOE B1 after optimised etching through SiN_x.
B7 (Beta B(C) 3 min O_2)	B1.	B1.	B6.	2x piranha clean $\sim$ 5 mins each.	RF power 25 W, ICP power 300 W. Pressure 10 mTorr. Temperature 24-25 ^{o}C DC bias 196-197 V 3 minutes.	1x Yes.	2x piranha, O_2 descum then BOE on B1 after optimised etching through SiN_x.
B8 (Beta F (E))	B1.	B1.	Temperature 24-26 ^oC (23-25 ^{o}C). DC bias 278-281 (276-284) V. 8 mins (9 mins 30 s). Calibrated etch through SiN_x mask with minimal GaN exposure to plasma.	Acetone rinse. 1x Piranha clean $\sim$ 5 minutes.	RF power 25 W, ICP power 300 W. Pressure 10 mTorr. Temperature 24 ^{o}C. DC bias 195-197 V. 3 minutes.	Yes. 1x.	1x acetone, 1x piranha clean, O_2 descum and then BOE after calibrated CHF_3 etch from B1 wafer.
B9 (1 min Pir no O_2)	B1.	B1.	Temperature 26-27 ^{o}C. Dc bias 278V-274 V. Time 8 minutes.	1x $\sim$ 1 minute.	No.	1x Yes ($\sim$ 20 seconds).	Piranha then BOE only.
B10 (1min Pir 1min O_2)	B1.	B1.	B9.	1x $\sim$ 1 minute.	Temperature 25-26 ^{o}C. DC bias 260-259 V. 1 minute.	1x Yes ($\sim$ 20 seconds).	Piranha, O_2 descum then BOE.
B11 (2 min Pir no O_2)	B1.	B1.	B9.	1x $\sim$ 2 minute.	No.	1x Yes ($\sim$ 20 seconds).	Piranha then BOE only.
B12 (2 min Pir 1min O_2)	B1.	B1.	B9.	1x $\sim$ 2 minute.	B10.	1x Yes ($\sim$ 20 seconds).	Piranha, O_2 descum then BOE.
B13 (3 min Pir no O_2)	B1.	B1.	B9.	1x $\sim$ 3 minute.	No.	1x Yes ($\sim$ 20 seconds).	Piranha then BOE only.
B14 (3 min Pir 1min O_2)	B1.	B1.	B9.	1x $\sim$ 3 minute.	B10.	1x Yes ($\sim$ 20 seconds).	Piranha, O_2 descum then BOE.